PRESENT-DAY ICE-MASS CHANGE AND GLACIAL-ISOSTATIC ADJUSTMENT IN THE POLAR REGIONS FROM SATELLITE GRAVIMETRY AND GEOPHYSICAL MODELLING

Dissertation

zur Erlangung des Doktorgrades
der Naturwissenschaften (Dr. rer. nat.)
im Fachbereich Geowissenschaften
der Freien Universität Berlin

vorgelegt von
Ingo Sasgen
aus Düsseldorf

Freien Universität Berlin, 2009

1. Gutachter:	Prof. Dr. Maik Thomas
2. Gutachter:	Prof. Dr. Zdeněk Martinec
Tag der Einreichung:	17. Oktober 2008
Tag der mündlichen Prüfung:	10. Februar 2009

Contents

Abstract

This work is concerned with the determination of present-day ice-mass changes and glacial-isostatic adjustment (GIA) in the polar regions from gravity-field data of the satellite mission Gravity Recovery and Climate Experiment (GRACE). Aim is the separation of cryospheric mass changes from the mass redistribution in the Earth's mantle due to GIA using geophysical modelling and the determination of the contribution of glaciated areas to global sea-level change. This is done by analyzing the time series of monthly GRACE gravity-field solutions with respect to their long-term temporal changes. Filters are developed to optimize the trade-off between noise and spatial resolution in the GRACE gravity fields. Also, a method for the evaluation and combination of GRACE gravity fields from different processing is developed. Forward models of the potential disturbance due to present-day ice-mass changes and GIA are adjusted with respect to the GRACE observations and then used to perform a joint gravity-field inversion for the causative mass changes on and within the Earth. For small spatial scales (e.g. individual drainage basins of glaciers), ambiguities in the solution of this gravimetric inverse problem are reduced by introducing *a priori* constraints. The relative weight of this information with respect to the GRACE data allows determining the regional spatial resolution of the long-term changes in the GRACE gravity fields. The main region of interest of this work is Antarctica. In addition, investigations concerned with present-day ice-mass changes in Alaska and Greenland are presented, along with results on the gravity-field inversion in terms of the viscosity distribution in the Earth's mantle under North America.

Zusammenfassung

Diese Arbeit beschäftigt sich mit der Bestimmung rezenter Eismassenänderungen und der glazial-isostatischen Anpassung (GIA) in den Polarregionen aus den Schwerefelddaten der Satellitenmission Gravity Recovery and Climate Experiment (GRACE). Ziel ist es, die heutigen Massenänderungen in den Eisgebieten von der durch GIA verursachten Massenumverteilung im Erdmantel mittels geophysikalischer Modelle zu separieren und den Beitrag der vereister Gebiete zur globalen Meeresspiegeländerung zu bestimmen. Dazu werden die Zeitreihen monatlicher GRACE-Schwerefelder in Hinblick auf langzeitliche Änderungen analysiert. Zum einen werden Filter entwickelt, welche die als komplementär anzusehende räumliche Auflösung und Genauigkeit der GRACE-Schwerefelder optimieren. Desweiteren wird eine Methode entwickelt, die es erlaubt, GRACE-Schwerefelder verschiedener Prozessierungszentren zu kombinieren und deren Qualität zu bewerten. Modelle des durch rezente Eismassenänderungen und GIA verursachten Störpotentials werden an die GRACE-Beobachtungen angepasst und dann in einer gemeinsamen Schwerefeldinversion hinsichtlich der ursächlichen Massenänderungen auf und in der Erde ausgewertet. Bei der Betrachtung kleinräumiger Skalen (z.B. einzelner Einzugsgebiete von Gletschern) werden Mehrdeutigkeiten, die bei der Schwerefeldinversion auftreten, durch a priori Informationen reduziert. Die relative Gewichtung dieser zusätzlichen Information bezüglich der Genauigkeit der GRACE-Daten erlaubt es, die regionale Auflösung langzeitiger Trends in den GRACE-Schwerefeldern zu bestimmen. Im Wesentlichen wird in dieser Arbeit das Gebiet der Antarktis untersucht. Darüberhinaus werden Ergebnisse zur Schwerefeldinversion hinsichtlich Eismassenänderung in Alaska und Grönland sowie hinsichtlich der Viskositätsverteitung im Erdmantel Nordamerikas präsentiert.

1

Introduction

Aim of the investigations presented in this thesis is the determination of the present-day ice-mass change and glacial-isostatic adjustment (GIA) of the Earth in response to the retreat of the major ice sheets in the polar regions from Gravity Recovery and Climate Experiment (GRACE) satellite gravity data.

During the GRACE mission the Earth's gravitational potential is determined with unprecedented accuracy at regular, typically monthly, time intervals (e.g. Tapley *et al.*, 2004). The potential's temporal variations represent a constraint on mass movement within the Earth system associated with various geophysical processes (Figure 1.1). The largest contribution to the potential's temporal variation is caused by the the seasonal redistribution of water on the Earth's surface associated with the global hydrological cycle. But the increasing length of the GRACE time series (currently ∼ 6 years) allows the temporal linear trend in the potential to be determined with increasing reliability. Over land, these long-term changes (∼ 10 to 100 a) are mainly caused by mass changes of glaciers and ice sheets and by GIA following the retreat of the major ice sheets after the Last Glacial Maximum (LGM), ∼ 21 ka before present (BP). Other processes include interannual variations of the hydrological cycle and mass movement within the Earth's deep interior. Figure 1.6 shows the degree power of the rate of geoid-height change predicted for various long-term processes. The separation and quantification of the individual components of mass changes in the GRACE data by filtering and subsequent inversion of GRACE data using a forward modelling approach is the focus of this thesis.

The relevant results of this project are published in three scientific articles, Sasgen *et al.* (2006) (Section 4.4), Sasgen *et al.* (2007a) (Section 4.4) and Sasgen *et al.* (2007b) (Section 6.1), as well as in a manuscript, which is currently under the co-authors' revision (Sasgen *et al.*, 2008) (Section 6.4). Being the first author of these publications, their content is mainly subject to my responsibility. Apart from general scientific advices of the co-authors, my supervisor Prof. Dr. Martinec assisted with the theoretical formulation of the filter techniques presented in Sasgen *et al.* (2006) and Sasgen *et al.* (2007a). This dissertation includes these publications, along with an outline of the scientific framework they are embedded in. Additional unpublished results of the project supplement the published material. Because the peer-reviewed papers are included in a closed form and with only minor modifications (e.g. revised equation and figure numbering), some information may be redundantly presented, for which I would like to apologize to reader.

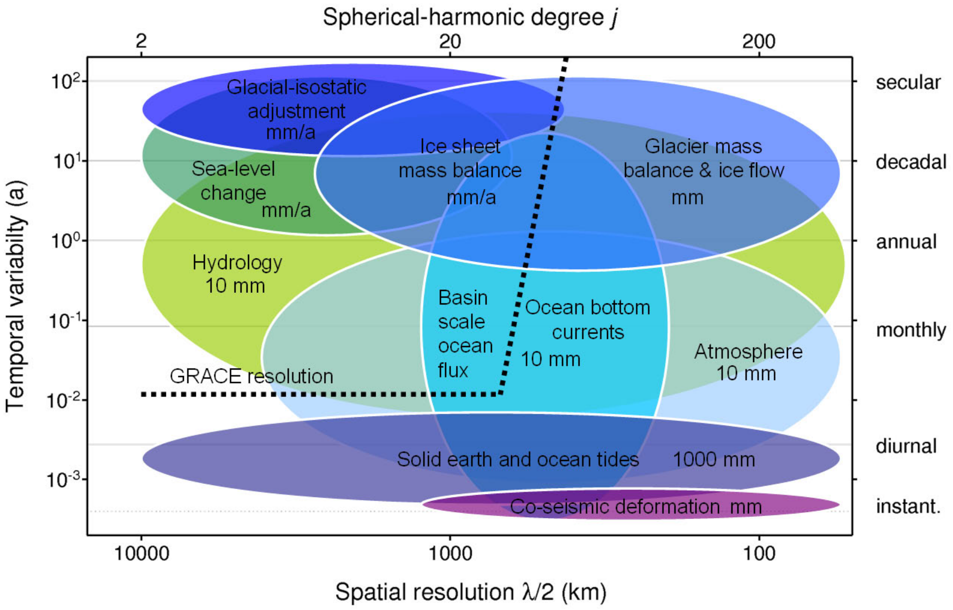

Figure 1.1: Geophysical processes and induced temporal variation of the geoid height (after Ilk *et al.*, 2005).

1.1 Polar ice sheets

The Antarctic Ice Sheet and the Greenland Ice Sheet are the largest contingent ice masses on Earth, and their development since their initial formation some 30 and 10 Ma ago, respectively, is closely linked to global climate and sea-level change (e.g. Siegert, 2001). The current mass of the Antarctic Ice Sheet is estimated to be ~ 56.6 m (Lythe *et al.*, 2001) that of the Greenland Ice Sheet to be ~ 7.3 m (Bamber *et al.*, 2001) equivalent sea-level (ESL)[1]. A better knowledge of the ice sheets' current state will lead to a better understanding of their role in the global climate system. This will contribute to better constraints on the cryosphere components of climate models and, hence, increase the reliability of climate predictions. The following summary is mainly based on Lemke *et al.* (2007), who the reader may consult for additional references.

The Transantarctic Mountains divide Antarctica into East and West Antarctica. The western part of the Antarctic Ice Sheet, the West Antarctic Ice Sheet, is based on bedrock below present-day sea-level with the majority of the slopes inclined land inward. This constellation disposes the West Antarctic Ice Sheet to rapid grounding line retreat favoring rapid disintegrations (Weertman, 1974; Oppenheimer, 1998; Schoof, 2007); the West Antarctic Ice Sheet holds the potential to change global mean sea level by 5 to 6 m ESL. Most vigorous changes are observed in the Amundsen Sea Sector, which is the region with discharge into Amundsen Sea, covering ~ 20% of the volume and area of the West Antarctic Ice Sheet. The ice streams and glaciers in this region are among the fastest in Antarctica exhibiting surface velocities of hundreds of m/a up to ~ 3 km/a (Figure 1.2). In contrast, most of the East Antarctic Ice Sheet rests on bedrock well above sea level in arid conditions and is therefore considered to be less sensitive to global climate change.

For Antarctica, most of the annual precipitation is assimilated by the ice sheet. The net annual flux of mass into the ice sheet, i.e. the sum of all processes of water transfer across its surface (precipitation, evaporation/sublimation, surface melting, wind abrasion, a. o.), is termed net surface-mass balance (Vaughan *et al.*, 1999) and is ~ -4.9 to -5.6 mm/a ESL. For comparison, the estimated sea-level contribution of the Antarctic Ice Sheet lies between -0.12 to 0.17 mm/a ESL (Shepherd & Wingham, 2007). The mass accumulated by the ice sheet is compacted to ice and moves, mainly driven by gravity, via ice streams (i.e. flow channeled in ice) and outlet glaciers (i.e. flow channeled in rock) to ice shelves in the periphery of the continent. From the ice shelves, to which the inflowing ice attaches, it is discharged to the ocean mainly by iceberg calving and basal melting, although re-freezing underneath the ice shelf may occur. The ice shelves represent ~ 10% of the area of the Antarctic Ice Sheet, and nearly all accumulated ice is discharged via the ice shelves, discharge rates being mainly controlled by ocean temperature and ocean circulation. Surface melting is of

---

[1] In this work, equivalent sea-level (ESL) is defined as the equivalent water volume of the ice mass under consideration divided by the global ocean area, fixed to $362 \times 10^6\,\mathrm{km}^2$, assuming the densities of water and ice of $\rho_\mathrm{W} = 910\,\mathrm{kg/m}^3$ and $\rho_\mathrm{I} = 1020\,\mathrm{kg/m}^3$, respectively. Values of the ESL are given in reference to the ocean system, meaning that a negative continental ice-mass change correspond to positive values of ESL.

minor importance for most of Antarctica. An exception is the Antarctic Peninsula, where mountain glaciers prevail that experience extensive surface melting in summer (e.g. van de Berg *et al.*, 2005). Figure 1.3 shows the spatial distribution of mean accumulation, approximated by the sum of precipitation and evaporation/sublimation) for the years 1958 to 2001 from the re-analysis project ERA-40 data of the European Centre for Medium-Range Weather Forecasts (ECMWF *[online]*). Accumulation rates are highest along the coastal fringe with its steep topographic gradient, along the Antarctic Peninsula and in the Amundsen Sea Sector.

Ice shelves appear to impede inflow of ice streams and glaciers, as they are stabilized by friction along their edges and by exalted seabed. It is observed that the collapse of an ice shelf can lead to acceleration of tributary ice streams and glaciers (e.g. Scambos *et al.*, 2004). Also, ice flow may be lubricated by water penetrating further into the interior of the ice sheet changing its basal conditions there. Ice shelves are in contact with ocean water that is considered to be an important factor for controlling its stability; warmer ocean temperatures may lead to increased basal melting and disintegration of ice shelves and, hence, reduce buttressing of ice streams and promote basal conditions of the ice sheets in favour of sliding and subglacial deformation. These changes of the glacier dynamics may penetrate tens to hundreds of km further into the ice sheet's interior (Thomas *et al.*, 2004; Rignot *et al.*, 2008) and may cause acceleration of ice flow, leading to negative ice mass balances and potentially to a further destabilization of the grounded portion of the ice sheet.

For the Greenland Ice Sheet, slow ice flow by internal deformation similar to that of the Antarctic Ice Sheet is important only in the central part of the ice sheet. Its extent is largely constrained by the topography and the continental shelf located some ten km from the present-day margin of ice sheet. Also, mainly due to warmer climate conditions, surface melting and associated discharge into the ocean accounts for about 60% of the mass outflow (Huybrechts *et al.*, 1991) and is particularly important for low-elevation regions along the coastal fringe, while above elevations of 2000 m it is rare. Most glaciers discharge directly into the ocean in fjords, although some ice shelves exist. Prominent region of extensive summer melting is the southernmost part, whereas mass loss by iceberg calving prevails in the eastern and western parts of the ice sheet. The climate conditions in the north are cold and dry, whereas the southeast expediences milder maritime conditions accompanied by larger precipitation due to this region's proximity to the North Atlantic.

Considering turnover times of the ice sheet on the order of several ka, delayed responses to past changes may partially be the cause for present-day ice-mass changes. However, it has been argued that the constraint on the ice sheet's past may not be sufficient for accurate predictions. Also, the spatial resolution of ice sheet-models for these predictions does not allow for small-scale processes and associated fast ice responses that are considered to be effective for readjusting to a dynamic equilibrium after perturbations in the past. Therefore, these processes are not considered in this investigation.

Primary indicator for an ice sheet's current state is the mass balance, which is the defined as the difference between mass input to the ice sheet and mass loss to the

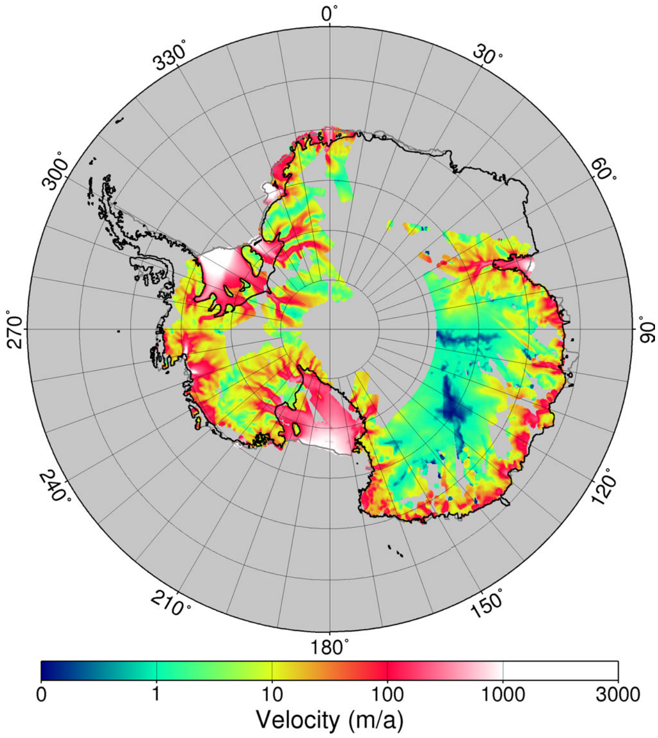

Figure 1.2: Ice-surface velocity in Antarctica from InSAR data (Rignot *et al.*, 2008).

ocean. It reflects the ice sheet's deviation from an idealized equilibrium state. It is influenced by interannual and long-term variability of the climate conditions and, hence, of the net surface-mass balance as well as by changes of the dynamics of the ice flow in response to contemporary and past variations of the ice sheet's boundary conditions (atmospheric, oceanic and basal conditions).

1.2 Mass balance estimates from satellite observations

Mass balances are estimated from Interferometric Synthetic Aperture Radar (InSAR) data using the mass budget method, which compares, for individual glacial drainage basins, InSAR-measured ice flow over the groundling line (Figure 1.2) with modelled or empirically estimated accumulation within each drainage basin. Outflow is determined by the surface velocity of the ice along the groundling line, which is considered to be representative also of flow velocities at greater depth of the moving ice column. Accumulation is often estimated using regional climate models, which are calibrated with *in situ* observations. Alternatively, *in situ* accumulation measurements are interpolated using horizons of snow layers identified, for example, by airborne radar measurements. The main uncertainty of this method are errors in the accumulation estimate, which are particularly large ($\sim 30\%$) for small and wet drainage basins (Rignot *et al.*, 2008).

Also, repeated measurements of the ice sheet's surface elevation with airborne|space

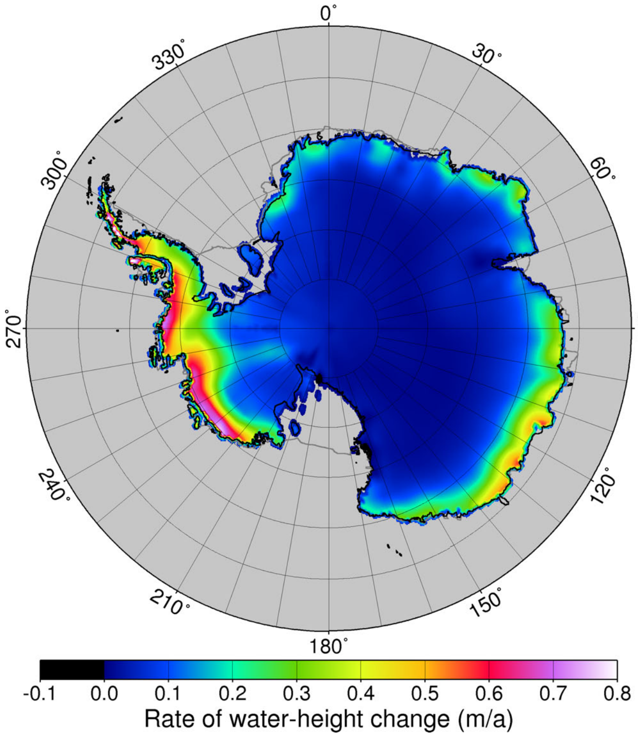

Figure 1.3: Spatial distribution of mean accumulation in Antarctica from ERA-40 data, approximated by the sum of precipitation and evaporation averaged for the years 1958 to 2001.

born radar|laser altimetry are used to estimate mass balances. Interpretation of surface-elevation changes in terms of ice-height changes requires the application of corrections for depth-dependent snow- and ice-density variations and for the vertical motion of the underlying bedrock. Most important is the accurate estimation of the snow column's density profile, with firn densification and snow compaction leading to uncertainties of 10 mm/a (Cuffey, 2001), compared to which bedrock motion is considerably smaller. For spaceborne radar altimetry measurements (e.g. European Remote Sensing Satellites, ERS-1 and ERS-2 *[online]*) an additional problem is the poor quality of the radar reflection for high-sloped regions along the fringe of the ice sheet, where most accumulation and discharge is expected to occur (Figure 1.3). Also, the reflection of high-elevation parts within the radar footprint (~ 20 km) dominates the signal, which may therefore contain only few information on changes of ice streams and glaciers residing in deep channels. Spaceborne laser altimetry operates with smaller footprints (65 m for the Ice, Cloud and Land Elevation Satellite, ICESat *[online]*) and is therefore also capable of resolving rougher terrain, but difficulties arise from cloud cover limiting the times for data acquisitions, as well as from the atmospheric conditions influencing the accuracy of the laser pointing.

The method investigated in this thesis focusses on the determination of the mass balance of the Antarctic Ice Sheet, the Greenland Ice Sheet and Alaska glaciers from

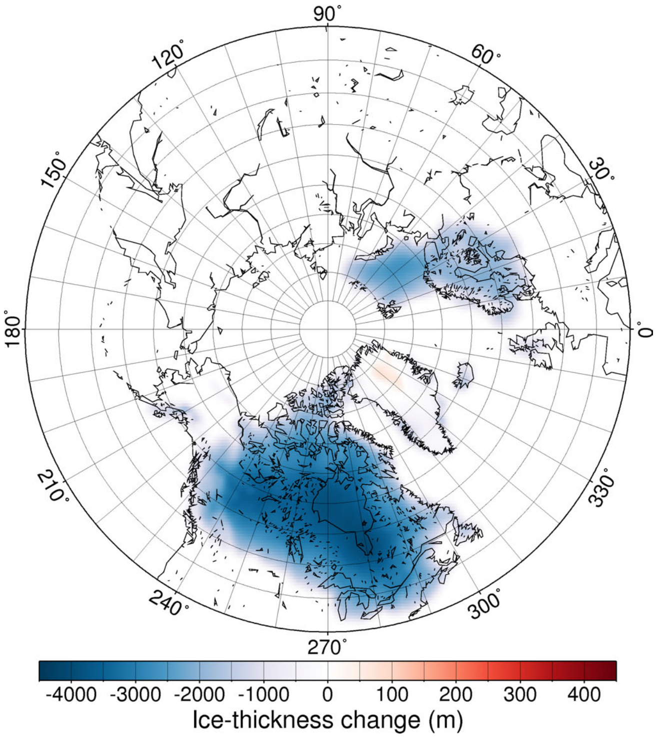

Figure 1.4: Northern Hemisphere deglaciation since the LGM as described by load model NAWI (Zweck & Huybrechts, 2005).

satellite-gravimetry measurements provided by GRACE. In contrast to the mass budget method and repeated altimetry, which are based on measurements of the ice sheets' geometry, GRACE data provide information on the temporal variations of the Earth's gravitational potential and, hence, indirectly on the causative mass changes. The principle problem with this method is that the potential disturbance represents the sum of various sources of mass change. In the polar regions, signal magnitudes comparable to those of present-day ice-mass changes are predicted for mass changes within the Earth's mantle due to GIA. To model this GIA signal and to separate it from the cryospheric changes in a combined inversion is the aim of this project.

1.3 Glacial-isostatic adjustment

Viscoelastic earth modelling

The Earth responds to changes of the load on its surface, for example, the retreat and re-advance of ice sheets, with viscoelastic deformation seeking to gain a new equilibrium state. This process is called GIA. The prediction of GIA is a classical problem in geophysics. Theory and numerical models solving this problem as well as first interpretations of GIA observations in terms of the Earth's viscoelastic structure date back to the mid-1970s (e.g. Peltier, 1974; Cathles, 1975). Since

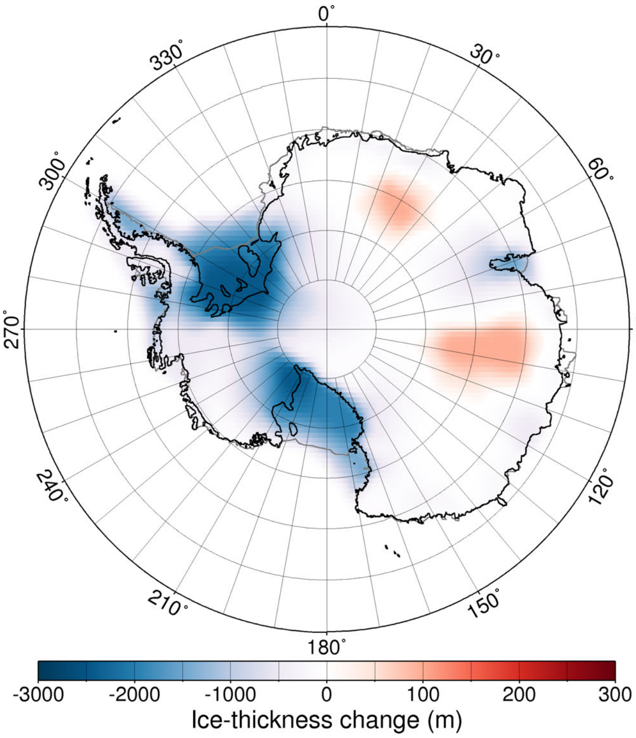

Figure 1.5: Antarctic deglaciation since the LGM as described by load model HUY (Huybrechts, 2002).

then, theoretical descriptions and their numerical implementation have continuously been advanced (e.g. Wu & Peltier, 1982; Yuen & Peltier, 1982; Wolf, 1987; Lambeck *et al.*, 1990; Mitrovica & Peltier, 1992; Fjeldskaar, 1994; Han & Wahr, 1995; Fang & Hager, 1995; Kaufmann & Wolf, 1996; Vermeersen *et al.*, 1996; Wu & Ni, 1996; Vermeersen & Sabadini, 1997; Nakada, 1999). Current models include the solution of the sea-level equation (Farrell & Clark, 1976; Hagedoorn *et al.*, 2007), which governs mass redistributions in the ice|ocean system and moving of coastlines, GIA-induced variations of the Earth's rotation (e.g. Mitrovica *et al.*, 2005; Martinec & Hagedoorn, 2005; Sabadini & Vermeersen, 2002) and two- and three-dimensional distributions of mantle viscosities (e.g. Gasperini & Sabadini, 1989, 1990; Kaufmann & Wolf, 1999; Wu *et al.*, 1998; Zhong *et al.*, 2005; Tromp & Mitrovica, 1999a,b; Martinec, 2000) and may allow for non-Newtonian rheologies (e.g. Giunchi & Spada, 2000) and compressible viscoelasticity (e.g. Zhong *et al.*, 2005). Further developments will allow us to consider non-hydrostatic pre-stresses obtained from mantle convection modelling and physical coupling of earth and load models as da well as ta assimilation. In this thesis, a radially symmetric self-gravitating Maxwell viscoelastic earth model based on the solution method proposed in Martinec (2000) is used. Its theory is outlined in Section 2.4.

Inversion of GRACE data for GIA

So far, most of the GIA-related investigations of GRACE data represent first comparisons of predictions and observations. For example, GIA signals were identified and evaluated over North America, (e.g Tamisiea *et al.*, 2007), Antarctica (e.g. Sasgen *et al.*, 2007a) and Fennoscandia, (e.g. Steffen *et al.*, 2008). Although most predicted GIA signals are distinct features in the gravity fields' linear trend, uncertainties remain with respect to contemporary mass-change processes overlapping GIA signals, such as interannual hydrological variations in North America (e.g. Rangelova *et al.*, 2007; Rangelova & Sideris, 2008) and present-day ice-mass changes and tidal aliasing in Antarctica (e.g Moore & King, 2008). Nevertheless, Paulson *et al.* (2007a,b) used GRACE over North America together with palaeo sea-level indicators (SLI) to invert the GIA signal for mantle viscosities. In contrast, Tamisiea *et al.* (2007) used the GRACE data as constraint on geometry of the Laurentide Ice Sheet in North America during the LGM.

1.4 Satellite gravimetry

For about three decades, measurements of satellite orbits, for example, by ground-based laser ranging within the Laser Geodynamics Satellite (LAGEOS) satellite mission, have been used to determine the static gravitational potential of the Earth. Early missions have mainly provided information on the long-wavelength component of the Earth's gravitational potential, because the satellites were released at high altitudes (LAGEOS at ~ 6000 km) to reduce the influence of non-gravitational accelerations (mainly atmospheric drag). Further shortcomings of the early missions were the insufficient reduction of residual non-gravitational accelerations, the poor orbit determination based on terrestrial networks only, and missing coverage at high latitudes (e.g. NRC Committee on Earth Gravity from Space, 1997).

The GRACE succeeds the Deutsche Zentrum für Luft- und Raumfahrt (DLR) mission Challenging Minisatellite Payload (CHAMP), which successfully implemented satellite-to-satellite tracking (SST) of type high-low (commonly between GPS satellites and LEOs) for satellite gravimetry, magnetometery and atmospheric sounding. For GRACE, high-low SST is combined with low-low SST (between two LEOs) by two identical satellites in the same near-polar orbit, which measure their distance with submicron precision by a mircowave ranging system. This measurement along with the measurements of gravitational and non-gravitational accelerations using onboard accelerometers allow the determination of the Earth's static gravity field and its temporal variations on time scales of ~ 30 days with unprecedented accuracy (e.g. Tapley *et al.*, 2004a).

Currently, the GRACE mission lifetime is estimated up to 2012 to 2018 (Schmidt, 2007), depending on the scenario of non-gravitational drag. A temporal satellite-gravimetry mission, GRAF, succeeding GRACE and continuing the time series is currently in discussion. Modifications of mission parameters (e.g. lower altitudes and larger masses of the satellites) for increasing mission performance (e.g. spatial

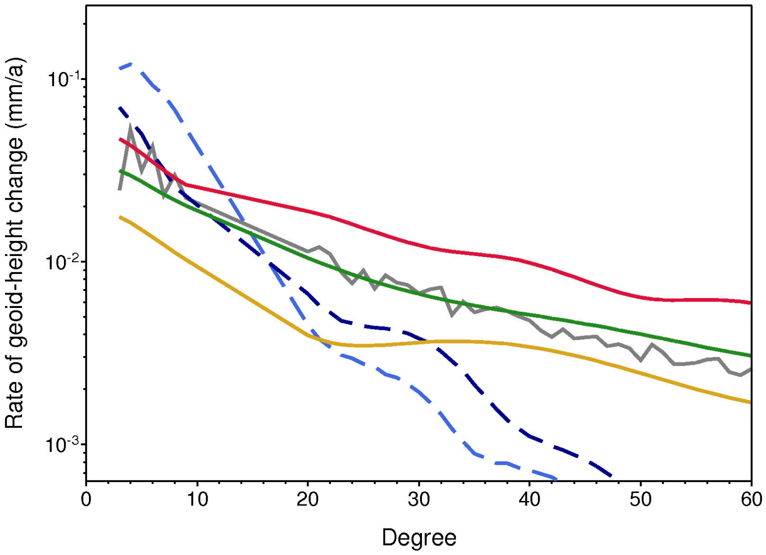

Figure 1.6: Degree-power spectrum of the predicted rate of geoid-height change due to present-day ice-mass changes and GIA. The predictions include glacier melting in Antarctica (Rignot & Thomas, 2002; Thomas *et al.*, 2004, red), Greenland (Krabill *et al.*, 2000; Rignot & Kanagaratnam, 2006, orange) and Alaska (Arendt *et al.*, 2002, green), GIA on the Northern Hemisphere (dark blue) and in Antarctica (light blue) calculated using the glacial histories of Huybrechts (2002) and Zweck & Huybrechts (2005), respectively. Also indicated is the temporal linear trend of the continental hydrological variations (grey) estimated from the WaterGAP Global Hydrology Model (WGHM, Döll *et al.*, 2003) for January 2002 to June 2007.

resolution) are currently assessed with simulations. In parallel, substantial changes of the mission geometry and satellite instrumentation, such as SST by a laser ranging system are investigated for the further development of temporal satellite gravimetry.

1.5 Outline

The thesis is organized as follows. Section 2 describes the forward modelling of potential disturbances in the polar regions related to mass redistribution on and within the Earth. Section 3 introduces satellite-based recovery of the Earth's gravitational potential with GRACE, while focussing on the dynamic approach of monthly gravity-field determination used at GFZ. In Section 4, error characteristics of the GRACE data are presented, along with post-processing methods for the enhancement of the desired geopysical signals. Section 5 introduces the gravimetric inverse problem of determining mass changes from their associated potential disturbances. Approaches to solve this problem for the GRACE data are outlined and the method of adjusting the forward models detailed in Section 2 is described. In Section 6 results of the inversion of GRACE data for ice-mass changes and GIA in the polar regions are presented and discussed. Section 7 summarizes the results of this project and presents ideas for further developements.

2

Modelling of potential disturbances in global ice regimes

This chapter outlines the basic theory underlying the computational forward models used in this study. Section 2.1, presents the solution of the Poisson equation represented in terms of spherical-harmonic functions. Section 2.2 introduces the concept of surface-mass changes and the associated potential disturbances. The theory for calculating the response of the Earth's body to surface-mass changes is described in Section 2.3 and Section 2.4. It is distinguished between instantaneous mass changes ($\sim 10\,\mathrm{a}$, present-day ice-mass changes), for which the Earth's response is assumed to be purely elastic, and long-term surface-mass changes (~ 100 to $1000\,\mathrm{a}$, glaciation histories), for which the consideration of the more complex viscoelastic deformation of the Earth's body is required. The outline of the viscoelastic theory is formulated according to Wolf (1997), Klemann *et al.* (2003) and Wolf (2003) and mainly taken from Sasgen *et al.* (2005). The solutions of the associated field equations subject to the interface conditions follows the spectral finite-element method developed by Martinec (2000), which is also the numerical approach underlying the computation of the perturbation of the viscoelastic earth model used in this study.

2.1 Solution of the Poisson equation for spherical geometry

The gravitational potential at point $(r, \mathbf{\Omega})$ of the density distribution $\varrho(r', \mathbf{\Omega}')$ within the Earth is expressed by Newton's integral

$$V(r, \mathbf{\Omega}) = G \int_{\mathbf{\Omega}_0} \int_{r'=0}^{r_s(\mathbf{\Omega}')} \frac{\varrho(r', \mathbf{\Omega}')}{|\mathbf{r} - \mathbf{r}'|} (r')^2 dr' d\mathbf{\Omega}', \tag{2.1}$$

where G is the gravitational constant of $6.67259 \times 10^{-11}\ \mathrm{m^3 kg^{-1} s^{-2}}$, and $\mathbf{\Omega}$ stands for the spherical co-latitude ϑ and longitude φ, hence $\mathbf{\Omega} := (\vartheta, \varphi)$, $\mathbf{\Omega}_0$ is the full solid angle and $d\mathbf{\Omega}$ is its infinitesimal element, and $r_s(\mathbf{\Omega})$ is the radial distance to the Earth's surface in a geocentric coordinate system. For the problems investigated here, spherical geometry is assumed and $r_s(\mathbf{\Omega})$ is approximated by R, which is the mean radius of the Earth.

The expansion of the reciprocal distance $|\mathbf{r} - \mathbf{r}'|^{-1}$ for $r > r'$ in the Legendre polynomials is (e.g. Heiskanen & Moritz, 1967)

$$\frac{1}{|\mathbf{r}-\mathbf{r}'|}=\frac{1}{r}\sum_{j=0}^{\infty}\left(\frac{r'}{r}\right)^{j}P_j(\cos\Psi), \tag{2.2}$$

where Ψ is the angular distance between $\mathbf{\Omega}$ and $\mathbf{\Omega}'$. Application of the addition theorem for spherical-harmonic functions (A.14) allows us to express the reciprocal distance according to

$$\frac{1}{|\mathbf{r}-\mathbf{r}'|}=\frac{4\pi}{r}\sum_{j=0}^{\infty}\frac{1}{2j+1}\left(\frac{r'}{r}\right)^{j}\sum_{m=-j}^{j}Y_{jm}(\mathbf{\Omega})Y^{*}_{jm}(\mathbf{\Omega}'), \tag{2.3}$$

where $Y_{jm}(\mathbf{\Omega})$ are the fully normalized surface spherical-harmonic functions (Section A.1) and the asterisk denotes complex conjugation.

With the spherical-harmonic expansion of the density distribution according to (A.1),

$$\varrho(r',\mathbf{\Omega}')=\sum_{j=0}^{\infty}\sum_{m=-j}^{j}\varrho_{jm}(r')Y_{jm}(\mathbf{\Omega}'), \tag{2.4}$$

and by substitution of (2.4) into (2.1) as well as by application of the orthonormality relation of the spherical-harmonic functions (A.5), Newton's integral (2.1) can be expressed by

$$V(r,\mathbf{\Omega})=4\pi G r\sum_{j=0}^{\infty}\sum_{m=-j}^{j}\left[\frac{1}{2j+1}\int_{r'=0}^{R}\left(\frac{r'}{r}\right)^{j+2}\varrho_{jm}(r')dr'\right]Y_{jm}(\mathbf{\Omega}). \tag{2.5}$$

For temporal variations of the density distribution, (2.1) becomes

$$V(r,\mathbf{\Omega},t)=G\int_{\mathbf{\Omega}_0}\int_{r'=0}^{R}\frac{\varrho(r',\mathbf{\Omega}',t)}{|\mathbf{r}-\mathbf{r}'|}(r')^2dr'd\mathbf{\Omega}', \tag{2.6}$$

and, by analogy,

$$V(r,\mathbf{\Omega},t)=4\pi G r\sum_{j=0}^{\infty}\sum_{m=-j}^{j}\left[\frac{1}{2j+1}\int_{r'=0}^{R}\left(\frac{r'}{r}\right)^{j+2}\varrho_{jm}(r',t)dr'\right]Y_{jm}(\mathbf{\Omega}), \tag{2.7}$$

for the associated temporal variations of the potential disturbances.

2.2 Potential disturbance of surface-mass changes

The external gravitational potential $V(r,\mathbf{\Omega})$ can be divided into the component induced by the density distribution within the Earth and within a thin layer of thickness h on its surface, $V^{\mathrm{I}}(r,\mathbf{\Omega})$ and $V^{\mathrm{S}}(r,\mathbf{\Omega})$, respectively. With the linearity of the Poisson equation with respect to the potential and source terms, it holds that

$V(r,\mathbf{\Omega}) = V^{\mathrm{I}}(r,\mathbf{\Omega}) + V^{\mathrm{S}}(r,\mathbf{\Omega})$. For the limit of surface masses in a layer of infinitesimal thickness, i.e. Helmert's second condensation (Helmert, 1884), Newton's integral simplifies to

$$V^{\mathrm{S}}(r,\mathbf{\Omega}) = G\int_{\mathbf{\Omega}_0} \frac{\sigma(\mathbf{\Omega}')}{|\mathbf{r}-\mathbf{r}'|} R^2 d\mathbf{\Omega}', \tag{2.8}$$

where

$$\sigma(\mathbf{\Omega}) = \frac{1}{R^2}\int_{r=R}^{R+h} \varrho(r,\mathbf{\Omega}) r^2 dr \tag{2.9}$$

is called surface-mass density. With (2.3) and $\sigma(\mathbf{\Omega}) = \sum_{jm}\sigma_{jm}Y_{jm}(\mathbf{\Omega})$, the potential disturbances at the Earth's surface are given by

$$V^{\mathrm{S}}(R,\mathbf{\Omega}) = 4\pi GR\sum_{j=0}^{\infty}\sum_{m=-j}^{j}\left[\frac{1}{2j+1}\sigma_{jm}\right]Y_{jm}(\mathbf{\Omega}). \tag{2.10}$$

Comparison with the expansion of the potential disturbance to fully normalized spherical harmonics,

$$V^{\mathrm{S}}(R,\mathbf{\Omega}) = \sum_{j=0}^{\infty}\sum_{m=-j}^{j} V^{\mathrm{S}}_{jm}Y_{jm}(\mathbf{\Omega}), \tag{2.11}$$

relates the potential coefficients, V^{S}_{jm}, to the coefficients of the distribution of the surface-mass density:

$$V^{\mathrm{S}}_{jm} = 4\pi GR\frac{1}{2j+1}\sigma_{jm}. \tag{2.12}$$

For some investigations with very small spatial scales, the Earth's body may be approximated as a rigid sphere and the potential disturbance can be calculated by (2.12). However, in general, the Earth responds to mass changes on its surface with deformation, which induces a potential disturbance V^{I} in addition to V^{S}. This contribution may be separated into an elastic component $V^{\mathrm{I}}_{\mathrm{el.}}$ caused by the Earth's instantaneous response to present-day surface-mass changes (Section 2.3), and a viscoelastic component $V^{\mathrm{I}}_{\mathrm{visc.}}$ induced by the delayed mass readjustment within the Earth to perturbations of the isostatic equilibrium of past surface-mass changes (i.e. increment of the gravitational potential $\phi^{(\Delta)}$ in Section 2.4).

Here, temporal variations of the potential disturbances are considered, $V(r,\mathbf{\Omega},t) = V^{\mathrm{I}}(r,\mathbf{\Omega},t) + V^{\mathrm{S}}(r,\mathbf{\Omega},t)$, which are discretized with regard to the temporal GRACE resolution according to $\Delta V(r,\mathbf{\Omega},t) = V(r,\mathbf{\Omega},t_n) - V(r,\mathbf{\Omega},t_m)$, with $t_m < t_n$ and $t_n - t_m \approx 30$ days, assuming that static components do not change for $t \in < t_m, t_n >$, which also removes unknown static components of the gravitational potential.

With Bruns's theorem (e.g. Heiskanen & Moritz, 1967; Martinec, 1998), the geoid height and its temporal variations, $N_{jm}(t)$, can be approximated by

$$N_{jm}(t) \approx \frac{V_{jm}(t)}{g_0} = \frac{4\pi GR}{g_0}\frac{1}{2j+1}\sigma_{jm}(t), \tag{2.13}$$

where $g_0 \approx 9.81\,\mathrm{m/s^2}$ is the mean gravitational acceleration on the Earth's surface and

$$N(\mathbf{\Omega}, t) = \sum_{j=0}^{\infty} \sum_{m=-j}^{j} N_{jm}(t) Y_{jm}(\mathbf{\Omega}). \tag{2.14}$$

Figures in this thesis represent potential disturbances by the associated change in the geoid height calculated according to (2.13) and (2.14).

2.3 Elastic earth response

For mass redistributions on time scales $\sim 10\,\mathrm{a}$, the Earth's deformation can be considered as instantaneous (e.g. Cathles, 1975; Klemann, 2003), independent of preceding mass redistributions and governed only by the Earth's elastic parameters, i.e. the elastic bulk modulus κ and elastic shear modulus μ (Section 2.4).

The elastic deformation and associated potential disturbance $V^{\mathrm{I}}_{\mathrm{el.}}$ is calculated by convolution of the Green's function to an impulsive forcing $q^{\delta}(\mathbf{\Omega})$ with the loading surface-mass distribution $\sigma(\mathbf{\Omega})$. The convolution is expressed by

$$V^{\mathrm{I}}_{\mathrm{el.}}(\mathbf{\Omega}) = 4\pi G R \int_{\mathbf{\Omega}_0} q^{\delta}(\mathbf{\Omega} - \mathbf{\Omega}') \sigma(\mathbf{\Omega}') d\mathbf{\Omega}'. \tag{2.15}$$

Following the derivation in Section A.2, the convolution integral's spectral representation with the simplification of a radially symmetric distribution of elastic parameters is

$$V^{\mathrm{I}}_{\mathrm{el.}}(\mathbf{\Omega}) = 4\pi G R \sum_{j} q^{\delta}_{j0} \sqrt{\frac{4\pi}{2j+1}} \sum_{m} \sigma_{jm} Y_{jm}(\mathbf{\Omega}). \tag{2.16}$$

With the normalization $q'_j = \sqrt{4\pi(2j+1)} q^{\delta}_{j0}$, the potential disturbance can be expressed by

$$V_{jm} = V^{\mathrm{I,el.}}_{jm} + V^{\mathrm{S}}_{jm} = 4\pi G R \frac{1}{2j+1} (q'_j + 1) \sigma_{jm}, \tag{2.17}$$

where q'_j are the elastic surface load Love numbers (e.g. Farrell, 1972; Wahr *et al.*, 1998; Han & Wahr, 1995). The elastic load Love numbers are shown in Figure 2.1 for the incompressible and compressible elastic parameterizations according to the Preliminary Reference Earth Model (PREM, Dziewonski & Anderson, 1981). Here, $q_j = q'_j + 1$ represents the potential disturbance by the surface-mass change and by the associated Earth's elastic deformation. For the approximation of the Earth's body as a rigid sphere $q'_j = 0$ and, hence, $q_j = 1$. The load Love number q'_j for $j = 0$, which describes the variation of the total mass within the Earth, is, by definition, 1 for mass conservation. The load Love number q'_j for $j = 1$ represents the variation of position of the center of mass with respect to the chosen coordinate system. It is here 0, such that the center of mass reference frame is realized.

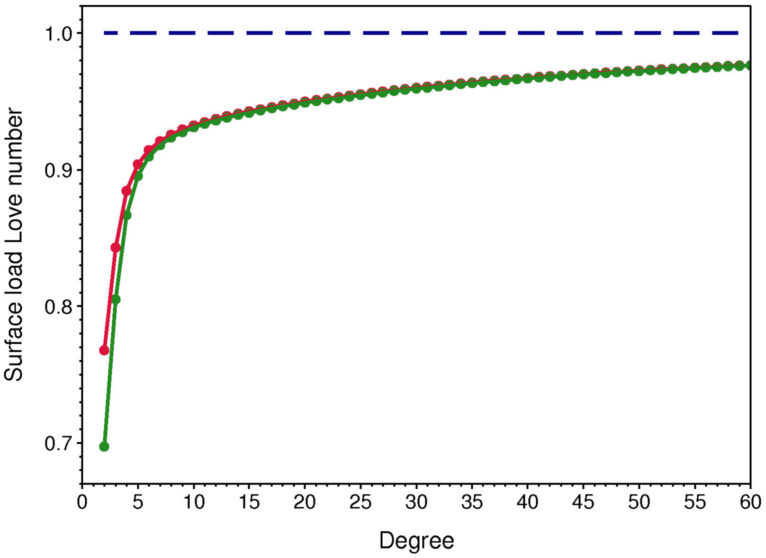

Figure 2.1: Spectral convolution function for the elastic-incompressible (red), elastic-compressible (green) and rigid (dashed blue line) earth model. Shown are $q_j = q'_j + 1$, which represent the sum of surface potential disturbances by direct gravitational attraction and by the elastic Earth response (surface load Love numbers).

2.4 Viscoelastic earth response

Glacial isostasy is concerned with the gravitational-viscoelastic response of the Earth to surface loads. To derive the governing incremental field equations and interface conditions, infinitesimal perturbations of a compositionally and entropically stratified, compressible Earth initially in hydrostatic equilibrium are considered, where the perturbations are assumed to be isocompositional and isentropic. In the following, the Lagrangian representation of arbitrary tensor fields, $f_{ij...}(\mathbf{X}, t)$, will be used, which refers the field values to the current position, $r_i(\mathbf{X}, t)$, of a particle whose initial position, X_i, at the time epoch $t = 0$ is taken as the spatial argument. The total field, $f_{ij...}(\mathbf{X}, t)$, is then decomposed according to $f_{ij...}(\mathbf{X}, t) = f^{(0)}_{ij...}(\mathbf{X}) + f^{(\delta)}_{ij...}(\mathbf{X}, t)$, where $f^{(0)}_{ij...}(\mathbf{X})$ is the initial field and $f^{(\delta)}_{ij...}(\mathbf{X}, t)$ is the material incremental field, i.e. the increment with respect to the particle. Sometimes, it is more convenient to consider the spatial incremental field, i.e. the increment with respect to a fixed location, given by $f^{(\Delta)}_{ij...} = f^{(\delta)}_{ij...} - f^{(0)}_{ij...,k} u_k$, where u_i is the particle displacement. For the material gradient of a field, we use $f_{ij...,k}(\mathbf{X}, t) := \partial f_{ij...}(\mathbf{X}, t)/\partial X_k$. Henceforth, the arguments r_i and t will be suppressed.

2.4.1 Equations for the total fields

For a gravitating Earth undergoing quasi-static perturbations of some initial state, the momentum equation is

$$\tau_{ij,j} + \rho^{(0)} g_i = 0, \tag{2.18}$$

where τ_{ij} is the non-symmetric Piola-Kirchhoff stress, $\rho^{(0)}$ the initial volume mass density and g_i the gravitational force per unit mass. The field g_i is given by

$$g_i = \phi_{,j} b^{-1}_{ji}, \tag{2.19}$$

with ϕ the gravitational potential and b^{-1}_{ij} the inverse of $b_{ij} := r_{i,j}$. The gravitational potential equation can be written as

$$j(\phi_{,ij} b^{-1}_{ik} b^{-1}_{jk} + \phi_{,i} b^{-1}_{ik,j} b^{-1}_{jk}) = -4\pi G \rho^{(0)}, \tag{2.20}$$

where $j := \det[b_{ij}]$ is the Jacobian determinant and G Newton's gravitational constant. The constitutive equation is of the form

$$t_{ij} = t^{(0)}_{ij} + \mathcal{M}_{ij}[r_{m,k}(t-t')\, r_{m,\ell}(t-t') - \delta_{k\ell}], \tag{2.21}$$

where $t_{ij} = j^{-1} b_{kj} \tau_{ik}$ is the symmetric Cauchy stress tensor, $\mathcal{M}_{ij}$ the anisotropic relaxation functional transforming the strain history given by the term in brackets into the current material incremental Cauchy stress, t' the excitation time epoch and δ_{kl} the Kronecker delta. With $\mathcal{M}_{ij}$, $t^{(0)}_{ij}$ and $\rho^{(0)}$ prescribed, (2.18)–(2.21) constitute the system of total field equations for r_i, t_{ij}, and ϕ.

In order to incorporate ice and water loads, the gravitating Earth is assumed to possess (internal or surficial) interfaces of discontinuity occupied by material sheets whose interface or surface mass density, σ, is prescribed. Then, according to Klemann (2003) and Wolf (2003) the following interface conditions result from (2.18)–(2.21):

$$[r_i]^+_- = 0, \tag{2.22}$$

$$[\phi]^+_- = 0, \tag{2.23}$$

$$[n_i \phi_{,j} b^{-1}_{ji}]^+_- = -4\pi G \sigma, \tag{2.24}$$

$$[n_j t_{ij}]^+_- = -g_i \sigma. \tag{2.25}$$

2.4.2 Equations for the initial fields

Commonly, the Earth is assumed to be initially in hydrostatic equilibrium, which results in a radially symmetric density distribution. With the mechanical pressure defined by $p := -t_{ii}/3$, then $t^{(0)}_{ij} = -\delta_{ij} p^{(0)}$ applies and (2.18)–(2.21) reduce to

$$-p^{(0)}_{,i} + \rho^{(0)} g^{(0)}_i = 0, \tag{2.26}$$

$$g^{(0)}_i = \phi^{(0)}_{,i}, \tag{2.27}$$

$$\phi^{(0)}_{,ii} = -4\pi G \rho^{(0)}, \tag{2.28}$$

$$p^{(0)} = \xi(\rho^{(0)}, \lambda^{(0)}, \psi^{(0)}). \tag{2.29}$$

The last expression is the state equation, ξ the state function, $\lambda^{(0)}$ a field representing the initial composition and $\psi^{(0)}$ the initial entropy density. With ξ, $\lambda^{(0)}$ and $\psi^{(0)}$ prescribed, (2.26)–(2.29) constitute the system of initial hydrostatic field equations for $g_i^{(0)}$, $p^{(0)}$, $\rho^{(0)}$ and $\phi^{(0)}$.

Supposing $\sigma^{(0)} = 0$, the following initial interface conditions are obtained from (2.22)–(2.25):

$$[r_i^{(0)}]_-^+ = 0, \tag{2.30}$$

$$[\phi^{(0)}]_-^+ = 0, \tag{2.31}$$

$$[n_i^{(0)}\phi_{,i}^{(0)}]_-^+ = 0, \tag{2.32}$$

$$[p^{(0)}]_-^+ = 0. \tag{2.33}$$

2.4.3 Equations for the incremental fields

After decomposition of the total fields in (2.18)–(2.21) into initial and incremental parts followed by linearization with respect to the increments, we obtain, for isotropy,

$$t_{ij,j}^{(\delta)} + (p_{,j}^{(0)}u_j)_{,i} - g_i^{(0)}(\rho^{(0)}u_j)_{,j} + \rho^{(0)}g_i^{(\Delta)} = 0, \tag{2.34}$$

$$g_i^{(\Delta)} = \phi_{,i}^{(\Delta)}, \tag{2.35}$$

$$\phi_{,ii}^{(\Delta)} = 4\pi G(\rho^{(0)}u_i)_{,i}, \tag{2.36}$$

$$\begin{aligned} t_{ij}^{(\delta)} &= \delta_{ij}\int_0^t [m_1(t-t') - \tfrac{2}{3}m_2(t-t')]\, d_{t'}[u_{k,k}(t')]\, dt' \\ &\quad + \int_0^t m_2(t-t')\, d_{t'}[u_{i,j}(t') + u_{j,i}(t')]\, dt', \end{aligned} \tag{2.37}$$

where m_1 and m_2 are the bulk- and shear-relaxation functions, respectively, and symbols d_t and d_t^2 denote the first- and second-order material time-derivative operators, respectively. With m_1 and m_2 prescribed and the initial fields given as the special solution to the initial field equations and interface conditions, (2.34)–(2.37) constitute the material-local form of the incremental gravitational-viscoelastic field equations for $g_i^{(\Delta)}$, $t_{ij}^{(\delta)}$, u_i and $\phi^{(\Delta)}$.

Decomposing the total fields in (2.22)–(2.25) into initial and incremental parts followed by linearization gives

$$[u_i]_-^+ = 0, \tag{2.38}$$

$$[\phi^{(\Delta)}]_-^+ = 0, \tag{2.39}$$

$$[n_i^{(0)}(\phi_{,i}^{(\Delta)} - 4\pi G\rho^{(0)}u_i)]_-^+ = -4\pi G\sigma, \tag{2.40}$$

$$[n_j^{(0)}t_{ij}^{(\delta)}]_-^+ = -g_i^{(0)}\sigma. \tag{2.41}$$

Before solving (2.34)–(2.37) subject to the interface conditions (2.38)–(2.41), the relaxation functions must be specified. In the following, (2.37) is specialized for elastic-compressible and a viscoelastic-incompressible material.

2.4.4 Elastic-compressible constitutive equation

Partial integration of (2.37) allows us to separate the stress depending on the current time epoch, i.e. the elastic stress, from the stress depending on all previous time epochs, i.e the viscoelastic stress:

$$\begin{aligned}
t_{ij}^{(\delta)} &= \delta_{ij}\big[m_1(0)u_{k,k}(t) - \tfrac{2}{3}m_2(0)u_{k,k}(t) \\
&\quad - \int_0^t d_{t'}m_1(t-t')\,[u_{k,k}(t')]\,dt' \\
&\quad + \tfrac{2}{3}\int_0^t d_{t'}m_2(t-t')\,[u_{k,k}(t')]\,dt'\big] \\
&\quad + m_2(0)[u_{i,j}(t)+u_{j,i}(t)] - \int_0^t d_{t'}m_2(t-t')\,[u_{i,j}(t')+u_{j,i}(t')]dt'.
\end{aligned} \tag{2.42}$$

This expression can be simplified by introducing the linearized strain $\epsilon_{ij} := [u_{i,j} + u_{j,i}]/2$, which can be decomposed according to $\epsilon_{ij}^{\mathrm{D}} := \epsilon_{ij} - \frac{1}{3}\delta_{ij}\epsilon_{kk}$ into deviatoric, $\epsilon_{ij}^{\mathrm{D}}$, and dilatational, $\delta_{ij}\epsilon_{kk}/3$, parts. Then, (2.42) becomes

$$t_{ij}^{(\delta)} = \delta_{ij}m_1(0)\epsilon_{kk} + 2m_2(0)\epsilon_{ij}^{\mathrm{D}} - 2\int_0^t d_{t'}m_2(t-t')\,\epsilon_{ij}^{\mathrm{D}}\,dt'. \tag{2.43}$$

On the assumption of perfect elasticity, the viscoelastic stress may be neglected and (2.43) reduces to

$$t_{ij}^{(\delta)} = \delta_{ij}m_1(0)\epsilon_{kk} + 2m_2(0)\epsilon_{ij}^{\mathrm{D}}, \tag{2.44}$$

where $m_1(0)$ and $m_2(0)$ correspond to the elastic bulk modulus κ and elastic shear modulus μ, respectively.

2.4.5 Viscoelastic-incompressible constitutive equation

The form of (2.37) for incompressibility is obtained if $\epsilon_{kk} \equiv u_{k,k} \rightarrow 0$ and $\kappa \rightarrow \infty$. Since $t_{ij}^{(\delta)}$ remains finite and the definition of the incremental mechanical pressure, $p^{(\delta)} := -t_{ii}^{(\delta)}/3 = -\kappa\epsilon_{kk}$, continues to apply, (2.43) reduces to (Wolf, 2003)

$$t_{ij}^{(\delta)} = -\delta_{ij}p^{(\delta)} + 2\mu\epsilon_{ij}^{\mathrm{D}} - 2\int_0^t d_{t'}m_2(t-t')\,\epsilon_{ij}^{\mathrm{D}}\,dt', \tag{2.45}$$

where the viscoelastic behaviour is controlled by the shear-relaxation function, m_2. Commonly, m_2 is chosen to represent a Maxwell-viscoelastic rheology:

$$m_2(t-t') := \mu e^{-\frac{\mu}{\eta}(t-t')}H(t-t'), \tag{2.46}$$

where η is the shear viscosity and H the Heaviside function[1].

---

[1] The Heaviside function of t is defined by $H(t-t') := \begin{cases} 0 \text{ for } t-t' \leq 0 \\ 1 \text{ for } t-t' > 0 \end{cases}$.

2.4.6 Spectral finite-element solution method

The solution of the field equations and interface conditions for the viscoelastic-incompressible case is implemented out following the time-domain spectral finite-element approach by Martinec (2000). In contrast to other solution methods, such as the normal-mode method (e.g. Wu & Peltier, 1982; Peltier, 1985; Han & Wahr, 1995) or the propagator-matrix method (e.g. Wolf, 1985c; Martinec & Wolf, 1998), this approach formulates the initial- and boundary-value problem in a weak sense (e.g Křížek & Neittaanmäki, 1990), i.e. it imposes the least constraints on the properties of the viscosity, elasticity and density distributions. Moreover, the time dependence is formulated as a time-evolution problem and allows the implementation of arbitrarily changing surface loads, which are considered directly in the solution at each time step. The solution for the elastic-compressible case is based on the standard approach of a spatial convolution of the load Love numbers (Farrell, 1972) with the load function, which is detailed in Section A.2. The determination of the load Love numbers is carried out following the the normal-mode method (e.g. Wu & Peltier, 1982; Peltier, 1985; Han & Wahr, 1995).

2.4.7 Time-difference scheme for Maxwell viscoelasticity

First, the time dependence of the viscoelastic-incompressible constitutive equation (2.45) is represented according to a time-difference scheme. The field variables u_i, $t_{ij}^{(\delta)}$, $p^{(\delta)}$ and $\phi^{(\Delta)}$ ($V_{\text{visc.}}^{\text{I}}$ in Section 2.2) are represented by their values at discrete time epochs, $t^0 = 0 < t^1 < ... < t^{t-1} < t^i < t^{i+1}$. With regard to a convenient numerical solution, the explicit Euler time-difference scheme is adopted. Then, the viscoelastic stress at the current time epoch, t^{i+1}, can be decomposed into the elastic stress at t^{i+1} and the viscous stress at the previous time epoch, t^i. The time step between two epochs must be chosen sufficiently small to guarantee the stability of the numerical solution.

2.4.8 Weak formulation of the initial and boundary-value problem

For the reformulation of the initial and interface conditions in a weak sense, the energy functional, $\mathcal{E}$, is defined as the sum of the energy associated with the pressure $\mathcal{E}_{\text{press}}$, the elastic shear energy $\mathcal{E}_{\text{shear}}$, the gravitational energy, $\mathcal{E}_{\text{grav}}$, and the term associated with the uniqueness of the solution, $\mathcal{E}_{\text{uniq}}$. The linear functional $\mathcal{F}^{i+1}$ is introduced as the sum of the dissipative part at t^i, $\mathcal{F}^i_{\text{diss}}$, and the part associated with the interface conditions $\mathcal{F}^{i+1}_{\text{inter}}$. After this, the variation equation of the energy functional $\delta\mathcal{E}$ and the linear functional $\delta\mathcal{F}^{i+1}$ is solved for a test function depending on the field variables u_i, $\phi^{(\Delta)}$ and $p^{(\delta)}$.

2.4.9 The spectral finite-element representation

In the next step, the field variables are expanded into spherical-harmonic functions. For a fixed time epoch, t^{i+1}, the angular dependence of the solutions is expressed as vector spherical harmonics for u_i and scalar spherical harmonics for $\phi^{(\Delta)}$ and $p^{(\delta)}$

(Section A.1) and substituted in the variation equation. The radial dependence of the variables is represented by finite elements, with the nodes $0 = r_1 < r_2 < ... < r_P < r_{P+1} = a$.

2.4.10 The Galerkin system

After introducing the spectral finite-element representation of the field variables, the Galerkin system is obtained as a system of $P + 1$ linear equations for u_i, $\phi^{(\Delta)}$ and $p^{(\delta)}$ and each spherical-harmonic degree and order. The Galerkin method for approximating the solution to the field equations and interface conditions is finding a distinct solution for a fixed time epoch, t^{i+1}, such that variational equality is satisfied. Such a solution of u_i, $\phi^{(\Delta)}$ and $p^{(\delta)}$ is called the spectral finite-element solution.

3

The Gravity Recovery and Climate Experiment (GRACE)

Primary objective of the GRACE space mission of the National Aeronautic and Space Agency (NASA) and the Deutsche Zentrum für Luft- und Raumfahrt (DLR), launched March 17, 2002, is the determination of the temporal variations of the Earth's gravitational potential with high temporal and spatial resolution and, thus, providing novel constraints on global mass transport within the Earth system (e.g. Tapley *et al.*, 2004a; Tapley *et al.*, 2004; Tapley & Reigber, 2001; Deutsches GeoForschungsZentrum, 2008 *[online]*). Secondary objective of the GRACE mission is the sounding of the Earth's atmosphere and ionosphere by Global Positioning System (GPS) radio-occultation measurements (e.g Wickert *et al.*, 2005).

The GRACE mission realizes SST of type low-low proposed by Wolf (1969) (Figure 3.2). It consists of two low-orbiting (altitude of ~ 300 to $450\,\mathrm{km}$) identically constructed satellites, GRACE-A and GRACE-B, flying in the same near-polar orbit with an inclination of 89.5° and eccentricity of < 0.005 accurately measuring their distance ($\sim 200\,\mathrm{km}$) and change of distance by a K- and Ka-band microwave ranging system. The principle idea is that the two satellites flying in along-track formation experience the inhomogeneities of the Earth's gravitational potential and the associated perturbations of their orbits with a time delay, which causes changes in the satellites' relative distance (i.e. range), velocity (i.e. range rate) and acceleration (i.e. range acceleration), measured by the K-band ranging systems (e.g. Case *et al.*, 2004).

Inferring changes in Earth's gravitational potential from range and range-rate data requires the determination of accelerations due to non-gravitational causes, such as atmospheric drag and pressure of solar radiation. These accelerations are measured for each satellite by on-board high-precision accelerometers and removed during gravity-field processing from the K-band measurements. Precise orbit determination is carried out using data of twelve channel two-frequency GPS receivers, while the satellites' relative orientation is determined by star cameras mounted onto the accelerometers. Additionally, each satellite carries a laser retroreflector, which allows calibration, mainly of the GPS-based positioning, using terrestrial laser ranging of the International Laser Ranging Service (ILRS, Pearlman *et al.*, 2002).

Within the GRACE mission, temporal variations of the gravitational potential are recovered as average monthly solutions of fully normalized Stokes gravitational potential coefficients, V_{jm}^{GRACE} (GRACE Level 2 product). Data sets of monthly solutions

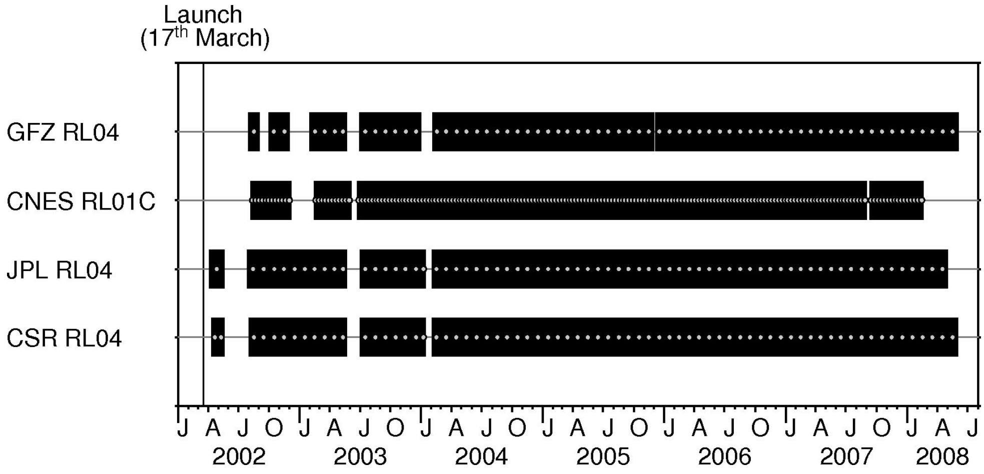

Figure 3.1: Availability of GRACE gravity-field solutions. Latest releases of the Science Data Systems are GFZ RL04 (65 months) (Flechtner, 2007), CSR RL04 (69 months) (Bettadpur, 2007a) and JPL RL04 (71 months) (Watkins & Dah Ning, 2007). The CNES RL01C release provides ten-day solutions based on the constrained gravity-field determination (equivalent to 64 months) (Biancale *et al.*, 2006).

are regularly computed at Deutsches GeoForschungsZentrum (GFZ), Center for Space Research (CSR) at the University of Texas, and Jet Propulsion Laboratory (JPL) in Pasadena and stored for the scientific community in the two GRACE archives ISDC *[online]* and PO.DAAC *[online]*. Also, ten-day solutions are computed, for example at the Bureau Gravimetrique International of the Centre National d'Ètudes Spatiales (CNES). All solutions are available as fully normalized Stokes potential coefficients and represent largely independent results of the satellite-based gravity-field determination. The data sets (i.e. GRACE releases) are continuously revised and improved; the temporal coverage of the most recent releases are shown in Figure 3.1.

This chapter is organized as follows. Section 3.1 presents the GRACE instrumentation and its measurements. Section 3.2 outlines the dynamic approach of gravity-field determination based on the satellites' measurements used at GFZ. Section 3.3 describes the background models required for the determination of GRACE solutions.

3.1 Satellite measurements

The most relevant instrumentation onboard each GRACE satellite are K-band microwave ranging system, accelerometer, GPS receiver and star camera (Figure 3.3). The initial measurements of these instruments are processed at JPL and made available as GRACE Level 1B product (Case *et al.*, 2004) within the GRACE archives. Processing steps common to all observations are 1) transformation of measurement units to Système international d'unités (SI) units, 2) time referencing (from onboard

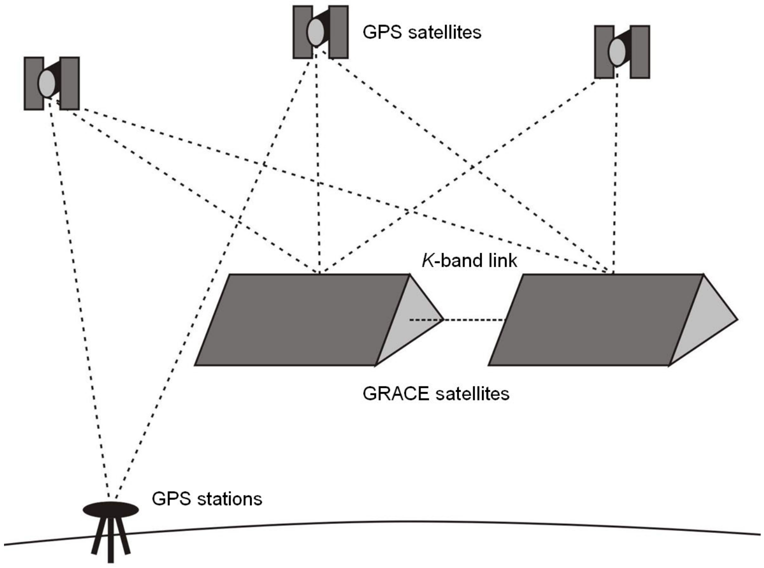

Figure 3.2: Principle of satellite-to-satellite tracking (SST) of type low-low and high-low realized implemented in the GRACE mission.

time based on the Ultra-Stable Oscillator to GPS-system time), 3) spatial referencing from the instruments' local reference frame to the unified Science Reference Frame, 4) elimination of outliers, and 5) joint noise filtering and data resampling. The following description follows Case *et al.* (2004) and Flechtner (2001øn).

3.1.1 K-band microwave ranging system (KBR)

The intra-satellite distance between GRACE-A and GRACE-B and its changes are measured with an accuracy of ∼1 μm using a K-band microwave ranging system (HAIRS, JPL, USA). Each satellite is equipped with a dual-frequency microwave transmitter and receiver operating in the K- (24 GHz) and K_a- (32 GHz) band. The K-band frequencies of the satellites are shifted by 500 KHz to avoid signal interferences. From four simultaneous phase measurements at a sampling rate of 10 Hz, dual-one-way ranges are calculated at JPL. During this procedure, it is necessary to correct the range data for biases of multiple integers of the carrier wavelength, distance changes of the satellites during signal propagation and misalignment of the satellites. From the range data, first and second time derivatives of the intra-satellite range, i. e. range rate and range acceleration, respectively, are calculated numerically. Additional processing steps include the transformation of the reference frame, low-pass noise filtering and accompanied resampling of the initial 10 Hz data at 0.2 Hz intervals.

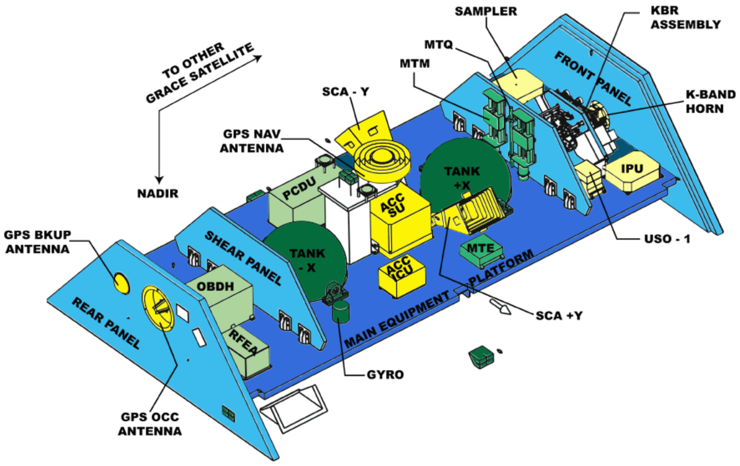

Figure 3.3: GRACE instrumentation (Flechtner, 2001øn).

3.1.2 Accelerometer (ACC)

In order to derive changes of the Earth's gravitational potential from inter-satellite range measurements from LEO satellites, it is necessary to account for contributions from non-gravitational forces acting on the spacecraft. For GRACE, the dominating terms come from the atmospheric drag, radiation pressure forces (solar and terrestrial), but also linear accelerations caused by imperfections of the attitude control system. Since existing models for the non-gravitational forces are not accurate enough, the GRACE satellites are equipped with capacitative accelerometers (SuperSTAR, CNES, France). The basic principle is to retain a proof mass (a small cube) floating inside a capacitor. When located precisely in the center of mass of the spacecraft, the motion of the proof mass is only affected by gravitational accelerations. In contrast, the motion of the capacitor, which is rigidly attached to the satellite, is driven by both gravitational and non-gravitational forces. Measuring the voltage necessary to retain the cube motionless thus provides information on the strength of the non-gravitational accelerations. The specified accuracy of the acceleration measurement is $1 \times 10^{-10}\,\mathrm{m/s^2}$ in radial and along-track direction and $1 \times 10^{-9}\,\mathrm{m/s^2}$ in cross-track direction for the cumulative frequency spectrum from 2×10^{-4} to 1×10^{-1} Hz (Schmidt, 2007). Current investigations indicate that this accuracy is not completely achieved (e.g. Fackler, 2005), which is one potential cause for observed degradations of the GRACE gravity fields. Due to the design of the accelerometer, the measurements need to be corrected for instrument-specific parameters, which comprise, for example, biases and scale factors for each instrumental axis. These must be estimated along with the gravity field and other orbital parameters, since a calibration on ground is not feasible. Additional details on the parameter model of the accelerometer and its relevance for the gravity-field recovery can be found in Schmidt (2007).

3.1.3 GPS receiver (GPS)

Precise orbit determination at the cm level is achieved by satellite-to-satellite tracking (SST) of the type high-low using GPS. Each satellite is equipped with a 16-channel dual-frequency GPS receiver (BlackJack, JPL, USA), which observes GPS code and phase measurements. Four out of the 16 channels are reserved for the reception of GPS-based occultation measurements, allowing for a radiometric sounding of the ionosphere and the atmosphere, which is the secondary mission objective. From precise measurements of the time delay between the occulted and non-occulted GPS signals, vertical atmospheric refractivity and temperature profiles are obtained with high vertical resolution (Wickert *et al.*, 2005).

3.1.4 Star camera assembly (SCA)

Data from two star camera assemblies (SCA) are used to determine the absolute and relative orientation of the GRACE satellites and the onboard instruments in the inertial space. The SCA consist of two simultaneously operating digital camera heads mounted at the port and starboard sides of the accelerometer at an angle of 45^o with respect to the zenith. Comparison of the images with onboard maps of star constellations allows the determination of the satellite attitude with an accuracy of $<0.3\,\mathrm{mrad}$. In flight, the SCA measurements are fed into the attitude and orbit control system AOCS to establish the K-band link, which requires a permanent 1.5 degree pitch of the two satellites.

3.1.5 Additional devices

The GRACE satellites are also equipped with a Coarse Earth and Sun Sensor (CES, Astrium GmbH, Germany), which provides an estimate of Sun and Earth position to allow for a coarse positioning of the satellite in cases of mode drops. In order to compensate for offsets of the accelerometers from the center of mass, mass trim units (MTU) are mounted onboard each satellite. Such deviations may occur in the course of the mission from asymmetric degassing of the cold gas tanks. The location is checked by means of satellite manoeuvres and the MTUs are used in case offsets larger than 0.2 mm are observed. For the generation of the KBR signal and time tagging, a Ultra-Stable Oscillator (USO, John Hopkins University, USA) is installed. Also mounted are laser-retro reflectors to enable precise Satellite Laser Ranging (SLR) measurements with stations of the International Laser Ranging Service (ILRS) network.

3.2 Dynamic approach for gravity-field determination

This section outlines the basic principles of satellite-based determination of the Earth's gravitational potential. The presentation, which largely follows Schmidt (2007), is limited to the recovery of the gravity field using the dynamic approach used at GFZ. Other methods of gravity field determination are based, for example, on the dynamic approach with the parametrization of local mass concentrations (e.g. Rowlands *et al.*, 2005; Luthke *et al.*, 2006), the consideration of the satellites' energy conditions (e.g. Han, 2004), or the modified dynamic approach based on the integral formulation of the equation of motion (e.g. Mayer-Gürr, 2007).

3.2.1 Equation of motion

The dynamic approach for the determination of the Earth's gravitational potential is based on Newton's equation of motion for a satellite in a geocentric inertial frame,

$$m\ddot{\boldsymbol{r}} = \boldsymbol{f}(t, \boldsymbol{r}, \dot{\boldsymbol{r}}), \tag{3.1}$$

where m is the mass of the satellite, and $\boldsymbol{r}$, $\dot{\boldsymbol{r}}$ and $\ddot{\boldsymbol{r}}$ are the vectors of the satellite's position, velocity and acceleration, respectively, with respect to the geocenter. $\boldsymbol{f}$ describes conservative (i.e. gravitational) and non-conservative (i.e. non-gravitational) forces exerting accelerations on the satellite,

$$\ddot{\boldsymbol{r}} = \boldsymbol{a}_{\mathrm{c}} + \boldsymbol{a}_{\mathrm{nc}}. \tag{3.2}$$

The gravitational acceleration,

$$\boldsymbol{a}_{\mathrm{c}} = -\frac{GM}{r^3}\boldsymbol{r} + \boldsymbol{a}_{\mathrm{STAT}} + \boldsymbol{a}_{\mathrm{ST}} + \boldsymbol{a}_{\mathrm{AOT}} + \boldsymbol{a}_{\mathrm{AOD}} + \boldsymbol{a}_{\mathrm{P}}, \tag{3.3}$$

consists of the attraction of the Earth as a point mass, $-GMr^3/\boldsymbol{r}$, static contributions from the Earth's potential, $\boldsymbol{a}_{\mathrm{STAT}}$, luni-solar solid-earth tides, $\boldsymbol{a}_{\mathrm{ST}}$, atmosphere and ocean tides, $\boldsymbol{a}_{\mathrm{AOT}}$, non-tidal mass variations of the atmosphere and ocean, $\boldsymbol{a}_{\mathrm{AOD}}$, and the direct gravitational attraction of celestial bodies, $\boldsymbol{a}_{\mathrm{P}}$. The gravitational potential of the Sun and planets are considered to arise from point masses, whereas the Moon's gravitational potential is expanded to spherical-harmonic degree and order four.

The sensitivity of the GRACE observation system requires to account for tidal, but also non-tidal short-term mass variations (i.e. hours to a few days). If such contributions remain unmodelled, it has been shown that such signal alias into the monthly mean estimates of the gravity field, causing characteristic striping features in its spatial representation. The phenomena that need to be considered mainly comprise short-term mass variations in the atmosphere and the oceans (see for the specifications on the models used as part of the background models). The reduction of such variations is referred to as de-aliasing.

The non-gravitational accelerations for GRACE are

$$\boldsymbol{a}_{\mathrm{nc}} = \boldsymbol{a}_{\mathrm{AD}} + \boldsymbol{a}_{\mathrm{SR}} + \boldsymbol{a}_{\mathrm{ER}} + \boldsymbol{a}_{\mathrm{CS}} + \boldsymbol{a}_{\mathrm{R}}, \tag{3.4}$$

where $\boldsymbol{a}_{\mathrm{AD}}$ refers to atmospheric drag, $\boldsymbol{a}_{\mathrm{SR}}$ and $\boldsymbol{a}_{\mathrm{ER}}$ to radiation pressure of the Sun and the Earth (surface albedo), $\boldsymbol{a}_{\mathrm{CS}}$ to accelerations caused by the satellites' attitude control system, and $\boldsymbol{a}_{\mathrm{R}}$ to residual contributions caused by, for example, interactions with the electromagnetic field or mechanical deformations due to temperature variations, which are usually not considered in gravity field determination. The sum of all non-gravitational accelerations are measured by the accelerometers of the GRACE satellites described in Section 3.1.2.

3.2.2 Equation of observations

The problem of solving the equation of motion based on satellite data is formulated by relating satellite observations, $\boldsymbol{d}$ (i.e. range, range rate, range acceleration, GPS-phase measurements, satellite orientation, etc.) to the satellites' position and velocity, $\boldsymbol{r}$, $\dot{\boldsymbol{r}}$ (3.1),

$$\boldsymbol{d} = \boldsymbol{F}(\boldsymbol{q}), \tag{3.5}$$

with $\boldsymbol{q} = (t, \boldsymbol{r}, \dot{\boldsymbol{r}}, \boldsymbol{p})$, where $\boldsymbol{p}$ contains the parameters of dynamic (e.g. the desired Stokes potential coefficients V_{jm}^{GRACE}), kinematic (e.g. K-band calibration) and geometric (e.g. GPS station coordinates) and other to be estimated unknowns (e.g. GPS phase ambiguities). The function $\boldsymbol{F}$ relating the observations and unknown parameters, which is in general non-linear, is linearized with respect to a set of reference parameters, $\boldsymbol{q}_0$, using a Taylor expansion series,

$$\boldsymbol{F}(\boldsymbol{q}) \approx \boldsymbol{F}(\boldsymbol{q}_0) + \left.\frac{\partial \boldsymbol{F}(\boldsymbol{q})}{\partial \boldsymbol{q}}\right|_{\boldsymbol{q}=\boldsymbol{q}_0} \Delta\boldsymbol{q}, \tag{3.6}$$

where $\boldsymbol{q}_0$ and $\boldsymbol{d}_0 = \boldsymbol{F}(\boldsymbol{q}_0)$ are reference values of the parameters and the associated predictions of the satellite measurements (i.e. theoretical observations), respectively. The partial derivatives of $\boldsymbol{F}$ with respect to $\boldsymbol{r}$, $\dot{\boldsymbol{r}}$ and the parameters $\boldsymbol{p}$ can be calculated from (3.5). The determination of the partial derivatives of $\boldsymbol{r}$, $\dot{\boldsymbol{r}}$ with respect to $\boldsymbol{p}$, which arise due to application of the chain rule, are calculated numerically along the satellite's orbit by integration of the associated variational equation; details are given by Schwintzer *et al.* (1991).

The linerization (3.6) allows us to reformulate the parameter estimation in terms of estimating deviations (improvements) of the initial set of parameters, $\hat{\boldsymbol{q}} = \hat{\boldsymbol{q}}_0 + \Delta\boldsymbol{q}$, that minimize, in a least-squares sense, the difference between observed and predicted satellite measurements. Introducing the matrix $\boldsymbol{A}$ containing the partial derivatives of the observations with respect to the unknowns,

$$\boldsymbol{A} = \left.\frac{\partial \boldsymbol{F}(\boldsymbol{q})}{\partial \boldsymbol{q}}\right|_{\boldsymbol{q}=\boldsymbol{q}_0}, \tag{3.7}$$

and using the linearization of (3.6), the minimization criterion takes the form

$$(\boldsymbol{A}\Delta\boldsymbol{q} - \Delta\boldsymbol{F})^{\mathrm{T}} \boldsymbol{C}_{\mathrm{D}}^{-1} (\boldsymbol{A}\Delta\boldsymbol{q} - \Delta\boldsymbol{F}) \overset{!}{=} \min_{\Delta\boldsymbol{q}}, \tag{3.8}$$

where $\Delta\boldsymbol{F} = \boldsymbol{F}(\boldsymbol{q}) - \boldsymbol{F}(\boldsymbol{q}_0)$, and $\boldsymbol{C}_{\mathrm{D}} = \mathrm{var}(\boldsymbol{d})$ represents the variance-covariance matrix of the satellite measurements. With (A.36), the least-squares solution of (3.8) for the optimal estimates of parameter deviations $\Delta\hat{\boldsymbol{q}}$, is

$$\Delta\hat{\boldsymbol{q}} = (\boldsymbol{A}^{\mathrm{T}} \boldsymbol{C}_{\mathrm{D}}{}^{-1} \boldsymbol{A})^{-1} \boldsymbol{A}^{\mathrm{T}} \boldsymbol{C}_{\mathrm{D}}{}^{-1} \Delta\boldsymbol{F}, \tag{3.9}$$

where $\boldsymbol{q} = \boldsymbol{q}_0 + \Delta\hat{\boldsymbol{q}}$. For simplification, it is usually assumed that all satellite measurements are uncorrelated, i.e. the off-diagonal elements of $\boldsymbol{C}_{\mathrm{D}}$ are zero. Also, the absolute error level is not known, but estimated in the adjustment. However, the relative error level in $\boldsymbol{C}_{\mathrm{D}}$, which attributes different weight to different measurements, is important. Following (A.37), the errors of $\boldsymbol{C}_\mathrm{D}$ are propagated to the parameter estimates $\Delta\hat{\boldsymbol{q}}$ according to

$$\tilde{\boldsymbol{C}}_\mathrm{M} = (\boldsymbol{A}^\mathrm{T}\boldsymbol{C}_\mathrm{D}^{-1}\boldsymbol{A})^{-1}. \tag{3.10}$$

The matrix contains the variances of the Stokes potential coefficients $\delta V_{jm}^{\mathrm{GRACE}}$ referred to as formal GRACE errors.

Monthly and long-term solutions of the gravity field are determined at GFZ. For monthly solutions, satellite data of ~ 30 days (i.e. one day acquires ≈ 15 revolutions) are used in the estimation of one set of parameter improvements (3.9). Shorter time intervals are possible, however, at the cost of being able to solve only for a smaller number of Stokes coefficients (i.e. a lower spatial resolution of the gravity field). This can be compensated by including more *a priori* information from background models (Section 3.3) or by regularization of the equations of observations using, for example, the Kaula rule of thumb (Kaula, 1966) in a constrained gravity-field determination. Long-term unconstrained solutions, such as the static gravity field EIGENCG03C (Förste *et al.*, 2005), involve satellite data of several years.

3.3 Background models

The dynamic approach carried out at GFZ relies on models of the static gravitational potential and its periodic and aperiodic temporal variations for the prediction of approximate satellite measurements (3.6). For GFZ RL04, the background models are specified in Flechtner (2007). Further investigations with regard to the influence of these background models on the resulting monthly solutions can be found in Schmidt (2007).

For GFZ RL04, static and periodically time-varying *a priori* background models are mainly implemented according to the International Earth Rotation and Reference Systems Service (IERS *[online]*) convention 2003 (Mc Carthy & Petit, 2004). They account for gravitational perturbations due to solid Earth, atmosphere and ocean tides. Also considered are changes in the gravitational potential due to the deformation of the solid Earth and the oceans associated with the changes in the Earth's centrifugal potential following variations in the Earth's pole of rotation (solid-Earth and ocean pole tide). The solid-Earth pole tide mainly influences the spherical-harmonic coefficients $j, m = 2, 1$, whereas the ocean pole tide must be considered up to degree and order 30. The static gravity-field solution used at GFZ is the EIGENCG03C (Förste *et al.*, 2005). It is complete to degree and order 360 and based on GRACE and CHAMP satellite data, which are combined with gravimetric and altimetric data for achieving higher spatial resolution.

Aperiodic mass redistributions are dominantly climatologically induced, mainly by the atmosphere and the ocean. These short-term mass variations, if not properly reduced from the satellite observations, may cause temporal aliasing and degradation of the mean monthly gravity-field solutions. At GFZ, these mass variations are predicted using atmospheric data from ECMWF and the baroclinic Ocean Model for Circulation and Tides (OMCT *[online]*, Dobslaw & Thomas, 2007), which is forced with ECMWF data. From the mass redistribution, changes of the gravitational potential and, eventually the accelerations acting on the satellites ($\boldsymbol{a}_{\mathrm{AOD}}$) are calculated and reduced in the observation equation. For GRACE investigations concerned with atmospheric and oceanic changes, the monthly means of these predictions are issued as Stokes potential coefficients (AODL1B product, Flechtner, 2006) and must be res-substituted into the de-aliased monthly gravity-field solution in order to approximately restore the atmospheric and oceanic signals. Other short-term mass variations, foe example, from continental hydrological processes, are currently not removed since their determination remains a dedicated mission objective.

4

Post-processing of GRACE gravity-field solutions

The purpose of data post-processing is the enhancement of the geophysical signal of interest, while reducing undesired signal components or contaminating noise. The choice of the appropriate filtering largely depends on the signal and noise characteristics and often *a priori* knowledge of both components enter the filter design and its optimization. This chapter describes a selection of post-processing methods developed for (or adapted to) monthly GRACE gravity-field solutions.

Filtering of GRACE solutions mainly aims at suppressing noise in the Stokes potential coefficients, which increases with increasing degree and order. Therefore, filters for GRACE data are commonly low-pass filters, although for some applications also the influence of low degrees and orders (e.g. $j, m = 2, 0$, which is not well-determined by GRACE) may need to be reduced. More literature about filtering GRACE data can be found in the database of GRACE publications *[online]*. The filters introduced in this chapter follow the convolution principle of Jekeli (1981). They operate in the spectral domain, which means that filter functions are applied directly to the GRACE potential coefficients. This assists the filter design and is computationally efficient.

This chapter is organized as follows. Section 4.1 presents the uncertainty characteristics of the GRACE data. In Section 4.2, linear spatial convolution filtering based on isotropic (i. e. order-independent) smoothing functions is introduced. In this context, the method of Wiener optimal filtering developed within this project (Sasgen *et al.*, 2006) is presented and compared with Gaussian filtering, which is commonly applied within the GRACE scientific community. Section 4.3 presents two methods of non-isotropic (i. e. order-dependent) filtering. First, the de-correlation filter of Swenson & Wahr (2006) is outlined, which aims at reducing empirically determined correlations between errors of GRACE coefficients. Then, the non-isotropic statistical filter is presented, which was developed within the research team at GFZ (e.g. Fleming *et al.*, 2006 *[online]*) for an improved separation of deterministic and stochastic components in the GRACE-coefficients time series.

4.1 Uncertainty characteristics of monthly solutions

The errors of the GRACE potential coefficients, δV_{jm}, can be divided into

$$\delta V_{jm}^{\text{GRACE}} = \delta V_{jm}^{\text{Inst.}} + \delta V_{jm}^{\text{Alias.}} + \delta V_{jm}^{\text{Reg.}}, \tag{4.1}$$

where $\delta V_{jm}^{\text{Inst.}}$ are the instruments' errors (KBR, ACC, GPS and SCA), $\delta V_{jm}^{\text{Alias.}}$ are the errors due to aliasing (quality of background models, temporal and spatial parameterizations) and $\delta V_{jm}^{\text{Reg.}}$ are the errors associated with regularization of the set of normal equations to be solved for V_{jm}^{GRACE} (Schmidt, 2007). Apart from stochastic noise, $\delta V_{jm}^{\text{GRACE}}$ may contain systematic errors, which can be attributed to one or more of the following categories: 1) measurement errors of the instruments (e.g. noise characteristic of the accelerometer), 2) spatial and temporal sampling errors (i.e. orbit coverage), 3) inaccuracies in the background models (e.g static gravity field) or 4) inappropriate parametrization of the geodetic model (e.g. insufficient number of Stokes potential coefficients). Investigations with regard to these error sources can be found in Schmidt (2007). Although systematic errors appear to be important, they are problematic to quantify and not further considered in this work. The investigation of GRACE data from different processing centers, however, provides some empirical estimate for this source of uncertainty.

4.1.1 Formal uncertainties

The uncertainty characteristic of the GRACE data is mainly a result of the satellites' orbit parameters. According to Newton's law of gravitation, the external gravitational potential decays inversely with distance from its source. This attenuation is dependent on the wavelength and results in increased damping of short-wavelength anomalies with increasing distance from their sources. Measurements of the gravitational potential at the satellite's altitude, H ($\sim 500\,\text{km}$ for GRACE), need to be downward continued to obtain the gravitational potential at the Earth's surface. Comparison of (A.19) with $V(r = R)$ and $V(r = R + H)$ gives the degree-dependent amplification factor $(R + H/R)^{j+1}$ for the harmonic downward continuation. Measurement errors are amplified in the same way and cause the uncertainties in the Stokes potential coefficients to become larger with increasing degree and order (Figure 4.1). Therefore, it is necessary to filter the Stokes coefficients with regard to balancing the trade-off between the gravity field's spatial resolution and its accuracy. The GRACE baseline shown in Figure 4.1 indicates the predicted GRACE accuracy at a satellite altitude of 500 km (NRC Committee on Earth Gravity from Space, 1997).

The spatial distribution of GRACE errors mainly results from the temporal and spatial sampling of the satellites in the near-polar orbit. With an along-track data sampling rate of $\sim 0.2\,\text{Hz}$ (e.g. Level 1B data of the K-band instrument) and the average velocity of the GRACE satellites of 7 km/s, an approximate spatial sampling in north-south direction of $\Delta_\lambda = 35\,\text{km}$ is obtained. The sampling in east-west direction is coarser and to obtain a spatial resolution of $\Delta_\lambda = 200\,\text{km}$, data acquisition over ~ 30 days is required. This poorer track coverage, particularly in equatorial regions,

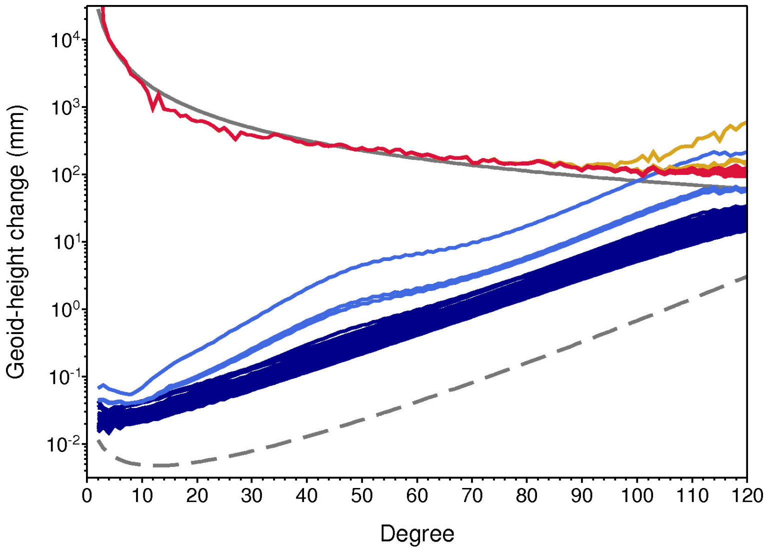

Figure 4.1: Degree-power spectrum of monthly GRACE solutions (red) and associated formal errors (blue) for the months August 2002 to August 2007 as well as the Kaula rule of thumb (grey solid line) and the GRACE baseline (grey dashed line). The solutions for August 2004, September 2004 and October 2004 (orange) are of poorer quality due to repeat orbits, which is also indicated by their large formal errors (light blue).

increases aliasing errors and degrades the determination of near-sectorial Stokes coefficients ($j \approx m$) visible as characteristic north-south oriented striping in the spatial gravity field.

Average monthly solutions represent a compromise between temporal resolution and spatial ground-track coverage, i.e. sufficient number of satellite revolutions within time interval. Shortage of data may occur when orbits are repeated within a month or longer time intervals, depending on the decrease in the satellites' altitude due to atmospheric drag (e.g. Wagner *et al.*, 2006). Repeat orbits also lead to an increase also of aliasing errors and a degradation of the gravity-field solutions. A prominent example is the 61/4 resonance orbit around September 2004 (61 revolution within 4 days) with exceptionally large errors in the Stokes potential coefficients (Figure 4.1).

4.1.2 Assessment of formal uncertainties

Figure 4.2 shows the degree-power spectrum of formal GRACE errors for the monthly solution of April 2004 obtained by error propagation according to (3.9). The errors are dominated by an increase in power with increasing degree. However, to asses whether the formal errors are an adequate representation of the true uncertainties, empirical errors are calculated. This is done by fitting a temporal model, which describes the deterministic signal components for each coefficients' time series by the method of least-squares (Section 4.3.2). The residual (i.e. data minus deterministic

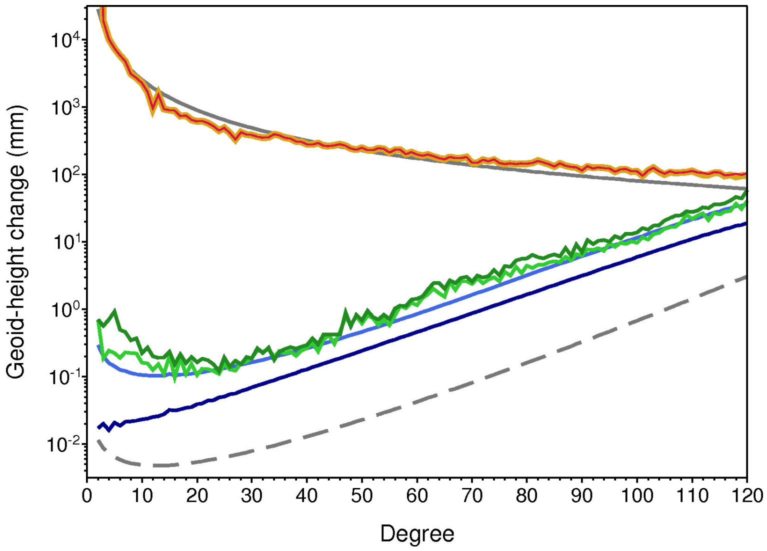

Figure 4.2: Degree-power spectrum of GRACE solution and associated errors for April 2004 (red) and with respect to static gravity-field solution EIGEN-CG03 (green, Förste *et al.*, 2005). Also shown are the associated formal (dark blue) and calibrated (light blue) errors, the Kaula rule of thumb (solid grey line) and the GRACE baseline (dashed grey line) as well as the static gravity-field solution EIGEN-CG03 (orange).

part) are interpreted as an empirical error estimate. Because this estimate may still contain geophysical signals that are not removed by the temporal model (e.g. the Sumatra earthquake in 2004, acceleration of glacier mass loss, interannual variations), it is considered as an upper bound on the GRACE errors (Wahr *et al.*, 2004). In the following, this error estimate will be referred to as *residual error*. Figure 4.2 shows that the uncertainty level represented by the formal errors lies between the GRACE baseline and the residual error. Particularly for low degrees, the formal errors appear to underestimate the uncertainties. Possible reasons are that the influence of inaccurate background models (e.g. the static gravity-field solution) is larger than assumed. To account for this shortcoming, formal errors are calibrated according to Schmidt *et al.* (2008) by applying a j-dependent scaling factor in order to best-fit the residual errors (Figure 4.2). The order-dependences of the formal and calibrated GRACE errors are shown in Figure 4.3. The spectrum of the residual errors and the ratio of calibrated and residual GRACE errors for April 2004 is shown in Figure 4.4. It is visible that large degree- and order-dependent differences between calibrated and residual errors remain. There are prominent stripes along j for given a order m of coefficients with j of equal (even/odd) parity that have been attributed to correlations between GRACE errors (Swenson & Wahr, 2006) and are further discussed in Section 4.3.

Figure 4.6 shows the spatial distribution of GRACE errors for calibrated errors and the ratio of calibrated and residual errors, averaged for the months August 2002 to August 2008. The calibrated errors do not show the north-south oriented striping

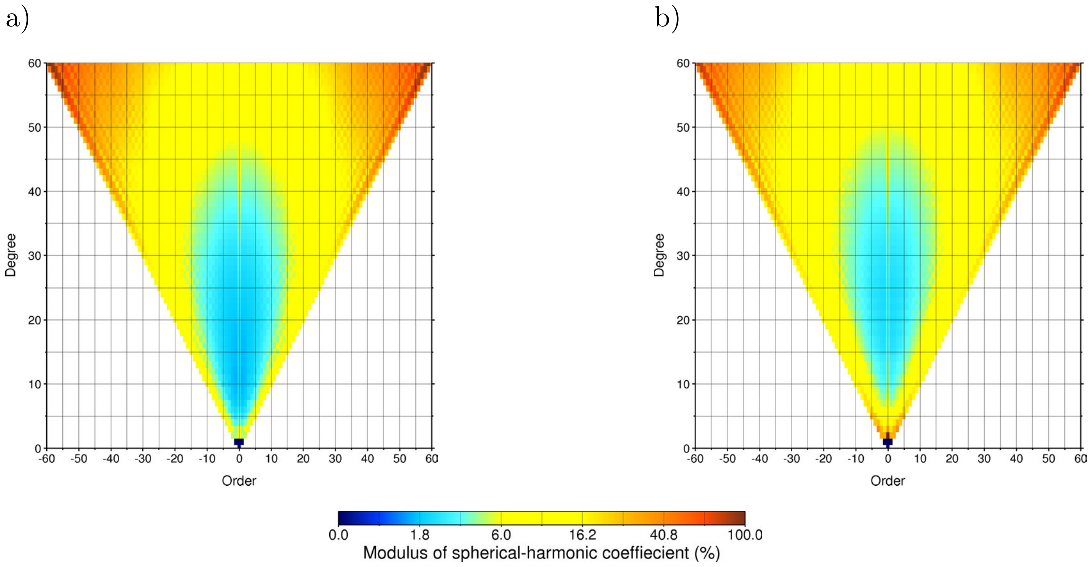

Figure 4.3: Spectrum of a) formal and b) calibrated errors of GRACE solution for April 2004.

characteristic for GRACE data due to missing covariances of the calibrated GRACE errors. The ratio of average calibrated and residual errors indicates that calibrated errors underestimate errors over the polar regions by ~30% and overestimate errors for the mid-latitudes by a factor of ~two. Dominant longitudinal striping, visible in the residual errors of a single monthly solutions (e.g. April 2004, Figure 4.5), are strongly reduced by the temporal averaging. This suggests that correlations between errors of different degree and order are temporally largely uncorrelated, although contradicting results are found with the statistical filter (Section 4.3.2).

4.2 Isotropic filtering

For linear convolution filtering, the output signal $y(\mathbf{\Omega})$ is given by the spatial convolution of the filter response function $h(\mathbf{\Omega})$ with the input signal $x(\mathbf{\Omega})$,

$$y(\mathbf{\Omega}) = \int_{\mathbf{\Omega}'_0} h(\mathbf{\Omega}')x(\mathbf{\Omega} - \mathbf{\Omega}')d\mathbf{\Omega}', \tag{4.2}$$

where Ω stands for the spherical co-latitude ϑ and longitude φ. Hence, $\Omega := (\vartheta, \varphi)$, Ω_0 is the full solid angle and $d\Omega$ its infinitesimal element.

The signals $x(\Omega)$ and $y(\Omega)$ are assumed to be square-integrable functions over the unit sphere and thus can be represented as series of scalar spherical harmonics. In the case of isotropic filtering, $h = h(\vartheta)$, and the convolution integral (A.11) in the spectral domain takes the form

$$y_{jm} = h_j x_{jm}, \tag{4.3}$$

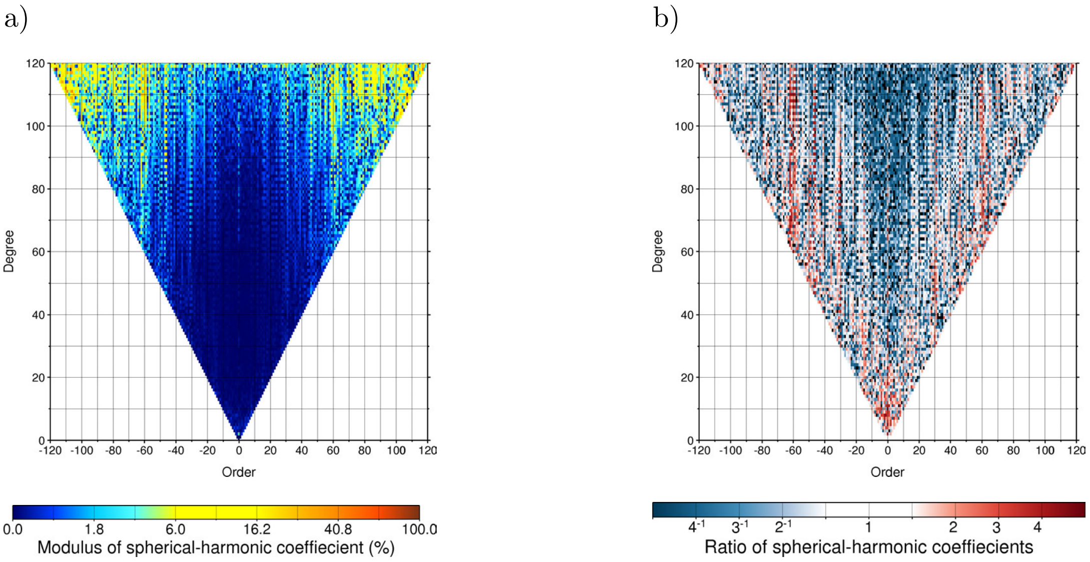

Figure 4.4: Spectrum of a) residual errors and b) ratio of residual and calibrated errors of the GRACE solution for April 2004.

where h_j and x_{jm} are the spherical-harmonic coefficients of the filter response function and the signal, respectively (Section A.2).

4.2.1 Gaussian smoothing

The GRACE gravity-field solutions are often smoothed with a Gaussian averaging filter introduced by Jekeli (1981), because it is an effective low-pass filter with smooth properties in the spectral and spatial domains. The Gaussian filter function can be represented by

$$h_{\mathrm{G}}(\vartheta) = h_0 e^{-\frac{1}{2}\left(\frac{\vartheta}{\vartheta_0}\right)^2}, \tag{4.4}$$

where ϑ_0 is the spatial half width, implicitly defined as $h(\vartheta_0) = 0.5h(0)$. The normalization factor h_0 is here defined as $h_0 = 1$ to assure that the input signals' amplitudes are not attenuated. The representation of $h_{\mathrm{G}}(\vartheta)$ in terms of spherical-harmonic coefficients, $h_{\mathrm{G},j}$, is obtained by numerical integration of (A.9), although recursion formulas can be found in Jekeli (1981) and Wahr *et al.* (1998).

The Gaussian spatial-averaging method has commonly been applied to monthly GRACE solutions with values of $h(\vartheta_0)$ ranging between 2 and 14^{o} corresponding to ~ 220 to 1550 km, respectively (Wahr *et al.*, 2004). Typically, $h(\vartheta_0) \approx 6.5^{\mathrm{o}}$ (720 km) is chosen, which is somewhat larger than the optimal Gaussian smoothing half-width of $\sim 4^{\mathrm{o}}$ determined by the Wiener optimal filter (Sasgen *et al.*, 2006, , Section 4.4 and Section 4.2.2).

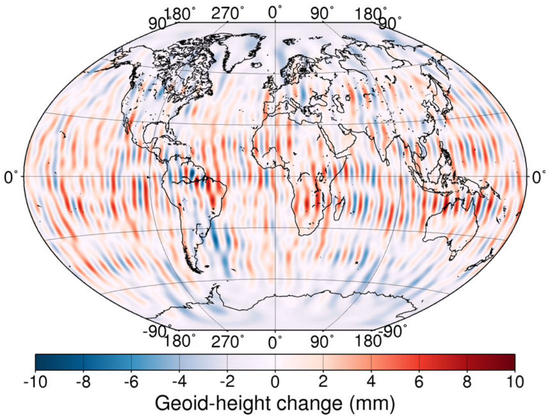

Figure 4.5: Spatial distribution of residual errors of the GRACE solution for April 2004. The cut-off degrees are $j_{\min} = 2$ and $j_{\max} = 50$.

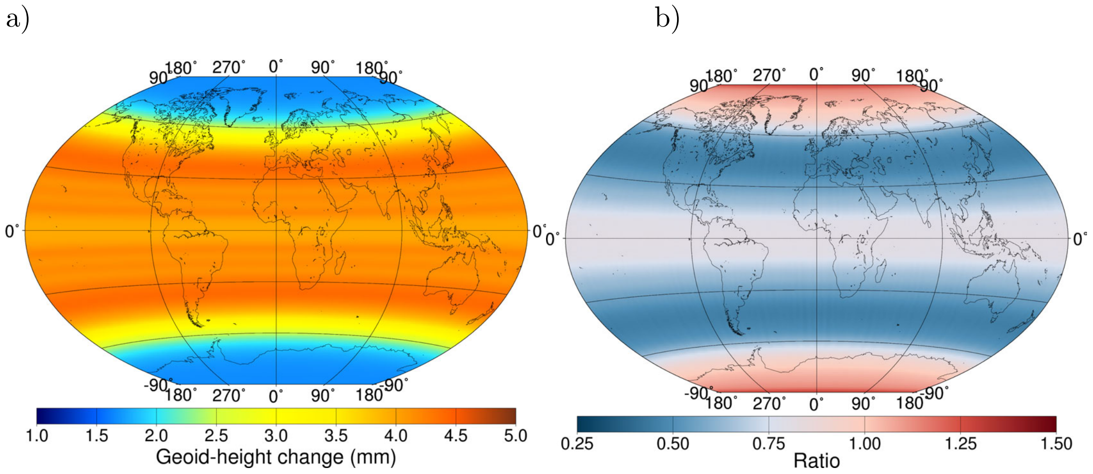

Figure 4.6: Spatial distribution of a) calibrated errors and b) ratio of residual and calibrated errors averaged for the GRACE solutions from August 2002 to August 2007. The cut-off degrees are $j_{\min} = 2$ and $j_{\max} = 50$.

4.2.2 Wiener optimal filtering

The spatial averaging method for GRACE data proposed by Sasgen *et al.* (2006) (Section 4.4) is based on the Wiener optimal filtering approach. In contrast to the Gaussian averaging method, which requires the *ad hoc* definition of the spatial half-width ϑ_0 of the filter function, the Wiener optimal filter is adaptive to *a priori* information on the degree-power spectra of the desired gravitational signal and the contaminating noise.

The filter coefficients of the Wiener optimal filter, $h_{\mathrm{W},j}$, are determined by least-squares minimization of the difference between the desired and the filtered signal, while assuming that the input signal consists of the true signal contaminated by an additive, uncorrelated noise. The minimization criterion results in the formula for the Wiener filter coefficients,

$$h_{\mathrm{W},j} = \frac{\sigma^2_{\mathrm{s},j}}{\sigma^2_{\mathrm{s},j} + \sigma^2_{\mathrm{n},j}}, \tag{4.5}$$

where $\sigma^2_{\mathrm{s},j}$ and $\sigma^2_{\mathrm{n},j}$ are the expected degree-power spectra of the desired signal and contaminating noise, respectively. The derivation of (4.5) is given in Sasgen *et al.* (2006) (Section 4.4).

The basic advantage of the Wiener filter is that the parameterized signal and noise degree-power models are adaptive to the actual signal-to-noise ratio of a given monthly GRACE solution. Figure 4.7 shows the spectral and spatial representation of the optimal filter function, $h_{\mathrm{W},j}$ and $h_{\mathrm{W}}(\vartheta)$, respectively, for the monthly solutions for April 2004 (standard-quality solution) and September 2004 (poor-quality solution due to repeat orbits). For comparison, the inferred optimal Gaussian filter functions are shown. It is visible that the Wiener optimal filter broadens with increasing error level in the GRACE data. This is also visible in Figure 4.8, which shows the optimal Gaussian filter width of monthly solutions for August 2002 to August 2008. Also indicated are optimal filter widths for the linear ($\sim 3.5^{\mathrm{o}}$) as well as annual ($\sim 4^{\mathrm{o}}$) and semi-annual ($\sim 4.5^{\mathrm{o}}$) oscillating temporal components of GRACE time series (Section 4.3.2).

The degree-power spectra used for estimation of the optimal filter coefficients $h_{\mathrm{W},j}$ represent global averages of signal and noise in the GRACE data. On the one hand, this is of advantage, because the *a priori* information entering the filter design is weak, which increases the filter's robustness with respect to the *a priori* assumptions. On the other hand, GRACE errors do not exhibit homogeneous global distributions. For example, for the polar regions formal errors are below the global average due denser ground-track coverage (Figure 4.6) and isotropic Wiener filtering may over-smooth signals. This problem can be solved by adapting the Wiener optimal-filtering principle to regional representations of the gravity field, such as localized spectral base functions (Wieczorek & Simons, 2005). Also, the Wiener optimal filter can be generalized for signal and noise models varying in both degree and order. This non-isotropic (order-dependent) filtering is advantageous to account of for the longitudinal variations of the GRACE errors (Han *et al.*, 2005).

4.3 Non-isotropic filtering

In this section, two methods for non-isotropic filtering are presented. The order-dependent filter of Swenson & Wahr (2006) determines the spectral components that vary smoothly as a function of even/odd degree (i.e. correlated components) by Savitzky-Golay filtering (Savitzky & Golay, 1964) and subtracts them from the original coefficients. The statistical filter, by contrast, makes use of the stochastic behavior of the degrading stripes over time, which leads to an exceptional high noise level in some coefficients. The Student's t-test and Fisher F-test allow us to identify and

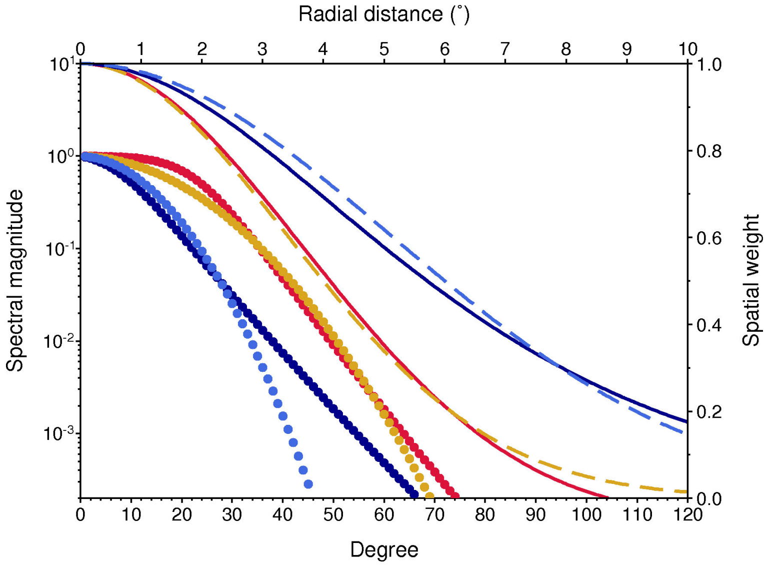

Figure 4.7: Comparison of Wiener optimal and Gaussian filter functions. Shown are the resulting filter coefficients (circles) and spatial weighting functions (lines) of the Wiener filter for April 2004 (red) and September 2004 (dark blue) together with the equivalent Gaussian filter of 4° (orange) and 6° (light blue).

remove these coefficients, as it compares the magnitude of the inferred temporal component with the coefficients' residual variability. In this work, statistical filtering is preferred as it results in a more consistent signal over the polar regions. The disadvantage of this filter is that it cannot be used to de-stripe single monthly solutions. Also, more important, there is indication that some coefficients' correlated errors are also correlated in time (Figure 4.9) and therefore passed-through by the statistical filter. The combined application of both filters may yield the best results (Davis *et al.*, 2008), given that they are optimized with respect to the signals investigated, which has not been done in this work.

4.3.1 De-correlation filtering

Swenson & Wahr (2006) empirically found that correlations between coefficients of degree with even/odd parity exist, while coefficients with different parity and different orders appear to be uncorrelated. The de-correlation filter determines, for each parity and order, spectral components that vary smoothly as a function of degree and subtracts them from the original coefficients. The de-correlation filtering follows three main steps. First, the spectrum of coefficients is split into two components with degrees of even and odd parity. Then, for all orders, the coefficients' spectra along j are smoothed with a Savitzky-Golay moving average filter (Savitzky & Golay, 1964), which is based on a polynomial fitted to the spectrum. Finally, the smoothed spectrum, which is interpreted as the GRACE coefficients' correlated noise, is subtracted

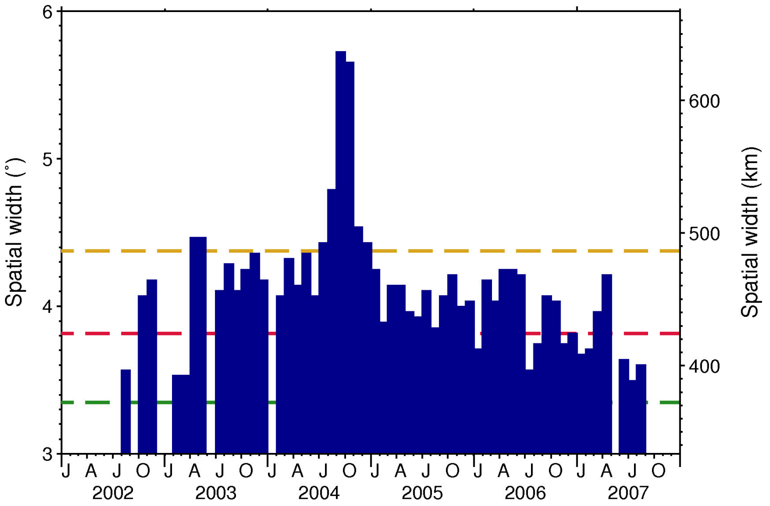

Figure 4.8: Optimal spatial half-width of the Gaussian filter derived from Wiener optimal filtering for the GRACE solutions from August 2002 to August 2008. Also indicated are optimal Gaussian filter widths for the temporal linear trend (green) as well as annually (red) and semi-annually (orange) oscillating components in the GRACE solutions' time series.

from the unfiltered spectrum.

The filter can be optimized by adjusting the order of the polynomial fitted to the spectrum and the width of the window used for averaging. Swenson & Wahr (2006) recommended using a polynomial of degree 2, but did not specify the appropriate width of the averaging window. It is evident that the filter width should decrease with increasing degree j, such that the resulting filtered signal approaches the input signal with increasing degree j, which means that most of the input signal is considered as correlated and filtered out. This should be at degrees ~ 40 to 50. The authors also recommended that input signals are passed-through for degrees $\leq \sim 8$ to avoid distortion of the low-wavelength geophysical signals. It is not the intention of this work to optimize the filter parameters, since an alternative method of de-correlation filtering is proposed in the next section. However, a de-correlation filter applied above degree and order ~ 8, with a polynomial of degree 2 and a window width of ~ 30 at $j = 9$, linearly decreasing to 3 for $j \sim 40$, produces satisfactory results (not shown).

4.3.2 Statistical filtering

The statistical filter presented by Fleming *et al.* (2006 *[online]*) is based on the assumption that the time series of each GRACE potential coefficient consists of a deterministic signal and stochastic noise. To each coefficients' time series, a parameterized model of the temporal variations of the GRACE coefficients is fitted by least-squares adjustment. Then, the statistical significance of each parameter is determined. If the test of significance is passed, the parameters are considered significant for representation of the temporal changes of the gravity field and are used; otherwise, the parameter is neglected (set to zero). With this information, the temporal model for each coefficient is reduced to include only significant temporal components, and the parameters of the temporal model are re-estimated.

Temporal decomposition

The temporal variations of the Stokes potential coefficients are described by

$$x_{jm}(t) = a_{jm}t + b_{jm} + \sum_{l=1}^{2}[c_{jm}^{l}\sin(l\omega t) + d_{jm}^{l}\cos(l\omega t)], \tag{4.6}$$

where a_{jm} is the linear trend, b_{jm} is a reference value, and c_{jm}^{l} and d_{jm}^{l} represent annual ($l = 1$) and semi-annual ($l = 2$) oscillations. The frequency ω is $2\pi/365.24\,\mathrm{day}^{-1}$. The terms c_{jm}^{l} and d_{jm}^{l} for $l = 1$, and to a much lesser extent for $l = 2$, are important for investigations of changes of the continental hydrology, whereas a_{jm} is related to long-term changes in the gravity field mainly arising from present-day ice-mass change and GIA. In the following, it is assumed that the coefficients' time series are uncorrelated and the indices j and m are omitted.

The system of linear equations relating the parameters of the temporal model to the observations $\{t_i,\, x(t_i)\}$, $i = 1, 2, ..., N$, is given by

$$\boldsymbol{x} = \boldsymbol{F}\boldsymbol{p} + \boldsymbol{e}, \tag{4.7}$$

where $\boldsymbol{p}$ is the vector containing the coefficients a, b, c^l, d^l, and $\boldsymbol{F}$ is the design matrix of the system,

$$\boldsymbol{F} = \left\{\begin{matrix} t_1 & 1 & \sin(\omega t_1) & \cos(\omega t_1) & \sin(2\omega t_1) & \cos(2\omega t_1) \\ t_2 & 1 & \sin(\omega t_2) & \cos(\omega t_2) & \sin(2\omega t_2) & \cos(2\omega t_2) \\ \cdots & \cdots & \cdots & \cdots & \cdots & \cdots \\ t_i & 1 & \sin(\omega t_i) & \cos(\omega t_i) & \sin(2\omega t_i) & \cos(2\omega t_i) \end{matrix}\right\}. \tag{4.8}$$

It is assumed that the coefficients' errors $\boldsymbol{e}$ have zero means, are normally distributed, independent and uncorrelated in time,

$$E(\boldsymbol{e}) = \boldsymbol{0},\ \mathrm{var}(\boldsymbol{e}) = C_{\mathrm{D}} = \sigma_i^2\boldsymbol{I}, \tag{4.9}$$

where E and var is the statistical expectancy and the variance-covariance matrix operator, respectively. According to Section A.6.1, the parameters' least-squares estimate is $\hat{\boldsymbol{p}} = (\boldsymbol{F}^{\mathrm{T}}C_{\mathrm{D}}^{-1}\boldsymbol{F})^{-1}\boldsymbol{F}^{\mathrm{T}}C_{\mathrm{D}}\boldsymbol{x}$ (A.34), where the parameter variances are obtained by error propagation (A.35),

$$\mathrm{var}(\hat{\boldsymbol{p}}) = (\boldsymbol{F}^{\mathrm{T}}C_{\mathrm{D}}^{-1}\boldsymbol{F})^{-1} = \sigma^2(\boldsymbol{F}^{\mathrm{T}}\boldsymbol{F})^{-1}. \tag{4.10}$$

The residuals are calculated as the difference between the data and the fitted model $\boldsymbol{r} = \boldsymbol{x} - \hat{\boldsymbol{x}}$, where $\hat{\boldsymbol{x}} = \boldsymbol{F}\hat{\boldsymbol{p}}$. They are used as *a posteriori* estimate of data variances,

$$\hat{s}^2 = \frac{\boldsymbol{r}^{\mathrm{T}}\boldsymbol{r}}{N-p}, \tag{4.11}$$

where p denotes the number of statistically significant terms of the temporal model (4.6), such that $E(\hat{s}^2) = \sigma^2$. As mentioned in Section 4.1, GRACE variances based on the residual represent maximum estimates, because they may contain unmodelled geophysical signal (e.g. Wahr *et al.*, 2004).

The statistical significance of the parameters $\hat{a}$ and $\hat{b}$ is tested with the T-test statistic,

$$T = \frac{|\hat{p}_{a,b}|}{\hat{s}_{a,b}}, \tag{4.12}$$

where $\hat{p}_{a,b}$ is calculated according to (A.35) and $\hat{s}^2$ as an estimate of σ^2. The t-test statistic follows a Student's t-distribution $t_{N-p}(\alpha)$ with $N-p$ degrees of freedom and the confidence level α. It is a measure of the deviation of the parameter $\hat{p}_{a,b}$ from zero in units of the associated standard deviation. Therefore, if $T > t_{N-p}(\alpha)$, the assumption that the parameters $\hat{p}_{a,b} = 0$ (null hypothesis) is rejected at the confidence level α in favour of the alternative hypothesis, $\hat{p}_{a,b} \neq 0$, and the parameter is considered to be significant for representation of the temporal variations.

The statistical significance for $\hat{c}^l$ and $\hat{d}^l$ is tested simultaneously using the Fisher F-test statistic, which is calculated according to

$$F = \frac{1}{2\hat{s}^2_{c^l,d^l}} (\hat{p}_{c^l}, \hat{p}_{d^l})^T \boldsymbol{W}^{-1} (\hat{p}_{c^l}, \hat{p}_{d^l}), \tag{4.13}$$

where $\boldsymbol{W}$ is a 2×2 matrix consisting of the diagonal block of $(\boldsymbol{F}^{\mathrm{T}}\boldsymbol{F})^{-1}$ associated with $(\hat{p}_{c^l}, \hat{p}_{d^l})$. The null hypothesis, $\hat{p}_{c^l} = \hat{p}_{d^l} = 0$, is tested using the Fisher F-distribution $F_{2,N-4}(\alpha)$ with 2 and $N-4$ degrees of freedom and rejected if $F > F_{2,N-4}(\alpha)$ at the confidence level α.

Filter design

The statistical filter for the GRACE data is represented by

$$y_{jm} = x_{jm} s^{\hat{\boldsymbol{p}}}_{jm}(\alpha), \tag{4.14}$$

where $s^{\hat{\boldsymbol{p}}}_{jm}(\alpha)$ is 1 if the parameter of the temporal component $\hat{\boldsymbol{p}}$ is statistically significant in the coefficients' time series $x_{jm}(t)$, otherwise it is 0. This statistical tests are implemented for a predefined confidence level α (here, 95 and 99 %).

Figure 4.9 shows the results of statistical tests at the confidence levels α of 95 (red and orange) and 99% (orange) for each GRACE coefficient. The distribution of coefficients with significant annual and linear temporal components is similar to the distribution of GRACE errors for the coefficients shown in Figure 4.3. Coefficients of high degree and order are dominated by noise, hence $s_{jm} = 0$. The number of significant coefficients is largest for the annual oscillation, which represents the largest signal in the GRACE data, followed by the linear-trend component. Semi-annual oscillations are nearly insignificant for the current length of the GRACE time series. However, it should be stated that several coefficients in noise-dominated spectral range ($\gtrsim 30$) show significant deterministic variations. In particular, a significant annual oscillation is determined for coefficients with $m \sim 12$ and j well above 30. This suggests that GRACE errors are, to some extent, correlated in time, which complicates the temporal decomposition and the interpretation of the resulting terms. It is also visible that correlations between coefficients of equal parity are reduced, but not entirely filtered out. For example, the linear temporal component retains the specific odd/even parity pattern (e.g. for $m = 7$) identified in the spectrum of the residuals (Figure 4.4). It is concluded that the correlated GRACE errors also exhibit systematic variations in time, which requires further investigation.

Figure 4.10 shows the degree-power spectra of the linear, annual, and semi-annual temporal components after statistical filtering and, for comparison, after 4^{o} Gaussian filtering and without filtering. It is visible that the statistical filter reduces the power similar to a Gaussian filter up to degree and order ~ 30. For higher degrees, increasing variability in the degree power of the statistical filtered data suggests incomplete noise reduction. It can also been seen that the filter is adaptive; the linear temporal component requires less smoothing than the annual component, which is also indicated in Figure 4.8.

Figure 4.11 and Figure 4.12 show the spatial representation of the statistical filter function. It represents the application of $s^{\hat{\boldsymbol{p}}}_{jm}(\alpha)$ to the spectral representation of a Dirac delta function located at the equator (0^{o} E; 0^{o} N) and approximately on the polar circle (0^{o} E; 65^{o} N), respectively. At the equator (Figure 4.11), the filter function associated with the annual component is similar to an ellipse with major and minor axes of $\sim 7^{\mathrm{o}}$ and 4^{o}, respectively. The filter function for the linear trend is also non-isotropic with stronger meridional averaging ($\sim 9^{\mathrm{o}}$ compared to 4^{o}). However, distinct side lobes are visible, which may arise from systematic noise not eliminated by the filter. The filter function for the semi-annual component represents an ellipse for values within its spatial half-width. Outside, side lobes are pronounced. Towards the pole (Figure 4.12), the spectrum of the Delta function becomes dominated by zonal harmonics and, as a consequence, the anisotropy of the filter response decreases. This exemplifies that the statistical filter rejects noisy coefficients without introducting/accouting for correlations between coefficients and their errors and reduces the full spectrum to a set of reliable coefficients. On the one hand this is of advantage, because signals are not distorted. On the other hand, correlated for errors between coefficients are only partially removed. The performance of the filter in the polar regions is exemplified for the temporally linear trend in the GRACE data for Antarctica (Figure 4.13). A comparison of the statistical filter, the Wiener optimal filter and the Gaussian filter is shown for the annually and semi-annually oscillating components in Figure 4.14.

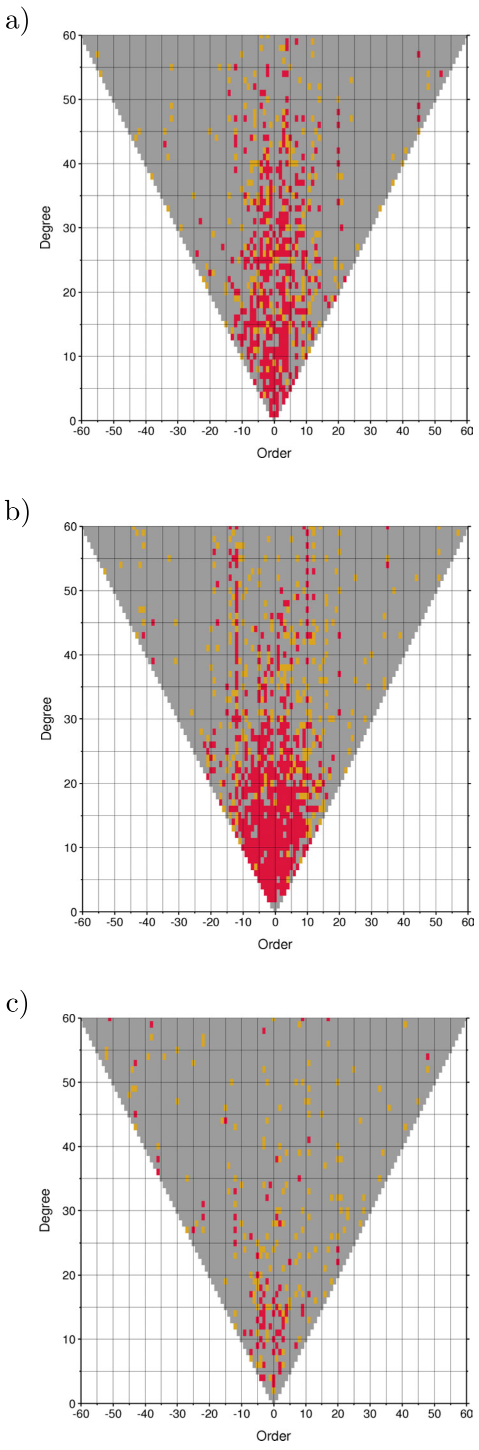

Figure 4.9: Statistical significance of the GRACE coefficients' temporal components. Shown are the results of the Student t-test for a) the linear trend and of the Fisher F-test for b) annual and c) semi-annual oscillations at a confidence level of 95% (red and orange) and 99% (orange).

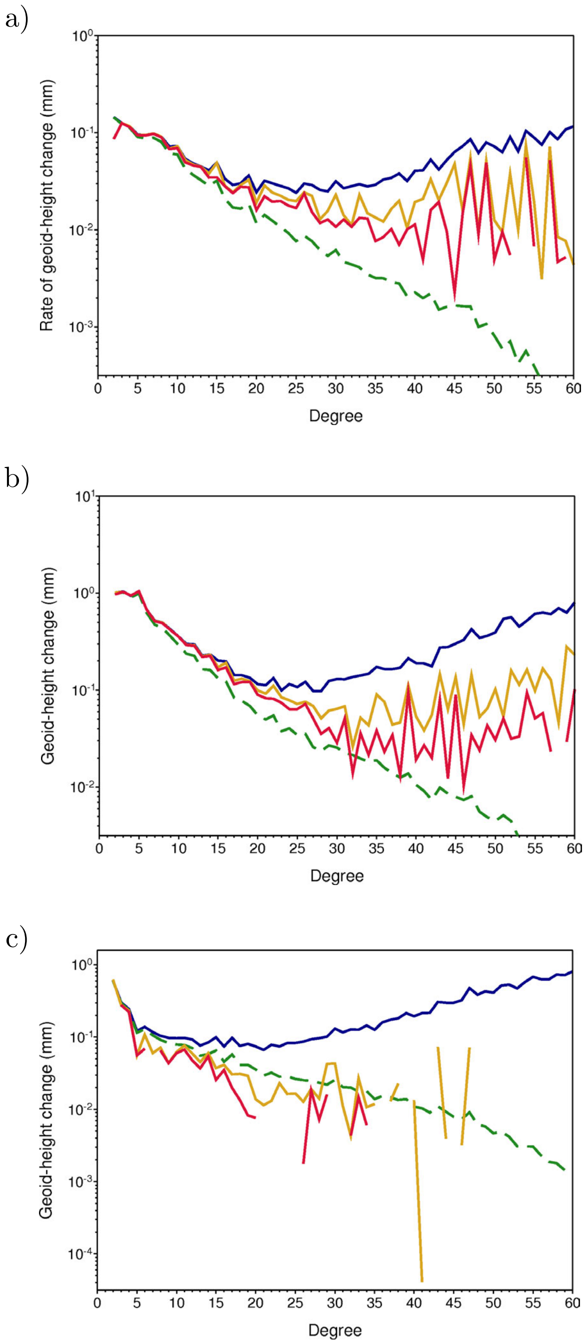

Figure 4.10: Degree-power spectrum of the GRACE coefficients' temporal components for a) the linear trend, b) annual and c) semi-annual oscillations, without excluding statistically insignificant coefficients (blue) and with excluding statistically insignificant coefficients at a confidence level of 95% (orange) and 99% (red), respectively. Also shown are the spectra after applying a 4° Gaussian filter (green)

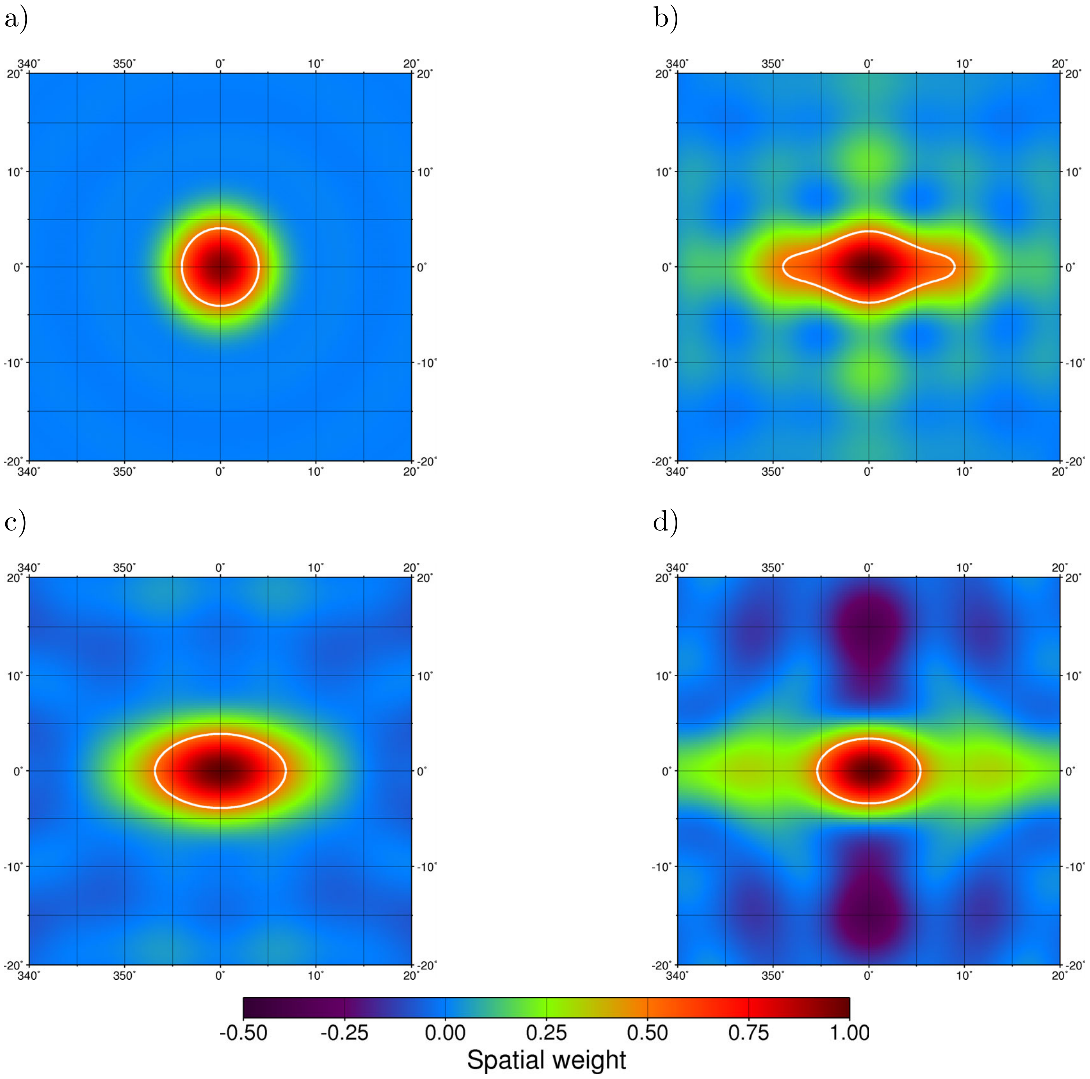

Figure 4.11: Spatial representation of statistical filter response functions. Shown are filter responses to a Dirac delta function located at (0°E; 0°N) for a) the 4° Gaussian filter, and the statistical filter for b) the linear trend as well as c) annual and d) semi-annual oscillations.

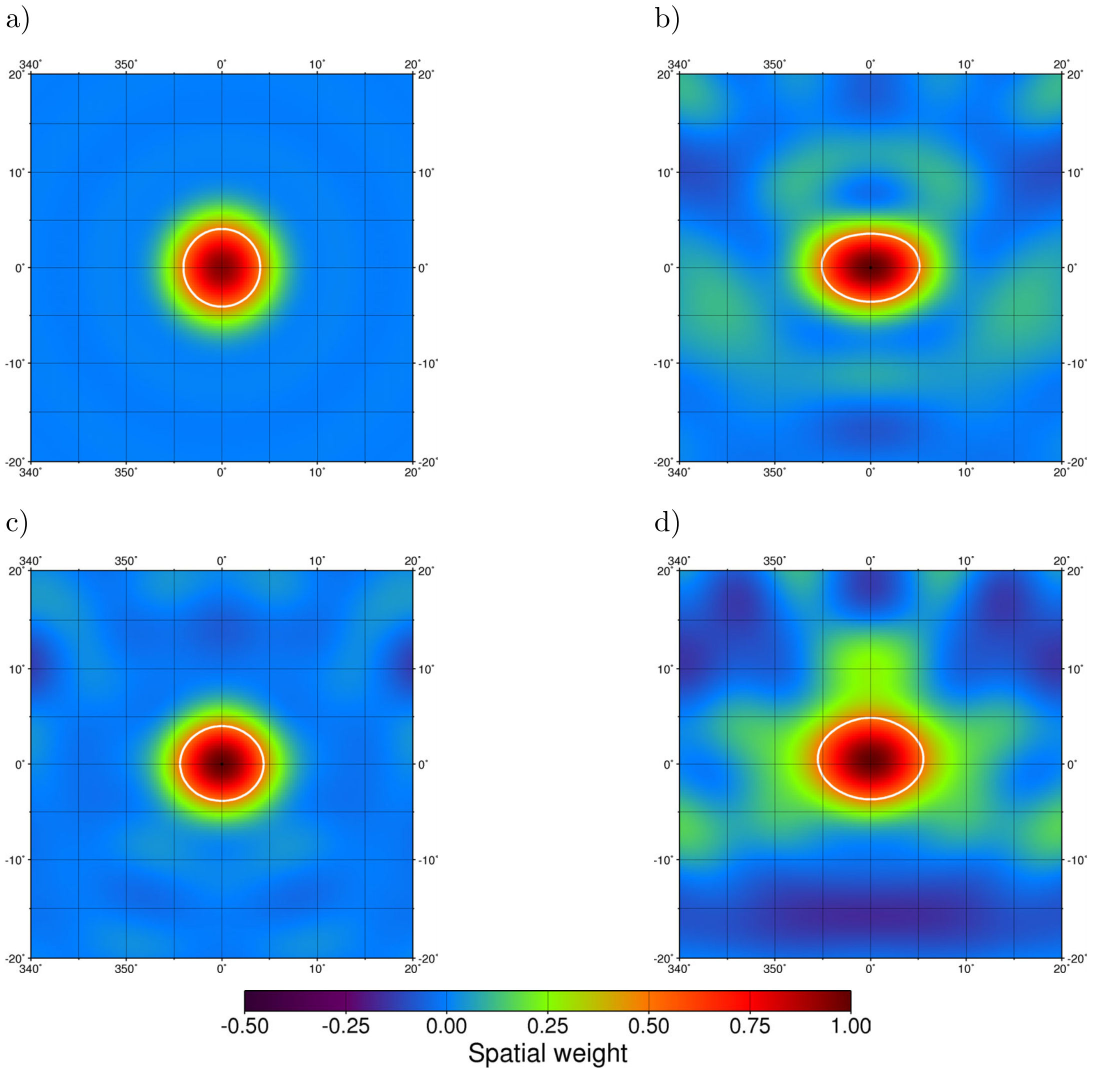

Figure 4.12: The same as Figure 4.11, but for a Dirac delta function located at (0°E; 65°N).

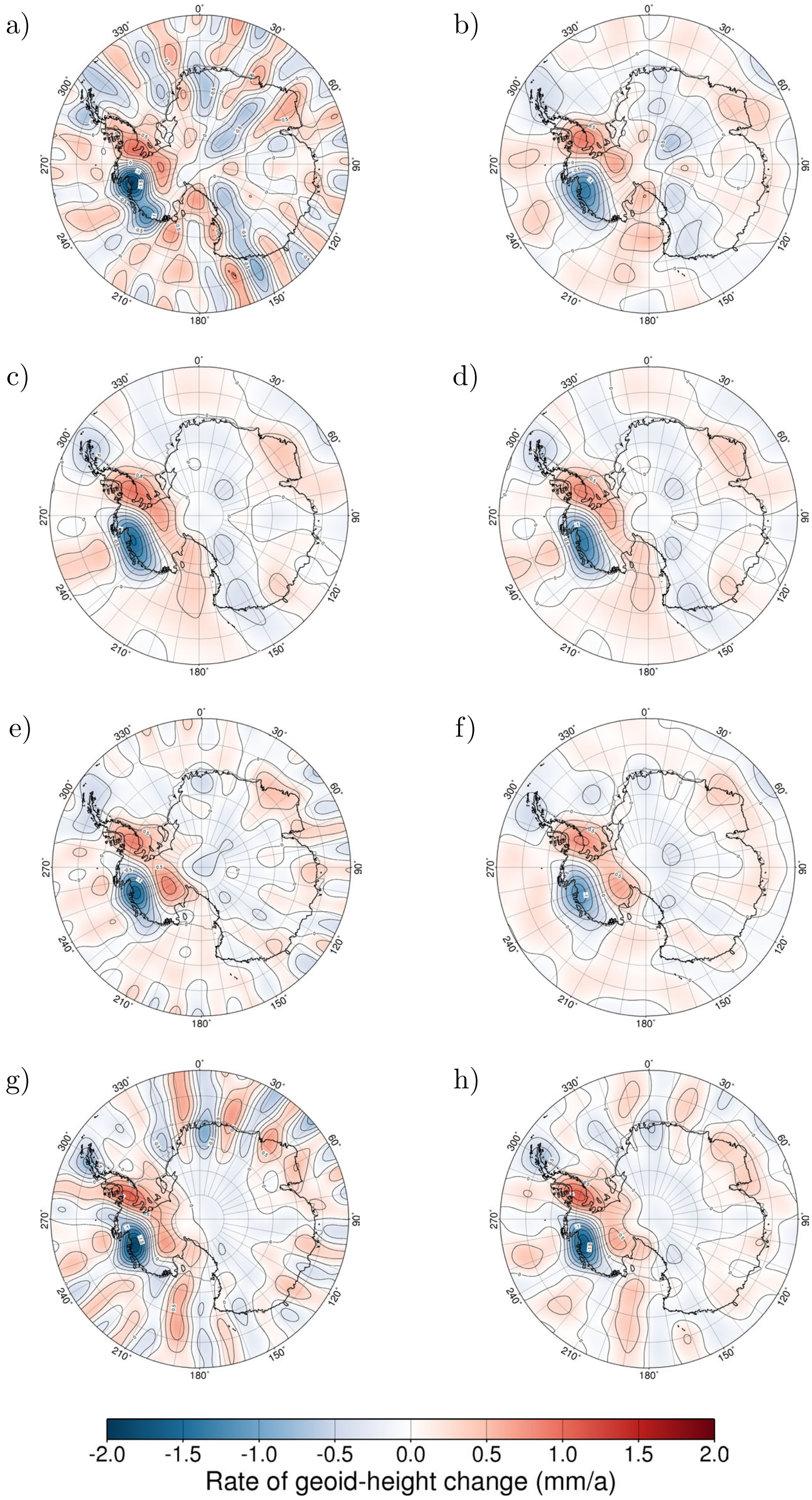

Figure 4.13: Filtered and unfiltered linear trend of the GRACE solutions over Antarctica for a) GFZ RL04, c) CNES RL01C, e) JPL RL04 and g) CSR RL04 without filtering and, respectively, b), d), f) and h) with statistical filtering. The cut-off degrees are $j_{\min} = 12$ and $j_{\max} = 50$. The solutions considered range from January 2003 to December 2006.

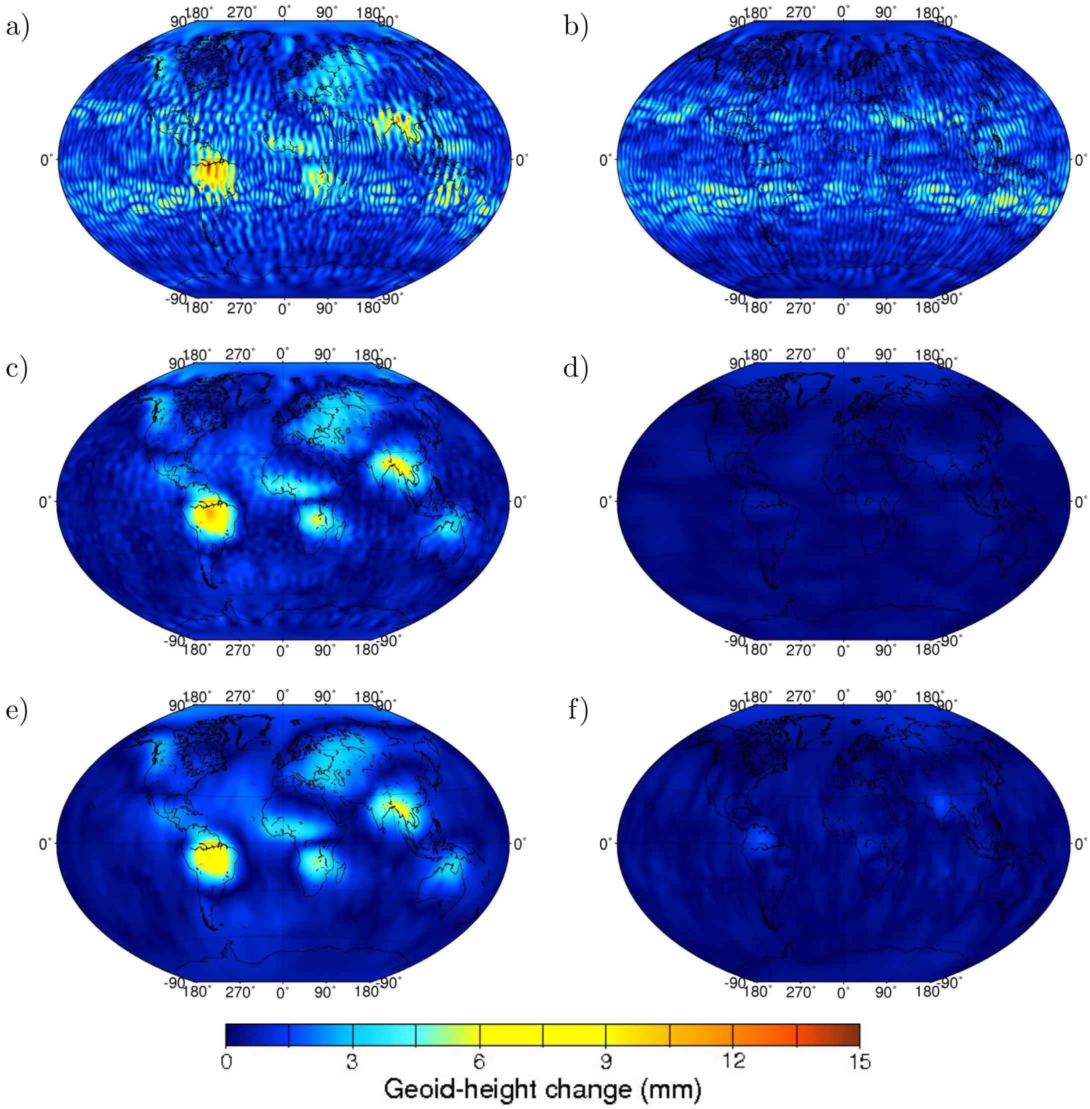

Figure 4.14: Annual and semi-annual temporal component of the GRACE solutions for August 2003 to August 2007, respectively, a) and b) without filtering, c) and d) with the statistical filter and e) and f) with the Wiener optimal filter. The cut-off degrees are $j_{\min} = 3$ and $j_{\max} = 60$.

4.4 Wiener optimal filtering of GRACE data (*published*)

Abstract[†]

We present a spatial averaging method for Gravity Recovery and Climate Experiment (GRACE) gravity-field solutions based on the Wiener optimal filtering.
The optimal filter is designed from the least-square minimization of the difference between the desired and filtered signals. It requires information about the power spectra of the desired gravitational signal and the contaminating noise, which is inferred from the average GRACE degree-power spectrum. We show that the signal decreases with increasing spherical harmonic degree j with approximately $1/j^b$, where $b = 1.5$ for GRACE data investigations. This is termed the Second Kaula rule of thumb for temporal variations of the Earth's gravity field. The degree power of the noise increases, in the logarithmic scale, linearly with increasing j.
The Wiener optimal filter obtained for the signal model with $b = 1.5$ closely corresponds to a Gaussian filter with a spatial half width of 4^o ($\sim$440 km). We find that the filtered GRACE gravity signal is relatively insensitive to the exponent b of the signal model, which indicates the robustness of Wiener optimal filtering. This is demonstrated using the GFZ-GRACE gravity-field solution for April 2004.

[†] Sasgen, I., Martinec, Z. & Fleming, K., 2006. Wiener optimal filtering of GRACE data. *Stud. Geophys. Geod.*, 50(4): 499–508. Received: November 24, 2005; Revised: February 3, 2006; Accepted: February 16, 2006. Copyright 2006 Springer Science and Business Media, Dodrecht, The Netherlands. Reproduced with kind permission of Springer Science and Business Media.

4.4.1 Introduction

The Gravity Recovery and Climate Experiment (GRACE) space mission was launched by the National Aeronautic and Space Agency (NASA) and the Deutsche Zentrum für Luft- und Raumfahrt (DLR) on March 17, 2002. The primary mission objective is to provide monthly solutions of the Earth's gravity field with a spatial resolution of $\sim$400 km. These solutions are of particular interest when attempting to investigate time-variable phenomena such as hydrological or oceanic mass variations (e.g. Tapley *et al.*, 2004; Reigber *et al.*, 2005).

The gravity-field solutions are available in the two GRACE archives, ISDC *[online]* and PO.DAAC *[online]*, as fully-normalized Stokes potential coefficients, which are independently computed at the GeoForschungsZentrum (GFZ) Potsdam, the Center for Space Research (CSR) at the University of Texas, and the Jet Propulsion Laboratory (JPL) in Pasadena. In this paper, we use 34 solutions from the years 2003 and 2004, that were provided by the CSR (18 solutions, release 2) and GFZ (16 solutions, release 3) processing centres.

In principle, the error of the GRACE potential coefficients increases with increasing spatial resolution, which implies that the error of the GRACE potential coefficients increases towards higher spherical-harmonic degrees. Spatial averaging of the GRACE gravity-field solutions allows optimizing the tradeoff between noise reduction and spatial resolution.

This has commonly been done using a Gaussian spatial averaging function (e.g. Wahr *et al.*, 1998; Swenson & Wahr, 2002), which requires an *ad hoc* definition of an averaging radius. In this paper, we present an alternate spatial averaging method based on the Wiener optimal filtering. In contrast to the Gaussian averaging method, the Wiener optimal filter is constructed using the degree-power spectra of the desired signal and the contaminating noise, which is a weaker constraint on the signal-to-noise ratio (e.g Press *et al.*, 1992).

The paper is organized as follows. First, we adapt the basic theory of the Wiener optimal filtering approach, originally applied to the analysis of time series, to spatial filtering on a sphere. Next, we determine the optimal filter coefficients for the available GRACE data, and then we compare the results with those based on Gaussian filtering.

The main objective of this paper is to present the theory of the degree-dependent Wiener (least-squares) optimal filtering on a sphere in a transparent way. Additionally, we develop signal and noise models summarizing the current data sets. In future, this theory can be generalized to allow for degree- and order-dependent filtering of GRACE data (e. g. Han *et al.*, 2005).

4.4.2 Wiener optimal filtering on a sphere

The Wiener filter (e.g. Wiener, 1949) is a linear convolution filter for which the actual output signal $y(\mathbf{\Omega})$ is given by the spatial convolution of the filter response function $h(\mathbf{\Omega})$ with the measured input signal $x(\mathbf{\Omega})$,

$$y(\mathbf{\Omega}) = \int_{\mathbf{\Omega}'_0} h(\mathbf{\Omega}')x(\mathbf{\Omega} - \mathbf{\Omega}')d\mathbf{\Omega}', \tag{4.15}$$

where $\mathbf{\Omega}$ stands for the spherical co-latitude ϑ and longitude φ. Hence $\mathbf{\Omega} := (\vartheta, \varphi)$, $\mathbf{\Omega}_0$ is the full solid angle and $d\mathbf{\Omega}$ its infinitesimal element. The signals $x(\mathbf{\Omega})$ and $y(\mathbf{\Omega})$ are assumed to be square-integrable functions over the unit sphere and thus can be represented as series of scalar spherical harmonics $Y_{jm}(\mathbf{\Omega})$ of degree j and order m,

$$\begin{bmatrix} x(\mathbf{\Omega}) \\ y(\mathbf{\Omega}) \end{bmatrix} = \sum_{j=0}^{\infty} \sum_{m=-j}^{j} \begin{bmatrix} x_{jm} \\ y_{jm} \end{bmatrix} Y_{jm}(\mathbf{\Omega}), \tag{4.16}$$

where x_{jm} and y_{jm} are the spherical-harmonic expansion coefficients of $x(\mathbf{\Omega})$ and $y(\mathbf{\Omega})$, respectively, and $Y_{jm}(\mathbf{\Omega}) = P_{jm}(\vartheta)e^{im\varphi}$, where $P_{jm}(\vartheta)$ is the fully-normalized associated Legendre function of degree j and order m. We assume that the Wiener filter is rotationally symmetric, $h = h(\vartheta)$, and can be represented as a series of Legendre polynomials $P_j(\cos\vartheta)$,

$$h(\vartheta) = \sum_{j=0}^{\infty} \frac{2j+1}{4\pi} h_j P_j(\vartheta), \tag{4.17}$$

where the factor $(2j + 1)/4\pi$ is introduced to normalize the expansion coefficients h_j. Considering the expansions (4.16) and (4.17) and applying the Laplace addition theorem for spherical harmonics (e.g Varshalovich *et al.*, 1989),

$$P_j(\cos\psi) = \frac{4\pi}{2j+1} \sum_{m=-j}^{j} Y^*_{jm}(\mathbf{\Omega}')Y_{jm}(\mathbf{\Omega}), \tag{4.18}$$

where ψ is the angular distance between points $\mathbf{\Omega}$ and $\mathbf{\Omega}'$ and the asterisk denotes the complex conjugation, the spherical-harmonic form of convolution (4.15) can be expressed as

$$y_{jm} = h_j x_{jm}. \tag{4.19}$$

The Wiener optimal filter (Figure 4.15) is designed such that (i) the actual output signal $y(\mathbf{\Omega})$ is close to a desired output signal $d(\mathbf{\Omega})$ in the least-square sense, such that

$$E^2 := \int_{\mathbf{\Omega}_0} \Big| y(\mathbf{\Omega}) - d(\mathbf{\Omega}) \Big|^2 d\mathbf{\Omega} = \sum_{j=0}^{\infty} \sum_{m=-j}^{j} \Big| y_{jm} - d_{jm} \Big|^2 \tag{4.20}$$

is minimized, where the equality is due to Parseval's identity for spherical-harmonic series, (ii) the measured signal $x(\mathbf{\Omega})$ consists of the true signal $s(\mathbf{\Omega})$ contaminated by an additive noise $n(\mathbf{\Omega})$,

$$x(\mathbf{\Omega}) = s(\mathbf{\Omega}) + n(\mathbf{\Omega}), \tag{4.21}$$

(iii) the signal $s(\mathbf{\Omega})$ and the noise $n(\mathbf{\Omega})$ are uncorrelated, so that their cross product, when integrated over the full solid angle, gives zero,

$$\int_{\mathbf{\Omega}_0} s(\mathbf{\Omega})n(\mathbf{\Omega})d\mathbf{\Omega} = \sum_{j=0}^{\infty} \sum_{m=-j}^{j} s_{jm}n^*_{jm} = 0, \tag{4.22}$$

and (iv) the desired output signal is identified with the uncontaminated original signal, $d(\mathbf{\Omega}) = s(\mathbf{\Omega})$.

Under these requirements, the least-square criterion E^2 takes the form

$$E^2 = \sum_{j=0}^{\infty} \Big\{ \sigma^2_{\mathrm{s},j}(1-h_j)^2 + \sigma^2_{\mathrm{n},j}h_j^2 \Big\}, \tag{4.23}$$

where

$$\sigma^2_{\mathrm{s},j} := \sum_{m=-j}^{j} |s_{jm}|^2, \qquad \sigma^2_{\mathrm{n},j} := \sum_{m=-j}^{j} |n_{jm}|^2,$$

are the degree power spectra of the signal $s(\mathbf{\Omega})$ and noise $n(\mathbf{\Omega})$, respectively. Thus, the aim is to search for such a h_j that minimizes E^2. Differentiating (4.23) with respect to h_j, and setting the result equal to zero gives

$$h_j = \frac{\sigma^2_{\mathrm{s},j}}{\sigma^2_{\mathrm{s},j} + \sigma^2_{\mathrm{n},j}}, \tag{4.24}$$

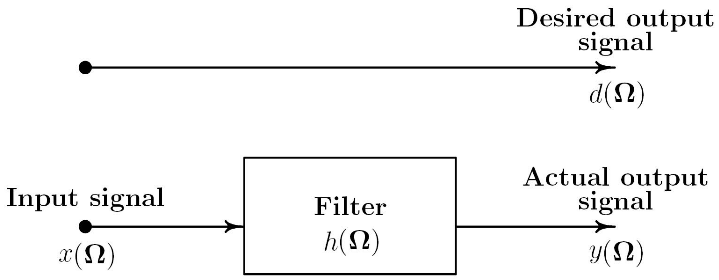

Figure 4.15: Principle of Wiener optimal filtering. The filter minimizes the difference between the desired output signal and the actual (filtered) output signal in a least-squares sense.

where $j = 0, 1, \ldots$. This is the formula for the optimal Wiener filter coefficients, which is also stated, without derivation, in Seo & Wilson (2005). Note that h_j approaches unity when the noise is negligible, and zero when the noise is dominant. Equation (4.24) therefore gives the optimal transition between these two extremes.

The Wiener filter is isotropic and depends only on the degree power of the signal and noise models. It is known, however, that the GRACE error is larger for higher orders than for lower orders, which induces longitudinal stripes in the gravity field solutions (Figure 4.19). In future, the presented theory can be generalized to accommodate signal and noise models dependent on both degree and order (e.g. Han *et al.*, 2005).

4.4.3 Signal and noise degree-power spectra from and for GRACE data

Determining the Wiener filter coefficients according to equation (4.24) requires a way of finding separate estimates of the degree-power spectra of the desired gravitational signal, $\sigma^2_{\mathrm{s},j}$, and the contaminating noise, $\sigma^2_{\mathrm{n},j}$. In fact, there is no way to do this from the measured signal $x(\mathbf{\Omega})$ alone without some additional information or some assumptions. Fortunately, extra information can be obtained from the GRACE data.

Figure 4.16 shows the average degree-power spectrum of the GRACE gravity-field solutions. This average spectrum is calculated by

$$< \sigma^2_{\mathrm{GRACE},j} >= \frac{1}{N}\sum_{n=1}^{N}\sigma^2_{\mathrm{GRACE_n},j} \tag{4.25}$$

for $N = 34$ monthly GRACE solutions with $2 \leq j \leq 120$. The solutions are taken relative to a reference field, which is computed as the average of the considered GFZ and CSR solutions, respectively. We chose this reference field, on the one hand, for its consistency with the GRACE data, and, on the other, to be assured that the computed relative solutions are not biased. In general, it is possible to use other reference fields, such as the static field EIGEN-CG03C (Förste *et al.*, 2005), without significantly changing the results presented in the following.

We assume that the lower-degree part ($j < 21$) of this averaged spectrum contains information about gravity signals, the spectrum for $j > 29$ reflects the noise contaminating the GRACE data, while the two overlap in the range of $20 < j < 30$. This intuitive division is in agreement with the generally accepted idea that the gravity field induced by hydrological and ocean-mass variations is the largest contribution to the GRACE gravity observations. The corresponding degree-power spectrum, shown in Figure 4.16 (Wahr *et al.*, 2004), gradually decreases with increasing degree j, supporting our assumption. The average GRACE degree-power spectrum of the gravity signals ($j < 21$), in terms of the geoid-height squared in mm^2, is parameterized by the inverse-power function of j,

$$< \sigma^2_{\mathrm{GRACE},j} >= \frac{10^a}{j^b}, \tag{4.26}$$

where the parameters $a = 0.48$ and $b = 1.5$ have been obtained by a least-squares adjustment.

We refer to this formula as the second Kaula rule of thumb for temporal variations of the Earth's gravity field, since function (4.26) for $a = 9.81$ and $b = 3$ is known as the Kaula rule of thumb (Kaula, 1966), which gives the estimate of the degree power of the Earth's static gravity field. Function (4.26) is then extrapolated into the region largely influenced by noise $j > 20$. Figure 4.16 shows that the extrapolation mimics the convex shape of degree-power spectrum of the hydrology and ocean models. The spectra do not coincide exactly, since there are other mass changes in the Earth system that contribute to the GRACE higher-degree power spectrum. We also confine the least-squares adjustment to degrees $j < 15$ in order to exclude GRACE coefficients which may be influenced by resonance effects in satellite-orbit determination, and to determine the sensitivity of b to the choice of degrees used for the adjustment. In this case, we obtained $a = 0.59$ and $b = 1.66$. Then, to test the sensitivity of the Wiener filter to the parameter b of the underlying signal model, we have additionally parameterized function (4.26) with $a = 0.97$ and $b = 2$ (Figure 4.16), which is in better agreement with the predictions from the hydrology and ocean models.

It should be emphasized that the second Kaula rule of thumb is derived empirically from the two years of GRACE data, and may change over time. The physical laws underlying this relationship are not understood. Nevertheless, it contains information about the time-varying gravity field that can be used during the processing of satellite data.

The degree-power spectrum of the average formal GRACE errors suggests the parametrization of the degree-power spectrum of the noise by a linear function in a logarithmic scale (Figure 4.16, black circles),

$$\log \sigma^2_{\mathrm{n},j} = c + dj. \tag{4.27}$$

The actual values of the parameters c and d have been obtained by a least-square procedure from the average GRACE degree-power spectrum for the range $j > 29$,

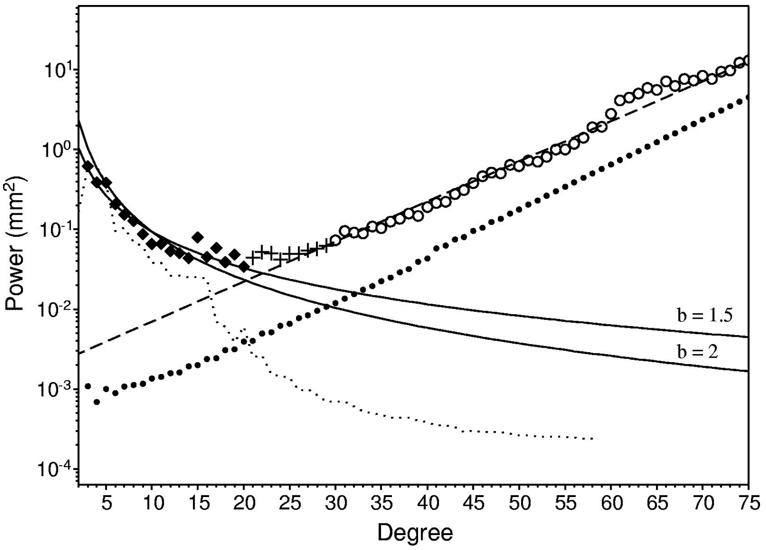

Figure 4.16: Signal and noise degree-power spectra. Shown is the average degree-power spectrum of 34 GRACE gravity-field solutions. According to predictions from hydrology and ocean models (Wahr *et al.*, 2004) (faint-dotted line) and the average formal GRACE errors (black circles), the average GRACE spectrum is divided into the region dominated by the signal ($j < 21$, black diamonds) and the region dominated by noise ($j > 29$, white circles). The corresponding regions are then used to design the best-fitting functions, (4.26) and (4.27) (see text), for the GRACE gravity signal (solid lines) and the contaminating noise (dashed line). The transition between the region dominated by the signal and the noise (crosses) is not used to design the filter.

resulting in $c = -2.66$ and $d = 0.05$ (Figure 4.16, dashed line). Finally, extrapolating the noise degree-power spectrum to the region dominated by the signal, that is for $j < 30$, and computing the difference

$$\sigma^2_{\mathrm{s},j} =< \sigma^2_{\mathrm{GRACE},j} > -\sigma^2_{\mathrm{n},j}, \tag{4.28}$$

we obtain the degree-power spectrum of the signal, $\sigma^2_{\mathrm{s},j}$, needed for constructing the Wiener filter coefficients.

One point needs to be emphasized. Because the Wiener optimal filter results from least-square minimization, the quality of the signal obtained by Wiener filtering differs from the true signal by an amount that is of the second order in precision compared to that from which the optimal filter is determined. This means that even a crude separation of the observation into signal and noise components can provide excellent results when it is applied to data. In particular, this suggests that the influence of the exponent b of the signal model is rather small, which will be demonstrated in the next section.

4.4.4 Application to GRACE gravity-field solution

Having specified the signal and noise degree-power spectra, we calculate the Wiener optimal filter coefficients according to equation (4.24) and transform this spectral response function to the spatial domain according to equation (4.17). Figure 4.17 shows the Wiener filter response function for the signal models with $b \in \{1.5, 2\}$ in the spectral and spatial domain. For comparison, we include the response functions of a Gaussian filter $h_{\mathrm{G}}(\vartheta)$ for 4° spatial half width ϑ_h, defined implicitly by $h_{\mathrm{G}}(\vartheta_h) = 0.5 h_{\mathrm{G}}(0)$.

We note that the Wiener optimal filter is a low-pass filter, that is, in general, similar to a Gaussian filter. In particular, the differences between the response functions of the Wiener filter assuming a signal model with $b = 1.5$ and the 4° Gaussian filter are small. If $b = 2$ instead of $b = 1.5$ is used, which assumes a larger power of the desired signal at the lower degrees, the spatial width of the Wiener filter broadens. In this case, its spatial half width corresponds approximately to that of a 4.5° Gaussian filter. This again exemplifies the basic principle of the Wiener optimal filter, which optimizes, based on relatively coarse assumptions about the expected degree-power spectra of the signal and the noise, the tradeoff between the spatial resolution and the noise reduction. For instance, given that the noise level of future GRACE solutions is expected to be lower, the filter will allow for a higher spatial resolution.

As an example, the Wiener optimal filter for $b = \{1.5, 2\}$ and the 4° Gaussian filter are applied to the GFZ-GRACE gravity-field solution for April 2004 (release 3). Figure 4.18 shows the degree-power spectra of the geoid-height changes after filtering. We again see that the Wiener optimal filter assuming $b = 1.5$ for the signal model (red circles) performs very similarly to the 4° Gaussian filter (blue circles). However, with regard to the higher degrees of the spectrum, the Wiener filter is adaptive to the power of the noise contaminating the GRACE data, since its filter coefficients reflect the signal-to-noise ratio specific for the actual data. For the same reason, the filter adjusts to the desired gravitational signal. If the signal is expected to be more powerful at the lower degrees, i. e. if $b = 2$ describes the desired signal more appropriately, then the filter coefficients are such that the decrease in power with increasing j is faster (green circles).

Figure 4.19 shows the spatial representation of the spectral results shown in Figure 4.18, that is the spatial geoid-height change of the GFZ-GRACE gravity-field solution for April 2004 before and after filtering. In general, the spatial patterns are very similar for all investigated filters. In particular, the differences between the Wiener filter assuming $b = 1.5$ for the signal model and the 4° Gaussian filter are negligible. The pattern obtained for the Wiener filter with $b = 2$ is slightly smoother, i. e. the power of the higher degrees has been reduced, which has already been indicated by the degree-power spectra shown in Figure 4.18. However, the general pattern is not changed, demonstrating the robustness of Wiener optimal filtering.

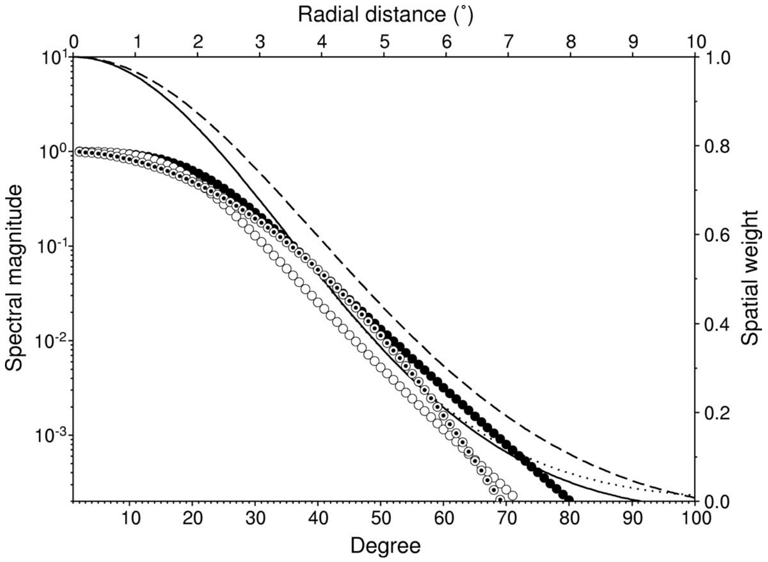

Figure 4.17: Wiener optimal and Gaussian filter response functions in the spectral (circles) and spatial (lines) domain. Shown are the Wiener optimal filter assuming $b = 1.5$ (full circles, solid line) and $b = 2$ (empty circles, dashed line) for the signal model (see text), and the 4° Gaussian filter (dotted circles, dotted line).

4.4.5 Summary

We have derived a spatial averaging method based on the Wiener optimal filtering on a sphere, which can be applied to the GRACE gravity-field solutions. For this approach, no spatial width of the filter needs to be specified. However, assumptions about the degree power of the desired gravitational signal and the contaminating noise must be made.

The spectra of the expected signal and noise were derived from the average degree-power spectrum of 34 GRACE solutions. We showed that the degree-power spectrum of the gravity signals contained in GRACE data decreases as $1/j^b$, where $b = 1.5$, with increasing spherical-harmonic degree j. We call this relation the Second Kaula rule of thumb for temporal variations of the Earth's gravity field. Additionally, the parameter $b = 2$ was used, which is in better agreement with predictions of the expected signal, to test the sensitivity of the results the choice of the signal model. As far as the contaminating GRACE data noise is concerned, the logarithm of its degree-power spectrum increases linearly with degree j.

The Wiener optimal filter is found to be a low-pass filter, and is similar to a Gaussian filter. In particular, for $b = 1.5$, the Wiener optimal filter performs similarly to a Gaussian filter with the spatial half-width of 4° ($\sim$440 km). Moreover, we demonstrated that the filter is relatively insensitive to the exponent b of the underlying signal model. Hence, we conclude that Wiener optimal filtering is a robust method of spatially averaging GRACE data. As mentioned, one basic advantage of this method is

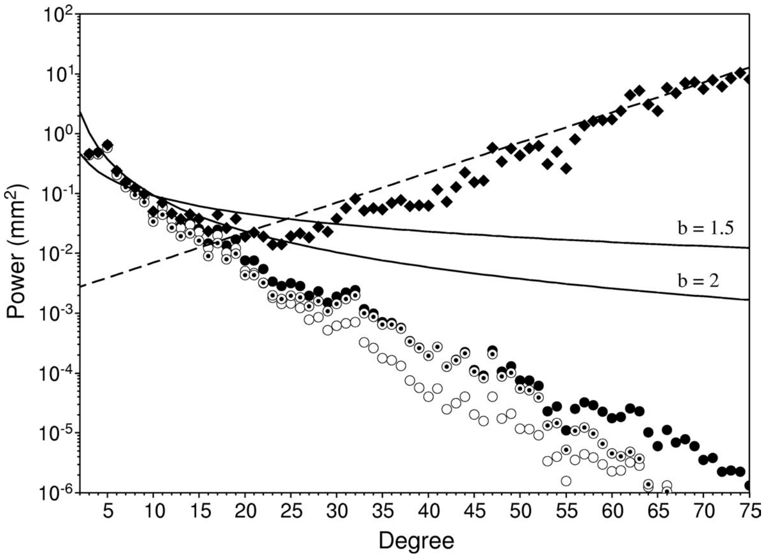

Figure 4.18: Degree-power spectrum of the geoid-height change of the GFZ-GRACE solution for April 2004, unfiltered (diamonds) and filtered (circles). Wiener filter assuming $b = 1.5$ (full circles) and $b = 2$ (empty circles) for the signal model (see text), and the 4^{o} Gaussian filter (dotted circles). Also shown are the degree-power models of the signal (solid lines) and the noise (dashed line) used for the design of the Wiener filter.

that no spatial half width has to be predefined. The Wiener filter is optimally adjusted to the desired gravitational signal and the noise specific to the available GRACE data.

In general, the Wiener optimal filter can be developed for signal and noise models that vary with both degree and order. This has not been included in this paper. However, recent investigations have pointed out that non-isotropic filtering (e. g. Han *et al.*, 2005) is advantageous since the orbit of the GRACE satellites causes larger errors in the potential coefficients of higher orders than of lower orders. This effect is visible e. g. in the longitudinal stripes and will, in future, be addressed by a more generalized Wiener optimal filter approach.

Acknowledgments

We thank Roland Schmidt from the GFZ Potsdam for helpful discussions, and two anonymous reviewers, whose comments have helped us to improve the manuscript. The second author acknowledges support from the Grant Agency of the Czech Republic through Grant No. 205/03/0778.

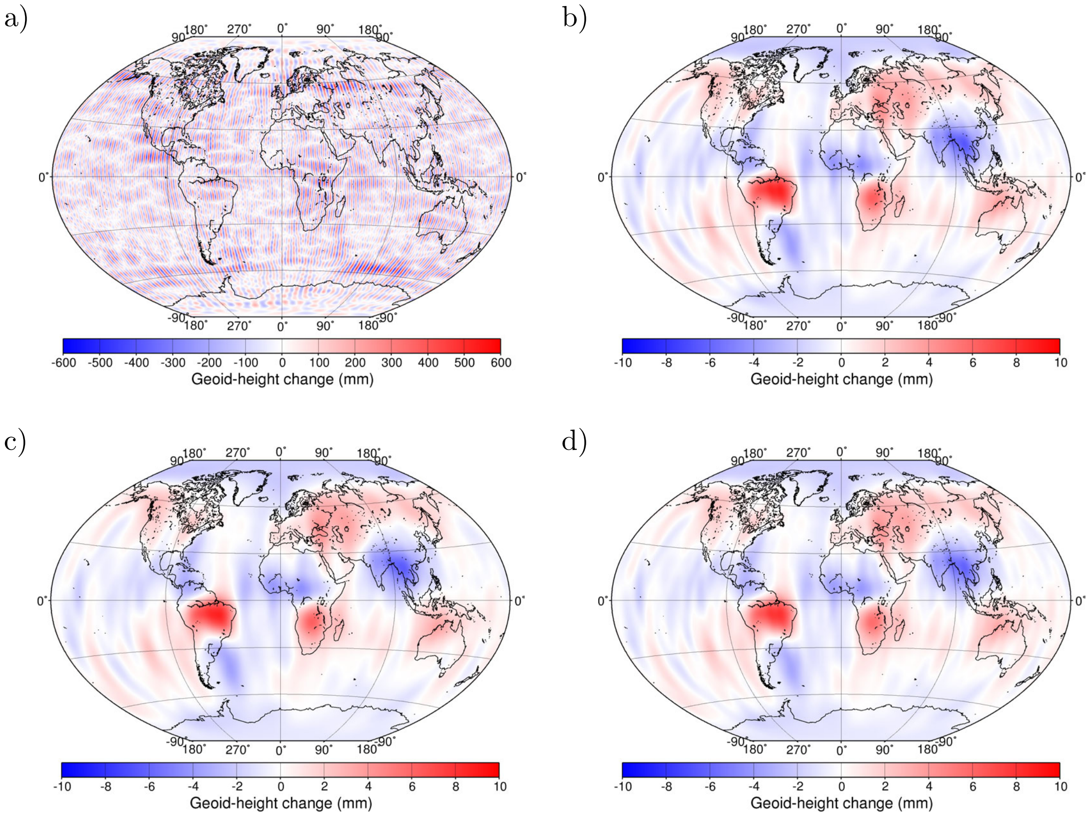

Figure 4.19: The geoid-height change of the GFZ-GRACE solution for April 2004 with respect to the GFZ reference field (see Section 3) (a) unfiltered and processed with the Wiener filter assuming (b) $b = 1.5$ and (c) $b = 2$ for the signal model, and (d) the 4^{o} Gaussian filter. The cut-off degrees are $j_{\min} = 3$ and $j_{\max} = 120$.

4.5 Wiener optimal combination and evaluation of the GRACE gravity fields over Antarctica (*published*)

Abstract[†]

We present an appraisal method for the Gravity Recovery and Climate Experiment (GRACE) gravity-field releases based on the Wiener optimal evaluation approach. The Wiener optimal evaluation uses linear convolution filtering and the subsequent addition of multiple inputs to minimize (in a least-squares sense) the difference between the combined optimal output and a desired output. Investigating the individual filtered outputs with respect to the desired output provides a measure of the quality of each input.

Here, the inputs are linear trends of the gravity-field change over Antarctica inferred from the Stokes potential coefficients of the 4 independent GRACE releases; GFZ RL03, CSR RL01C, JPL RL01C and CNES RL01C, each with at least 27 months worth of data. The desired output is based on the predicted gravity-field change over Antarctica resulting from by present-day ice-mass changes and ongoing glacial-isostatic adjustment (GIA). We demonstrate that the combined output of the Wiener optimal evaluator improves the quality of the signal over Antarctica with regards to the desired output. We show that 3 of the 4 GRACE releases essentially constitute the desired signal in the optimal combination, while one mainly reduces the contaminating noise over the oceans. The best agreement with the predicted gravity-field change over Antarctica is represented by the release CNES RL01C.

[†] Sasgen, I., Martinec, Z. & Fleming, K., 2007. Wiener optimal combination and evaluation of GRACE gravity fields over Antarctica. *J. Geoph. Res.*, B(112): B04401. Received: June 29, 2006; Revised: October 25, 2006; Accepted: November 13, 2006.

4.5.1 Introduction and Motivation

For almost 4 years, the Gravity Recovery and Climate Experiment (GRACE) space mission of the National Aeronautic and Space Agency (NASA) and the Deutsche Zentrum für Luft- und Raumfahrt (DLR) has provided monthly solutions of the Earth's gravity field with a spatial resolution of $\sim$400 km (Bettadpur, 2004b; Tapley & Reigber, 2001; Tapley *et al.*, 2004a). The increasing length of the time series allows us to determine, in addition to the periodic variations, a statistically reliable linear trend in the temporal gravity-field change induced by, for example, present-day ice-mass variations and ongoing glacial-isostatic adjustment (GIA).

In this study, we consider the monthly gravity-field solutions provided by the Science Data System (SDS) centers - the GeoForschungsZentrum (GFZ) Potsdam, the Center for Space Research (CSR) at the University of Texas, and the Jet Propulsion Laboratory (JPL) in Pasadena, as well as the GRACE solutions determined by the Bureau Gravimetrique International of the Centre National d'Ètudes Spatiales (CNES). All solutions are available as fully-normalized Stokes potential coefficients and represent independent determinations of the gravity field (Figure 4.20).

The process of determining the Stokes potential coefficients from the various measurements made by the GRACE satellites is complex, and requires a number of assumptions to be made concerning processing and noise-reduction strategies and background models, which sometimes differ between the solution providers. In addition, updates to a provider's solutions, issued as releases, are also based on revised assumptions and procedures, and may result in considerably different solutions.

Stochastic descriptions of the GRACE gravity-field solutions usually indicate that later releases are of a better quality than earlier releases. However, it is also necessary to evaluate the GRACE solutions from the perspective of geophysical modeling in order to identify and understand the disagreements that arise between predictions and GRACE observations, which may arise from inaccurate temporal background models used during solution processing (e.g. Flechtner *et al.*, 2006 *[online]*).

It is the aim of this paper to provide a method for the optimal combination and evaluation of different GRACE releases with respect to a predicted gravity-field signal. The method is based on the Wiener filtering technique, which has been used in geodetic problems to reduce noise (e.g. Kotsakis & Sideris, 2004; di Leonardo & Dickmann, 2004). Here, it is applied to the spherical-harmonic coefficients representing the temporal linear trend in the gravity fields of different GRACE releases with the aim of reducing non-geophysical components that are considered as noise.

The paper proceeds as follows. First, we present the theory of the Wiener optimal evaluator. Then, we focus on the region of Antarctica and predict the contemporary gravity-field change using a viscoelastic earth model subject to reconstructions of present and past changes of the Antarctic Ice Sheet (AIS). Next, we identify the linear trends in the temporal gravity-field change over Antarctica as observed by GRACE by considering the 4 independent releases of the Stokes potential coefficients. Finally, we use the Wiener optimal evaluator to combine the resulting trend-only fields and evaluate their qualities with respect to the predicted gravity-field change.

4.5.2 Wiener optimal combination and evaluation

The Wiener optimal evaluator is based on linear convolution filtering and subsequent addition of 2 or more inputs, with the aim of optimally adjusting the filtered output to be close to a desired output (Figure 4.21). The filtered output is optimal in the sense that it is the closest (in terms of least squares) to the desired output that the filter can produce. This convolution can be expressed as

$$y(\boldsymbol{\Omega}) = \int_{\boldsymbol{\Omega}_0'} \boldsymbol{h}(\boldsymbol{\Omega}').\boldsymbol{x}(\boldsymbol{\Omega} - \boldsymbol{\Omega}')d\boldsymbol{\Omega}', \tag{4.29}$$

where y is the optimal output, and $\boldsymbol{x}$ and $\boldsymbol{h}$ are K-dimensional vectors of K measured inputs (here, K GRACE releases) and the associated filter functions (determined from the inputs and the desired output), respectively, for $k = 1, ..., K$ where $K \geq 2$. The dot denotes the scalar product of vectors and $\boldsymbol{\Omega}$ stands for the spherical co-latitude ϑ and longitude φ. Hence, $\boldsymbol{\Omega} := (\vartheta, \varphi)$, where $\boldsymbol{\Omega}_0$ is the full solid angle and $d\boldsymbol{\Omega}$

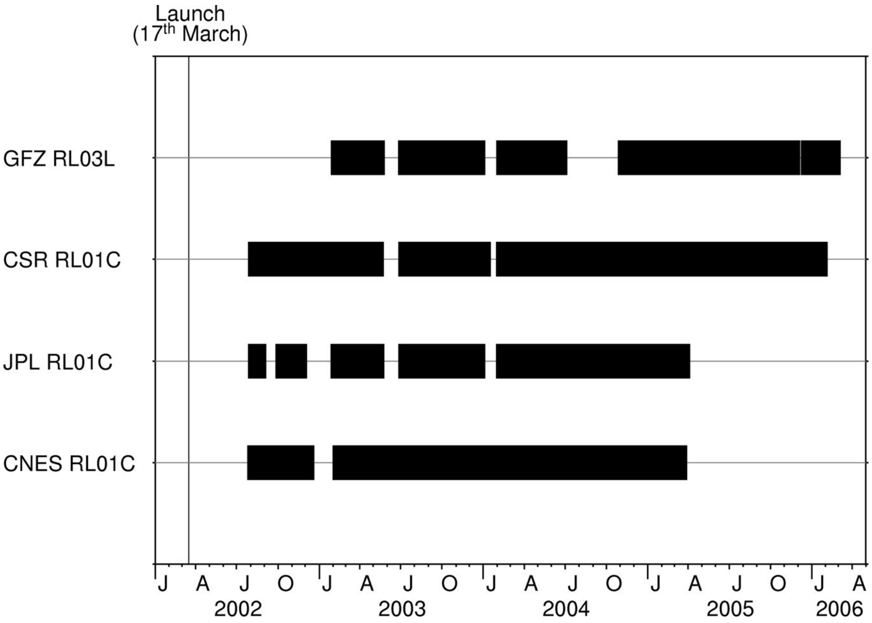

Figure 4.20: Temporal coverage of the four GRACE releases used in this paper (see also Section 4.5.5). The time series consist of 31 (GFZ RL03L), 41 (CSR RL01C), and 27 (JPL RL01C) monthly solutions, as well as 86 10-day solutions (CNES RL01C)

its infinitesimal element. The inputs $\boldsymbol{x}(\boldsymbol{\Omega})$ and the output $y(\boldsymbol{\Omega})$ are assumed to be square-integrable functions over the unit sphere and can be represented as a series of scalar spherical harmonics $Y_{jm}(\boldsymbol{\Omega})$ of degree j and order m, as defined in Sasgen *et al.* (2006),

$$\begin{bmatrix} \boldsymbol{x}(\boldsymbol{\Omega}) \\ y(\boldsymbol{\Omega}) \end{bmatrix} = \sum_{j=0}^{\infty} \sum_{m=-j}^{j} \begin{bmatrix} \boldsymbol{x}_{jm} \\ y_{jm} \end{bmatrix} Y_{jm}(\boldsymbol{\Omega}), \tag{4.30}$$

where $\boldsymbol{x}_{jm}$ and y_{jm} are the spherical-harmonic coefficients of $\boldsymbol{x}(\boldsymbol{\Omega})$ and $y(\boldsymbol{\Omega})$, respectively. Assuming that the spatial filter functions are rotationally symmetric, the spherical-harmonic form of convolution (4.29) can be expressed as

$$y_{jm} = \boldsymbol{h}_j . \boldsymbol{x}_{jm}. \tag{4.31}$$

More explicitly, the combined optimal output y_{jm} is formed from the individual outputs $y_{k,jm}$, that is $y_{jm} = \sum_{k=1}^{K} y_{k,jm}$, where $y_{k,jm}{=}h_{k,j}x_{k,jm}$.

The optimal filter coefficients $h_{k,j}$ are designed such that the combined output $y(\boldsymbol{\Omega})$ is close to a desired output $d(\boldsymbol{\Omega})$ in a least-square sense, such that $E^2 := \int_{\boldsymbol{\Omega}_0} \left| y(\boldsymbol{\Omega}) - d(\boldsymbol{\Omega}) \right|^2 d\boldsymbol{\Omega} = \sum_{j=0}^{\infty} \sum_{m=-j}^{j} \left| y_{jm} - d_{jm} \right|^2$ is minimized with respect to $h_{k,j}$. Introducing the matrices of the degree cross-power spectra of the multiple inputs, $\boldsymbol{S}^{\mathrm{xx}}_{kl,j} := \sum_{m=-j}^{j} x_{k,jm} x^*_{l,jm}$, for $k, l = 1, ..., K$, and of the multiple inputs and the desired output, $\boldsymbol{S}^{\mathrm{xd}}_{k,j} := \sum_{m=-j}^{j} x_{k,jm} d^*_{jm}$, for $k = 1, ..., K$ (the asterisk denotes

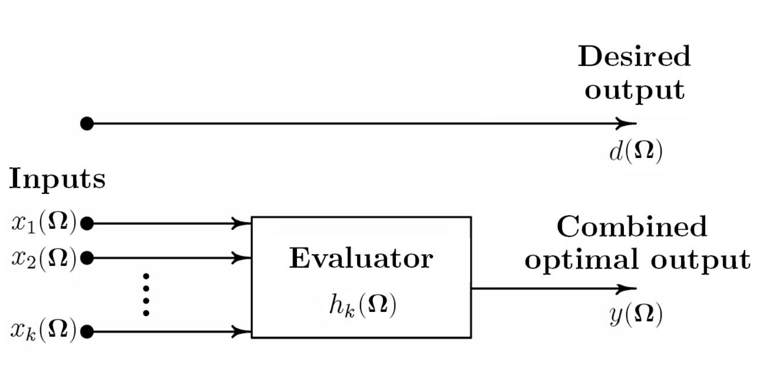

Figure 4.21: Principle of the Wiener optimal evaluator. Here, $x_k(\Omega)$ are the GRACE gravity-field solutions, $d(\Omega)$ is a geophysical-model prediction, $y(\Omega)$ is the optimally combined GRACE solution, and $h_k(\Omega)$ are the filter functions to be determined from the inputs and the desired output.

the complex conjugation), and the scalar of the degree-power spectrum of the desired output, $\sigma^2_{\mathrm{d},j} = \sum_{m=-j}^{j} d_{jm}d^*_{jm}$, the least-squares criterion E^2 takes the form

$$E^2 = \sum_{j}^{\infty}[\boldsymbol{h}_j.\boldsymbol{S}^{\mathrm{xx}}_j.\boldsymbol{h}^*_j - \boldsymbol{h}_j.\boldsymbol{S}^{\mathrm{xd}}_j - \boldsymbol{h}^*_j.\boldsymbol{S}^{*\mathrm{xd}}_j + \sigma^2_{\mathrm{d},j}]. \tag{4.32}$$

Thus, the aim is to search for a $\boldsymbol{h}_j$ that minimizes E^2. Differentiating (4.32) with respect to $\boldsymbol{h}_j$, and setting the result equal to zero gives

$$\boldsymbol{h}_j = [\boldsymbol{S}^{\mathrm{xx}}_j]^{-1}.\boldsymbol{S}^{\mathrm{xd}}_j, \tag{4.33}$$

which is the formula for the optimal filter coefficients.

4.5.3 Predicted gravity-field change over Antarctica (construction of the desired output)

Present-day ice-mass balance

Figure 4.22 presents the rate of geoid-height change over Antarctica associated with the ice-mass balance of the 33 Antarctic drainage basins (after Rignot & Thomas (2002); Thomas *et al.* (2004), Ivins, *pers. comm.*, 2005) and glaciers at the tip of the Antarctic Peninsula (Rignot *et al.*, 2004), as determined mainly from airborne- and satellite altimetry measurements. At present, two regions are subject to vigorous ice-mass changes and cause a large geoid-height change: the Antarctic Peninsula (∼ −0.4 mm/a), and the area adjacent to the Amundsen Sea in West Antarctica (∼ −2.0 mm/a), with East Antarctica being essentially in balance. Along the Antarctic Peninsula, the predicted rates of the geoid-height change are low, despite this region being responsible for a significant proportion of Antarctica's contribution to global mean sea-level change (i.e. 0.07 mm/a for this region compared to ∼ 0.24 mm/a for the

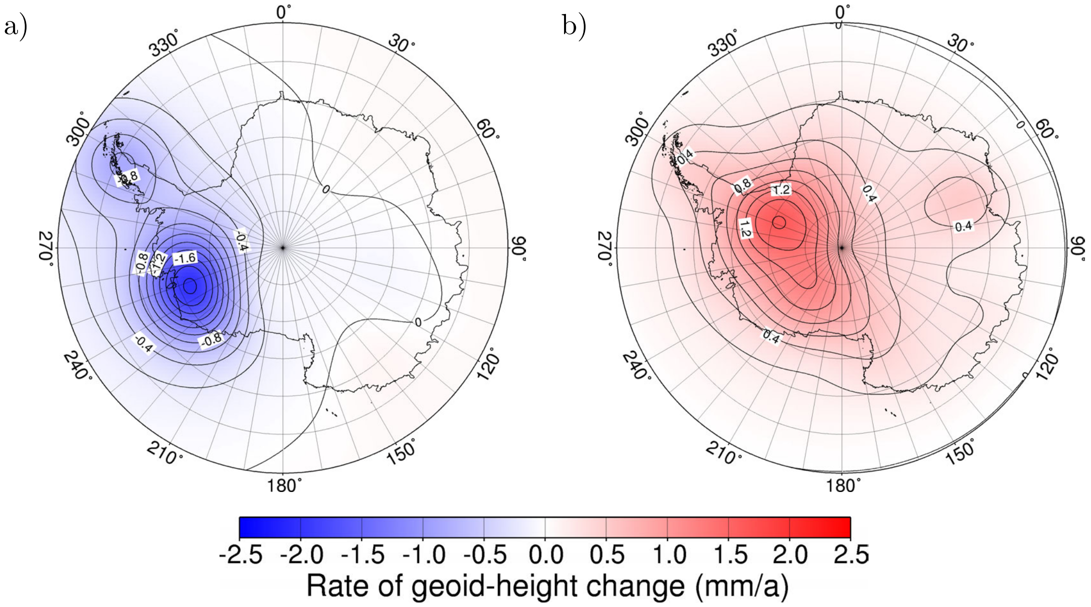

Figure 4.22: Rate of geoid-height change induced by (a) present-day ice-mass changes and (b) ongoing GIA. The results are filtered to simulate the current GRACE resolution using the Wiener optimal filter (Sasgen *et al.*, 2006). The addition of both signals (desired output model) is shown in Figure 6a.

glaciers draining into the Amundsen Sea). This is due to GRACE being less sensitive to smaller spatial wavelengths of the geoid-height change, that are strongly reduced by spatial filtering, here done with the Wiener optimal filtering.

Glacial-isostatic adjustment

We predict the glacial-isostatic adjustment-induced rate of geoid-height change (Figure 4.22) by subjecting a gravitationally self-consistent viscoelastic earth model (Martinec, 2000) to a glacial history of the AIS based on the thermomechanical model of Huybrechts (2002). The earth model consists of 4 radially symmetric layers: an elastic lithosphere with a thickness of 100 km, the upper-mantle with a viscosity of 5.2×10^{20} Pa s, the lower-mantle with a viscosity of 5.9×10^{21} Pa s and a liquid core. The values of the earth model are based on an analysis of GIA in Fennoscandia (Martinec & Wolf, 2005) and lie within the range of earth-model parameters usually considered for Antarctica (e. g. Zwartz *et al.*, 1998). The reconstruction of the AIS is adjusted to incorporate additional ice during the Last Glacial Maximum equivalent to a global mean sea-level change of -10 m, the largest amount being attributed to the region of the Ronne Ice Shelf, West Antarctica. This value is in agreement with the estimate of Ivins & James (2005), and lies within the range proposed by Bentley (1999).

The earth model and the AIS reconstruction used here result in rather small values for the associated glacial-isostatic adjustment, with the largest rate of geoid-height change, ~ 1.6 mm/a, occuring over the Ronne Ice Shelf, West Antarctica ($\sim 293^{\circ}$E,

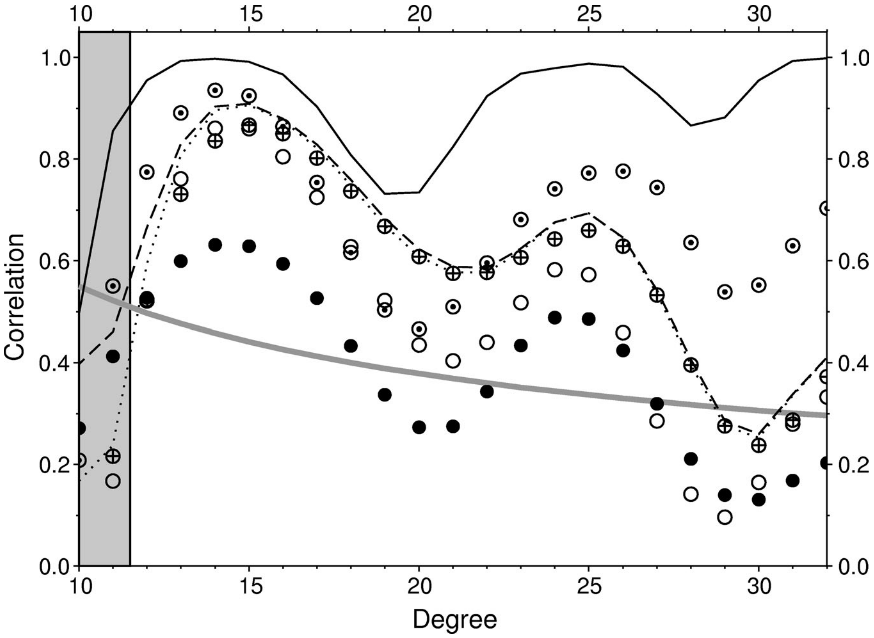

Figure 4.23: Degree correlation between the desired output and the various inputs; GFZ RL03L (white circles), CSR RL01C (crossed circles), JPL RL01C (black circles) and CNES RL01C (dotted circles), and the optimal output considering all 4 (solid line), 3 (dashed line; GFZ RL03L, CSR RL01C and JPL RL01C), and 2 (dotted line; GFZ RL03L, CSR RL01C) GRACE releases. The 95% statistical significance is indicated by the grey line.

81°S). We consider this conservative prediction to be appropriate, since at present, the GRACE data do not indicate a larger glacial-isostatic adjustment signal.

4.5.4 GRACE gravity-field change over Antarctica

4.5.5 Releases considered

We investigate the linear trends of the temporal gravity-field change over Antarctica inferred from 4 GRACE data sets, the GFZ release 3 unconstrained (GFZ RL03) (Flechtner, 2005), CSR release 1 constrained (CSR RL01C) (Bettadpur, 2004a), JPL release 1 constrained (JPL RL01C) (Watkins, 2003) and the constrained CNES release (CNES RL01C) (Biancale *et al.*, 2006). These time series represent the longest time series of - preferably constrained - gravity-field solutions that are available from the SDS centers and CNES (see also Figure 1), and capture some of the variety existing among the different GRACE data sets. The gravity field solutions used are corrected for gravitational variations induced by, for example, solid-Earth tides, pole tides, ocean tides, as well as atmosphere processes, as well as ocean processes, except for the GFZ RL03L, for which the ocean de-aliasing product AOD1B RL03 was found to introduce artificial trends over land (Flechtner, 2006; Bettadpur *et al.*, 2006).

4.5.6 Temporal trend

We determine the linear temporal trends in the GRACE gravity fields by decomposing the time series of the Stokes potential coefficients into linear and annual-oscillating components. We perform a Student's t-test to analyze the statistical significance of the linear terms, and neglect the statistically insignificant coefficients at the 95% confidence level, which decreases the noise level and reduces the latitudinal striping attributed to correlations between potential coefficients (Swenson & Wahr, 2006). The GFZ RL03L solutions, which are based on an unconstrained gravity-field determination, are filtered using the Wiener optimal filter (Sasgen *et al.*, 2006). The filter reduces the power of the coefficients, particularly at higher degrees and orders, with respect to the expected signal-to-noise ratio, in a manner similar to smoothing with a Gaussian averaging function of $\sim 3^{\circ}$ spatial half width. Because the solutions of the other selected releases are a product of constrained gravity-field determinations, this additional filtering is not necessary.

To investigate the gravity-field change over Antarctica, data north of 60°S are masked out. This is done by calculating a new set of Stokes coefficients representing the product of the original GRACE gravity fields and a mask which is 1 south of 60°S and 0 everywhere else, using the method of vector-coupled sums (e.g. Martinec, 1989). We also only consider the linear-trend coefficients that lie within the spectral range from degree and order 12 to 50. The upper limit represents the maximum cut-off degree of the CNES RL01C solutions, which is applied to all other solutions for consistency. The choice of this limit is not crucial, since the power of the filtered and constrained gravity fields decreases by more than 3 orders of magnitude by degree and order 50. The lower limit is determined by the degree below which the degree correlation (e.g. Martinec, 1994) between the GRACE coefficients and the predicted gravity-field change over Antarctica is not significant (Figure 4.23). We apply this limit to reduce the influence of the long-wavelength gravity-field anomalies that arise from sources in the farfield with respect to Antarctica. For a global application, e. g. the combination and evaluation of global hydrological models, the truncation of the lower degrees may not be necessary. However, in this case, care must be taken not to misinterpret low-degree geoid-height changes that are influenced by processes in the Earth's interior.

Figure 4.24 shows the rate of geoid-height change over Antarctica inferred from the time series of the Stokes potential coefficients of the 4 GRACE releases considered. All results indicate a strong negative trend in the geoid-height change of up to ~ -0.9 mm/a (GFZ RL03L), -1.4 mm/a (CSR RL01C), -1.4 mm/a (JPL RL01C) and -1.4 mm/a (CNES RL01C) over the Amundsen Sea sector, West Antarctica, which we attribute to the previously noted rapid glacier melting in this region (Velicogna & Wahr, 2006). In addition, a rapid rise in the geoid height at the rate of up to ~ 1.1 mm/a (GFZ RL03L), 1.1 mm/a (CSR RL01C), 1.6 mm/a (JPL RL01C) and 1.0 mm/a (CNES RL01C) occurs in the region of the Ronne Ice Shelf, and is explained by the inflow of mantle material due to GIA. We note that, however, the location of the strongest positive anomaly differs between the releases. A comparison with the predicted or desired signal (Figure 4.25) shows that for GFZ RL03L, CSR RL01C, and JPL RL01C, the strongest positive anomaly is northwest of the predicted location, while for CNES RL01C, the predicted and observed locations generally agree. Another area of rising geoid, at least partially associated with glacial-isostatic adjustment, is observed over the Ross Ice Shelf. However, the rates are lower and the spatial pattern of the anomaly less pronounced, with greater interference with the anomalies over the ocean, particularly for JPL RL01C. There are also several anomalies over the land and ocean that require further investigation to determine whether they can be explained by geophysical processes, or represent observational noise in the GRACE solutions. It should be stated that the anomalies over the ocean after correction with a de-aliasing product (CSR RL01C, JPL RL01C and CNES RL01C), are of the same order of magnitude as when this correction is not done (GFZ RL03L). This suggests that either there are unmodeled geophysical processes, or that the de-aliasing atmospheric and oceanic models introduce additional noise into the GRACE solutions.

4.5.7 Combination of GRACE gravity fields over Antarctica

Figure 4.25 shows the desired output and the optimal (filtered) output of the Wiener optimal evaluator for the combination of the 4 GRACE releases considered. In general, the gravity-field change of the optimal and desired output agree to a large extent, with the negative trend over West Antarctica due to glacier melting and the positive trend over the Ronne and Ross Ice Shelves arising from glacial-isostatic adjustment being well pronounced. The magnitudes of the contaminating anomalies over the ocean are reduced in the optimal output to a level considerably below the peak magnitudes of the changes over land. The combination of all 4 releases shows the highest level of adjustment of the desired output. Using only 3 (GFZ RL03L, CSR RL01C and JPL RL01C) and 2 (GFZ RL03L, CSR RL01C) releases decreases the adjustment, which is indicated by a lower degree correlation between the combined outputs and the desired output, as shown in Figure 4.23. This means that the excluded releases contain useful information about the gravity field over Antarctica, and/or contribute to the removal of unmodeled signals or observational noise.

4.5.8 Evaluation of GRACE gravity fields over Antarctica

Investigating the individual outputs that, by summation, form the combined, output allows us to identify the specific contribution of each release. Figure 4.26 shows the 4 individual outputs from each release that form the combined output (Figure 4.25). We see that the CNES RL01C makes the largest contribution to the optimal output, followed by CSR RL01C. The other releases have lower magnitudes and are, to a large extent, used to minimize the unmodeled signals over the oceans and reduce the strong positive anomaly over East Antarctica (~ 55°E, 68°S), especially present in the original trends from CSR RL01C (Figure 4.24) and CNES RL01C releases (Figure 4.24). We rank the 4 releases using the normalized energy of the residual, $R_k = \frac{\sum_j \sum_{m=-j}^{j} r_{jm} r^*_{jm}}{\sum_j \sum_{m=-j}^{j} r_{k,jm} r^*_{k,jm}}$, where $r_{k,jm}$ is the residual of the k-th input and the associated

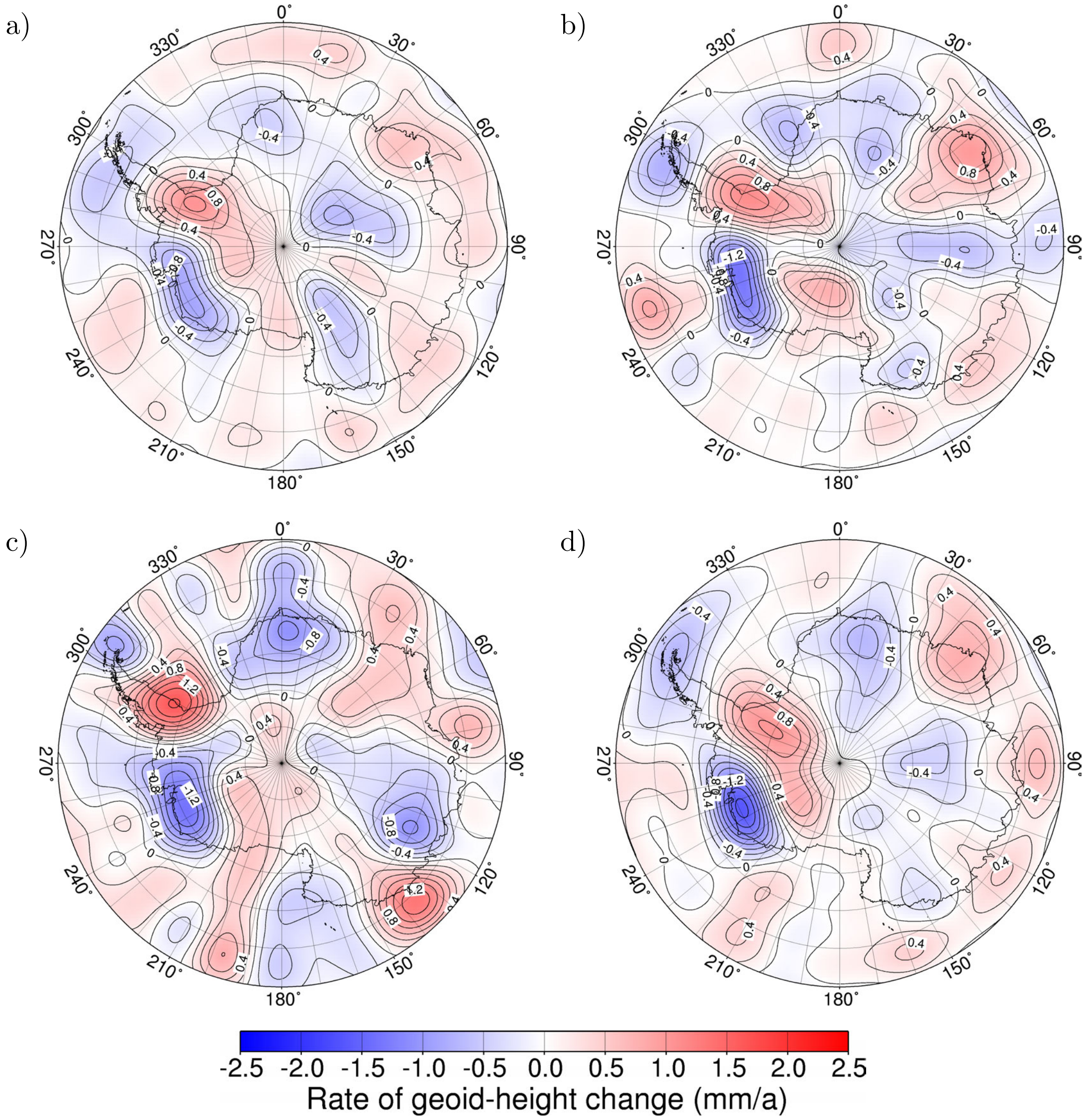

Figure 4.24: Rate of geoid-height change over Antarctica for the GRACE releases (a) GFZ RL03L (filtered, see text), (b) CSR RL01C, (c) JPL RL01C and (d) CNES RL01C. The cut-off degrees are $j_{\min} = 12$ and $j_{\max} = 50$.

individual output, and r_{jm} is the residual of the desired output and the optimal output. R_k approaches 0 for a total disagreement between the k-th input and the optimal output, and 1 for a full agreement between the k-th input and the optimal output. We obtain the following ranking: CNES RL01C (0.85), CSR RL01C (0.58), GFZ RL03L (0.56) and JPL RL01C (0.42).

The CNES RL01C dominates the optimal output as its spatial pattern shows the strongest similarity to the desired output. The Wiener optimal evaluator is sensitive to the spatial pattern of the desired output, owing to the assumption that the function used for the linear convolution filtering is isotropic, which, for example, does not

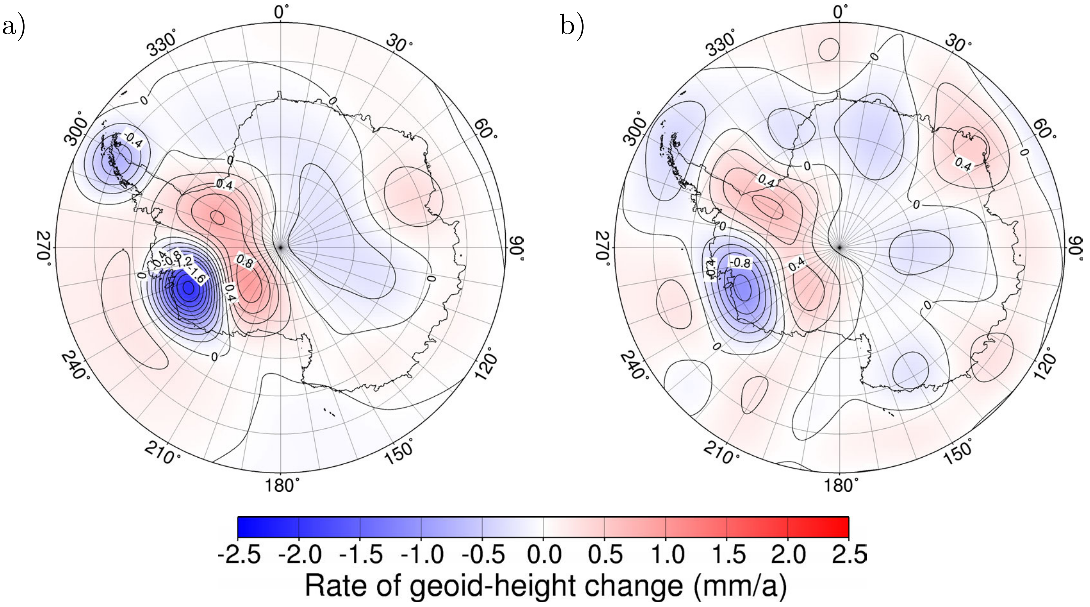

Figure 4.25: Rate of geoid-height change over Antarctica for (a) the desired output, and the optimal (filtered) output for the combination of (b) 4 (GFZ RL03L, CSR RL01C, JPL RL01C and CNES RL01C) GRACE releases. The cut-off degrees are $j_{\min} = 12$ and $j_{\max} = 50$.

allow any rotation or translation of the spatial pattern of the input. We consider this behaviour to be advantageous for the evaluation of the releases, since the expected areas of major gravity-field change in Antarctica correspond to regions undergoing geophysical processes that have been identified from other data sources. Moreover, the filtering needs to be constrained to isotropic averaging functions, otherwise any output could, in principal, be generated from any input.

4.5.9 Summary

We have presented the Wiener optimal evaluator as method for the optimal combination and evaluation of multiple inputs with respect to a desired output. The method is based on the least-squares minimization of the difference between the optimal and desired outputs using isotropic filtering and the subsequent summation of the multiple inputs. It represents a first step in rationalizing and testing a filter technique, and allows us to evaluate the GRACE gravity-field solutions from a geophysical perspective.

We have applied this method to investigate linear trends in the temporal gravity-field change over Antarctica inferred from 4 independent GRACE releases. The desired output represents the gravity-field change induced by present-day ice-mass changes and glacial-isostatic adjustment. We demonstrate that the linear trends identified in the GRACE solutions essentially reflect these processes. However, one problem with applying this method to Antarctica is the lack of constraints on the geophysical processes that are being modeled, and that assuming an *a priori* spatial pattern may

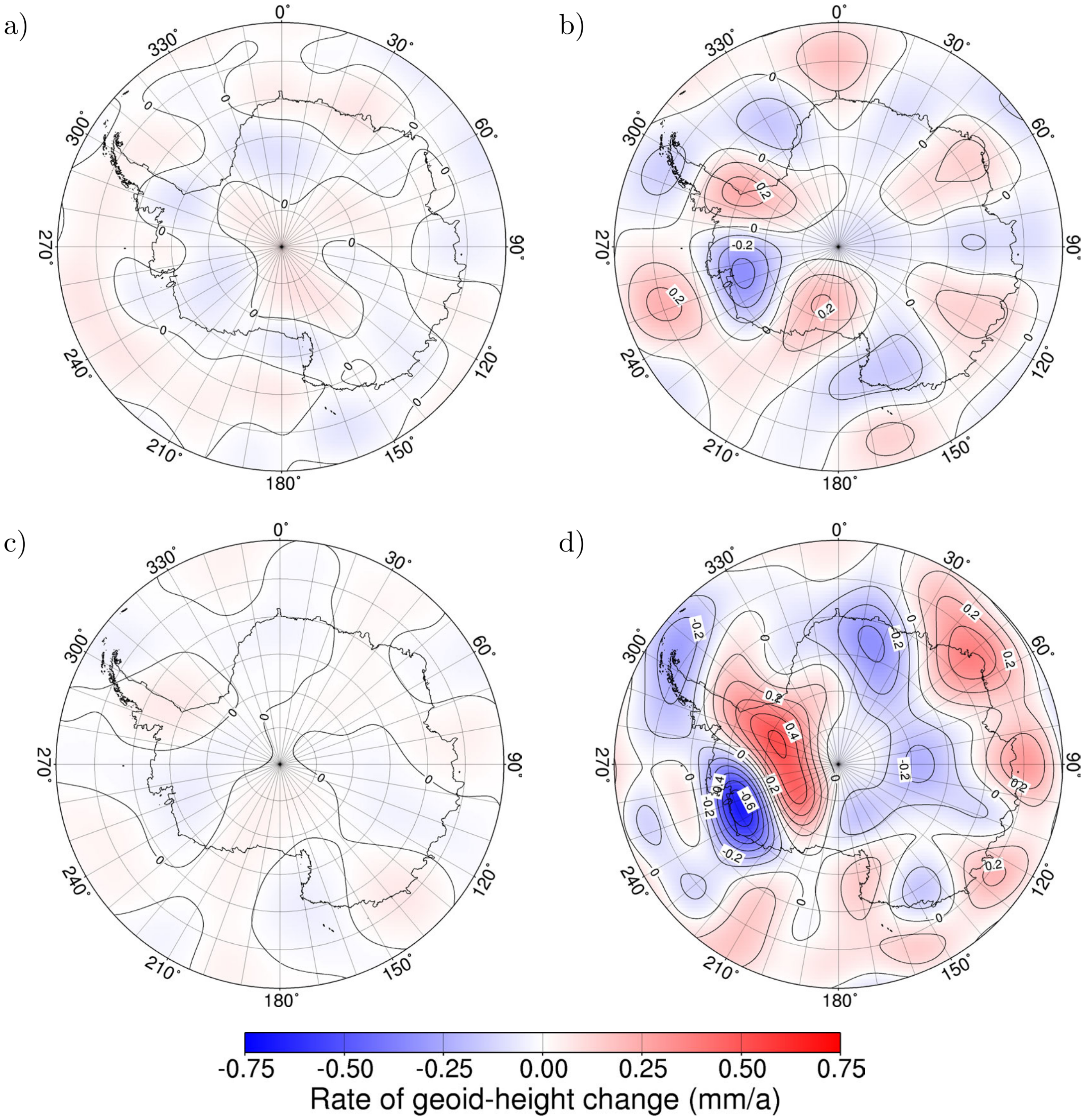

Figure 4.26: Individual outputs of the Wiener optimal evaluator for the releases (a) GFZ RL03L, (b) CSR RL01C, (c) JPL RL01C and (d) CNES RL01C. The cut-off degrees are $j_{\min} = 12$ and $j_{\max} = 50$.

lead to some error. This would, to larger extent, also be true for processes operating over other temporal scales, such as sub-annual, annual, and inter-annual.

We have shown that the optimal combination of several GRACE releases agrees better with the prediction and reduces unmodeled anomalies over the ocean, with the level of adjustment decreasing for smaller numbers of releases used in the combination. This means that all included releases contain useful information about the gravity-field change over Antarctica, or, at least, contribute to the removal of undesired signal or noise.

We found that the linear trend inferred from CNES RL01C represents the largest contribution to the combined output, since its spatial pattern of gravity-field change largely corresponds to the spatial pattern of the prediction. The trends from the GFZ RL03L and the CSR RL01C solutions represent an equal, but considerably lower, contribution to the combined output. The JPL RL01C represents the smallest contribution to the optimal output.

It should be mentioned that the validity of the ranking the GRACE releases is limited to the region of Antarctica. The results described here are not representative for other regions. However, given an appropriate desired output, the Wiener optimal evaluator is applicable to various spatial and temporal scales and is useful for (1) producing an optimal combination from multiple GRACE releases, (2) quantifying the (dis)agreement between predictions and observations, and, if desired, (3) assist with the selection of one specific GRACE release for further investigation.

One possible application of the Wiener optimal evaluator with respect to the improvement of the GRACE accuracy discussed by Schrama & Visser (2007) is the generation of a refined temporal background model. For example, using a combination of GRACE data and global hydrological models during the level 2 data processing may increase the accuracy of the resulting gravity-field solutions.

Acknowledgments

We thank Roland Schmidt and Frank Flechtner from GFZ Potsdam, and Erik Ivins from JPL in Pasadena for helpful discussions. The first author thanks Anny Cazenave for the encouragement to publish the material presented in this paper. The second author acknowledges support from the Grant Agency of the Czech Republic through Grant No. 205/06/0580. The authors thank Dr. Rowlands and an anonymous reviewer for their comments that have helped us to greatly improve the manuscript.

5

Methods of GRACE gravity-field inversion

This chapter is concerned with the inversion of the gravitational potential in terms of the for mass density distribution in the Earth system, which is known as the gravimetric inverse problem. The problem is ill-posed in the sense that its solution is 1) unstable, which means that the mass-change solution diverges with decreasing wavelength (increasing spatial resolution), and 2) non-unique, which means that the number of solutions (mass density distributions) producing the same external gravitational potential is infinite.

Section 5.1 introduces the gravimetric inverse problem. Section 5.2 outlines the method for the inversion of GRACE gravity field developed by Swenson & Wahr (2002) used to determine optimal average values of mass change in confined regions. Section 5.3 presents the forward modelling approach for the solution of the gravimetric inverse problem applied in this study.

5.1 Gravimetric inverse problem

The gravimetric inverse problem is concerned with the determination of the mass distribution within the Earth from its external gravitational potential, i.e. finding $\varrho(r, \mathbf{\Omega})$ from known $V(r, \mathbf{\Omega})$ in (2.1).

The instability of the solution to this problem can be seen from (2.5), where the integration over r results in $V(r, \mathbf{\Omega}) \propto 1/j^2$. This means that the inverse transfer function from $V(r, \mathbf{\Omega}) \to \varrho(r, \mathbf{\Omega})$ diverges $\propto j^2$ for $j \to \infty$. The instability reduces to $V(r, \mathbf{\Omega}) \propto 1/j$ for the condensation of the masses within a layer on the Earth's surface (2.10). Furthermore, the instability of the solution can be overcome by the truncation of series of Stokes potential coefficients at some cut-off degree $j_{\max}$ or by reducing the influence of high-frequency components (smoothing).

The non-uniqueness is demonstrated according to Martinec (1998) as follows. Given is the mass density distribution ϱ_0 that satisfies (2.1), and let ∂B of the body B have a continuous normal $\mathbf{n}$, then additional solutions can be represented as

$$\varrho = \varrho_0 + \nabla^2 h, \text{ with } h\big|_{\partial B} = \frac{\partial h}{\partial n}\bigg|_{\partial B} = 0. \tag{5.1}$$

These do not represent a contribution to the external gravitational potentials, which is proven by Green's third identity (e.g. Weisstein, 2008 *[online]*),

$$V(r>R)=G\int_B\frac{\nabla h(r')}{|\mathbf{r}-\mathbf{r}'|}dV'=G\int_{\partial B}\Big(\frac{\partial h(r')}{\partial n}\frac{1}{|\mathbf{r}-\mathbf{r}'|}-h(r')\frac{\partial}{\partial n}\frac{1}{|\mathbf{r}-\mathbf{r}'|}\Big)dS'=0. \tag{5.2}$$

The non-uniqueness can be handled by introducing meaningful *a priori* constraints on the mass distribution. For example, the concentration of the mass changes into a thin layer on the Earth's surface results in the unique solution of the inverse gravimetric problem (2.17). However, for the GRACE data this assumption is not justified for regions with GIA, where mass changes within the Earth's interior cause potential disturbances that may be misinterpreted as surface-mass changes.

5.2 Optimized basin averaging

A method often used to invert GRACE potential coefficients in terms of surface-mass changes is described in Swenson & Wahr (2002). The principle idea is to determine average mass-change values within specific regions, $\mathbf{\Omega}_\mathrm{R}$, bound by distinct geographical features, e.g. water divides. Let $f(\mathbf{\Omega})$ be the spatial representation of the basin function defined by

$$f(\mathbf{\Omega}):=\begin{cases}1, & \mathbf{\Omega}\in\mathbf{\Omega}_\mathrm{R}\\ 0, & \mathbf{\Omega}\notin\mathbf{\Omega}_\mathrm{R}\end{cases}, \tag{5.3}$$

with the area $\mathbf{\Omega}_\mathrm{R}=\int_{\mathbf{\Omega}_0}f(\mathbf{\Omega})d\mathbf{\Omega}'$ and $f(\mathbf{\Omega})=\sum_{jm}f_{jm}Y_{jm}(\mathbf{\Omega})$[1]. With the assumption that all mass changes are concentrated on the Earth's surface, the gravitational potential can be inverted directly for the mass-change distribution $\sigma(\mathbf{\Omega})=\sum_{jm}\sigma_{jm}Y_{jm}(\mathbf{\Omega})$ is according to (2.17)

$$\sigma_{jm}=\frac{1}{q_j}\frac{1}{4\pi GR}(2j+1)V_{jm}. \tag{5.4}$$

Then, $F(\mathbf{\Omega})=f(\mathbf{\Omega})\sigma(\mathbf{\Omega})$ describes the mass change within the basin by

$$F(\mathbf{\Omega})=f(\mathbf{\Omega})\sigma(\mathbf{\Omega})=\sum_{\substack{j_1m_1\\ j_2m_2}}f_{j_1m_1}\sigma_{j_2m_2}Y_{j_1m_1}(\mathbf{\Omega})Y_{j_2m_2}(\mathbf{\Omega})\overset{!}{=}F_{jm}Y_{jm}(\mathbf{\Omega}). \tag{5.5}$$

The product of the two scalar surface spherical-harmonic functions can be solved by the Clebsh-Gordon series

$$Y_{j_1m_1}(\mathbf{\Omega})Y_{j_2m_2}(\mathbf{\Omega})=\sum_{jm}Q^{jm}_{j_1m_1j_2m_2}Y_{jm}(\mathbf{\Omega}), \tag{5.6}$$

where $Q_{j_1m_1j_2m_2}$ are the Clebsh-Gordon coefficients (e.g. Martinec, 1989), such that

$$F_{jm}=\sum_{\substack{j_1m_1\\ j_2m_2}}f_{j_1m_1}\sigma_{j_2m_2}Q^{jm}_{j_1m_1j_2m_2}. \tag{5.7}$$

---

[1] $\sum_{j=0}^{\infty}\sum_{m=-j}^{j}$ is henceforth denoted by $\sum_{jm}$.

The total integrated mass change within the basin is according to (A.7)

$$\int_{\mathbf{\Omega}_0} F(\mathbf{\Omega})d\mathbf{\Omega}' = \int_{\mathbf{\Omega}_0} f(\mathbf{\Omega})\sigma(\mathbf{\Omega})d\mathbf{\Omega}' = \sqrt{4\pi}F_{00}, \tag{5.8}$$

where

$$F_{00} = \sum_{\substack{j_1m_1\\j_2m_2}} f_{j_1m_1}\sigma_{j_2m_2}Q^{00}_{j_1m_1j_2m_2} = \frac{1}{\sqrt{4\pi}}\sum_{jm} f_{jm}\sigma^*_{jm}. \tag{5.9}$$

The average mass change within the drainage basin, $\overline{\sigma}_\mathrm{R}$, is then obtained by

$$\overline{\sigma}_\mathrm{R} = \frac{1}{\mathbf{\Omega}_\mathrm{R}}\int_{\mathbf{\Omega}_0} F(\mathbf{\Omega})d\mathbf{\Omega}' = \frac{1}{\sqrt{4\pi}}\frac{1}{f_{00}}\sum_{jm} f_{jm}\sigma^*_{jm}. \tag{5.10}$$

It is obvious from (5.4) and (5.10) that $(2j+1)f_{jm}V^*_{jm} \to 0$ for $j, m \to \infty$ is required to obtain convergence of the summation in (5.10). Also, for GRACE data, potential coefficients of high degree and order need to be suppressed, e.g. in the simplest case by isotropic filtering h_jV_{jm} (Section 4) to reduce the error of the resulting average mass change $\overline{\sigma}_\mathrm{R}$. Regarding h_j being applied to f_{jm} rather than to V_{jm} shows that this filtering can also be considered as smoothing the basin averaging function and, thus, including more signal from outside the basin (leakage) in the basin average. Swenson & Wahr (2002) developed several strategies to optimize smoothed basin averaging functions in order to reduce GRACE errors, leakage errors or both.

5.3 Forward modelling

Here, the gravimetric inverse problem is solved by adjusting forward models of mass-change processes such that predicted and observed potential disturbances agree. The major advantage of this approach is that superimposed signals in the gravitational potential can be separated and attributed to individual sources of mass change. Additionally, ambiguities in the inversion are reduced by constraining the inversion to produce solutions that are geophysically meaningful. Moreover, errors due to truncation or smoothing of the potential coefficients are small, as filtering is applied in the data and the model domain.

As described in Section 2, long-term changes of the gravitational potential in the polar regions are dominantly caused by present-day ice-mass changes and GIA. The relation of the Earth's elastic response to surface-mass changes, (2.17), can be generalized for a viscoelastic continuum according to

$$V_{jm}(s) = 4\pi GRq_j(s)\frac{1}{2j+1}\sigma_{jm}(s), \tag{5.11}$$

where s is the Laplace variable and $q_j(s)$ are the viscoelastic surface-load Love numbers in the Laplace domain for a specified viscosity distribution (e.g. Wu & Peltier, 1982). For instantaneous mass variations (present-day ice-mass changes), $s \to 0$ and $q_j(s)$ approaches the elastic surface-load Love numbers q_j of (2.17). Due to the linearity of the GIA problem with respect to its boundary conditions, the potential disturbances, $V_{jm}(s)$, scale linearly with the surface loading σ_{jm}, given that the viscosity distribution and temporal evolution of the glacial history remain unchanged. Although this relation is a first-order approximation, which neglects non-linear coupling in the ice|ocean|earth system described by the sea-level equation (e.g. Farrell & Clark, 1976; Hagedoorn, 2005), it allows a simultaneous linear adjustment of signal amplitudes of present-day ice-mass changes and GIA in a joint inversion.

5.3.1 Design matrix

The changes in the Stokes potential coefficients due to surface mass changes, σ_R, within the region $\mathbf{\Omega}_\mathrm{R}$, are

$$V_{jm}^\mathrm{R} = H_j \int_{\mathbf{\Omega}_0} \sigma_\mathrm{R}(\mathbf{\Omega}) Y_{jm}^*(\mathbf{\Omega}) d\mathbf{\Omega}, \text{ with } V_\mathrm{R}(\mathbf{\Omega}) = \sum_{jm} V_{jm}^\mathrm{R} Y_{jm}(\mathbf{\Omega}), \tag{5.12}$$

where $\sigma_\mathrm{R}(\mathbf{\Omega}) = 0$ outside the region and $H_j = 4\pi G R q_j (2j+1)^{-1}$. For mass conservation, $\sigma_\mathrm{R}(\mathbf{\Omega})$ is compensated by a water layer uniformly distributed over the area of the present-day oceans, which is neglected in the following derivation. It is of advantage to separate σ_R into the normalized mass distribution function $w(\mathbf{\Omega})$ and the total mass change m_R within the region,

$$w_\mathrm{R}(\mathbf{\Omega}) := \begin{cases} 1, & \mathbf{\Omega} \in \mathbf{\Omega}_\mathrm{R} \\ 0, & \mathbf{\Omega} \notin \mathbf{\Omega}_\mathrm{R} \end{cases}, \text{ and } \int_{\mathbf{\Omega}_0} w(\mathbf{\Omega}) d\mathbf{\Omega} = 1, \tag{5.13}$$

such that $\sigma_\mathrm{R}(\mathbf{\Omega}) = m_\mathrm{R} w_\mathrm{R}(\mathbf{\Omega})$. Then, (5.12) becomes

$$V_{jm}^\mathrm{R} = H_j m_\mathrm{R} \int_{\mathbf{\Omega}_0} w_\mathrm{R}(\mathbf{\Omega}) Y_{jm}^*(\mathbf{\Omega}) d\mathbf{\Omega} = H_j m_\mathrm{R} w_{jm}^\mathrm{R}. \tag{5.14}$$

The disturbing potential associated with more than one mass change region $\Omega_{\mathrm{R}_\alpha}$, $\alpha = 1, 2, ..., K$, are obtained by summation,

$$V^\mathrm{Model}(\mathbf{\Omega}) = \sum_\alpha V_{\mathrm{R}_\alpha}(\mathbf{\Omega}) = \sum_\alpha \sum_{jm} V_{jm}^{\mathrm{R}_\alpha} Y_{jm}(\mathbf{\Omega}) = \sum_\alpha \sum_{jm} H_j w_{jm}^{\mathrm{R}_\alpha} m_{\mathrm{R}_\alpha} Y_{jm}(\mathbf{\Omega}). \tag{5.15}$$

The aim is to minimize the difference between GRACE and modelled potential disturbances, $V^\mathrm{GRACE}(\mathbf{\Omega})$ and $V^\mathrm{Model}(\mathbf{\Omega}, m_{\mathrm{R}_\alpha})$, respectively, in the L_p-norm sense with respect to the total mass change within each region, m_{R_α}. This is expressed by

$$\| \sum_\alpha \int_{\mathbf{\Omega}_{\mathrm{S}_\alpha}} [V^\mathrm{GRACE}(\mathbf{\Omega}) - V^\mathrm{Model}(\mathbf{\Omega}, m_{\mathrm{R}_\alpha})] d\Omega \|_{L_p} \overset{!}{=} \min_{m_{\mathrm{R}_\alpha}}, \tag{5.16}$$

where $\mathbf{\Omega}_{\mathrm{S}_\alpha}$ are the adjustment areas that potentially differ from $\mathbf{\Omega}_{\mathrm{R}_\alpha}$. In this work, $\mathbf{\Omega}_{\mathrm{S}_\alpha}$ are defined to include the peak potential disturbances of $V^\mathrm{Model}(\mathbf{\Omega})$.

5.3.2 Unconstrained estimate

The minimization criterion (5.16) can be considered by the method of least squares. Let $\boldsymbol{V}(\boldsymbol{\Omega}) = \{V_{\mathrm{R}_\alpha}(\boldsymbol{\Omega})\}^{\alpha=1,2,\ldots,K}$, be the vector containing the normalized potential disturbances for the K regions, along with the vector containing the total mass change within each region $\boldsymbol{m} = \{m_{\mathrm{R}_\alpha}\}^{\alpha=1,2,\ldots,K}$, such that $V^{\mathrm{Model}}(\boldsymbol{\Omega}) = \boldsymbol{V}\boldsymbol{m}$. Then, the cost function (5.16) in the L_2-norm becomes

$$\| \int_{\boldsymbol{\Omega}_{\mathrm{S}_\alpha}} \left[V^{\mathrm{GRACE}}(\boldsymbol{\Omega}) - \boldsymbol{V}(\boldsymbol{\Omega})\boldsymbol{m}\right] d\Omega \|^2 \overset{!}{=} \min_{m_{\mathrm{R}_\alpha}}. \tag{5.17}$$

With the spatial discretization

$$V_{\mathrm{R}_\alpha}(\boldsymbol{\Omega}_i) = \sum_{jm} H_j w_{jm}^{\mathrm{R}_\alpha} Y_{jm}(\boldsymbol{\Omega}_i), \tag{5.18}$$

$\boldsymbol{\Omega}_i \in \boldsymbol{\Omega}_{\mathrm{S}}, i = 1,2,...,N$, the data vector $\boldsymbol{V}^{\mathrm{GRACE}} = \{V^{\mathrm{GRACE}}(\boldsymbol{\Omega}_i)\}_{i=1,2,\ldots,N}$, and the design matrix of the linear problem can be formulated according to $\boldsymbol{F} = \{V_{\mathrm{R}_\alpha}(\boldsymbol{\Omega}_i)\}_{i=1,2,\ldots,N}^{\alpha=1,2,\ldots,K}$. Then, the minimization criterion (5.17) takes the form

$$(\boldsymbol{V}^{\mathrm{GRACE}} - \boldsymbol{F}\boldsymbol{m})^{\mathrm{T}} \boldsymbol{C}_{\mathrm{D}} (\boldsymbol{V}^{\mathrm{GRACE}} - \boldsymbol{F}\boldsymbol{m}) \overset{!}{=} \min_{\boldsymbol{m}}. \tag{5.19}$$

The estimated solution $\hat{\boldsymbol{m}}$ of (5.19) is (Section A.6)

$$\hat{\boldsymbol{m}} = (\boldsymbol{F}^{\mathrm{T}} \boldsymbol{C}_{\mathrm{D}}^{-1} \boldsymbol{F})^{-1} \boldsymbol{F}^{\mathrm{T}} \boldsymbol{C}_{\mathrm{D}} \boldsymbol{V}^{\mathrm{GRACE}}, \tag{5.20}$$

with the optimal model $\hat{V}^{\mathrm{Model}}(\boldsymbol{\Omega}) = \boldsymbol{V}(\boldsymbol{\Omega})\hat{\boldsymbol{m}}$. In (5.19) and (5.20), $\boldsymbol{C}_{\mathrm{D}}$ (dimension $N \times N$) is the variance-covariance matrix of the data, which represents the spatial representation of GRACE-coefficient errors (Section A.4).

5.3.3 Constrained estimate

In some cases, the least-squares solution (5.20) may not give acceptable results from a geophysical point of view. For example, estimates of m_{R_α} and the associated signals of potential disturbances V_{R_α} may exhibit large variations between neighboring regions, which compensate each other. Such oscillations can be reduced by including *a priori* constraints on the model parameters along with their uncertainties in the definition of the cost function (5.19). In the inversion for present-day ice-mass changes and GIA, additional constraints may come from independent observational data (e.g. InSAR mass-budget estimates, Section 6.4) and constraints on the glacial history, respectively.

The *a priori* constrained solution of (5.17), which is described in more detail in Section A.6.2 is

$$\hat{\boldsymbol{m}} = \boldsymbol{m}^{\mathrm{P}} + (\boldsymbol{F}^{\mathrm{T}} \boldsymbol{C}_{\mathbf{D}}{}^{-1} \boldsymbol{F} + \boldsymbol{C}_{\mathbf{M}}{}^{-1})^{-1} \boldsymbol{F}^{\mathrm{T}} \boldsymbol{C}_{\mathbf{D}}{}^{-1} (\boldsymbol{V}^{\mathrm{GRACE}} - \boldsymbol{F}\boldsymbol{m}), \tag{5.21}$$

where $\boldsymbol{m}^{\mathrm{P}}$ and $\boldsymbol{C}_{\mathrm{M}}$ represent the parameters and variance-covariance matrix of the *a priori* model.

6

Interpretation of GRACE gravity-field changes

The present chapter presents results of the GRACE gravity-field inversion for mass changes in Antarctica. The results described in Section 6.1 are taken from the publication Sasgen *et al.* (2007b). Additional investigations supplementing this publication are presented in Section 6.2. The inversion for mass changes in North America and Greenland are presented in Section 6.3. Also, first assessments of GRACE as a constraint on mantle viscosities below North America are made, although further investigations, considering complementary data, such as GPS, tide gauges and SLIs, are required. Section 6.4 shows the results of mass changes in individual West Antarctic drainage basins obtained by the constrained inversion of GRACE and InSAR data. These investigations are currently prepared for publication (Sasgen *et al.*, 2008).

6.1 Regional ice-mass changes and glacial-isostatic adjustment in Antarctica from GRACE (*published*)

Abstract[†]

We infer regional mass changes in Antarctica using ca. 4 years of Gravity Recovery and Climate Experiment (GRACE) level 2 data. We decompose the time series of the Stokes coefficients into their linear as well as annual and semi-annual components by a least-squares adjustment and apply a statistical reliability test to the Stokes potential coefficients' linear temporal trends. Mass changes in three regions of Antarctica that display prominent geoid-height change are determined by adjusting predictions of glacier melting at the tip of the Antarctic Peninsula and in the Amundsen Sea Sector, and of the glacial-isostatic adjustment (GIA) over the Ronne Ice Shelf. We use the GFZ RL04, CNES RL01C, JPL RL04 and CSR RL04 potential-coefficient releases, and show that, although all data sets consistently reflect the prominent mass changes, differences in the mass-change estimates are considerably larger than the uncertainties estimated by the propagation of the GRACE errors. We then use the bootstrapping method based on the four releases and six time intervals, each with 3.5 years of data, to quantify the variability of the mean mass-change estimates. We find 95% of our estimates to lie within 0.08 and 0.09 mm/a equivalent sea-level (ESL) change for the Antarctic Peninsula and within 0.18 and 0.20 mm/a ESL for the Amundsen Sea Sector. Forward modelling of the GIA over the Ronne Ice Shelf region suggests that the Antarctic continent was covered by 8.4 to 9.4 m ESL of additional ice during the Last-Glacial Maximum (ca. 22 to 15 ka BP). With regards to the mantle-viscosity values and the glacial history used, this value is considered as a minimum estimate. The mass-change estimates derived from all GRACE releases and time intervals lie within ca. 20% (Amundsen Sea Sector), 30% (Antarctic Peninsula) and 50% (Ronne Ice Shelf region) of the bootstrap-estimated mean, demonstrating the reliability of results obtained using GRACE observations.

[†] Sasgen, I., Martinec, Z. & Fleming, K., 2007. Regional ice-mass changes and glacial-isostatic adjustment in Antarctica from GRACE. *Earth Planet. Sci. Lett.*, (264): 391–4001. Received: May 10, 2007; Revised: September 19, 2007; Accepted: September 20, 2007. Copyright 2007 Elsevier, Oxford, United Kingdom. Reproduced by kind permission of Elsevier.

6.1.1 Introduction

The determination of the Earth's gravity field at regular time intervals by the Gravity Recovery and Climate Experiment (GRACE) allows the investigation of mass movement within the Earth system (e.g. Tapley *et al.*, 2004a). GRACE consists of two low-orbiting satellites in the same near-polar orbit, accurately measuring their separation (ca. 200 km) by a k-band ranging system. These data, together with GPS, accelerometer and star-camera measurements (GRACE Level 1 data), are used to solve for the spectral representation of the Earth's gravitational potential or Stokes potential coefficients at approximately monthly time intervals (GRACE Level 2 data).

The largest contribution to the gravity field's temporal variability arises from the seasonal redistribution of water associated with hydrological processes. In addition, the increasing length of the GRACE time series (currently ca. 4 years) allows secular changes in the gravity field to be inferred with increasing reliability. Over land, this secular trend is mainly induced by changes in the mass of ice sheets and glaciers and by the inflow of mantle material into regions of former glaciation arising from the glacial-isostatic adjustment (GIA) following the Last-Glacial Maximum (LGM, ca. 22 to 15 ka BP). Other sources of long-term changes include, for example, imbalances in the hydrological cycle and processes in the Earth's deep interior.

Within this context, GRACE observations have been employed to determine the mass balance of polar ice sheets by mainly using the following three approaches. The first, basin averaging, is commonly applied to determine average mass changes in predefined geographical regions, for example drainage basins (e.g. Swenson & Wahr, 2002; Velicogna & Wahr, 2005; Ramillien *et al.*, 2006; Velicogna & Wahr, 2006). This approach can be optimized with respect to the expected signal and the influence of observational noise, such as far-field signals or the increasing uncertainty associated with GRACE coefficients of higher spherical-harmonic degree and order. Often, forward modelling is applied in estimating the signal loss due to filtering. An alternative method is based on simulations or forward modelling of the mass change of interest using independent geophysical information (e.g. Chen *et al.*, 2006b). Depending upon the nature of the problem, different methods of adjusting the forward models to the GRACE gravity-field solutions are used. The relationship between the changes in the gravitational potential and the sources of mass change is given by the forward models. In contrast, the third approach determines local mass concentrations directly using k-band and other GRACE Level 1 data, together with *a priori* information concerning the geometry and location of the mass changes under consideration (e.g. Luthke *et al.*, 2006). Compared to the first two approaches, its main advantage is that regionally a spatial resolution is achieved. Also, the resulting distribution of surface masses do not require additional calibration.

Despite using similar or identical sets of GRACE coefficients, the various approaches have produced significantly different estimates of secular ice-mass change in the polar regions, with their equivalent sea-level (ESL) change ranging, for example, for the Greenland Ice Sheet from 0.23 ± 0.06 (Velicogna & Wahr, 2005) to 0.54 ± 0.05 mm/a ESL (Chen *et al.*, 2006a) and for the Antarctic Ice Sheet from 0.14 ± 0.09 (Ramillien *et al.*, 2006) to 0.38 ± 0.20 mm/a ESL (Velicogna & Wahr, 2006). For Antarctica, a large cause of the discrepancy between these estimates is the uncertainty in the contributions from GIA.

This paper aims to quantify the most prominent glacier melting and the GIA in Antarctica using the second approach. We refine the previous study of Chen *et al.* (2006b) by a noise reduction strategy applied to the GRACE data and extend their investigation by simultaneously considering three regions of prominent geoid-height change shown in Figure 6.1. In contrast to previous studies, we estimate the GIA signal from the GRACE observations and do not apply an *a priori* GIA correction.

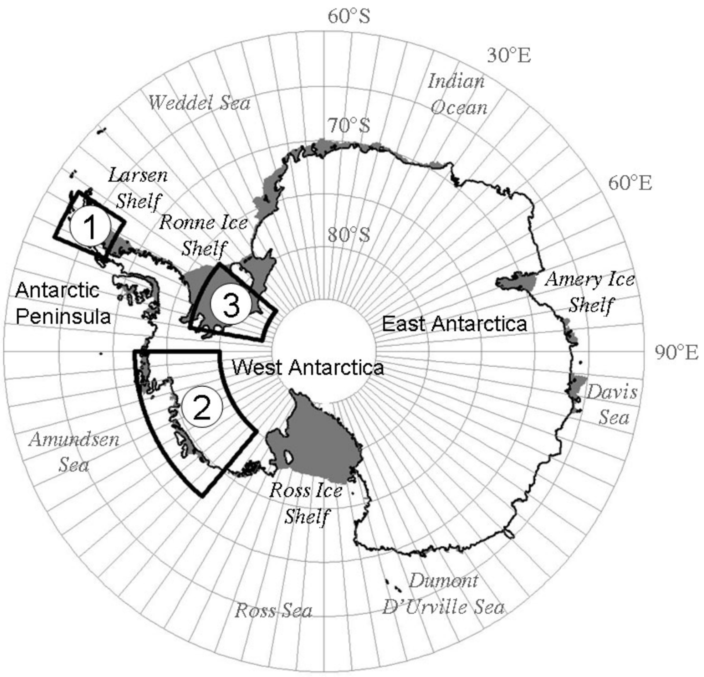

Figure 6.1: Map of Antarctica based on the Antarctica Digital Database (ADD Consortium, 2000) and the Digital Chart of the World (ESRI, 2003). We focus our investigation to the regions delimited by the coordinate rectangles (solid lines), namely (1) the tip of the Antarctic Peninsula, (2) the Amundsen Sea Sector and (3) the Ronne Ice Shelf region.

Also, we assess the robustness of our mass-change estimates with respect to the different GRACE releases and the observational period chosen by the application of the bootstrap method.

6.1.2 Geoid-height change over Antarctica from GRACE

We investigate four independent time series of the GRACE Stokes potential coefficients that describe the gravity-field changes mainly occurring over land (GSM Level 2 data): GFZ RL04 (Flechtner, 2007), JPL RL04 (Watkins & Dah Ning, 2007), CSR RL04 (Bettadpur, 2007a) of the GRACE Science Data System (SDS) centers and CNES RL01C (Biancale *et al.*, 2006 *[online]*). The solutions of the SDS centers are unconstrained determinations of the gravity field at approximately monthly time intervals. The solutions of the CNES RL01C represent moving averages of three 10-day solutions and were computed using a regularization method. This method allows the determination of the gravity field during periods of low ground-track coverage that is during resonances in the satellites' orbit and the Earth's rotation. The releases contain at least 48 months of data, respectively, and represent the processing centers' latest gravity-field solutions. In order to homogenize the temporal coverage of the data sets, only solutions between January 2003 and December 2006 are used. Although the solutions include the same GRACE Level 1 data (Bettadpur, 2007b), we consider them as independent representations of the gravity field, since the individual processing strategies, e.g. the choice of background and de-aliasing models, induce differences in the gravity fields that are above the expected GRACE uncertainty.

We decompose the time series of the Stokes potential coefficients into their linear as well as annual and semi-annual components by a least-squares adjustment, assuming constant variances over time. Using the Student's t-test statistic, we set to zero the resulting linear trend terms x^{o}_{jm} for the time series of each coefficient of spherical-harmonic degree j and order $m > 25$ not exhibiting a statistically significant linear trend at a confidence level of 99%. The minimum of the degree power of unconstrained gravity-field solutions at $j \approx 25$ indicates that coefficients of lower degrees and orders are signal dominated and do not require filtering (e.g. Sasgen *et al.*, 2006). In turn, the significant deviation of the degree power of constrained and unconstrained solutions for $j > 25$ suggests that noise reduction should be applied above this degree and order.

The noise reduction strategy applied can be summarized as $y^{\mathrm{p|o}}_{jm} = x^{\mathrm{p|o}}_{jm} s_{jm}$, where $y^{\mathrm{p|o}}_{jm}$ are the filtered coefficients of the predicted|observed temporal linear trend $x^{\mathrm{p|o}}_{jm}$, respectively, and s_{jm} represents the statistical filter that is 1 if the trend x^{o}_{jm} is statistically significant, otherwise it is 0 ($s_{jm} = 1$ for $j, m \leq 25$). According to this criterion, we omit, for example, a number of the near-sectorial coefficients ($j \approx m$), since these are degraded by the satellites' less dense across-track sampling, resulting in the often discussed north-south striping (Swenson & Wahr, 2006). This degradation is also reflected in the coefficients' large stochastic variability when compared to their inferred temporal linear trend. Additional spatial smoothing of the gravity fields is not applied.

The higher-degree and -order coefficients of the constrained CNES RL01C solutions contain less noise than those of unconstrained solutions due to the Kaula regularization method applied during the CNES processing. This regularization stabilizes the fluctuations in the higher spectral range by constraining the solution to the mean field, which allows an improvement to the signal-to-noise ratio by weighing more the better-quality data (Lemoine *et al.*, 2007). In the spatial domain, the regularization results in smoother and less noisy gravity fields. As mentioned above, a comparison of the degree-power spectra of unconstrained and the constrained CNES RL01C solutions indicates that this *a priori* noise reduction is effective for coefficients with $j > 25$. Hence, for coefficients in this spectral range, we estimate an equivalent *a posteriori* noise reduction that is then applied to the prediction when investigating the CNES RL01C solutions. The filtering procedure used is similar to Wiener optimal filtering (e.g. Seo & Wilson, 2005; Sasgen *et al.*, 2006) and it involves the ratio of the degree power of the CNES RL01C trend and the degree power of the unconstrained GFZ RL04 trend. In general, the application of this additional smoothing filter to the prediction is necessary to derive unbiased mass-change estimates from constrained gravity-field solutions, such as the CNES RL01C.

We also confine our investigation to the Stokes coefficients with $j, m \geq 12$ to reduce the long-wavelength signal in the GRACE data arising from mass changes in the far-field with respect to Antarctica and from the Earth's deep interior. The removal of these long wavelengths also reduces the overlap of signals from the individual regions. This limit is determined by calculating the degree correlation of the predicted geoid-height change over Antarctica described in the following section and the GRACE observations (e.g. Sasgen *et al.*, 2007a). Figure 6.2 shows that the degree correlation for all releases is statistically significant for $j \geq 12$ (the 95% confidence limit is indicated by the dashed line).

It should be mentioned, however, that the geoid-height change induced by mass changes of small spatial scales is not only reflected by coefficients of higher degrees and orders, and vice versa. Therefore, it is necessary to reconsider the coefficients of the lower degrees and orders that were omitted during the adjustment procedure in the mass-change models in order to obtain meaningful mass-change estimates.

Figure 6.3 shows the resulting rate of geoid-height change over Antarctica as inferred from the four GRACE releases considered. All releases show three prominent anomalies that are associated with known mass change processes, namely at the tip of the Antarctic Peninsula and in the Amundsen Sea Sector, where rapid glacier melting observed by other methods (e.g. laser altimetry) induces a negative rate of geoid-height change, and over the Ronne Ice Shelf (West Antarctica), where the GIA-induced inflow of mantle material following the retreat of the Antarctic Ice Sheet after the LGM causes an increase in the geoid height. In the following, we adjust the mass-change models for these three regions with respect to the noise-reduced GRACE observations. The source of the distinct positive geoid-height change in East Antarctica (centered ca. 50$^\text{o}$ E; 70$^\text{o}$ S) is not identified and will therefore be excluded from this investigation.

It should be noted that the inferred rates of geoid-height change shown in Figure 6.3 may differ due to the noise-reduction function s_{jm}, which is specific for each individual GRACE release. This will be accounted for by applying each reduction to the mass-change models. The remaining variability is due to observational uncertainties in the GRACE releases and the slightly different months of gravity-field determination considered and will be used to assess the robustness of our mass-change estimates.

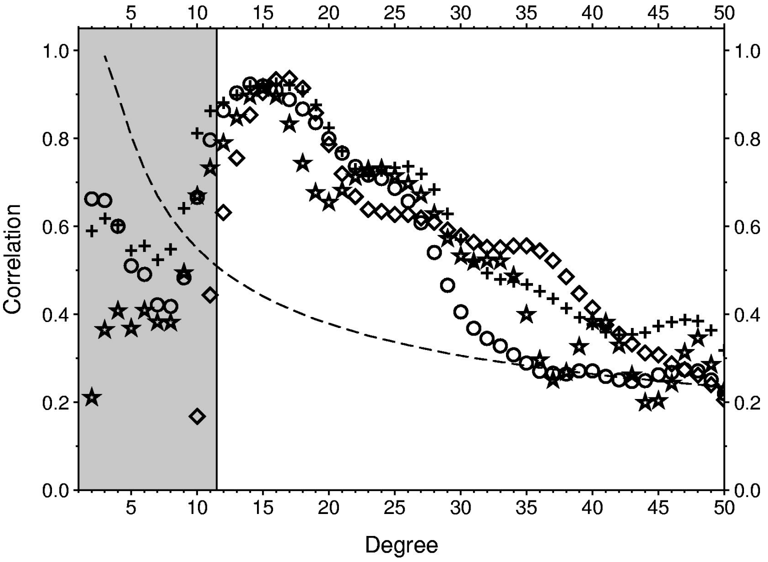

Figure 6.2: Degree correlation between the predicted and observed rate of geoid-height change over Antarctica for GFZ RL04 (circles), CNES RL01C (asterisk), JPL RL04 (diamonds) and CSR RL04 (crosses). The 95 % significance level is indicated by the dashed line. The investigation is limited to the Stokes potential coefficients of $12 \leq j, m \leq 50$, for which all releases show a significant correlation with the geoid-height change predicted by the mass-change models employed.

6.1.3 Modeled geoid-height change due to present-day ice-mass changes and GIA

The geoid-height change over Antarctica is predicted using a viscoelastic earth model subjected to surface-mass changes occurring in selected Antarctic drainage basins and to the glacial history of the entire ice sheet for the last glacial cycle. The predicted geoid-height change x_{jm}^{p} can be expressed as

$$x^{\mathrm{p}}(s) = \frac{R^2}{g_0} \sum_j q_j(s) \frac{4\pi}{2j+1} \sum_m \sigma_{jm}(s) Y_{jm}, \tag{6.1}$$

where R is the Earth's radius, g_0 is the normal gravity at the Earth's surface, Y_{jm} are fully normalized scalar spherical-harmonic functions, σ_{jm} are the spherical-harmonic expansion coefficients of surface-mass change, s is the Laplace variable, and q_j are the viscoelastic surface-load Love number in the Laplace domain for a specified viscosity distribution (e.g. Wu & Peltier, 1982). For quasi-instantaneous mass variations ($s \rightarrow 0$), such as present-day ice-mass changes, q_j approaches the surface-load elastic Love numbers.

Altimetry and Interferometric Synthetic Aperture Radar (InSAR) measurements of the Antarctic Ice Sheet indicate that there are two regions experiencing prominent ice-mass change: the tip of the Antarctic Peninsula, where particularly the glaciers Hektoria/Green/Evans, Jorum, Crane, Flask, Leppard and Drygalski were observed to rapidly retreat following the collapse of the Larsen B Ice Shelf in March 2002, resulting in an estimated mass loss of ca. 0.07 mm/a ESL (Rignot *et al.*, 2004; Scambos *et al.*, 2004) and the Amundsen Sea Sector, in particular the glaciers Pine Island, Thwaites, Smith and Kohler, with an estimated total loss of ca. 0.24 mm/a ESL (Thomas *et al.*, 2004). Other drainage basins of the ice sheet appear to be almost in balance (e.g. Remy & Frezzotti, 2006), except for Ice Stream C (ca. 230° E; 85 ° S), West Antarctica, which is observed to be accumulating mass at a rate of -0.05 mm/a ESL due to a decrease in its flow velocity (Rignot & Thomas, 2002). The geoid-height change associated with these mass changes is calculated according to (6.1) assuming an elastic earth model.

The GIA-induced geoid-height change is calculated according to (6.1) using a viscoelastic earth model combined with the glacial history of Huybrechts (2002). The Huybrechts (2002) reconstruction is based on results from a thermomechanical ice-sheet model that simulates the variation in the volume and extent of the Antarctic Ice Sheet. The temporal evolution used here is linearly interpolated from four snapshots of the state of the ice sheet at 15, 7, 4 ka BP and at present. Its main characteristic is the late deglaciation of the Ronne Ice Shelf region, which continues until today. In agreement with glaciological and geomorphologic evidence (e.g. Bentley, 1999; Anderson *et al.*, 2002; Ivins & James, 2005), the reconstruction also features the largest reduction of ice mass in Antarctica around the region of the Ronne Ice Shelf. This, in turn, leads to the largest GIA-induced geoid-height change signal consistent with that predicted using the geomorphologic reconstruction of Lambeck & Chappell (2001). Although the glacial history of Peltier (2004) based on globally distributed paleo sea-level indicators also requires a rather late initiation of Antarctic deglaciation (ca. 15 ka BP), it includes the largest retreat of ice, hence, the largest GIA signal over the Ross Ice Shelf. In this work, we focus on the GIA signal over the Ronne Ice Shelf to adjust the glacial history of Huybrechts (2002), as the predicted GIA signals in the other regions of the Antarctic continent are considerably smaller in magnitude, which, in turn, is supported by the GRACE observations.

We use a four-layer viscoelastic earth model consisting of an elastic lithosphere of thickness $h_{\mathrm{L}} = 100\,\mathrm{km}$, an upper mantle of viscosity $\eta_{\mathrm{UM}} = 5.2 \times 10^{20}\,\mathrm{Pa\,s}$, a lower mantle of viscosity $\eta_{\mathrm{LM}} = 5.9 \times 10^{21}\,\mathrm{Pa\,s}$ and a fluid core. This viscosity profile corresponds to that determined for Fennoscandia using the relaxation time spectrum derived from regional paleo-shorelines (Martinec & Wolf, 2005). However, it is also satisfactory when reproducing global sea-level change over the past 20 ka, and we therefore consider it to be a global-average earth model also appropriate for the mantle beneath West Antarctica, of which very little is known. However, we also modify the viscosity profile within a plausible range to assess its influence on our mass-change estimates. As a result, we find that changing the viscosity values mainly influences the magnitude of the predicted GIA-induced geoid-height change, while its spatial pattern is retained (not shown here).

6.1.4 Mass-change estimate

The predictions representing the geoid-height change over all regions of interest, i. e. the Antarctic Peninsula, the Amundsen Sea Sector and the Ronne Ice Shelf, are filtered by the version of the statistical filter, s_{jm} discussed above, that is adapted to the noise level of the GRACE release under consideration. This is necessary to verify the consistency of the modeled geoid-height change after the noise reduction and avoids biasing the resulting mass-change estimates. For the investigation of the trends inferred from CNES RL01C solutions, the modeled geoid-height changes are additionally smoothed by the spatial-averaging filter described in Section 2.

After filtering, we synthesize the coefficients with $12 \leq j, m \leq 50$ of the predicted and observed geoid-height change, y^{p}_{jm} and y^{o}_{jm}, to obtain their associated spatial representation, y^{p}_{i} and y^{o}, respectively. Here, the index i refers to the modeled geoid-height change including the signal over the region of interest, i. e. the Antarctic Peninsula ($i = 1$), the Amundsen Sea Sector ($i = 2$) and the Ronne Ice Shelf region ($i = 3$).

We adjust the magnitude of each modeled geoid-height change to fit the GRACE data such that the residual signals over the three areas, $\mathbf{\Omega}_i, i = 1, 2, 3$ (coordinate rectangles in Figure 6.1 and Figure 6.3), are minimized in the L_1-norm sense. The size of the three adjustment areas is chosen to be consistent with the spatial GRACE resolution of ca. 4°, which is estimated from the signal-to-noise ratio of the degree-power spectrum using the Wiener optimal-filtering approach (Sasgen *et al.*, 2006). The adjustment is carried out on a 0.25° × 0.25° grid. The L_1 norm is used as it is most sensitive to extreme values, which are, for the GRACE data, the most robust with respect to the remaining observational noise. We include an adjustment area around the peak values of the geoid-height change to assure that the fitting is insensitive to changes in the spatial pattern of the geoid-height change or lateral variations in the positions of the extreme values due to residual noise.

We make use of the cost function E defined as

$$E := \sum_{i=1}^{3} \int_{\mathbf{\Omega}_i} \left\| y^{\mathrm{o}}(\mathbf{\Omega}) - y^{\mathrm{p}}_{i}(\mathbf{\Omega})\alpha_i \right\|_{L_1} d\mathbf{\Omega}, \tag{6.2}$$

which is minimized with respect to the scale factors α_i. Having determined α_i, the optimal model of the geoid-height change for Antarctica is given by the scaling and summation of the three geoid-height change models, $y^{\alpha} = \sum_{i=1}^{3} y^{\mathrm{p}}_{i}(\mathbf{\Omega})\alpha_i$. The surface-mass change of interest is then determined by using the linear relation between the source of the mass change and the associated variation of the gravitational potential according to (6.1). This is done by considering the full spectral range of the models of the geoid-height change.

It should be mentioned that even though the adjustment areas $\mathbf{\Omega}_i$ and peak mass changes are spatially separated, the modeled geoid-height change for each of the three regions will overlap with the other, even after reducing the long-wavelength components of the gravity field. We account for the remaining overlaps by adjusting the models of all three regions simultaneously, as expressed by the summation in (6.2).

Also, data outside of the areas $\boldsymbol{\Omega}_i$ are not considered when determining the scale factors α_i.

6.1.5 Uncertainty in the mass-change estimate

One method used to determine the uncertainty in our mass-change estimates is by the propagation of the variance of the least-squares regression parameters, $\mathrm{var}(x^{\mathrm{o}}_{jm})$, to the parameters α_i. For uncertainties arising from the use of a single GRACE release, we assume no covariances between the linear-trend coefficients. The variance with respect to two spatial coordinates $\boldsymbol{\Omega}_{k,l}$ on the adjustment grid can be expressed by

$$\mathrm{var}(x^{\mathrm{o}})_{kl} = \sum_{jm} Y_{jm}(\boldsymbol{\Omega}_k)\mathrm{var}(x^{\mathrm{o}}_{jm})Y_{jm}(\boldsymbol{\Omega}_l). \tag{6.3}$$

The variance of the adjustment parameter α_i is given by (e.g. Koch, 1999)

$$\mathrm{var}(\alpha_i) = \frac{\sum_{kl} y^{\mathrm{P}}_i(\boldsymbol{\Omega}_k)\mathrm{var}_{kl}(x^{\mathrm{o}})y^{\mathrm{P}}_i(\boldsymbol{\Omega}_l)}{[\sum_{kl} y^{\mathrm{P}}_i(\boldsymbol{\Omega}_k)y^{\mathrm{P}}_i(\boldsymbol{\Omega}_l)]^2}, \tag{6.4}$$

where y^{P}_i denotes the spatial representation of the modeled geoid-height change for the individual regions and $\boldsymbol{\Omega}_{k,l} \in \boldsymbol{\Omega}_i$ represent the spatial coordinates within the associated adjustment area.

Another method used to assess the robustness of our results is by conducting a bootstrap estimate (e.g. Efron & Tibshirani, 1993) of the mean mass change. The bootstrap estimate can be used to infer the statistical properties of a distribution from a small number of samples (ca. 20) on the assumption that each individual sample captures the essential properties of the underlying population. Here, the sample observations are the 24 mass-change estimates for each of the three regions derived from the four GRACE releases using six 3.5 year-long time intervals that are shifted with respect to each other by one month. The first interval is January 2003 to June 2006, hence the last time interval is June 2003 to November 2006. For comparison, we also obtain estimates using the full four-year period, January 2003 to December 2006. Shifting the time intervals allows us to assess the stationarity of the signals investigated and the uncertainty that arises from not including other time variations into our model, such as accelerations and longer-term oscillations. We randomly draw a collection of 24 samples from our 24 mass-change estimates and calculate their mean assuming equal probability of each mass-change estimate. The procedure is repeated 1000 times. The resulting distribution of means provides a measure of the uncertainty of the inferred mean mass change, which includes the differences between the GRACE releases and the variations in the temporal linear trend with respect to the observation period.

6.1.6 Results and discussion

The top of Figure 6.4 shows the mass-change estimates based on the four-year period (January 2003 to December 2006) of the GFZ RL04, CNES RL01C, JPL RL04 and

CSR RL04 releases; (a) ice loss at the tip of the Antarctic Peninsula and in the Amundsen Sea Sector and (b) mass change of the Antarctic Ice Sheet since LGM, as inferred from the GIA signal over the Ronne Ice Shelf (third region). The values in (b) correspond to the additional ice mass required with respect to the reconstruction of Huybrechts (2002) at 15 ka BP that is necessary to produce the observed geoid-height change over the Ronne Ice Shelf regions, given the earth-model parameters employed ($h_{\mathrm{L}} = 100\,\mathrm{km}$, $\eta_{\mathrm{UM}} = 5.2\times 10^{20}\,\mathrm{Pa\,s}$ and $\eta_{\mathrm{LM}} = 5.9\times 10^{21}\,\mathrm{Pa\,s}$). Here, we assume that the scale factor determined also applies to the other regions of Antarctica with past ice-mass changes described in the glacial history, for example, the region of the Ross Ice Shelf and the Amery Ice Shelf (East Antarctica). The associated error bars are calculated according to (6.3) and (6.4). It is noticeable that the results obtained from the four releases differ significantly, in particular the mass-change estimates derived from the signal over the Ronne Ice Shelf. Similar results using the unfiltered spectral range of the GRACE data indicate that this variability is not a product of the noise reduction applied. In general, the GFZ RL04 and the CSR RL04 give very similar results, compared to which the values of the CNES RL01C are slightly higher, and the values of the JPL RL04 are somewhat lower. This variability in the results with respect to the different releases is probably due to observational uncertainties that are underestimated by the propagated errors. As shown in Figure 6.3, all releases consistently reflect the predicted geoid-height change and are therefore considered to be appropriate for deriving mass-change estimates.

The bottom of Figure 6.4 presents the results of the bootstrap estimate. Shown are histograms of 20 equidistant bins that indicate the frequency of each mean mass-change estimate. The diamond and bar above each histogram represent the mean of the population and the interval bracketing 95% of the estimates, respectively. The grey-shaded areas indicate the variability of all 24 underlying mass-change estimates.

For the Antarctic Peninsula, our inferred mean mass change of 0.08 mm/a ESL (± ca. 6 %) agrees well with the values determined from radar interferometry (0.07 mm/a ESL; Rignot *et al.*, 2004). This is remarkable since the mass change in this region is very localized and is likely to be influenced by mass changes associated with the Antarctic Circumpolar Current. However, we observe that the values for all releases and all six time intervals are bracketed between 0.07 and 0.11 mm/a ESL, with most of the CNES RL01C estimates being higher and a slight increase of mass loss for later time intervals. The increasing values for later time intervals indicate a non-stationary process that may, for example, be caused by an acceleration of the melting of glaciers in this region, a period of enhanced melting during the end of 2006, or a long-term mass change in the surrounding ocean.

For the Amundsen Sea Sector, 95% of our bootstrap estimates of the mean mass change lie between 0.18 and 0.20 mm/a ESL, the values of all releases and time intervals ranging between 0.16 and 0.23 mm/a ESL. The mass loss for each of the time intervals investigated is nearly constant, meaning that the variability mainly arises from the differences in the releases. Also for this region, the GFZ RL04 and the CSR RL04 produce results which are closest to each other ($\sim\pm 0.01$ mm/a ESL), while the CNES RL01C and JPL RL04 based estimates are ca. 0.03 mm/a ESL higher and lower, respectively. The bootstrap-estimated mean of 0.19 mm/a ESL(± 6%) is considerably lower than the most recent estimate based on aircraft- and satellite-laser altimetry, ca. 0.24 mm/a ESL (Thomas *et al.*, 2004), but it is somewhat higher than a previous estimate of 0.17 ± 0.03 mm/a ESL (Rignot & Thomas, 2002). It is close to the minimum of the range of 0.21 ± 0.04 to 0.28 ± 0.05 mm/a ESL presented by Chen *et al.* (2006b), who investigated using a forward modelling approach the constrained CSR RL01C gravity fields. However, our estimate is much lower than the rate of 0.30 ± 0.06 mm/a ESL determined by Ramillien *et al.* (2006) using the basin-analysis approach and the CNES RL01C release. An explanation for this large deviation is that the authors considered a larger number of West Antarctic glaciers and also applied an *a priori* GIA correction of 0.06 mm/a ESL to the mass-change estimate.

For the Ronne Ice Shelf region, based on the glacial history of Huybrechts (2002) and the earth model parameters used ($h_{\mathrm{L}} = 100\,\mathrm{km}$, $\eta_{\mathrm{UM}} = 5.2 \times 10^{20}$ Pa s and $\eta_{\mathrm{LM}} = 5.9 \times 10^{21}$ Pa s), 95% of the adjusted models of the GIA-induced geoid-height change suggest that the Antarctic continent was covered by 8.4 to 9.5 m ESL of additional ice during the LGM. The range of values inferred from all releases and time intervals is 6.1 to 10.8 m, representing a larger variability than the values for the other two regions. A possible explanation is that the ocean tides under the Ronne Ice Shelf may not have been completely removed from the GRACE gravity-field solutions (King *et al.*, 2005; King & Padman, 2005; Han *et al.*, 2005b). The bootstrap-estimated mean mass change is 9.0 m ESL(± ca. 6 %). It lies in the range of 6.1 to 13.1 m ESL proposed by Bentley (1999) and largely agrees with the value of 10.1 m ESL of Ivins & James (2005). The value corresponds to a maximum rate of geoid-height change over the Ronne Ice Shelf region (ca. 293° E; 81° S) of 1.5 mm/a when synthesizing the full spectral range ($2 \leq j, m \leq 50$). This rate of geoid-height change is at the lower end of the range predicted by Kaufmann (2002) (ca. 1.5 to 3 mm/a), but it is 2 to 3 times larger than the range of 0.4 to 0.6 mm/a predicted by Ivins *et al.* (2001).

It should be stated that our interpretation of the GIA signal depends on the assumed earth model, and, to a much greater extent, on the details of the Antarctic deglaciation. The combination of the viscosity profile and glacial history used here results in a rather large GIA signal over the Ronne Ice Shelf, and we therefore consider our value to be a minimum estimate. For example, using higher upper-mantle viscosities of $\eta_{\mathrm{UM}} = 6 \times 10^{20}$ Pa s and $\eta_{\mathrm{UM}} = 8 \times 10^{20}$ Pa s, reduces the magnitude of the GIA signal over the Ronne Ice Shelf. This can be compensated by a ca. 10% and ca. 15%, respectively, larger mass change of the Antarctic Ice Sheet since the LGM. In contrast, a reduced upper-mantle viscosity of $\eta_{\mathrm{UM}} = 4 \times 10^{20}$ Pa s suggests a ca. 5% smaller amount of additional ice during the LGM. The mass-change estimates are not sensitive to the lower-mantle viscosity, because variations in the gravity field that would arise from changing this parameter are important only in the lower spectral range that is not considered.

A similar GIA signal is obtained using the reconstruction of Lambeck & Chappell (2001), which features ca. 33 m ESL of additional ice at the LGM and a much earlier retreat compared to the glacial history of Huybrechts (2002). This illustrates the ambiguity inherent in the inversion of the GIA signal and emphasizes that additional constraints on the timing of the deglaciation are required. However, the mass-change estimates for the Antarctic Peninsula and the Amundsen Sea Sector are not significantly influenced when the reconstruction of Lambeck & Chappell (2001) is used, owing it producing an similar GIA signal in Antarctica as the Huybrechts (2002) model.

6.1.7 Conclusions

We have determined noise-reduced temporal linear trends in geoid-height change over Antarctica from four independent GRACE releases and have fitted these observations by adjusting mass-change models reflecting three regions of prominent ice-mass loss (Antarctic Peninsula and the Amundsen Sea Sector) and GIA (Ronne Ice Shelf region).

We have shown that the mass-change estimates of the GRACE releases differ significantly and that the conventional propagation of GRACE errors underestimates these uncertainties. We have then calculated a bootstrap estimate of the mean mass change based on 24 mass-change estimates, each of which was derived from 3.5 years worth of data, allowing us to assess the robustness of our results.

For the Antarctic Peninsula, the ice-mass loss estimated for all releases and time intervals considered is bracketed between 0.07 and 0.11 mm/a ESL, the bootstrap-estimated mean mass change being 0.08 mm/a ESL (± ca. 6 %), which agrees with values inferred from radar interferometry (0.07 mm/a ESL; Rignot *et al.*, 2004). For the Amundsen Sea Sector, the ice-mass loss determined is between 0.16 and 0.23 mm/a ESL, the bootstrap estimate giving 0.19 mm/a ESL(± 6%). This is considerably lower than an laser-altimetry measurement of 0.24 mm/a ESL(Thomas *et al.*, 2004) and close to the minimum of the previous GRACE-based estimate of Chen *et al.* (2006b) (0.21±0.04 to 0.28±0.05 mm/a ESL). We have interpreted the signal over the Ronne Ice Shelf in terms of GIA using a viscoelastic earth model and the glacial history of Huybrechts (2002). For all releases and time intervals, the signal suggest a mass change of the Antarctic Ice Sheet since the LGM of between 6.1 and 10.8 m ESL, the value varying by ca. 15% for the range of plausible viscosity profiles. The bootstrap estimate of 9.0 m ESL (± ca. 6 %) agrees with the geomorphologic estimate of 6.1 and 13.1 m ESL by Bentley (1999). We have found that the mass-change estimates for all releases and time intervals lie within ca. 20% (Amundsen Sea Sector), 30% (Antarctic Peninsula) and 50% (Ronne Ice Shelf region) of the bootstrap-estimated mean, demonstrating the reliability of mass-change estimates in Antarctica from GRACE observations.

Acknowledgments

The first author thanks Christoph Reigber for his continuous support, Erik Ivins for helpful discussions and Detlef Wolf for the improvement to the manuscript. The second author acknowledges support from the Grant Agency of the Czech Republic through Grant No. 205/06/0580. The authors thank Georg Kaufmann and one anonymous reviewer for their constructive comments that have helped to improve the manuscript.

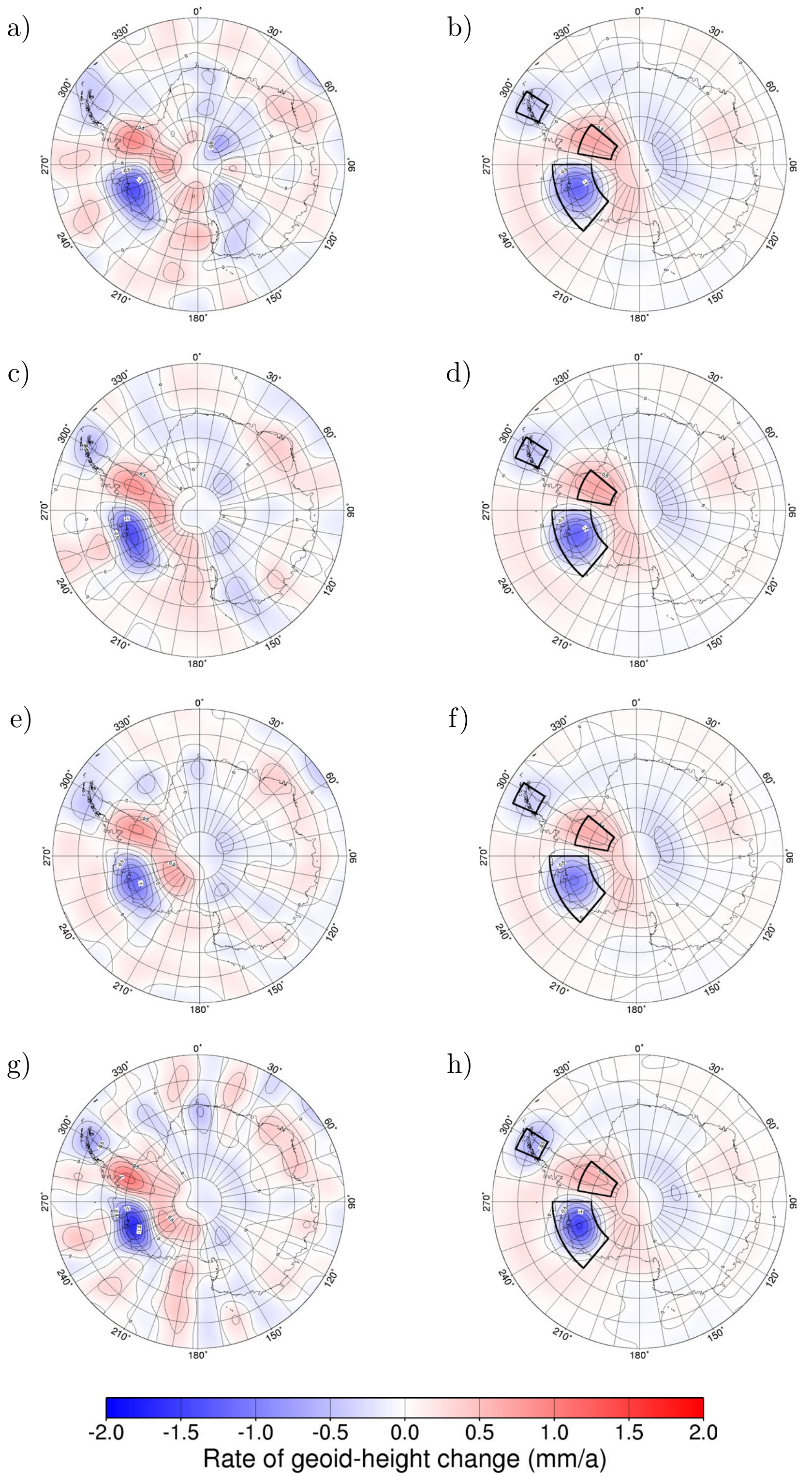

Figure 6.3: Rate of geoid-height change over Antarctica determined from (a) GFZ RL04, (c) CNES RL01C, (e) JPL RL04 and (g) CSR RL04, and the associated adjusted geoid-height change resulting from present-day ice-mass changes and GIA for (b) GFZ RL04, (d) CNES RL01C, (f) JPL RL04 and (h) CSR RL04. The three coordinate rectangles (solid lines) indicate the areas used for the adjustment of the geoid-height change models, namely the Antarctic Peninsula, the Amundsen Sea Sector and the Ronne Ice Shelf region. The cut-off degrees are $j_{\min} = 12$ and $j_{\max} = 50$.

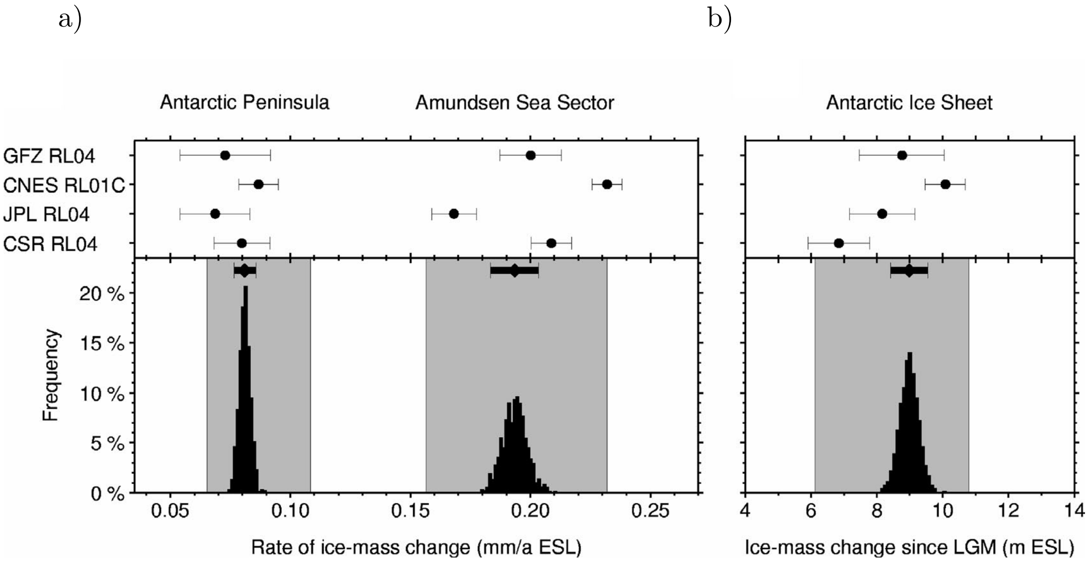

Figure 6.4: Mass changes in Antarctica as inferred from the four GRACE releases. (a) Present-day ice-mass changes along the Antarctic Peninsula (i.e. Hektoria/Green/Evans, Jorum, Crane, Flask, Leppard and Drygalski glaciers) and the Amundsen Sea Sector (i.e. Pine Island, Thwaites, Smith and Kohler glaciers) and (b) mass change of Antarctic Ice Sheet since the LGM. Top: Mass-change estimates and associated propagated errors for the four GRACE releases considering the four-year period January 2003 to December 2006. Bottom: Histogram of bootstrap-estimated mean mass changes. The grey-shaded area indicate the minimum and maximum mass changes obtained using all GRACE releases and time intervals.

6.2 Supplement to publication of previous section

In addition to the results published in Sasgen *et al.* (2007b) (Section 6.1), investigations concerned with the temporal linear trend of the mass changes in Antarctica are presented. The results indicate that the stochastic averaging (bootstrap estimation) carried out in the paper may not be fully justified, since deterministic temporal mass variations can be identified in all GRACE releases, and, even more importantly, since the GRACE releases show systematic biases.

Figure 6.5 shows the values of mass change for the Antarctic Peninsula, West Antarctica and for the Antarctic Ice Sheet since the LGM as inferred from the GIA signal over the Ronne Ice Shelf region. For the Antarctic Peninsula, mass-loss rates increase by 0.02 mm/a ESL with shifting of the time interval used for the computation of the trend towards later times for all releases except CSR RL04. The differences between the GRACE releases amount to $\sim$0.04 mm/a ESL. For West Antarctica, interannual variations of the linear trend are $\lesssim$0.01 mm/a ESL. However, the range of estimates exhibited by the GRACE releases is large, ranging between 0.16 (JPL RL04) and 0.23 mm/a ESL (CNES RL01C). The amplitude of the inferred GIA signal decreases with proceeding time interval for GFZ RL04 and JPL RL04, while largely remaining constant for CNES RL01C and CSR RL04. Again, also the differences between releases are large (between 6.4 and 10.2 m ESL for JPL RL04 and CNES RL01C, respectively).

The reason for the instability of the temporal trend over the Ronne Ice Shelf is not clear. Potential cause is inaccurate modelling of ocean tides underneath the ice shelf during GRACE processing, which then alias into long-term changes of the gravity field. Significant aliasing errors are predicted mainly for the K_1 and K_2 tides using CSR RL04; tidal errors for GFZ RL04 are smaller (Moore & King, 2008). The biases of the different releases can partially be explained by the power of the GRACE gravity fields. Figure 6.6 shows the cumulative degree power of the gravity fields' temporal linear trend for the four releases investigated with (except for CNES RL01C) and without statistical filtering. First, it is visible that the power of the constrained CNES RL01C fields are higher than that of the remaining releases in the unfiltered spectral range $j < 22$. The CNES solution providers claim that merely coefficients of degree and order $j > 30$ are stabilized by a Kaula-type regularization. However, the diagram shows that coefficients with degrees and orders > 25 appear to be increasingly constrained, i.e. unconstrained and constrained spectra are no longer parallel. However, JPL RL04 typically results in smaller values, for which Figure 6.6 gives no indication.

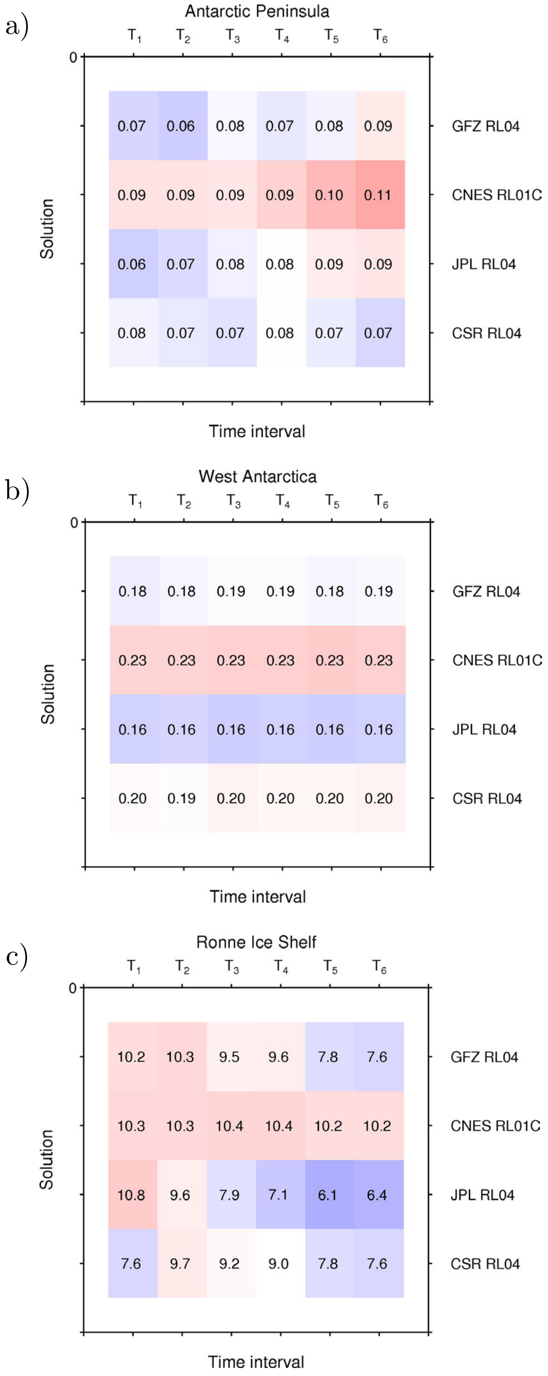

Figure 6.5: Mass changes in Antarctica from four GRACE releases. Present-day ice-mass changes along a) the Antarctic Peninsula and b) the Amundsen Sea Sector in mm/a ESL, and c) mass change of the Antarctic Ice Sheet since the LGM as inferred from the GIA signal over the Ronne Ice Shelf region in m ESL.

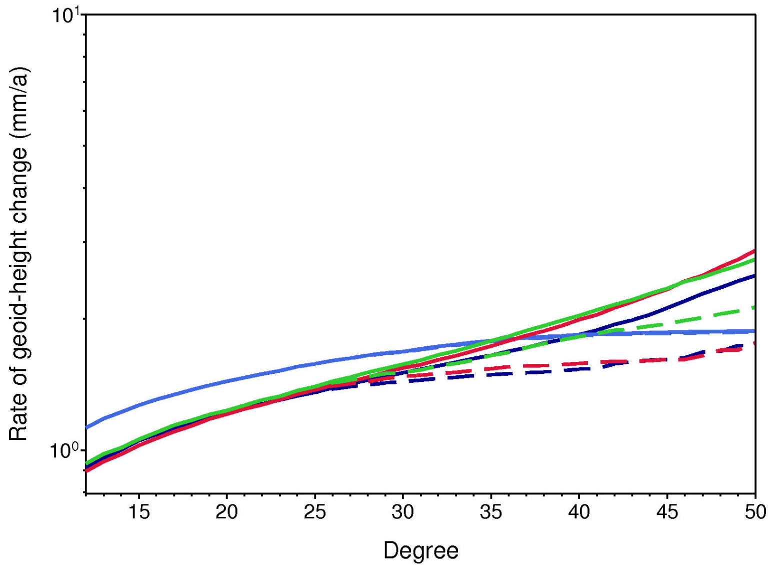

Figure 6.6: Cumulative degree-power spectrum of the GRACE coefficients' linear trend for GFZ RL04 (dark blue), CNES RL01 (light blue), JPL RL04 (red) and CSR RL04 (green). The respective spectra after statistical filtering for $j, m \geq 25$ are shown as dashed lines. The lower cut-off degree is $j_{\min} = 3$.

6.3 North America and Greenland ice-mass changes and GIA

The following investigation is an attempt to invert GRACE data for present-day ice-mass changes in Alaska and Greenland as well as for GIA over North America, applying the methods developed for Antarctica (Sasgen *et al.*, 2007b). Improvements to this study are suggested in Section 6.3.5.

The results are based on the unconstrained GRACE solutions of GFZ RL04, CSR RL04 and JPL RL04 as well as the constrained GRACE solutions of CNES RL01C, for the time interval January 2003 to December 2006. The full time interval T_{FULL} is divided into six 3.5 a subintervals, $T_1, T_2, ..., T_6$, each of which being shifted by one month. For each subinterval, the time series of Stokes potential coefficients are decomposed according to (4.6) into linear trend, offset as well as annual and semi-annual oscillating components by the method of least-squares assuming constant variances over time. In Sasgen *et al.* (2008) (Section 6.4), a weighted least-squares decomposition is used to account for GRACE solutions of poor quality associated with periods of repeat orbits.

6.3.1 Forward modelling of the geoid-height change

Present ice-mass change in Alaska

Arendt *et al.* (2002) determined the mass balance of 28 Alaskan glaciers for the years mid-1990 to 2001 by considering repeated airborne laser-altimetry measurements. The glaciers cover ~13% of the glaciated area in Alaska and were among 39 other glaciers, whose mass changes were determined for 1950 to 1996. By extrapolating data to unmeasured glaciers, Arendt *et al.* (2002) found a rate of mass loss for the entire region of 0.28 ± 0.10 mm/a ESL (mid-1990 to 2001), which is nearly twice the value of 0.14 ± 0.04 mm/a ESL obtained for the earlier measurement period (1950 to 1996). The largest portion of this value (~75%) is attributed to glaciers draining into the Gulf of Alaska. The mass balance model of Arendt *et al.* (2002) used for calculating the potential disturbance according to (2.17) is shown in Figure 6.7.

Present ice-mass change in Greenland

The forward model for the Greenland Ice Sheet is based on elevation changes observed by airborne laser altimetry between the years 1994 to 1999 (Krabill *et al.*, 2000). The surveyed area mainly covers the interior of the ice sheet with elevations $>$ 2000 m, but Krabill *et al.* (2000) extrapolated values towards the coast by estimating thinning rates from surface-air temperature using positive degree-day models (e.g. Braithwaite, 1995). Other discharge processes, such as dynamic thinning of the ice and acceleration of glaciers are neglected. The distribution of elevation changes for the Greenland Ice Sheet is shown in Figure 6.7. The minimum sea-level contribution of these glacial changes is ~0.13 mm/a ESL, although Krabill *et al.* (2000) do not assign errors to this estimate. It is recognized that glaciers in Greenland are diverse and exhibit complex behaviour (e.g Howat *et al.*, 2007). Assuming that mass changes are linearly

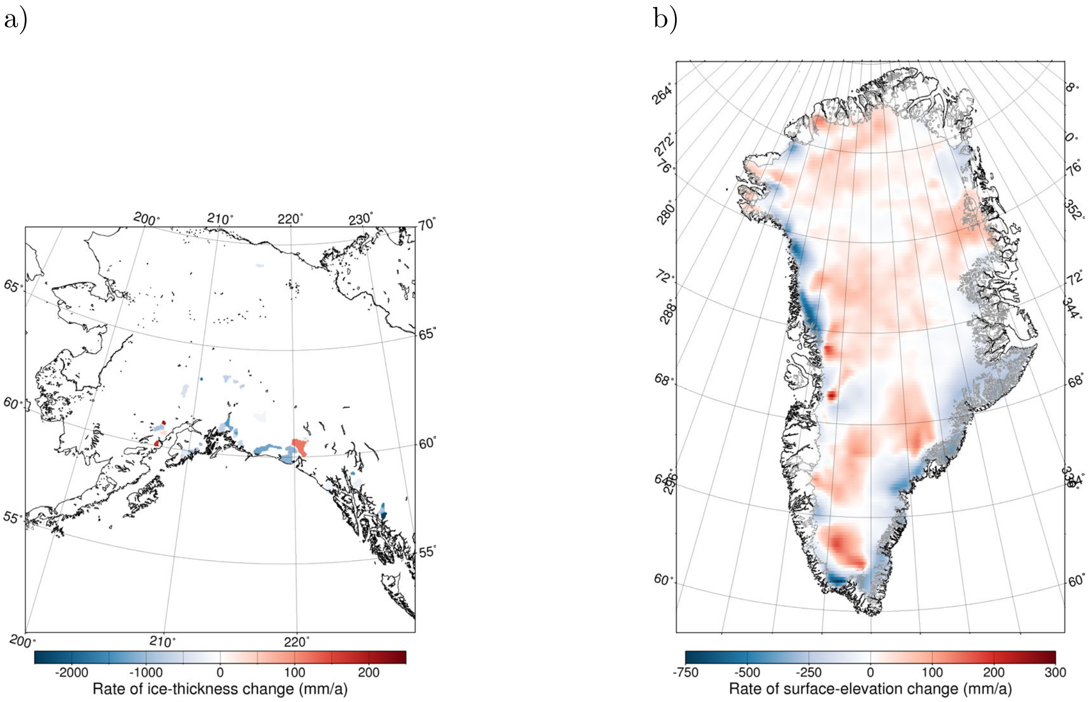

Figure 6.7: Ice-thickness change observed in a) Alaska (Arendt *et al.*, 2002) and b) Greenland (Krabill *et al.*, 2000) from airborne laser altimetry.

proportional to elevation changes is a major simplification, which needs to be refined in future investigations.

Past ice-mass change in North America and Greenland

The glaciation history used for calculating the viscoelastic Earth response over North America and Greenland is load model NAWI (Zweck & Huybrechts, 2005). This reconstruction is based on the results of the glaciological modelling of the evolution of the area and volume of the Pleistocene Ice Sheets in response to climatic forcing during the last-glacial cycle. The time series of the climatic forcing, i.e. temporal variations of precipitation and temperature anomalies, are based on climate models, which were adjusted to reconcile with the δ^{18}O record of the Greenland Ice Core Project (GRIP *[online]*). The version of load model NAWI employed here features additional ice in the Northern Hemisphere during the LGM (~20 ka BP) relative to present day of ~102.2 m ESL, distributed as 76.3 (Laurentide), 23.6 (Eurasia), 2.0 (Greenland) and 0.3 m ESL (Iceland). The spatial distribution of the ice thickness change since the LGM for North America, Greenland and Iceland is shown in Figure 6.8. The temporal evolution described by NAWI is characterized by a gradual increase in ice volume from 120 to 20 ka BP followed by a rather abrupt deglaciation (Figure 6.9). Later, NAWI will be adjusted with respect to the GRACE-observed GIA signal over North America; the relative distribution of ice mass in the Northern Hemisphere,

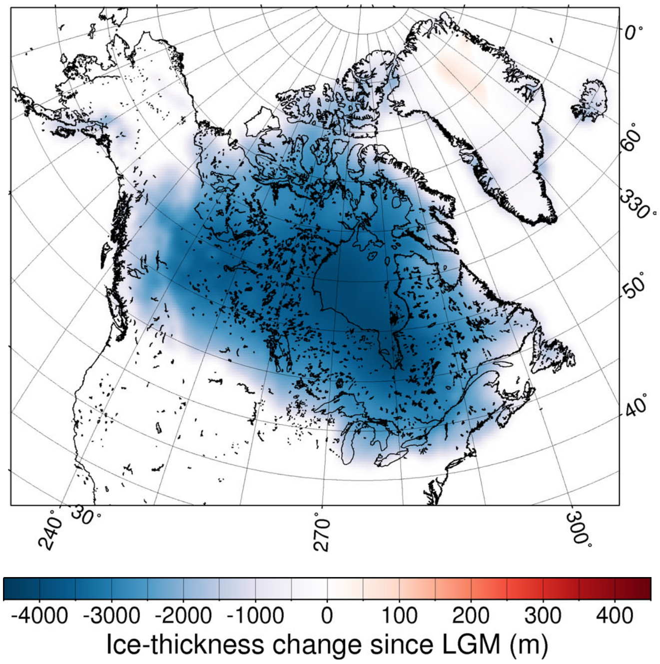

Figure 6.8: Ice-thickness change since the LGM over North America, Greenland and Iceland as described by load model NAWI.

however, is held fixed, which represents a strong simplification.

The earth model parameter values employed $h_{\mathrm{L}} = 100\,\mathrm{km}$, $\eta_{\mathrm{UM}} = 6.0 \times 10^{20}$ Pa s and $\eta_{\mathrm{LM}} = 2.0 \times 10^{22}$ Pa s, are close to the values determined by Wolf *et al.* (2006). Later, also the viscosity values are varied within plausible bounds to assess the results' sensitivity to the Earth's viscoelastic structure. The investigations presented are limited to GIA predictions based on the glaciological model NAWI. So far, other reconstructions, such as the geomorphological model ICE-5G (Peltier, 2004) have not been used.

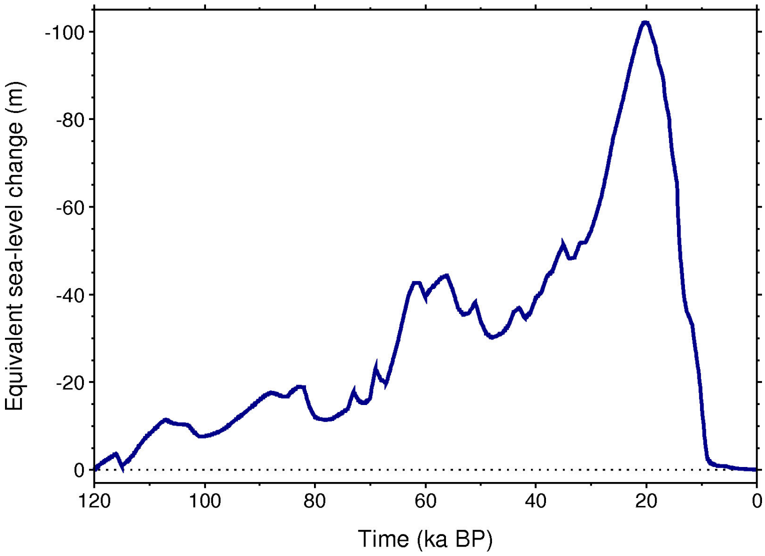

Figure 6.9: Mass change of the Northern Hemisphere ice sheets during the Last-Glacial Cycle for load model NAWI.

6.3.2 Post-processing of GRACE data

After temporal decomposition (Section 4.3.2), the statistical filter, s_{jm}, is applied to the coefficients linear trend component for degrees and orders $j, m \geq 25$. No additional smoothing is applied. To the forward model used in conjunction with the constrained CNES RL01C solutions, an equivalent smoothing filter is applied, which accounts for the *a priori* noise reduction used during the solution processing. The lower cut-off degree is determined using the degree correlation of $V^{\mathrm{Model}}(\mathbf{\Omega})$ and $V^{\mathrm{GRACE}}(\mathbf{\Omega})$ calculated according to (A.29). Figure 6.10 shows that coefficients with $j < 5$ exhibit no significant correlations for all releases and are therefore omitted. Most coefficients in the high spectral range are eliminated by the statistical filter due to their poor signal-to-noise ratio (Section 4.1), and the spherical harmonic series is truncated at cut-off degree $j_{\mathrm{max}} = 50$. Filtering or truncation of the spherical-harmonic expansion series is equally applied to the forward model and the GRACE data, which obviates biases of the mass change estimates. The rate of geoid-height change for the forward model and GRACE, with and without statistical filtering, are shown in Figure 6.13 (GFZ RL04), Figure 6.14 (CNES RL01C), Figure 6.15 (JPL RL04) and Figure 6.16 (CSR RL04).

Over North America, GRACE data is corrected for trends of potential disturbances due to interannual variations in total hydrological water storage. These trends are predicted using the WGHM model (Döll *et al.*, 2003) for each GRACE time interval $(T_{\mathrm{full}}, T_1, T_2, ..., T_6)$. The statistical filter for each interval and release is applied to the spectral representation of the potential disturbances caused by the WGHM trend, and the filtered signal is subtracted from the GRACE data (Figures 6.13 to 6.16). So far, WGHM has not been validated with respect to modelling long-term changes (~ 10 a). However, for the length of time intervals investigated here (~ 4 a), linear trends in hydrology are primarily due to interannual variations in precipitation and surface storage, for which the model has been designed.

6.3.3 Model adjustment

The forward model is adjusted to the GRACE data according to (5.16). The adjustment areas, $\mathbf{\Omega}_{\mathrm{S}_\alpha}$, $\alpha = 1, 2, 3$, are coordinate rectangles (Figures 6.13 to 6.16), which encompass the prominent potential disturbances predicted for Alaska (56.5 to 63.5 °N and −155 to −135 °E), Greenland (62 to 70 °N and −46 to −28 °E) and North America (50 to 65 °N and −110 to −70 °E). Following Sasgen *et al.* (2007b), the L_1-norm is used in the definition of the cost function (5.16), since it is less sensitive to outliers. This, however, requires a numerical search for the optimal solution.

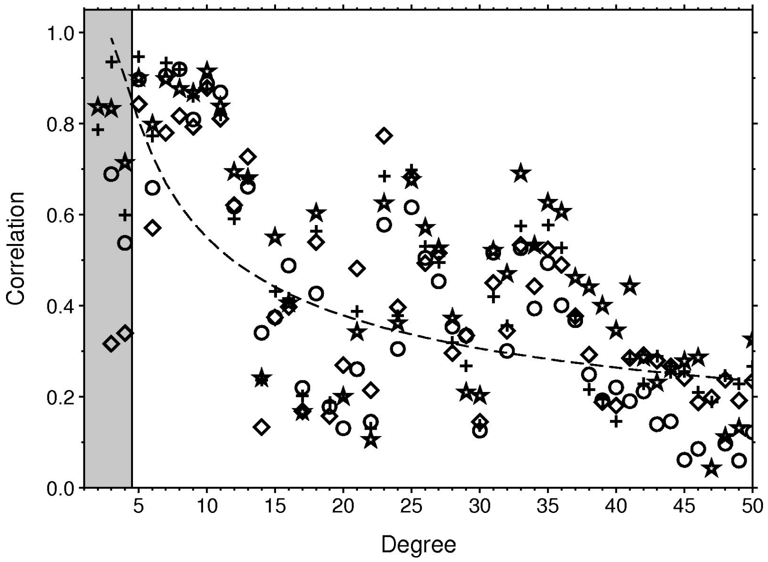

Figure 6.10: Degree correlation between the predicted and observed rate of geoid-height change over the Northern Hemisphere for GFZ RL04 (circles), CNES RL01C (asterisk), JPL RL04 (diamonds) and CSR RL04 (crosses) for the time interval January 2003 to December 2006. The 95 % confidence level is indicated by the dashed line. Stokes potential coefficients with $j, m < 5$ are exluded due to insignificant correlation (grey-shaded area).

6.3.4 Results and Discussion

This section describes the results of the GRACE gravity-field inversion over North America and Greenland. The top of Figure 6.11 shows the present-day ice-mass changes of the Alaskan glaciers and the Greenland Ice Sheet, as well as the sea-level contribution of NAWI since the LGM necessary to reproduce the GIA signal over North America for fixed earth-model parameters ($h_{\mathrm{L}} = 100\,\mathrm{km}$, $\eta_{\mathrm{UM}} = 6.0 \times 10^{20}$ Pa s and $\eta_{\mathrm{LM}} = 2.0 \times 10^{22}$ Pa s). The estimates are based on the time interval T_{full}, and the error bars are calculated according to (6.3) and (6.4). The bottom of Figure 6.11 represents the bootstrap-estimated mean value for each region based on the 24 individual estimates (4 releases and 6 subintervals), along with the minimum and maximum estimates indicated by the gray-shaded area. The individual estimates are shown Figure 6.12.

Alaska

The mass change of the glaciers in Alaska is estimated to lie between 0.17 and 0.29 mm/a. The bootstrap-estimated mean of 0.21 mm/a ESL (± 7%) is lower than the value of 0.28 ± 0.10 mm/a ESL obtained by airborne laser altimetry, however, both values agree within their ranges of uncertainties. It is also less than the values of 0.31 ± 0.09 mm/a ESL (Tamisiea *et al.*, 2005) and 0.28 ± 0.06 mm/a ESL (Chen *et al.*, 2006c) obtained from GRACE data (CSR releases) for mid-2002 to mid-2004 and mid-2002 to 2006, respectively. However, Figure 6.12 shows that, although mass-loss rates are largely independent of the subinterval, large differences between the GRACE releases' values exist; CSR RL04 and CNES RL01 produce larger values compared to GFZ RL04 and JPL RL04. Also, for CSR RL04, later time intervals produce significantly smaller mass-loss rates, more than for the other releases. For the earliest time interval T_1, which best corresponds to the period investigated by Tamisiea *et al.* (2005) and Chen *et al.* (2006c), the mass-loss rate is 0.25 mm/a ESL and in closer agreement with their values. Nevertheless, the residual, i.e. $V(\boldsymbol{\Omega})^{\mathrm{GRACE}} - \hat{V}(\boldsymbol{\Omega})^{\mathrm{Model}}$, indicates additional mass losses along the coast between 50 °N and 60 °N (Figures 6.13 to 6.16). This region is included in the forward model (Figure 6.7), but it is not individually parameterized and, therefore, not separately adjusted; further refinement of the forward model is necessary.

Without the GIA correction, i.e. excluding the GIA component from the forward model, mass-loss rates increase by ~0.05 mm/a ESL, with an uncertainty of <0.01 mm/a ESL for the range of plausible viscosity values (Figure 6.17), which confirms the estimate of Tamisiea *et al.* (2005). The sign of the GIA correction (apparent mass loss) is explained by the outflow of mantle material associated with the collapse of the viscoelastic forebulge, which is the dominant GIA signature along the margin of the former Laurentide Ice Sheet (Figure 6.8). GIA due to local ice-mass variations during the late Pleistocene or early Holocene in Alaska is expected to be small owing to the low viscosity values of the Earth's upper mantle in this region (e.g. Tamisiea *et al.*, 2005; Larsen *et al.*, 2003). Also, the influence of oceanic mass variations is estimated to be small (Tamisiea *et al.*, 2005) and not investigated further in this work.

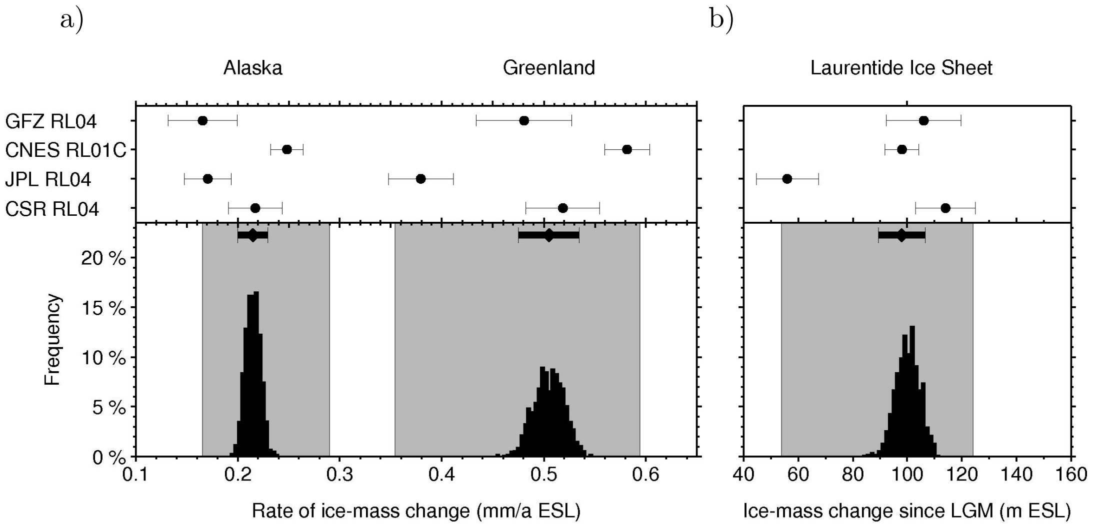

Figure 6.11: Bootstrap-estimated mass change in North America and Greenland from four GRACE releases. a) Present-day ice-mass changes of glaciers in Alaska and of the Greenland Ice Sheet and b) mass change of Laurentide Ice Sheet since the LGM. Top: Mass-change estimates and associated propagated errors for the four GRACE releases considering the four-year period January 2003 to December 2006. Bottom: Histogram of bootstrap-estimated mean mass changes. The grey-shaded area indicate the minimum and maximum mass changes obtained using all GRACE releases and time intervals.

Variations of the mass-change estimates with regard to the chosen subinterval are $< 10\%$ for individual releases (Figure 6.12). In contrast, differences between releases are 2 to 3 times larger. So far, the reason for these biases is not known. However, they appear to result from differences in the solution processing rather than from shortcomings in the filtering and inversion of the potential fields. An indication of this is the cumulative degree power spectrum from cut-off degree $j_{\min} = 3$ (Figure 6.6). For example, CNES RL01C exhibits larger power compared to all other releases, even for degrees $j < 25$, which have not been regularized during processing. In contrast, JPL RL04 often recovers lower amplitudes compared to the other releases (Figures 6.13 to 6.16). This tendency has also been observed for Antarctica (Figure 6.5).

Greenland

The mass loss of the Greenland Ice Sheet is estimated to lie between 0.35 to 0.60 mm/a ESL, the bootstrap-estimated mean being 0.51 mm/a ESL (±6%). This value is almost four times the minimum estimate of 0.13 mm/a ESL obtained from laser-altimetry measurements (Krabill *et al.*, 2000) for the years 1994 to 1999. More recent laser-altimetry estimates with more realistic considerations of snowfall, dynamic thinning and surface melting in coastal low-elevation regions result in mass-loss rates of $\sim 0.22 \pm 0.03$ mm/a ESL between 1997 and 2003 (Krabill *et al.*, 2004). InSAR measurements of the ice-surface velocity indicate ice discharge increasing from 0.23 ±

0.08 mm/a ESL in 1996 to 0.57 ± 0.10 mm/a ESL in 2005 (Rignot & Kanagaratnam, 2006). The year 2005 value, which represents approximately the mid-point of the GRACE time interval, is in close agreement with the bootstrap estimated mean of 0.51 mm/a (± 6%).

For each release, values vary within <10% of their mean. Most of this variation is caused by increasing values at later time intervals explained by the acceleration of the ice sheet's discharge, mainly south of 66 °N before the year 2000 and up to 70 °N by the year 2005 (Lemke *et al.*, 2007). For example, CSR RL04 mass-loss rates gradually increase from 0.51 (T_1) to 0.58 mm/a ESL (T_6), although previous GRACE estimates based on shorter time series also suggested a doubling of discharge rates for the years 2004 to 2006 compared to the years 2002 to 2004 (Velicogna & Wahr, 2006).

Previous mass-change estimates from GRACE range between 0.28 ± 0.04 mm/a ESL (Luthke *et al.*, 2006, years 2003 to 2005, mass concentration approach) to 0.63 ± 0.10 mm/a ESL (Velicogna & Wahr, 2006, years 2003 to 2006, CSR RL01, optimized basin analysis), which largely coincides with the range of 0.35 to 0.60 mm/a ESL obtained from this investigation considering all releases and all time intervals. Again, variability of the values is mainly caused by systematic biases in the releases (Figure 6.12); GFZ RL04 and CSR RL04 produce similar results, while CNES RL01 and JPL RL04 give higher and lower estimates, respectively. This behaviour is similar to the mass-loss rates obtained for West Antarctica (Figure 6.5).

Without removing GIA, mass-loss rates are larger by ~ 0.08 mm/a ESL owing to not correcting for the collapse of the viscoelastic forebulge largely encompassing North America. The uncertainty based on the range of plausible viscosity values (Figure 6.17) is <0.05 mm/a ESL. This value, based on glacial history NAWI and the earth model parameters given in Section 6.3.1, is 3 to 4 times larger than the correction calculated by Velicogna & Wahr (2005) using the glacial histories ICE-5G (Peltier, 2004) and ICE-3G (Tushingham & Peltier, 1991) outside Greenland, together with ICE-5G and GREEN1 (Fleming *et al.*, 2004; Fleming & Lambeck, 2004) for Greenland.

The residual (i.e. $V^{\mathrm{GRACE}} - \hat{V}^{\mathrm{Model}}$) is close to zero over most of the Greenland Ice Sheet (Figures 6.13 to 6.16). At the most northern part, however, all releases (except JPL RL04) indicate additional mass loss not adequately represented by the forward model based on Krabill *et al.* (2000) (rate of geoid-height change ~ −0.5 mm/a).

Laurentide Ice Sheet and associated GIA

The amount of additional ice in the Northern Hemisphere necessary to produce the North American GIA signal observed by GRACE lies between 53.2 and 112.5 m ESL (without JPL RL04 between 104 and 127 m ESL), for load model NAWI and fixed earth-model parameters ($h_{\mathrm{L}} = 100\,\mathrm{km}$, $\eta_{\mathrm{UM}} = 6.0 \times 10^{20}$ Pa s and $\eta_{\mathrm{LM}} = 2.0 \times 10^{22}$ Pa s). The bootstrap-estimated mean of 101.2 m ESL (±6%) for all releases is in close agreement with the initial value of 102.2 m supported by the glacial history NAWI. As for the region of Alaska and Greenland, the variability of the values with respect to the chosen time interval is small (~ 3% for GFZ RL04, CNES RL01C and CSR RL04, ~ 14% for JPL RL04), however, biases between releases are large. CNES RL01C

(Figure 6.14) and JPL RL04 (Figure 6.15) show two distinct anomalies east and west of Hudson Bay, presumably caused by GIA. It has been argued that the Laurentide Ice Sheet consisted at some stage of two distinct ice complexes (Peltier, 2004) and, recently, Tamisiea *et al.* (2007) have interpreted the GRACE data in favour of such a scenario. This two-dome structure is not particularly pronounced in the glacial history NAWI, but two GIA centers can also be accommodated by forward models with large upper- and lower-mantle viscosities (Figures B.1 to B.4), if the description of the sea-level equation allows for migration of coastlines (Hagedoorn, 2005). However, GFZ RL04 (Figure 6.13) and CSR RL04 (Figure 6.16) do not exhibit this distinct spatial pattern. The area of the Hudson Bay is a shallow-water region, and models of the ocean tides underlying GRACE processing have low accuracy under these conditions and may produce artefacts. Therefore, more investigations are needed to conclude whether a two-dome ice geometry existed.

Constraint on mantle viscosities

Figure 6.17 shows the sensitivity of the adjustment of load model NAWI with respect to different viscosity values underlying the GIA prediction. Varying the mantle viscosities results in changes in the predicted GIA signal and, therefore, may change the misfit between the data and model. The values indicated represent deviations in the ESL of load model NAWI required to compensate the changes in the predicted GIA to again minimize the misfit. For load model NAWI, a minimum misfit (required scaling of the load $< 2\%$) is achieved for upper- and lower-mantle viscosities ($\eta_{\mathrm{UM}}; \eta_{\mathrm{LM}}$) of $(4 \times 10^{20}; 4 \times 10^{22})$ Pa s for GFZ RL04, $(6 \times 10^{20}; 2 \times 10^{22})$ Pa s for CNES RL01C, and $(8 \times 10^{20}; 1 \times 10^{22})$ Pa s for CSR RL04. For JPL RL04, magnitude of the misfit comparable to those of the other releases is not achieved within the range of plausible viscosity values, which is further indication that this release has some bias.

A possibility to improve the uncertainty with respect to the volume involved in the glacial history is proposed by Paulson *et al.* (2007b). For a set of viscosity parameters, a scaling factor for the glacial history is first estimated with respect to minimizing the misfit between GRACE data and the GIA model. Because unrealistic scaling of the load can be partially compensated employing unrealistic viscosity values and can still provide minimal misfit, it is recommended to limit the scaling of NAWI to a plausible range, which is, however, difficult to quantify. One constraint on NAWI is represented by indicators of eustatic sea-level change suggesting a total sea-level change between 116 and 121 ± 5 m ESL due to ice-sheet melting. The current version of the model contains 102.2 m ESL, while the minimum contribution of Antarctica is estimated to be 9 ± 3 m ESL (Sasgen *et al.*, 2007b). Therefore, upscaling NAWI by at most 17% is possible without violating the estimate of 121 ± 5 m ESL. A down-scaling should be $< 17\%$, because the current sea-level contribution of NAWI and Antarctica results in a value of 112.2 m ESL, which is already below the geological record of 121 ± 5 m ESL. After scale adjustment of the load model, the misfit is evaluated according to

$$\chi^2 := \frac{1}{\mathbf{\Omega}_{\mathrm{S}_\alpha}} \int_{\mathbf{\Omega}_{\mathrm{S}_\alpha}} \left[\frac{V^{\mathrm{GRACE}}(\mathbf{\Omega}) - \hat{V}^{\mathrm{Model}}(\mathbf{\Omega})}{\delta V^{\mathrm{GRACE}}(\mathbf{\Omega})} \right]^2 d\mathbf{\Omega}, \tag{6.5}$$

where $\delta V^{\mathrm{GRACE}}(\mathbf{\Omega})$ is the spatial representation of the GRACE variances (Section A.4). The misfit is then mainly governed by the regional agreements of the spatial patterns. Due to the temporal evolution of the load distribution, spatial patterns of the GIA signal are sensitive to the viscosity distribution. Figure 6.18 shows the misfit of the GIA model and the GRACE data with respect the viscosity distribution. The best fitting viscosity distribution under the condition that the scaling of NAWI is $< 17\%$ is summarized in Table 6.1.

Reference	Load model	Data inverted	Viscosity	
			η_{UM} (Pa s)	η_{LM} (Pa s)
Wolf *et al.* (2006)	ICE-3G	TG, GPS, AG, SLI	3×10^{20}	1.6×10^{22}
Paulson *et al.* (2007b)	ICE-5G	CSR RL04, SLI	5.3×10^{20}	2.3×10^{21}
This study	NAWI	GFZ RL04	4×10^{20}	4×10^{22}
		CNES RL01C	6×10^{20}	2×10^{22}
		CSR RL04	6×10^{20}	2×10^{22}

Table 6.1: Viscosity values obtained from inversion of the GRACE-observed GIA signal over North America. The load models are ICE-3G (Tushingham & Peltier, 1991), ICE-5G (Peltier, 2004) and NAWI (Zweck & Huybrechts, 2005). The data are tide gauges (TG), absolute gravimetry (AG) and indicators of later- or post-glacial relative sea-level change (SLI). The lithosphere thickness h_{L} is held constant at 100 (Wolf *et al.*, 2006, this study) and 120 km (Paulson *et al.*, 2007b).

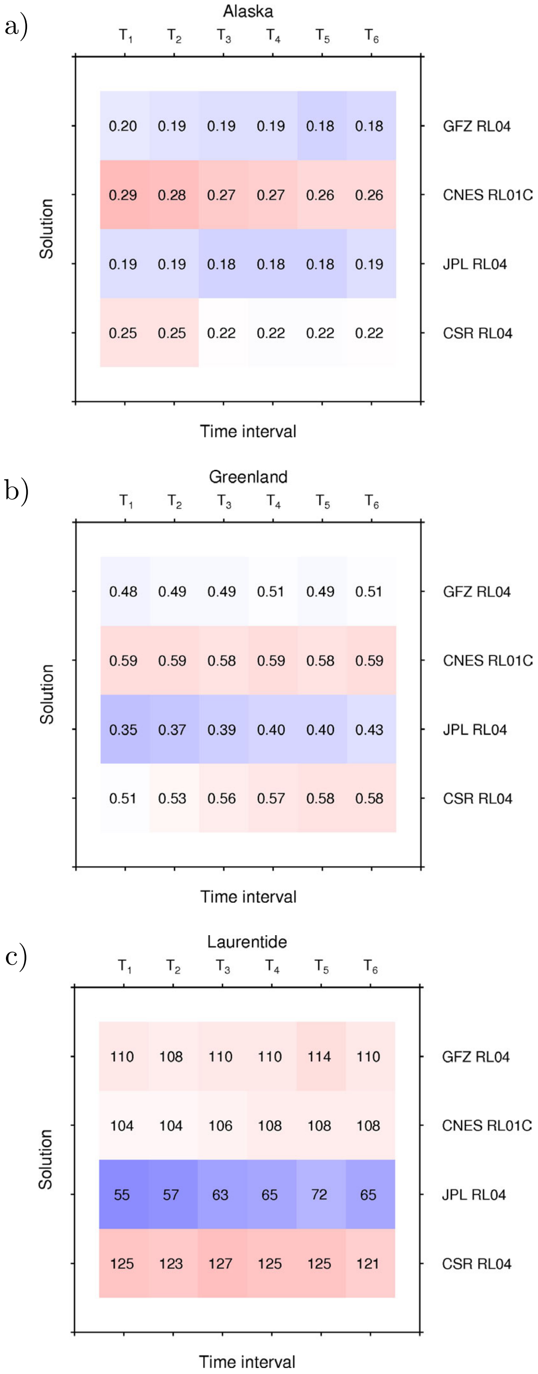

a) Alaska

Solution	T_1	T_2	T_3	T_4	T_5	T_6
GFZ RL04	0.20	0.19	0.19	0.19	0.18	0.18
CNES RL01C	0.29	0.28	0.27	0.27	0.26	0.26
JPL RL04	0.19	0.19	0.18	0.18	0.18	0.19
CSR RL04	0.25	0.25	0.22	0.22	0.22	0.22

b) Greenland

Solution	T_1	T_2	T_3	T_4	T_5	T_6
GFZ RL04	0.48	0.49	0.49	0.51	0.49	0.51
CNES RL01C	0.59	0.59	0.58	0.59	0.58	0.59
JPL RL04	0.35	0.37	0.39	0.40	0.40	0.43
CSR RL04	0.51	0.53	0.56	0.57	0.58	0.58

c) Laurentide

Solution	T_1	T_2	T_3	T_4	T_5	T_6
GFZ RL04	110	108	110	110	114	110
CNES RL01C	104	104	106	108	108	108
JPL RL04	55	57	63	65	72	65
CSR RL04	125	123	127	125	125	121

Figure 6.12: Mass changes in North America and Greenland from four GRACE releases. Present-day ice-mass changes for a) Alaskan glaciers and b) the Greenland Ice Sheet in mm/a ESL, and c) mass change of the Northern Hemisphere ice sheets inferred from the GIA signal over North America in m ESL.

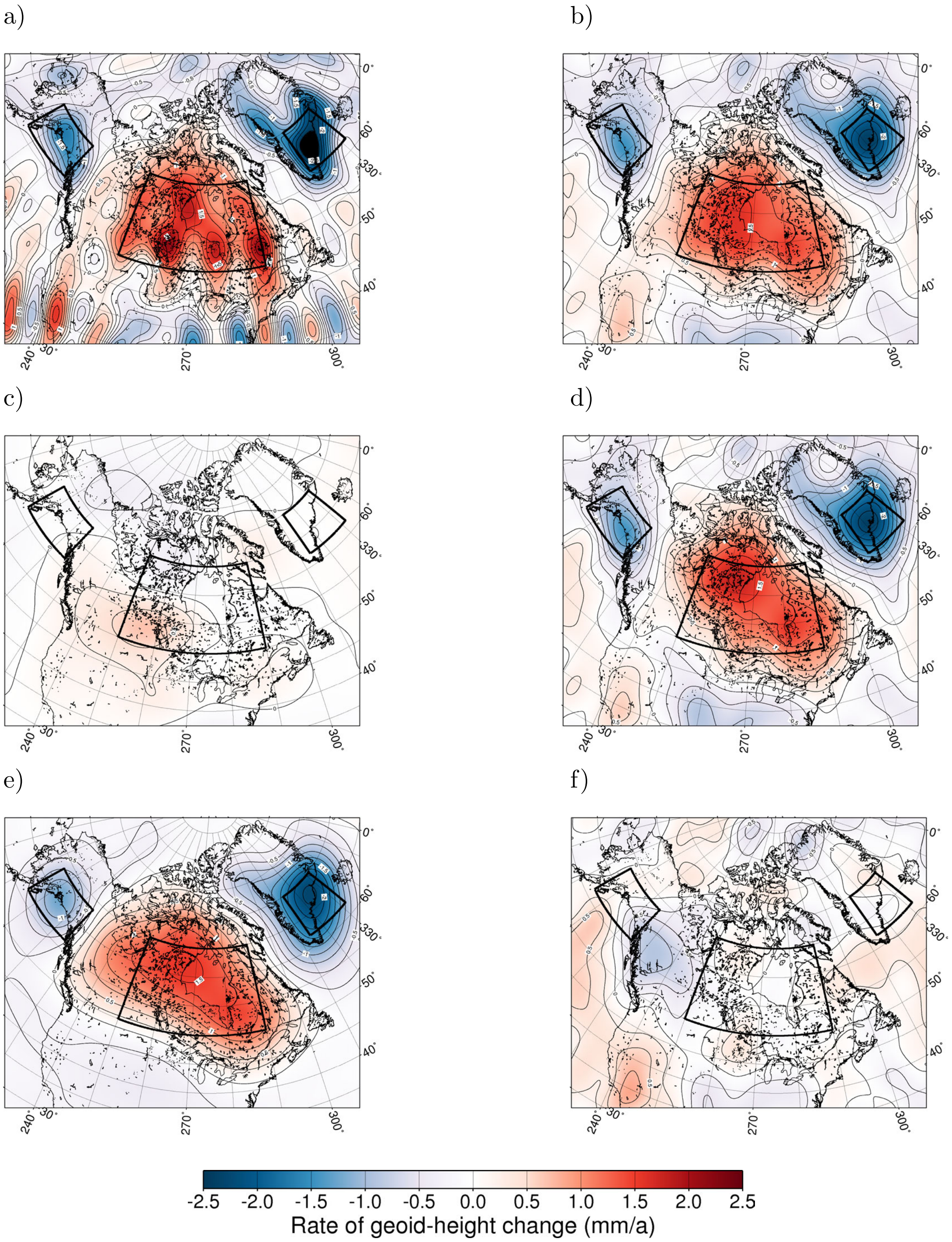

Figure 6.13: Predicted and observed rate of geoid-height change over North America and Greenland for a) GFZ RL04 unfiltered and b) with the statistical filter applied, c) WGHM, d) statistically filtered GFZ RL04 minus WGHM, i.e. b) minus c), e) adjusted models of present-day ice-mass changes and GIA, and f) residuals, i.e. d) minus e).

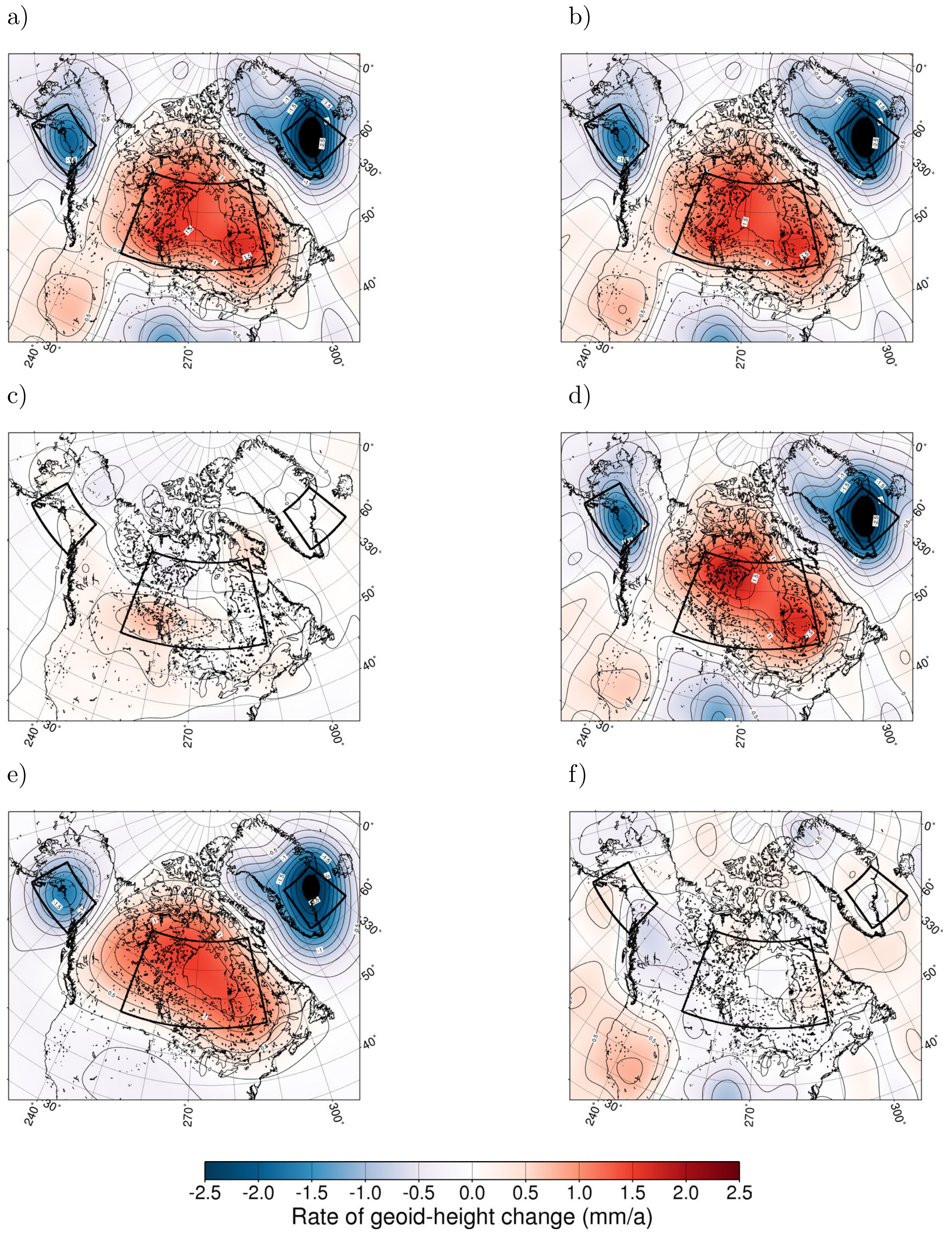

Figure 6.14: The same as Figure 6.13, but for CNES RL01C.

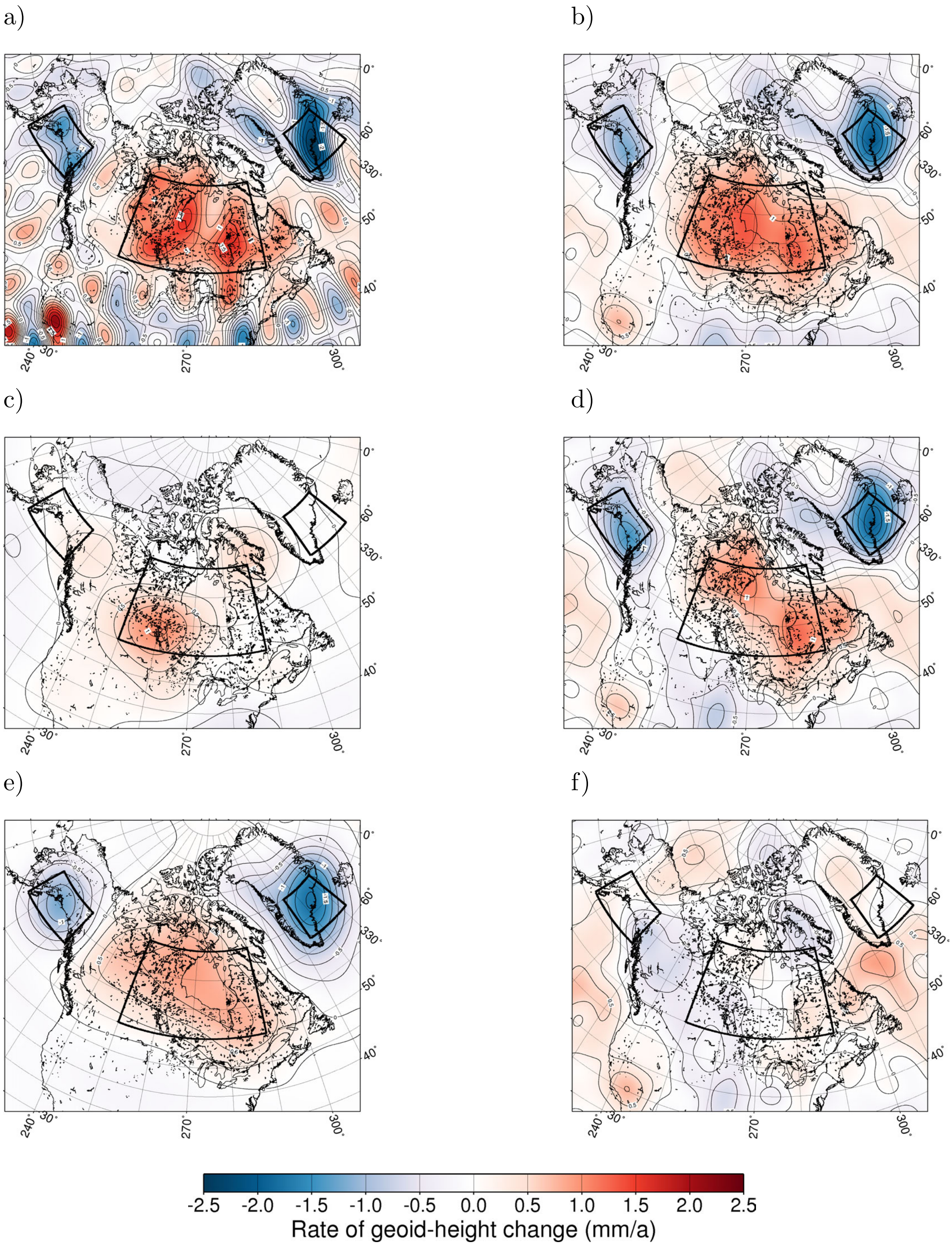

Figure 6.15: The same as Figure 6.13, but for JPL RL04.

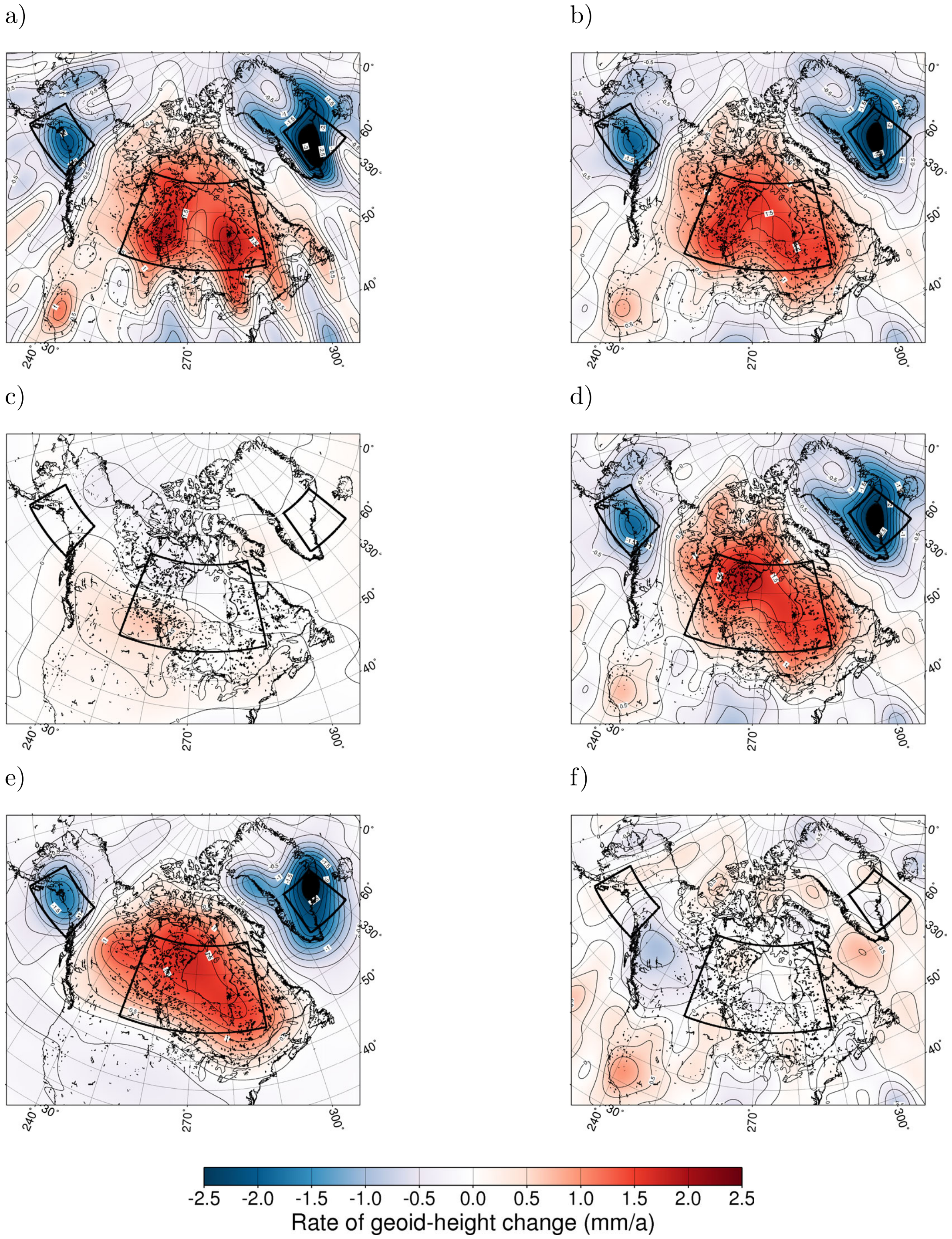

Figure 6.16: The same as Figure 6.13, but for CSR RL04.

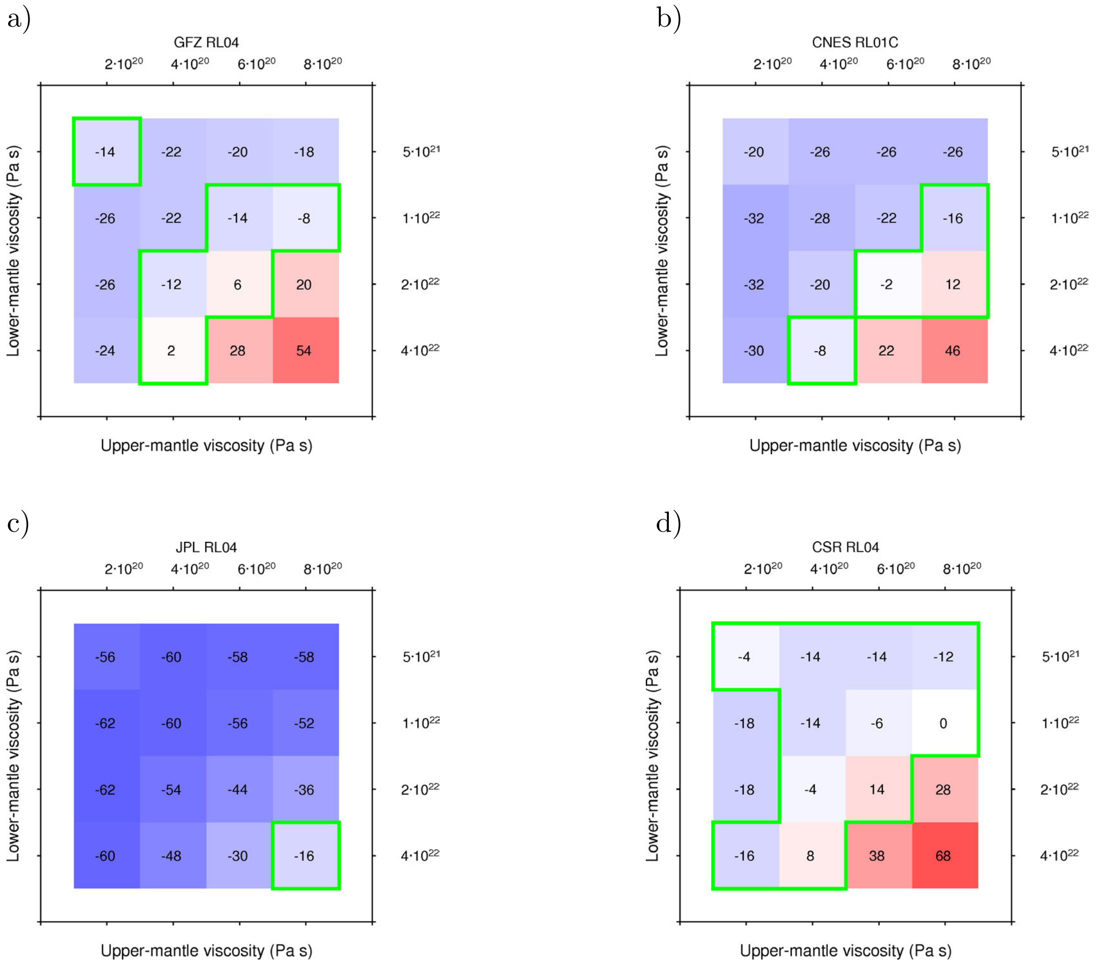

Figure 6.17: Sensitivity of the adjustment of the GIA signal over North America to upper- and lower-mantle viscosities for a) GFZ RL04, b) CNES RL01C, c) JPL RL04 and d) CSR RL04. Values refer to scaling factors determined for load model NAWI in %. Viscosity values that require adjustment of load model NAWI by $< 17\%$ are outlined in green.

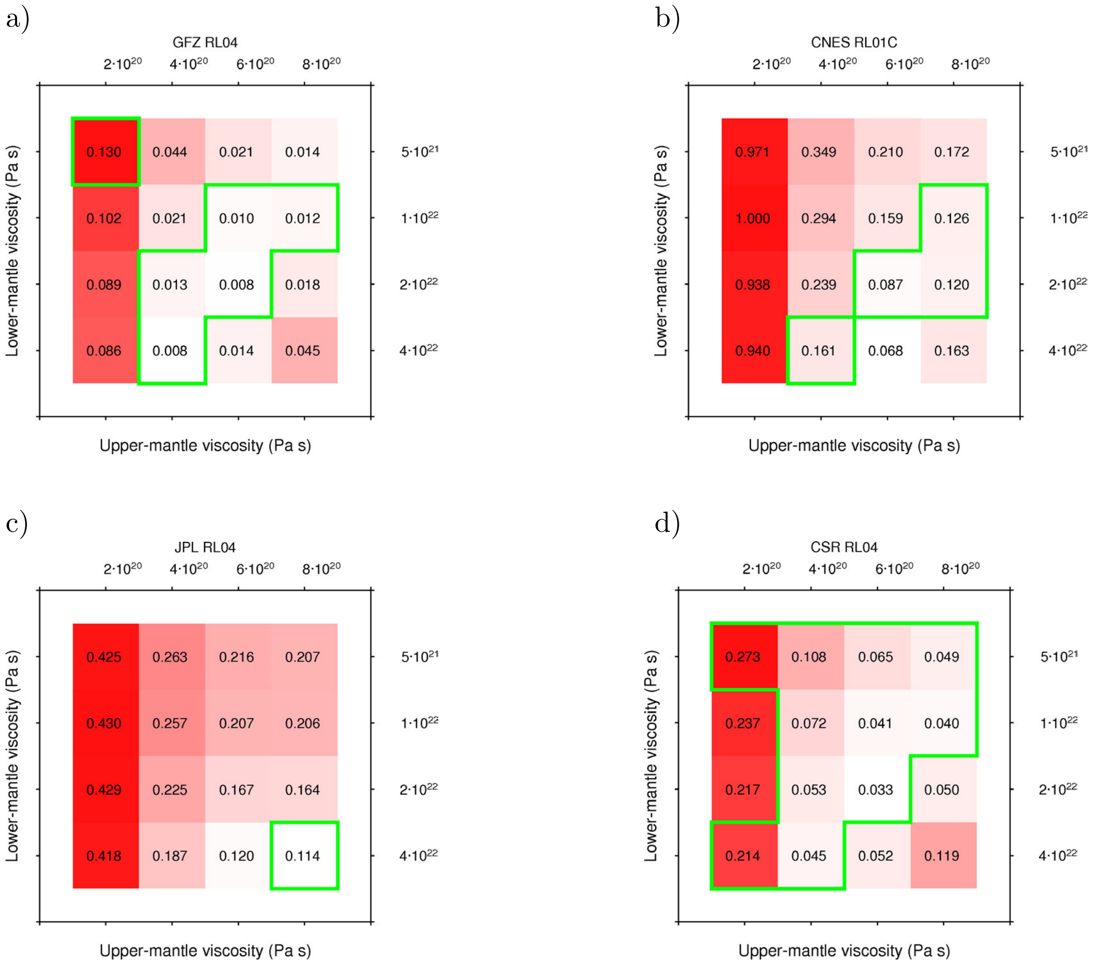

Figure 6.18: Misfit between predicted and observed rate of geoid-height change over North America after scale adjustment of NAWI for a) GFZ RL04, b) CNES RL01C, c) JPL RL04 and d) CSR RL04. Viscosity values that require adjustment of load model NAWI by < 17% are outlined in green.

6.3.5 Concluding remarks

For the Greenland Ice Sheet, accelerating mass loss is observed, which should be considered, for example, as quadratic term in the temporal model. Also, the forward model should be refined to describe individual drainage basins, for which mass changes observed by GRACE can be determined using the constrained inversion presented for West Antarctica in Section 6.4. Over North America, it is required to assess the quality of the hydrological signal of WGHM, at least by employing alternative hydrological models. Glacial histories with a more pronounced two-dome structure (e.g. ICE-5G) should be tested, as very different results of the inversion for mantle viscosities may be obtained. Also, individual deglaciation scenarios for the various Northern Hemisphere ice sheets need to be considered. Linear scaling of the glacial history of the Laurentide Ice Sheet is not adequate due to non-linear coupling between ice and water loads and the Earth's deformation. In contrast to Antarctica, additional constraints on the GIA signal exist (e.g. GPS, tide-gauge, SLI and terrestrial gravimetric data) and should be considered in a joint inversion.

6.4 Combined InSAR and GRACE estimate of West Antarctic glacial changes (*in prep.*)

Abstract[†]

We estimate ice-mass loss in seven drainage basins in West Antarctica from the Gravity Recovery and Climate Experiment (GRACE) data (GFZ RL04, GSM Level 2) using an inverse gravimetric approach. The inversion is constrained by InSAR data to minimize the ambiguity of the resulting mass estimates. We use InSAR observations of the ice-surface velocity as an indication of mass change, assuming that large mass loss occurs in areas of fast glacier flow. From these mass distribution functions we construct forward models of the geoid-height change and their spatial correlations for each drainage basin. Then, the difference between the GRACE data and the forward model is minimized by adjusting the total amount of mass change within each drainage basin. To overcome the ambiguity inherent in this inverse problem, we constrain its solution by including *a priori* InSAR estimates of drainage basins' mass change using the minimization criterion. The amount of constraining (stabilization) is dependent on the uncertainties of the forward model as well as of the GRACE data, for which three error scenarios are investigated. This approach allows the determination of the spatial resolution of GRACE over West Antarctica. We find that unconstrained (GRACE only) mass change estimates are possible to carry out for three to four combined drainage basins. The unconstrained GRACE estimate ($-85.8\,$Gt/a, for the years 2002 to 2007) is lower than the InSAR mass-change rate ($-94.3\,$Gt/a, for the years 1996 and 2000), however, the results from both data sets are in general agreement.

[†] Sasgen, I., Martinec, Z. & Bamber, J., 2008. Combined InSAR and GRACE estimate of West Antarctic glacial changes. *in prep.*

6.4.1 Introduction

The West Antarctic Ice Sheet mostly rests on bedrock below present-day sea level and is therefore considered to be rather unstable and sensitive to global climate changes (e.g. Lemke *et al.*, 2007). Based on data for the last decade, the associated contribution to sea-level change from the West Antarctic Ice Sheet is estimated to be ~ 0.13 to 0.38 mm/a (Shepherd & Wingham, 2007). Its potential contribution to global sea-level change is ~ 5 m (Lythe *et al.*, 2001).

At present, most prominent changes, such as rapid thinning, fast glacier flow and large mass loss, are observed mainly for glaciers and ice streams discharging into Amundsen Sea Embayment and, to a lesser extent, for glaciers further west along the coast towards the Wrigley Gulf. Repeated laser and radar altimetry show decreasing ice-surface elevations (e.g. Davis *et al.*, 2005) and Interferometric Synthetic Aperture Radar (InSAR) records exceptionally high (up to ~ 3 km/a) and in some parts increasing ice-surface velocities (e.g. Thomas *et al.*, 2004). Mass-balance estimates from these measurements indicate that the West Antarctic Ice Sheet loses mass between ∼ 0.13 ± 0.01 (Zwally *et al.*, 2005, for 1992 to 2002) and 0.31 ± 0.15 mm/a (Rignot *et al.*, 2008, for 2006) of equivalent sea-level change.

Recently, data from the Gravity Recovery and Climate Experiment (GRACE) mission (e.g. Tapley *et al.*, 2004a; Tapley *et al.*, 2004; Tapley & Reigber, 2001) have successfully been analyzed to determine the ice sheet's mass balance (Shepherd & Wingham, 2007). The GRACE consists of two satellites lying in near-polar orbits at an altitude of ∼ 450 km. The GRACE satellites are separated by ∼ 200 km and continuously measure their separation by a microwave link with an accuracy at the μm level. This measurement, together with on-board accelerometer measurements of non-gravitational force, star cameras and GPS data of the satellites' orientation and position, respectively, allows the determination of the Earth's gravitational potential with unprecedented accuracy at monthly time intervals (Schmidt *et al.*, 2008). The temporal variations of the gravity field can be inverted for mass changes in the Earth's interior (e.g. Tamisiea *et al.*, 2007; Sasgen *et al.*, 2007b; Paulson *et al.*, 2007b) and on its surface and provide a new method for monitoring the mass balance of the Antarctic Ice Sheet (e.g. Ramillien *et al.*, 2006; Velicogna & Wahr, 2006).

The principal problem of the gravity field inversion for mass changes is that the signals observed are the sum of various sources of mass change. With increasing spatial resolution, lateral overlapping can be reduced, but for the GRACE data, better resolution also implies greater noise (e.g. Jekeli, 1981; Swenson & Wahr, 2002). The globally optimized trade-off between resolution and noise results in a spatial resolution of ∼ 500 km (e.g. Sasgen *et al.*, 2006; Schrama & Visser, 2007), which is largely governed by the altitude of satellites' measurements of the gravitational potential. Additionally, signals arising from on the surface of the Earth (e.g. glacier melting) may overlap with signals arising from within the Earth (e.g. glacial-isostatic adjustment, GIA), and numerical models with additional constraints are required to separate the individual contributions.

In this paper, we determine mass balances of seven West Antarctic drainage basins by the inversion of GRACE gravity fields. We minimize the ambiguity of the resulting mass-change estimates by constraining the inversion with forward models based on InSAR data. We determine the number of drainage basins resolvable by GRACE and provide the associated mass-change estimates. Additionally, combined GRACE and InSAR estimates are given. Throughout this paper, values with the units mm/a refer to the rate of geoid-height change, whereas values with units Gt/a refer to surface-mass changes.

6.4.2 Observations

GRACE data

We use 55 unconstrained GRACE monthly solutions of the Earth's gravity field provided by the German Research Centre For Geosciences (Flechtner, 2005, GFZ RL04, GSM Level 2 data, *[online]*). The time series of Stokes gravitational potential coefficients are complete to degree and order 120 and cover ∼ 5 years from August 2002 to

August 2007. Missing months within this interval are June 2003 (problems with accelerometer data) as well as September 2002, December 2002, January 2003, January 2004 and May 2007 (in preparation at the time of writing). Each Stokes coefficients' time series is decomposed into an annual and semiannual oscillating component, a linear trend and an offset by the method of least squares. After removal of these temporal components, we find that the residual retains quasi-periodic variations with a period of ~ 2.3 a. We attribute these mass changes to inter-annual variations mainly in snow accumulation (a detailed analysis is currently being prepared) and repeat the temporal decomposition by additionally including this term, which reduces the residual's RMS by $\sim 14\%$. During decomposition and throughout this paper, three models of GRACE variances are used: formal (Flechtner, 2005), calibrated (Schmidt *et al.*, 2008) and one based on the residual after removing deterministic signal components (residual). No additional filtering or smoothing is applied. Instead, we repeat our calculations for increasing spherical-harmonic cut-off degrees, such that increasing noise in the GRACE coefficients propagates to the resulting mass-change estimate. Uncertainties at high latitudes are significantly below the global average (e.g. Schmidt *et al.*, 2008) and show less striping, particularly for the temporal trend (Sasgen *et al.*, 2007b; Davis *et al.*, 2008) due to denser track coverage. Therefore, we do not to apply *a priori* smoothing or decorrelation filtering (Swenson & Wahr, 2006), but consider the regional noise characteristics during the inversion.

InSAR data

We use ice-surface velocities from InSAR (Figure 6.19) as an indication of the spatial distribution of mass changes in the Amundsen Sea Sector (Rignot *et al.*, 2008). The InSAR data covers nearly all of the drainage basins in the Amundsen Sea Sector, i.e. Pine Island Glacier (PIG), Thwaites (THW), Haynes/Smith/Kohler (HSK), Getz (GET) and DeVicq (DVQ). For Hull (HUL) and Land (LAN), which are not completely covered by this InSAR data set, modelled balance velocities are used (Rignot & Thomas, 2002). In addition, mass-budget estimates of the drainage basins' mass balance derived from this data set are used (Rignot *et al.*, 2008) (Table 6.2 and Table 6.2). The values represent the difference between average accumulation (input) for the years 1980 to 2004 obtained from regional atmospheric climate modelling for Antarctica (RACMO2/ANT, van den Broeke *et al.*, 2006a; van de Berg *et al.*, 2006; van den Broeke *et al.*, 2006b), whereas outflow is calculated from InSAR measured ice-flow velocity over the grounding line for the years 1996 (GET, DVQ, HUL and LAN) and 2000 (PIG, THW and HSK). The thickness of the ice along the grounding line and its position are determined from digital elevation models and InSAR, respectively. Flow velocity is assumed to be constant for the ice column above the grounding line. The main uncertainty arising from the mass-budget method is associated with the input (accumulation) estimate and amounts to $\sim 10\%$ for dry, large basins and to $\sim 30\%$ for wet, small basins in the vicinity of the coast; outflow uncertainties lie between 2 to 15% (Rignot *et al.*, 2008).

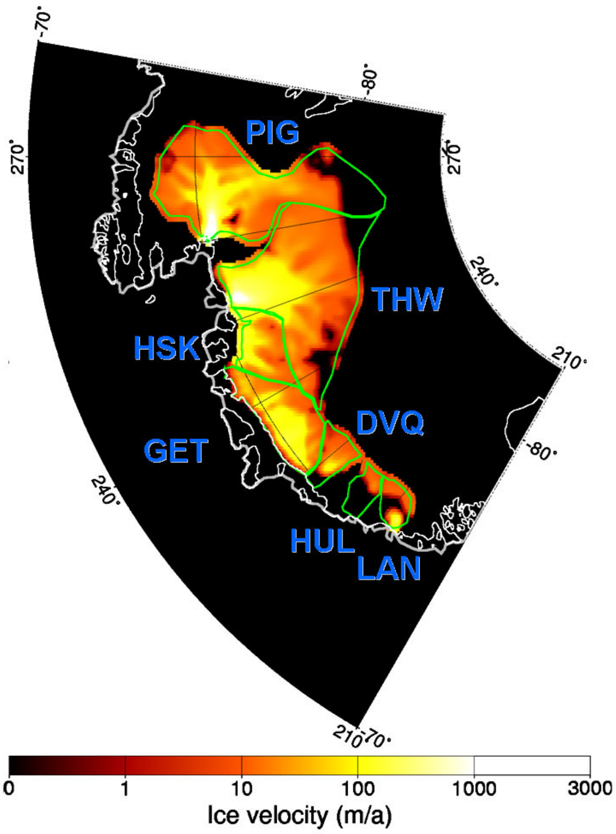

Figure 6.19: Ice-surface velocity in the Amundsen Sea Sector from InSAR (Rignot *et al.*, 2008). The drainage basins (green outlined) are Pine Island Glacier (PIG), Thwaites (THW), Haynes/Smith/Kohler (HSK), Getz (GET), DeVicq (DVQ), Hull (HUL) and Land (LAN).

6.4.3 GIA correction

We subtract the trend in the gravity field caused by GIA in Antarctica, y^{GIA}, from the GRACE observation, y^{GRACE} (Figure 6.20). GIA is modelled using the viscoelastic earth model of Martinec (2000) consisting of an elastic lithosphere of thickness $h_{\mathrm{L}} =$ 100 km, an upper mantle of viscosity $\eta_{\mathrm{UM}} = 5.2 \times 10^{20}$ Pa s, a lower mantle of viscosity $\eta_{\mathrm{LM}} = 5.9 \times 10^{21}$ Pa s and a fluid core. The earth model is subjected to the glacial history of the Antarctic Ice Sheet for the last 120 ka based on the thermomechanical ice-sheet model of Huybrechts (2002) (HUY). Following Sasgen *et al.* (2007b), HUY was scaled to an Antarctic contribution to sea-level change since the Last-Glacial Maximum (LGM) of 9 m, such that the predicted GIA amplitude over the Ronne Ice Shelf (*ca.* 1.5 mm/a, full spectral range) agrees with the GRACE observations for the viscosity structure specified above. Over the Amundsen Sea Sector, GIA due to HUY is less important (*ca.* <1 mm/a, full spectral range). Similar amplitudes are also obtained using the geomorphologic reconstruction of Lambeck & Chappell (2001)

(ANU). Regional details of Paleocene and Holocene ice retreat in the Amundsen Sea Sector that may have induced a local GIA signal are not sufficiently well known to be included in this modelling. Instead, differences between the deglaciation scenarios HUY and ANU are investigated. For comparison, we also calculate mass-change estimates without GIA corrections, as well as a minimum and maximum estimates. In the following, the GIA corrected trend in the GRACE gravity fields (Figure 6.20) is denoted as

$$y(\mathbf{\Omega}) = y^{\mathrm{GRACE}}(\mathbf{\Omega}) - y^{\mathrm{GIA}}(\mathbf{\Omega}), \tag{6.6}$$

where $\mathbf{\Omega} := (\vartheta, \varphi)$ are the spherical colatitude ϑ and longitude φ.

6.4.4 Forward modelling of gravity-field changes

We model the trend in the gravity field arising from mass changes in $k = 1, 2, ..., 7$ drainage basins in the Amundsen Sea Sector (PIG, THW, HSK, GET, DVQ, HUL and LAN, Figure 6.19) by allocating their total mass change, $\mathbf{m} = \{\mathrm{m}_k\}_{k=1,2,...,7}$, according to the spatial mass-distribution function $\mathbf{w}(\mathbf{\Omega})$. Inside each basin, $\mathrm{w}_k(\mathbf{\Omega})$ is linearly proportional to the ice-surface velocity from InSAR (Figure 6.19), outside the basin $\mathrm{w}_k(\mathbf{\Omega}) = 0$. The underlying assumption is that mass loss in the Amundsen Sea Sector predominantly occurs in areas of fast glacier flow, which is supported by empirical and theoretical evidence (Rignot *et al.*, 2008).

We normalize the spatial mass distribution function according to $\int_{\mathbf{\Omega}_0} \mathrm{w}_k(\mathbf{\Omega}) d\mathbf{\Omega} = 1$ for all k and expand it to the fully normalized spherical harmonics of degree j and order m, $Y_{jm}(\mathbf{\Omega})$, where $\mathbf{w}(\mathbf{\Omega}) = \mathbf{w}_{jm} Y_{jm}(\mathbf{\Omega})$. Then, for each drainage basin, the normalized geoid-height change $\mathbf{x}(\mathbf{\Omega}) = \{x_k(\mathbf{\Omega})\}_{k=1,2,...,7}$ is calculated by

$$x_k(\mathbf{\Omega}) = \frac{R^2}{g_0} \sum_{j_{\min}}^{j_{\max}} q_j \frac{4\pi}{2j+1} \sum_m \mathrm{w}^k_{jm} Y_{jm}(\mathbf{\Omega}), \tag{6.7}$$

where R is the radius of the Earth, g_0 the gravity at the Earth's surface, and q_j are the elastic-compressible surface-load Love numbers (e.g. Farrell, 1972). Multiplication of each drainage basin's normalized geoid-height change signal $x_k(\mathbf{\Omega})$ with its total mass change m_k and subsequent superposition of signals results in the forward gravity model for the entire Amundsen Sea Sector (Figure 6.20),

$$y^{\mathrm{P}}(\mathbf{\Omega}) = \sum_k x_k(\mathbf{\Omega}) m_k. \tag{6.8}$$

Table 6.2 lists the InSAR-based mass-change estimates, $\mathbf{m}$, along with their uncertainties $\sigma = \{\sigma_k\}_{k=1,2,...,7}$. As a consequence, the forward model's uncertainties are described by the *a priori* covariance matrix, $\mathbf{C}_{\mathrm{M}} = \gamma_{kl}\sigma_k\sigma_l$, where γ_{kl} is the spatial correlation (e.g. Gubbins, 2004) between the drainage basins' signals of geoid-height change, $\gamma_{kl} := \mathrm{corr}(x_k(\mathbf{\Omega}), x_l(\mathbf{\Omega}))$.

Figure 6.21 shows the correlations of the forward models γ_{kl} of the seven drainage basins for upper spherical-harmonic cut-off degrees $j_{\max} = 30$, 55 and 80, which are ordered according to their geographical proximity. As expected, increasing the cut-off degree reduces correlations between signals. At cut-off degree 30, the correlation matrix shows ~two distinct blocks (green outline in Figure 6.21), consisting of the drainage basins PIG, THW, HSK and the drainage basins GET, DVQ, HUL and LAN, respectively. This suggests that mass changes derived from the gravity field can be retrieved for these regions independently. At cut-off degree 55, combined signals from ~four regions are resolvable. However, even at cut-off degree 80, significant overlaps between the seven drainage basins' signals exist, which may lead to ambiguous and unrealistic results of the gravity-field inversion.

6.4.5 Inversion of the gravity-field changes

We aim at finding the mass-change distribution in the Amundsen Sea Sector that produces the gravity-field change $y(\mathbf{\Omega})$ observed by GRACE ((6.6)), such that $\|y(\mathbf{\Omega}) - y^{\mathrm{P}}(\mathbf{\Omega})\|$ is minimized, where $y^{\mathrm{P}}(\mathbf{\Omega})$ is the forward gravity model in (6.8). We formulate this inverse problem in terms of the design matrix $\mathbf{F}$, which consists of the normalized geoid-height change arising from the k-th drainage basin at the i-th spatial grid point, $\mathbf{\Omega}_i$, $i = 1, 2, ..., N$ (here, a 0.25°×0.25° grid), $\mathbf{F} = \{x_k(\mathbf{\Omega}_i)\}_{i=1,2,...,N}^{k=1,2,...,7}$. Then, the spatially gridded forward model is expressed by $\mathbf{y}^{\mathrm{P}} = \{y^{\mathrm{P}}(\mathbf{\Omega}_i)\}_{i=1,2,...,N} = \mathbf{Fm}$ and the L_2-norm minimization criterion takes the form

$$(\mathbf{y} - \mathbf{y}^{\mathrm{P}})^2 \overset{!}{=} \min_{\mathbf{m}}. \tag{6.9}$$

The inversion of GRACE data for mass changes is non-unique and unstable due to the limited resolution of the GRACE data and the smoothing (integral) property of the measured gravitational potential, which is visible from (6.7). The system of equations resulting from (6.9) is possibly underdetermined and it may be necessary to stabilize its solution by including *a priori* constraints on the parameterized total mass change $\mathbf{m}$ and their uncertainties σ. This constrained solution is given by (e.g. Gubbins, 2004; Tarantola, 2005)

$$\tilde{\mathbf{m}}_{\mathrm{c}} = \mathbf{m} + (\mathbf{F}^{\mathrm{T}}\mathbf{C}_{\mathrm{D}}^{*-1}\mathbf{F} + \mathbf{C}_{\mathrm{M}}^{-1})^{-1}\mathbf{F}^{\mathrm{T}}\mathbf{C}_{\mathrm{D}}^{*}(\mathbf{y} - \mathbf{Fm}), \tag{6.10}$$

where $\mathbf{C}_{\mathrm{D}}^{*} = \mathbf{C}_{\mathrm{GRACE}} + \mathbf{C}_{\mathrm{GIA}}$ is the covariance matrix of the data, which consists of GRACE uncertainties as well as of the GIA uncertainties discussed later, and T denotes matrix transposition.

The amount of *a priori* information included in the inversion is governed by the balance between data and model variances. It can be quantified by the resolution matrix, $\mathbf{R} = \mathbf{I} - \tilde{\mathbf{C}}_{\mathrm{M}}\mathbf{C}_{\mathrm{M}}{}^{-1}$, where $\tilde{\mathbf{C}}_{\mathrm{M}}$ represents the *a posteriori* parameter covariances of the GRACE+InSAR model given by $\tilde{\mathbf{C}}_{\mathrm{M}} = (\mathbf{F}^{\mathrm{T}}\mathbf{C}_{\mathrm{D}}^{*-1}\mathbf{F} + \mathbf{C}_{\mathrm{M}}^{-1})^{-1}$ (e.g. Gubbins, 2004; Tarantola, 2005). The trace of the resolution matrix, $tr\mathbf{R}$, is commonly interpreted as the number of parameters resolved by the data (here, the GRACE data),

$$tr\mathbf{R} = tr\mathbf{I} - tr(\tilde{\mathbf{C}}_{\mathrm{M}}\mathbf{C}_{\mathrm{M}}{}^{-1}), \tag{6.11}$$

whereas $tr\mathbf{I}$ and $tr(\tilde{\mathbf{C}}_{\mathrm{M}}\mathbf{C}_{\mathrm{M}}{}^{-1})$ are the total number of parameters (here, seven drainage basins) and the number of parameters constituted by *a priori* information (here, the InSAR model), respectively.

The spatial representation of the GRACE variances, $\mathbf{C}_{\mathrm{GRACE}}$, is calculated from the uncertainties of the Stokes potential coefficients according to $e_i^2 = \sum_{jm} \sigma_{jm}^2 Y_{jm}^2(\mathbf{\Omega}_i)$. Covariances are not considered, such that $\mathbf{C}_{\mathrm{GRACE}} = \mathbf{eIe}^{\mathrm{T}}$, where $\mathbf{I}$ is the identity matrix and $\mathbf{e} = \{e(\mathbf{\Omega}_i)\}_{i=1,2,\ldots,N}$. As mentioned above, we use estimates of σ_{jm}^2 based on formal, calibrated and residual GRACE errors.

The uncertainty of the GIA correction, $\mathbf{C}_{\mathrm{GIA}}$, is assumed to be proportional to its magnitude, $e_i = \beta \mathbf{y}_i^{\mathrm{GIA}}$, where constraints on Antarctic GIA from various GRACE data sets indicate $\beta \approx 0.2$ (Sasgen *et al.*, 2007b). Also, covariances in $\mathbf{C}_{\mathrm{GIA}}$ are assumed to be zero, such that $\mathbf{C}_{\mathrm{GIA}} = \mathbf{eIe}^{\mathrm{T}}$.

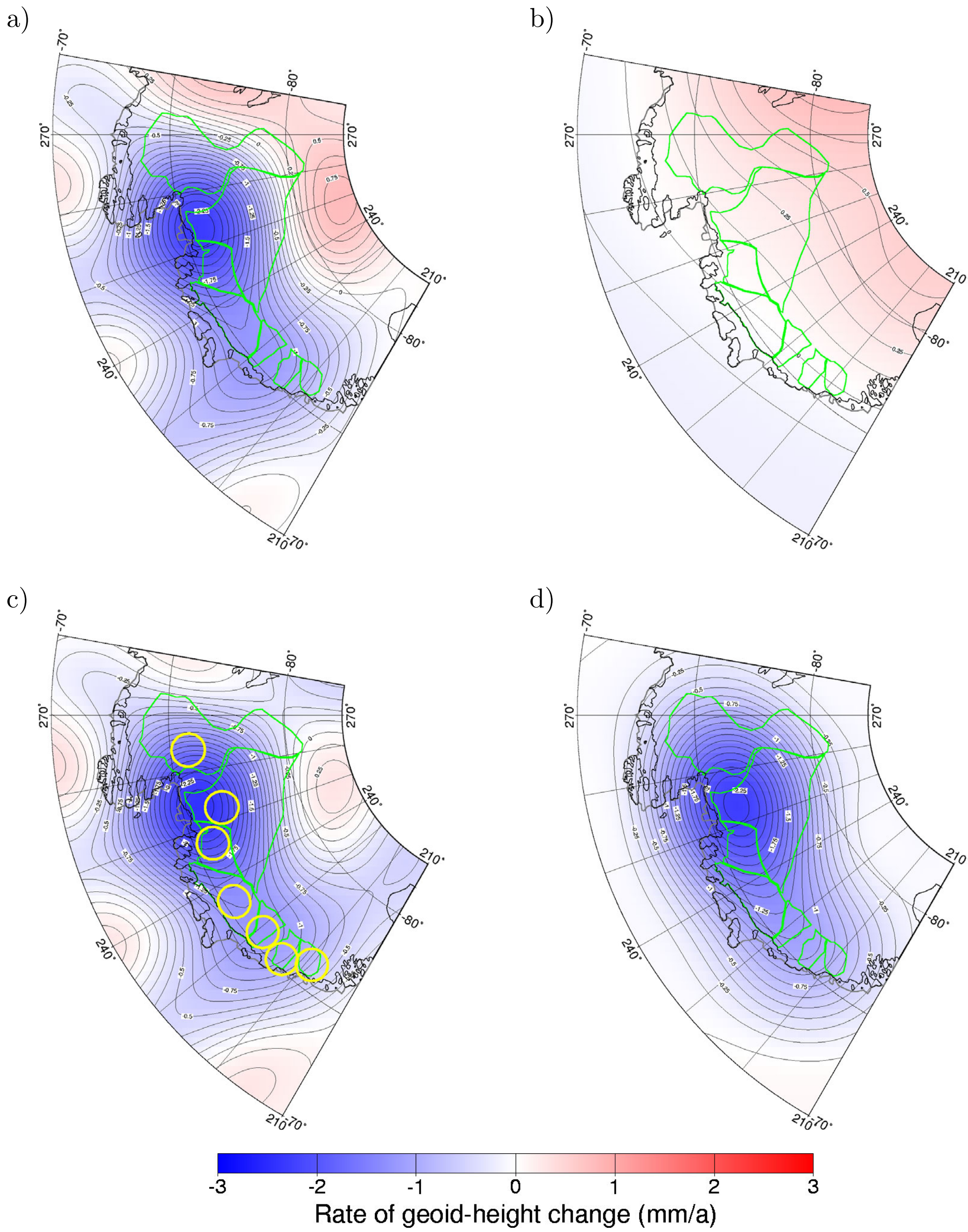

Figure 6.20: Predicted and observed rate of geoid-height change over West Antarctica for (a) GFZ RL04 (without GIA correction), (b) GFZ RL04 with GIA correction, (c) GFZ RL04 minus GIA correction, and (d) optimal forward model based on combined InSAR and GRACE data. The cut-off degrees are $j_{\min} = 7$ and $j_{\max} = 55$. The yellow circles indicate the area used for the adjustment of the forward model.

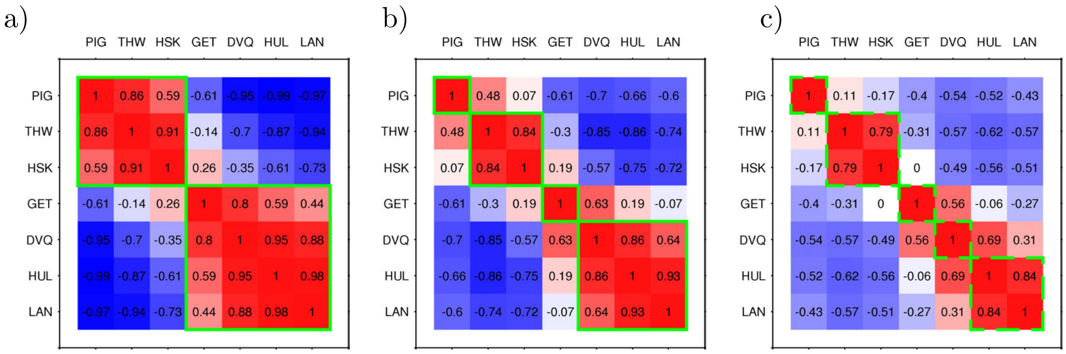

Figure 6.21: Correlation of model parameters for cut-off degrees $j_{\min} = 7$ and (a) $j_{\max} = 30$, (b) $j_{\max} = 55$ and (c) $j_{\max} = 80$.

6.4.6 Results

Influence of cut-off degree and GIA correction

Figure 6.22 shows the total mass change for all Amundsen Sea Sector drainage basins, $\sum_{k=1}^{7} m_k$, for the unconstrained (dashed, GRACE) and constrained (solid, GRACE-+InSAR) inversion. With GIA correction (green for HUY and blue for ANU), resulting mass changes are largely constant for cut-off degrees between 30 and 60, lying within $\sim 3\%$ of their mean. Above degree 60, the mass-loss signal is increasingly degraded by noise in the GRACE data.

The insensitivity of the results with respect to the chosen cut-off degree indicates that the forward model and GRACE data have similar spectral characteristics. This suggests that GIA (which is not part of the forward model) has been successfully removed from the GRACE data. It also verifies that mass biases are not introduced by limiting our analysis to a given spectral range. For comparison, without GIA correction in (6.6), unconstrained estimates (dashed red line) show significant biases, particularly for the lower degrees, for which the GIA signal has the largest amplitude.

For cut-off degrees 40 to 60, unconstrained mass-change rates range between -78 and $-86\,\mathrm{Gt/a}$, or $\sim 5\%$ around their mean, when correcting with the minimum and maximum GIA prediction for HUY (grey shaded area). This GIA uncertainty estimate is conservative and encompasses values obtained when using the ANU model, as well as when varying the upper- and lower-mantle viscosities between 4×10^{20} and $8 \times 10^{20}\,\mathrm{Pa\,s}$, and 5×10^{21} and $4 \times 10^{22}\,\mathrm{Pa\,s}$, respectively, for the HUY model. Constraining the inversion with InSAR mass-budget estimates according to (6.10) leads to stronger negative mass loss rates between ~ -83 and $-88\,\mathrm{Gt/a}$, which are closer estimates based on InSAR data only of $\sim -94.3 \pm 18.5\,\mathrm{Gt/a}$.

Resolvability of individual drainage basins

Figure 6.23 shows the number of parameterized drainage basins resolved by the GRACE data for cut-off degrees between 30 and 80, which is calculated according to (6.11). For calibrated GRACE uncertainties (green), the number of drainage basins resolved increases from ~ two at cut-off degree 30 to a maximum of ~ four at cut-off degree 50 and remains constant until degree 80. At cut-off degree ~ 42, GRACE and InSAR constitute ~ three and a half drainage basins each, meaning that both data sets are combined in the inversion with approximately equal weights. With the more pessimistic model of GRACE uncertainties based on the residual (blue), not more than ~ three drainage basins can be resolved. For formal GRACE uncertainties (red), which are currently too optimistic but represent the announced mission accuracy, at most five drainage basins can be resolved. We conclude that GRACE data alone does not allow the determination of individual mass change estimates for all seven drainage basins in the Amundsen Sea Sector.

Mass change for four combined drainage basins

With regard to the GRACE resolution for calibrated uncertainties (Figure 6.23), we combine the seven drainage basins to four. This is done by merging drainage basins with high signal correlations γ_{kl} in the forward model (Figure 6.21), i.e. PIG,

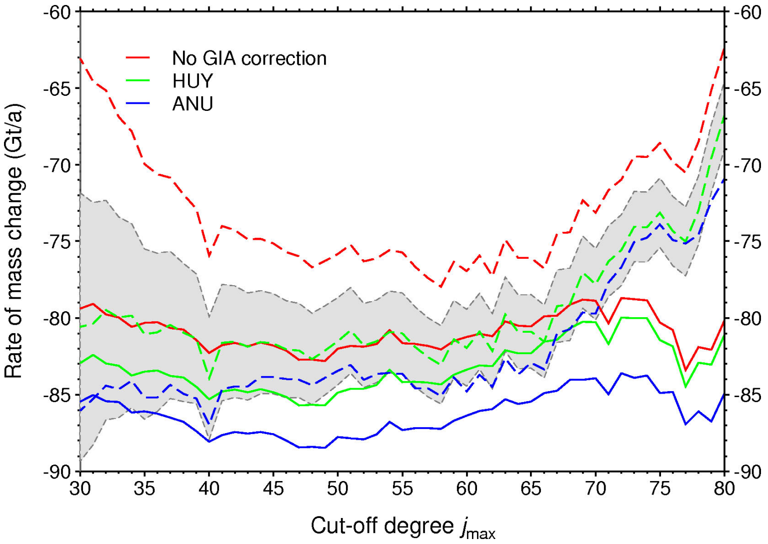

Figure 6.22: Mass change in the Amundsen Sea Sector obtained by constrained (solid) and unconstrained (dashed) inversion of GRACE gravity fields without GIA correction (red) as well as with GIA corrections based on HUY (green), minimum|maximum HUY (grey-shaded area, unconstrained solution) and ANU (blue) for cut-off degrees $j_{\max} = 30$ to 80.

THW|HSK, GET and HUL|DVQ|LAN. The GRACE spatial resolution for the independent retrieval of the mass signal for these four drainage basins is equivalent to $\sim 200\,\mathrm{km}$. For the reduced number of parameters (i.e. $k \lesssim \mathrm{tr}\mathbf{R}$), the unconstrained solution of the inverse problem is about equal to the constrained solution and given by $\tilde{\mathbf{m}}_{\mathrm{u}} = (\mathbf{F}^{\mathrm{T}}\mathbf{C}_{\mathrm{D}}^{*-1}\mathbf{F})^{-1}\mathbf{F}^{\mathrm{T}}\mathbf{C}_{\mathrm{D}}^{*}\mathbf{y}$.

Table 6.2 lists mass changes for the four merged drainage basins obtained from InSAR (Rignot *et al.*, 2008), GRACE and combined GRACE+InSAR data for cut-off degree 55. Uncertainties are calculated according to $\tilde{\sigma}_{\mathrm{c|u}} = \sqrt{\mathrm{diag}(\tilde{\mathbf{C}}_{\mathrm{M}})}$. We find that independent estimates of InSAR and GRACE data compare well, particularly for HUL|DVQ|LAN, and lie within ~4 Gt/a around their combined estimates. An exception is GET, for which InSAR indicates a mass loss of $-11.1\,\mathrm{Gt/a}$, however, with an uncertainty of $18.3\,\mathrm{Gt/a}$, whereas GRACE suggests values close to 0 ($-0.5 \pm 0.9\,\mathrm{Gt/a}$). For GET, the combined GRACE+InSAR estimate of $-1.2 \pm 0.9\,\mathrm{Gt/a}$ is closer to the GRACE estimate due to a weak constraint by a large uncertainty of the InSAR data.

Mass change for seven drainage basins

The mass changes for all seven seven drainage basins based on InSAR and GRACE+InSAR data for cut-off degree 55 are shown in Table 6.3. For this number of drainage basins, the inversion of GRACE data is unstable (values of neighboring drainage basins oscillate between $\sim \pm 40\,\mathrm{Gt/a}$); results are therefore not shown. Stabilization overcomes these ambiguities and leads to similar values for InSAR and GRACE+InSAR esti-

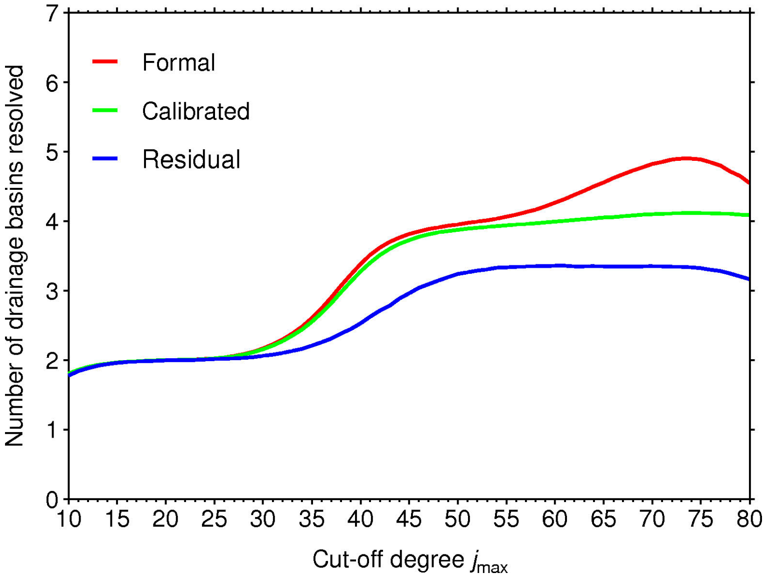

Figure 6.23: Number of parameters resolved by GRACE for cut-off degrees $j_{\max} = 30$ to 80 and formal, calibrated and residual GRACE uncertainties.

mates, with differences below ~4 Gt/a. As for the four previous drainage basins, an exception is GET, for which the combined estimate of -3 ± 0.8 Gt/a lies ~8 Gt/a below the InSAR value.

6.4.7 Discussion

Total mass change in the Amundsen Sea Sector estimated from GRACE is -85.8 ± 1.5 Gt/a (Table 6.2), which is somewhat lower than the value of -94.3 ± 18.5 Gt/a from InSAR, yet within its uncertainty. For the constrained inversion (GRACE+InSAR, Table 6.3), mass loss is -87.0 ± 1.2 Gt/a and lies within the range of the independent InSAR and GRACE values. The largest uncertainty in the InSAR mass budget relates to GET, for which errors in accumulation and outflow are exceptionally large. Neglecting this drainage basin, reconciles InSAR (-86.6 ± 2.7 Gt/a) and GRACE (-85.8 ± 1.5 Gt/a) estimates within their respective uncertainties.

An overestimation of mass loss by InSAR for GET may be a consequence of larger accumulation within the GRACE time interval (years 2002 to 2007) compared to the mean for the years 1980 to 2004. Interannual variations in accumulation rate with respect to the mean are estimated to ~15% (Shepherd & Wingham, 2007) and may therefore compensate the drainage basins' imbalances by increased outflow (~10 to 50%). On the other hand, GRACE may underestimate mass loss if the GIA signal subtracted is too low in amplitude, although corrections in excess of an additional -5 Gt/a are not supported by our GIA models (Figure 6.22). Also, there is evidence of accelerating outflow of PIG, THW, and HSK for the years 1974 to 2007 from InSAR, which should in future be considered as, for example, a quadratic term in the temporal decomposition of the GRACE time series.

6.4.8 Conclusion

We used forward models based on InSAR data to constrain the inversion of GRACE gravity fields for mass changes of seven West Antarctic drainage basins. We analysed the GRACE resolution over the Amundsen Sea Sector and found that unconstrained (GRACE only) mass balance estimates are possible for three to four combined drainage basins. For these basins, results lie within $\sim \pm 4\,\mathrm{Gt/a}$ of the InSAR estimates. An exception is GET, for which GRACE indicates no significant imbalance as opposed to large values inferred from InSAR. This deviation introduces somewhat lower mass-loss rates for the entire Amundsen Sea Sector of $-85.5 \pm 1.5\mathrm{Gt/a}$ (for the years from 2002 to 2007) based on GRACE compared to $-94.3 \pm 1.5\,\mathrm{Gt/a}$ based on InSAR (outflow measurements for the years 1996 and 2000). The difference may arise from the underestimation of accumulation in the InSAR data and/or a too small GIA correction applied to GRACE. Finally, we combined InSAR and GRACE data for the seven drainage basins with about equal weights, resulting in a mass loss of $-87.0 \pm 1.2\,\mathrm{Gt/a}$ for the entire Amundsen Sea Sector.

Drainage basin			InSAR		GRACE		GRACE + InSAR	
	Area ($10^3\mathrm{km}^2$)	Year	m (Gt/a)	σ (Gt/a)	$\tilde{m}_\mathrm{u}$ (Gt/a)	$\tilde{\sigma}_\mathrm{u}$ (Gt/a)	$\tilde{m}_\mathrm{c}$ (Gt/a)	$\tilde{\sigma}_\mathrm{c}$ (Gt/a)
PIG	164.0	2000	-23.7	1.5	-19.8	0.7	-21.5	0.7
THW|HSK	218.4	2000	-38.0	3.8	-43.3	0.7	-42.2	0.7
GET	92.1	1996	-11.1	18.3	-0.5	0.9	1.2	0.9
DVQ|HUL|LAN	43.0	1996	-21.6	3.5	-22.1	0.7	-21.7	0.7
Total	517.5		-94.3	19.1	-85.8	1.5	-86.7	1.5

Table 6.2: Ice-mass change for four combined drainage basins in the Amundsen Sea Sector. For InSAR data, the year of the outflow measurement is indicated. The mid-point of the time interval for the GRACE data is 2004/2005. Calibrated GRACE errors and cut-off degrees $j_\mathrm{min} = 7$ and $j_\mathrm{max} = 55$ are used.

Drainage basin			InSAR		GRACE + InSAR	
	Area ($10^3\mathrm{km}^2$)	Year	m (Gt/a)	σ (Gt/a)	$\tilde{m}_\mathrm{c}$ (Gt/a)	$\tilde{\sigma}_\mathrm{c}$ (Gt/a)
PIG	164.0	2000	-23.7	1.5	-21.9	0.4
THW	181.9	2000	-22.1	1.9	-22.5	0.3
HSK	36.5	2000	-15.9	3.3	-19.0	0.4
GET	92.1	1996	-11.2	18.3	-3.0	0.8
DVQ	16.0	1996	-14.0	2.8	-11.7	0.5
HUL	14.2	1996	-3.7	1.5	-3.9	0.1
LAN	12.8	1996	-3.9	1.5	-5.1	0.3
Total	517.5		-94.3	19.0	-87.0	1.2

Table 6.3: Ice-mass change for 7 drainage basins in the Amundsen Sea Sector. For InSAR data, the year of the outflow measurement is indicated. The mid-point of the time interval for the GRACE data is 2004/2005. Calibrated GRACE errors and cut-off degrees $j_\mathrm{min} = 7$ and $j_\mathrm{max} = 55$ are used.

7

Summary

In this study, the GRACE time series of potential coefficients was used to quantify present-day ice-mass changes and their associated sea-level change, as well as GIA in the polar regions.

The work included the development of the Wiener optimal filter for GRACE data. The filter is isotropic, and its filter function resembles a Gaussian function in the spatial domain. Its width, however, is adaptive to signal-to-noise ratio of the GRACE potential coefficients and, therefore, allows the determination of an optimal spatial half-width for individual monthly solutions as well as for the temporal components extracted from the time series of GRACE solutions. For monthly solutions of standard quality (e.g. April 2004), the Wiener optimal filter function is largely equivalent to a 4^o-Gaussian filter function; for months with poor quality (e.g. September 2004), it is $\sim 6^o$. Correlations between the GRACE coefficients' errors were not considered, and a future generalization of the theory for anisotropic filter functions may enhance the filter's performance. Another improvement can be made by the regionalization of the filter using local base functions instead of spherical harmonics.

Another possibility for geophysical-signal extraction was presented with the statistical filtering, which tests, for each coefficient's time series, the significance of deterministic temporal components. It was been shown that this allows the identification of coefficients with low signal-to-noise ratios that degrade the GRACE solutions. Although the basic assumption of this approach is the independence of each coefficient, also with respect to time, the statistical filter partially reduces also the coefficients' correlated errors. The spatial response function of the statistical filter is anisotropic at the equator, but towards the pole anisotropy decreases. For Antarctica, a significant noise reduction is achieved without distortion of modelled signals. However, mass change signals remain in the desert areas of central Antarctica. This suggests that GRACE errors are, to some extent, also correlated with respect to time. This problem needs to be further addressed.

The inversion of potential disturbances for their sources of mass change was carried out using the forward modelling approach. The principle idea is to find a linear combination of modelled signals that optimally adjust the observed potential disturbances. In this work, minimization is done with respect to scaling factors of the forward models that describe potential disturbances due to present-day ice-mass changes and GIA. For GIA, linear scaling of the forward model is justified by the linear dependence of the GIA signal on the amplitude of the forcing load model for fixed glacial history and fixed earth-model parameters. This approximation neglects non-linear coupling in the earth|ice|ocean system, but avoids elaborate computations, such as Monte Carlo simulations for finding optimal model parameters. In the future, the GIA modelling will be refined by quantifying parameter sensitivities with respect to GRACE data and other observations. For Antarctica, mass changes of individual drainage basins were been modelled. The potential disturbances produced are similar to those of point masses, and the model adjustment is similar to the determination of mass concentrations (e.g. Rowlands *et al.*, 2005), although this approach is usually applied to GRACE Level 1B data to increase spatial resolution that is otherwise lost for GRACE solutions of the Stokes potential coefficients.

Table 7.1 summarizes the results of the GRACE potential-field inversion. Present-day ice-mass changes are observed to lie between 0.17 and 0.29 mm/a ESL (±5%) for Alaska, 0.35 and 0.60 mm/a ESL (±3%) for Greenland, 0.06 and 0.11 mm/a ESL (±14%) for the Antarctic Peninsula, and 0.16 and 0.23 mm/a ESL (±2%) for the Amundsen Sea Sector in West Antarctica (Pine Island, Thwaites, Smith and Kohler glaciers). The errors in brackets refer to propagated GRACE errors calculated according to (6.3) and (6.4). The range of the values is mainly due to differences in the results from different releases, which remains one of the principle problems of GRACE data that needs further investigation. The influence of GIA on the results is small (< 6 % for the given range of plausible viscosity profiles), also for West Antarctica, owing to simultaneously including (instead of *a priori* subtracting) GIA in the adjustment of forward models of present-day ice-mass changes. The adjusted GIA models, in addition, indicate mass changes since the LGM between 55 to 127 m ESL (±6%) for the Laurentide Ice Sheet and between 6.1 and 10.4 m ESL (±4%) for the Antarctic Ice Sheet assuming standard viscosity values. Without JPL RL04, which appears to be significantly biased, the range of values for the Lauerentide Ice Sheet reduces to 104 to 127 m ESL. Changes of the viscosities within plausible bounds can compensate scaling for the ice sheets within the range of -28 to 50% for the Laurentide Ice Sheet and between -4 to 30% for the Antarctic Ice Sheet, which demonstrates the ambiguity in the GIA inversion and the necessity for further constraints. Ambiguities of the inversion of GRACE data for mass changes of individual drainage basins in West Antarctica can be reduced, for example, by InSAR estimates, although for $\sim$ four combined drainage basin separated by $\sim$ 250 km meaningful estimates are possible only using GRACE data.

Region	GFZ RL04	CNES RL01C	JPL RL04	CSR RL04	GIA uncert.
	Present-day ice-mass change (mm/a ESL)				
Alaska	0.17(±7)	0.17(±4)	0.25(±3)	0.22(±5)	(±6)
Greenland	0.48(±4)	0.58(±2)	0.38(±3)	0.52(±3)	(±5)
Antarctic Peninsula	0.08(±10)	0.08(±5)	0.07(±10)	0.07(±7)	(±3)
Amundsen Sea Sector	0.21(±2)	0.24(±1)	0.17(±2)	0.20(±1)	(±5)
	Past ice-mass change (m ESL)				
Northern Hemisphere ice sheets	108.4(±7)	100.2(±1)	57.2(±6)	116.5(±5)	(−28 to 50)
Antarctic Ice Sheet	6.5(±4)	10.3(±2)	8.2(±4)	4.4(±3)	(−4 to 30)

Table 7.1: Present-day and past ice-mass changes in the polar regions from GRACE. Uncertainties (%) associated with the GRACE releases refer to propagated residual GRACE errors. The GIA uncertainty represents the variation (%) of the mass-change estimates with respect to changing the viscosity distributions within plausible bounds.

A

Mathematical supplements

A.1 Surface spherical harmonics

A scalar field described by a square-integrable function $f(\vartheta, \varphi)$ defined on the unit sphere $\mathbf{\Omega}_0 := [0, \pi] \times [-\pi, \pi]$ can be expanded into a series of surface spherical harmonics in the form

$$f(\vartheta, \varphi) = \sum_{j=0}^{\infty} \sum_{m=-j}^{j} f_{jm} Y_{jm}(\vartheta, \varphi), \tag{A.1}$$

where f_{jm} are the complex, fully normalized spherical-harmonic coefficients of degree j and order m, ϑ and φ are co-latitude and longitude, respectively, and $Y_{jm}(\vartheta, \varphi)$ are the surface spherical-harmonic functions given by

$$Y_{jm}(\vartheta, \varphi) = P_{jm}(\cos\vartheta) e^{\mathrm{i}m\varphi}, \tag{A.2}$$

with $P_{jm}(\cos\vartheta)$ the fully normalized associated Legendre functions of degree j and order m. The summation $\sum_{j=0}^{\infty} \sum_{m=-j}^{j}$ is henceforth denoted by $\sum_{jm}$. The surface spherical harmonics $Y_{jm}(\vartheta, \varphi)$ are symmetric,

$$\begin{aligned} Y_{j,-m}(\vartheta, \varphi) &= (-1)^m Y_{jm}^*(\vartheta, \varphi), \\ Y_{j,-m}(\pi - \vartheta, \varphi) &= (-1)^{j+m} Y_{jm}(\vartheta, \varphi), \end{aligned} \tag{A.3}$$

complete,

$$\sum_{jm} Y_{jm}(\vartheta, \varphi) Y_{jm}(\vartheta', \varphi') = \delta(\cos\vartheta - \cos\vartheta') \delta(\varphi - \varphi'), \tag{A.4}$$

and orthonormal,

$$\int_{\mathbf{\Omega}_0} Y_{j_1 m_1}(\vartheta, \varphi) Y_{j_2 m_2}^*(\vartheta, \varphi) \sin d\vartheta d\varphi = \delta_{j_1, j_2} \delta_{m_1, m_2}, \tag{A.5}$$

where the asterisk denotes complex conjugation.

This allows the coefficients f_{jm} to be expressed as

$$f_{jm} = \int_{-\pi}^{\pi} \int_{0}^{\pi} f(\vartheta, \varphi) Y_{jm}^*(\vartheta, \varphi) \sin\vartheta d\vartheta d\varphi, \tag{A.6}$$

where, in particular,

$$f_{00} = \frac{1}{\sqrt{4\pi}} \int_{-\pi}^{\pi} \int_{0}^{\pi} f(\vartheta, \varphi) \sin\vartheta d\vartheta d\varphi \tag{A.7}$$

represents the integral of $f(\vartheta, \varphi)$ over the unit sphere. In addition, if $f(\vartheta, \varphi)$ is a real function,

$$f_{j,-m} = (-1)^m f^*_{jm} \tag{A.8}$$

holds, and f_{j0} are the real zonal coefficients. Functions depending on colatitude only, $f = f(\vartheta)$, can be expanded into a series of Legendre polynomials, $P_j(\vartheta)$, with the expansion coefficients

$$f_j = \int_0^{\pi} f(\vartheta) P_j(\vartheta) \sin\vartheta d\vartheta. \tag{A.9}$$

In geodesy, the spherical-harmonic expansion is particularly relevant for the description of the Earth's gravitational potential. However, it is common to adopt the geodetic norm (e.g. Heiskanen & Moritz, 1967) rather than the quantum-mechanics norm (e.g. Varshalovich *et al.*, 1989) employed in this study and express functions in terms of the fully normalized Stokes coefficients, $\bar{C}_{jm}$ and $\bar{S}_{jm}$, which are related to the coefficients in the quantum-mechanics norm by

$$\begin{aligned} f_{j0} &= \sqrt{4\pi}\bar{C}_{j0}, && m = 0, \\ \operatorname{Re} f_{jm} &= (-1)^m \sqrt{2\pi}\bar{C}_{jm}, && m \neq 0, . \\ \operatorname{Im} f_{jm} &= (-1)^{m+1} \sqrt{2\pi}\bar{S}_{jm}, && m \neq 0. \end{aligned} \tag{A.10}$$

A.2 Spatial convolution

For linear convolution filtering the output signal $y(\Omega)$ is given by the spatial convolution of the filter response function $h(\Omega)$ with the input signal $x(\Omega)$,

$$y(\Omega) = \int_{\Omega'_0} h(\Omega') x(\Omega - \Omega') d\Omega', \tag{A.11}$$

where Ω represents for the spherical co-latitude ϑ and longitude φ. Hence $\Omega := (\vartheta, \varphi)$, Ω_0 is the full solid angle and $d\Omega$ its infinitesimal element.

The signals $x(\Omega)$ and $y(\Omega)$ are assumed to be square-integrable functions over the unit sphere and, thus, can be represented as series of scalar spherical harmonics $Y_{jm}(\Omega)$ of degree j and order m (Section A.1),

$$\begin{bmatrix} x(\Omega) \\ y(\Omega) \end{bmatrix} = \sum_{j=0}^{\infty} \sum_{m=-j}^{j} \begin{bmatrix} x_{jm} \\ y_{jm} \end{bmatrix} Y_{jm}(\Omega), \tag{A.12}$$

with x_{jm} and y_{jm} being the associated spherical-harmonic expansion coefficients of $x(\Omega)$ and $y(\Omega)$, respectively. In the case of isotropic filtering, $h = h(\vartheta)$, the filtering function can be represented as a series of Legendre polynomials $P_j(\cos\vartheta)$,

$$h(\vartheta) = \sum_j h_{j0}\sqrt{\frac{2j+1}{4\pi}}P_j(\cos\vartheta), \tag{A.13}$$

where, using the addition theorem for spherical-harmonic functions (e.g Varshalovich *et al.*, 1989, Sect. 5.17.2.),

$$P_j(\cos\psi) = \frac{4\pi}{2j+1}\sum_m Y_{jm}(\mathbf{\Omega})Y^*_{jm}(\mathbf{\Omega}'). \tag{A.14}$$

Considering the expansions (A.12) and (A.13), $y(\mathbf{\Omega})$ takes the form

$$y(\mathbf{\Omega}) = \int_{\mathbf{\Omega}'}\sum_j h_{j0}\sqrt{\frac{4\pi}{2j+1}}\sum_m Y_{jm}(\mathbf{\Omega})Y^*_{jm}(\mathbf{\Omega}')\sum_{j'm'} x_{j'm'}Y_{j'm'}(\mathbf{\Omega}')d\mathbf{\Omega}' \tag{A.15}$$

and reduces according to the orthormality (A.5) to

$$y(\mathbf{\Omega}) = \sum_j h_{j0}\sqrt{\frac{4\pi}{2j+1}}\sum_m x_{jm}Y_{jm}(\mathbf{\Omega}). \tag{A.16}$$

With $y(\mathbf{\Omega}) = \sum_{jm} y_{jm}Y_{jm}(\mathbf{\Omega})$, the convolution in the spectral domain becomes

$$y_{jm} = \sqrt{\frac{4\pi}{2j+1}}h_{j0}x_{jm}, \tag{A.17}$$

where the factor $\sqrt{2j+14\pi}$ is introduced to normalize the expansion coefficients h_{j0}, such that

$$y_{jm} = h_j x_{jm}. \tag{A.18}$$

A.3 Stokes potential coefficients

The external gravitational potential of the Earth can be expressed as an expansion of solid spherical-harmonic functions, which represent solutions of the Laplace equation for the gravitational potential in the source-free space. The external gravitational potential $V(r,\mathbf{\Omega})$ is expressed by

$$V(r,\mathbf{\Omega}) = \frac{GM}{R}\sum_{j=0}^{j_{\max}}(\frac{R}{r})^{j+1}\sum_{m=-j}^{m=j} V_{jm}Y_{jm}(\mathbf{\Omega}), \tag{A.19}$$

where G is the gravitational constant, M is the Earth's total mass, R is the equatorial semi-axis of the Earth's reference ellipsoid, and V_{jm} are the fully normalized (unitless) potential coefficients associated with the spherical-harmonic functions $Y_{jm}(\mathbf{\Omega})$. The factor GM/r represents the gravitational potential of a spherically symmetric body with mass M, i.e. point mass M, and, thus the coefficients V_{jm} with $j > 0$ describe the deviations of the gravitational potential from spherical symmetry.

A.4 Spatial distribution of GRACE variances

The spatial distribution of GRACE variances of the potential, $\mathrm{var}(V(\boldsymbol{\Omega}))$, is calculated from the GRACE coefficients' variances, $\mathrm{var}(V_{jm})$, by linear error propagation. Let $\boldsymbol{\beta} = \{\beta_{jm}\}$ and $\boldsymbol{\gamma} = \{\gamma_{jm}\}$ be column vectors of the real and imaginary part of the GRACE coefficients V_{jm}, respectively,

$$\begin{aligned} \beta_{j0} &= V_{j0}, && m = 0, \\ \beta_{jm} &= 2\mathrm{Re}V_{jm}, && m > 0, \\ \gamma_{jm} &= -2\mathrm{Im}V_{jm}, && m > 0, \end{aligned} \tag{A.20}$$

and let $\boldsymbol{B}_i^{\mathrm{c|s}} = \{Y_{jm}^{\mathrm{c|s}}(\boldsymbol{\Omega}_i)\}$ be the associated vectors of the cosine term $Y^{\mathrm{c}}(\boldsymbol{\Omega}) = P_{jm}(\vartheta)\cos(m\varphi)$ and sine term $Y^{\mathrm{s}}(\boldsymbol{\Omega}) = P_{jm}(\vartheta)\sin(m\varphi)$ of the spherical harmonic functions, $Y_{jm}(\boldsymbol{\Omega})$ at the spatial point $\boldsymbol{\Omega}_i$. Then, the potential at this point is given by

$$V(\boldsymbol{\Omega}_i) = \boldsymbol{B}_i^{\mathrm{c}}\boldsymbol{\beta} + \boldsymbol{B}_i^{\mathrm{s}}\boldsymbol{\gamma}. \tag{A.21}$$

Linear error propagation gives the spatial representation of the variance-covariance matrix of the potential,

$$\begin{aligned} \mathrm{var}(V(\boldsymbol{\Omega}_{kl})) = \; & \boldsymbol{B}_k^{\mathrm{c}}\,\mathrm{var}(\boldsymbol{\beta})\boldsymbol{B}_l^{\mathrm{c}} + \boldsymbol{B}_k^{\mathrm{s}}\,\mathrm{var}(\boldsymbol{\gamma})\boldsymbol{B}_l^{\mathrm{s}} + \\ & \boldsymbol{B}_k^{\mathrm{c}}\,\mathrm{cov}(\boldsymbol{\beta},\boldsymbol{\gamma})\boldsymbol{B}_l^{\mathrm{s}} + \boldsymbol{B}_k^{\mathrm{s}}\,\mathrm{cov}(\boldsymbol{\gamma},\boldsymbol{\beta})\boldsymbol{B}_l^{\mathrm{c}}. \end{aligned} \tag{A.22}$$

For uncorrelated errors between cosine and sine terms, $\mathrm{cov}(\boldsymbol{\beta},\boldsymbol{\gamma}) = \mathrm{cov}(\boldsymbol{\gamma},\boldsymbol{\beta}) = \emptyset$. Additionally, for uncorrelated errors between coefficients of different j and m,

$$\begin{aligned} [\mathrm{var}(\boldsymbol{\beta})]_{j_1m_1,j_2m_2} &= \sigma^2_{\beta_{jm}}\delta_{j_1j_2}\delta_{m_1m_2}, \\ [\mathrm{var}(\boldsymbol{\gamma})]_{j_1m_1,j_2m_2} &= \sigma^2_{\gamma_{jm}}\delta_{j_1j_2}\delta_{m_1m_2}, \end{aligned} \tag{A.23}$$

and the sum in (A.22) takes the form

$$\mathrm{var}(V(\boldsymbol{\Omega}_{kl})) = \sum_{jm}[Y_{jm}^{\mathrm{c}}(\boldsymbol{\Omega}_k)\sigma^2_{\boldsymbol{\beta}_{jm}}Y_{jm}^{\mathrm{c}}(\boldsymbol{\Omega}_l) + Y_{jm}^{\mathrm{s}}(\boldsymbol{\Omega}_k)\sigma^2_{\boldsymbol{\gamma}_{jm}}Y_{jm}^{\mathrm{s}}(\boldsymbol{\Omega}_l)]. \tag{A.24}$$

A.5 Characteristic geodetic quantities

A.5.1 Spatial resolution

The spatial wavelength of a spherical harmonic of degree j at the Earth's surface is $\lambda = 2\pi R/j \approx 40 \times 10^6\,\mathrm{m}/j$. The minimum resolvable (alias-free) wavelength $\lambda_{\min}$ is related to the spatial resolution Δ_λ by the Shannon-Nyquist criterion,

$$\lambda_{\min} > 2\Delta_\lambda, \tag{A.25}$$

which gives the spatial resolution of the spherical harmonic of degree j of $\Delta_\lambda \approx 20 \times 10^6\,\mathrm{m}/j$.

A.5.2 Degree power

The power $|f_j|^2$ of the function $f(\mathbf{\Omega})$ for a specific degree j corresponding to a specific spatial wavelength is called degree power, and its square root is called degree amplitude, $|f_j|$. The degree power $|f_j|^2$ is obtained from the spherical-harmonic expansion coefficients f_{jm} by

$$|f_j|^2 = \int_{\mathbf{\Omega}_0} f_j(\mathbf{\Omega}) f_j(\mathbf{\Omega}) d\mathbf{\Omega} = \sum_{m=-j}^{j} f_{jm} f_{jm}^* = 4\pi \sum_{m=0}^{j} (\bar{C}_{jm}^2 + \bar{S}_{jm}^2), \tag{A.26}$$

where

$$f_j(\mathbf{\Omega}) = \sum_{m=-j}^{j} f_{jm} Y_{jm}(\mathbf{\Omega}) \tag{A.27}$$

with $\bar{C}_{jm}^2$ and $\bar{S}_{jm}$ are the fully normalized Stokes coefficients in the geodetic norm (A.10).

The power of the function $f(\mathbf{\Omega})$ in the spectral band $[j_1, j_2]$ is called the cumulative degree power,

$$|f_{j_1,j_2}|^2 = \sum_{j=j_1}^{j_2} |f_j|^2. \tag{A.28}$$

In general, the coefficients in the spherical-harmonic expansion of a function depend on the choice of the coordinate system. However, $|f_j|^2$ and $|f_{j_1,j_2}|^2$ are quantities independent of the orientation of the coordinate system and, therefore, allow the comparison of the spectra of two scalar fields. A graph of $|f_j|^2$ versus j is called a degree-power spectrum, whereas a graph of $|f_j|$ versus j is called a degree-amplitude spectrum. In this study, spectra of the geoid height, N, and the rate of geoid-height change, $\dot{N}$, are plotted in the geodetic norm as degree-amplitude spectra.

A.5.3 Degree correlation

The degree correlation, r_j, of two functions $f(\mathbf{\Omega})$ and $g(\mathbf{\Omega})$ is given by (e.g Martinec, 1994)

$$r_j = \frac{1}{\sqrt{|f_j|^2 |g_j|^2}} \int_{\mathbf{\Omega}_0} f_j(\mathbf{\Omega}) g_j(\mathbf{\Omega}) d\mathbf{\Omega} = \frac{\sum_{m=-j}^{j} f_{jm} g_{jm}^*}{\sqrt{\sum_{m=-j}^{j} f_{jm} f_{jm}^*} \sqrt{\sum_{m=-j}^{j} g_{jm} g_{jm}^*}}. \tag{A.29}$$

A.6 Least-squares solution of linear inverse problem

This section introduces the concept of solving the linear inverse problem by the method of least-squares. More details can be found in, for example, Tarantola (2005) and Gubbins (2004), upon which this summary is based.

The inverse problem is concerned with the determination of $\boldsymbol{m} = \{m_k\}^{k=1,2,\dots,K}$, parameters of the model according to $d_i, i = 1, 2, ..., N$, data samples, assuming that $\boldsymbol{m}$ and $\boldsymbol{d}$ are quantitatively related. In general, the relation between $\boldsymbol{m}$ and $\boldsymbol{d}$ can be arbitrary complicated involving, for example, implicit and non-linear functional dependencies.

For linear problems or problems that can be linearized, the relation between $\boldsymbol{d}$ and $\boldsymbol{m}$ of the forward model is expressed by a system of linear equations,

$$\boldsymbol{d} = \boldsymbol{F}\boldsymbol{m}, \tag{A.30}$$

where $\boldsymbol{F}$ is the $N \times K$ design matrix of the problem, which is independent of $\boldsymbol{d}$ and $\boldsymbol{m}$. Equi-determined problems ($N = K$) have exactly one solution, i.e. $\boldsymbol{m} = \boldsymbol{F}^{-1}\boldsymbol{d}$. Overdetermined problems, i.e. problems with more equations than parameters ($N > K$), have multiple approximate solutions from which, according to a *a priori* specified criterion (e.g. minimization of errors), an optimal solution is selected (Section A.6.1). Underdetermined problems ($N < K$), or problems that are underdetermined with respect to a particular, and overdetermined with respect to other parameters, also have a variety of solutions, from which one is selected by limitation of the solution space or placing constraints on the parameters (Section A.6.2).

In general, observations $\boldsymbol{d}$ are likely to be contaminated by stochastic noise, $\boldsymbol{e}$, which introduces inconsistencies to be included in (A.30) according to

$$\boldsymbol{d} = \boldsymbol{F}\boldsymbol{m} + \boldsymbol{e}. \tag{A.31}$$

Suppose that $\hat{\boldsymbol{m}}$ is an estimate of model parameters obtained, for example, by $\hat{\boldsymbol{m}} = \boldsymbol{F}'^{-1}\boldsymbol{d}$, where $\boldsymbol{F}'$ represents the square matrix for the number of equations reduced by $N - K$ for the equi-determined system. Then, the prediction of the data, $\hat{\boldsymbol{d}}$, is obtained by $\hat{\boldsymbol{d}} = \boldsymbol{F}\hat{\boldsymbol{m}}$, and its residual from the data is $\boldsymbol{r} = \boldsymbol{d} - \hat{\boldsymbol{d}}$. The minimization of $\boldsymbol{r}$ with respect to $\boldsymbol{m}$ in the L_2-norm is expressed by

$$E := \boldsymbol{r}^{\mathrm{T}}\boldsymbol{r} \overset{!}{=} \min_{m_k}, \tag{A.32}$$

which is the criterion most frequently used for the solution of linear inverse problems.

A.6.1 Unconstrained estimate

Minimization of the residual $\boldsymbol{r}$ in the L_2-norm (A.32) means that an $\boldsymbol{m}$ needs to be found, such that

$$\frac{\partial E}{\partial m_k} = \frac{\partial(\boldsymbol{r}^{\mathrm{T}}\boldsymbol{r})}{\partial m_k} \overset{!}{=} 0. \tag{A.33}$$

Here, it is assumed that m_k are independent of each other, which means that $\partial m_k \partial m_l = \delta_{kl}$. The estimated solution $\hat{\boldsymbol{m}}$ to (A.33) is given by (e.g. Gubbins, 2004)

$$\hat{\boldsymbol{m}} = (\boldsymbol{F}^{\mathrm{T}}\boldsymbol{F})^{-1}\boldsymbol{F}^{\mathrm{T}}\boldsymbol{d} \tag{A.34}$$

if $(\boldsymbol{F}^{\mathrm{T}}\boldsymbol{F})^{-1}$ exists, which is the case if $\boldsymbol{F}^{\mathrm{T}}\boldsymbol{F}$ is non-singular. The solution (A.34) is based on the assumption of equal quality of the data $\boldsymbol{d}$. However, it may be useful to introduce weights in the least-squares criterion (A.32), such that

$$E_{\mathrm{W}} := \boldsymbol{r}^{\mathrm{T}}\boldsymbol{W}_{\mathrm{D}}\boldsymbol{r} \overset{!}{=} \min_{m_k}, \tag{A.35}$$

where $\boldsymbol{W}_{\mathrm{D}}$ refers to the weighting matrix associated with the data and may be, for example, the inverse variances matrix of the data, $\boldsymbol{C}_{\mathrm{D}}^{-1}$, such that a large weight is placed upon data with small errors. Then, the solution to $\partial E_{\mathrm{W}}\partial m_k \overset{!}{=} 0$ becomes

$$\hat{\boldsymbol{m}} = (\boldsymbol{F}^{\mathrm{T}}\boldsymbol{C}_{\mathrm{D}}^{-1}\boldsymbol{F})^{-1}\boldsymbol{F}^{\mathrm{T}}\boldsymbol{C}_{\mathrm{D}}^{-1}\boldsymbol{d} \tag{A.36}$$

with the *a posteriori* covariance matrix of the model,

$$\tilde{\boldsymbol{C}}_{\mathrm{M}} = (\boldsymbol{F}^{\mathrm{T}}\boldsymbol{C}_{\mathrm{D}}^{-1}\boldsymbol{F})^{-1}. \tag{A.37}$$

A.6.2 Constrained estimate

For problems that are mildly underdetermined with respect to m_k, but overdetermined with respect to other m_k, the least-squares solution (A.34) may not produce satisfactory results in the sense that the estimated parameters $\hat{\boldsymbol{m}}$ are far from some *a priori* value of $\boldsymbol{m}^{\mathrm{P}}$ obtained from independent data. In these cases, the solution $\hat{\boldsymbol{m}}$ typically shows an undesired oscillatoric character that can be damped by including *a priori* constraints on the parameters, $\boldsymbol{m}^{\mathrm{P}}$, along with their uncertainties in the minimization criterion.

The most elementary stabilization is to include the norm of the solution, $N = \boldsymbol{m}^{\mathrm{T}}\boldsymbol{m}$, in the minimization criterion (A.35) according to

$$E_{\mathrm{C}}(\boldsymbol{m}) = E_{\mathrm{W}} + \gamma^2 N, \tag{A.38}$$

where γ is a regularization parameter that governs the contribution of E_{W} versus N in (A.38). The choice of γ is not unique, but depends on the characteristics of the inverse problem. The solution of $\partial E_{\mathrm{C}}\partial m_k \overset{!}{=} 0$ is (e.g. Gubbins, 2004)

$$\hat{\boldsymbol{m}} = (\boldsymbol{F}^{\mathrm{T}}\boldsymbol{C}_{\mathrm{D}}^{-1}\boldsymbol{F} + \gamma\boldsymbol{I})^{-1}\boldsymbol{F}^{\mathrm{T}}\boldsymbol{C}_{\mathrm{D}}^{-1}\boldsymbol{d}. \tag{A.39}$$

Often, it is more appropriate to constrain the solution to be close to an independent *a priori* parameter estimate, $\boldsymbol{m}^{\mathrm{P}}$, and minimize $N = \Delta\boldsymbol{m}^{\mathrm{T}}\Delta\boldsymbol{m}$, where $\Delta\boldsymbol{m} = \boldsymbol{m} - \boldsymbol{m}^{\mathrm{P}}$ such that the solution of the minimization (A.38) becomes

$$\hat{\boldsymbol{m}} = \boldsymbol{m}^{\mathrm{P}} + (\boldsymbol{F}^{\mathrm{T}}\boldsymbol{C}_{\mathbf{D}}{}^{-1}\boldsymbol{F} + \gamma\boldsymbol{I})^{-1}\boldsymbol{F}^{\mathrm{T}}\boldsymbol{C}_{\mathbf{D}}{}^{-1}(\boldsymbol{d} - \boldsymbol{F}\boldsymbol{m}^{\mathrm{P}}). \tag{A.40}$$

Instead of controlling the influence of the *a priori* estimate m^{P} in (A.40) by the parameter γ, it is possible to introduce weights represented by the inverse matrix of the variances of the model parameters, $\boldsymbol{C}_{\mathrm{M}}$, analogue to the weight matrix for the data. Then, the solution takes the form

$$\hat{\boldsymbol{m}} = \boldsymbol{m}^{\mathrm{P}} + (\boldsymbol{F}^{\mathrm{T}}\boldsymbol{C}_{\mathrm{D}}^{-1}\boldsymbol{F} + \boldsymbol{C}_{\mathrm{M}}^{-1})^{-1}\boldsymbol{F}^{\mathrm{T}}\boldsymbol{C}_{\mathbf{D}}{}^{-1}(\boldsymbol{d} - \boldsymbol{F}\boldsymbol{m}^{\mathrm{P}}). \tag{A.41}$$

With the propagation of the variance for linear operators, the *a posteriori* covariance matrix of the parameter estimates, $\hat{\boldsymbol{C}}_\mathrm{M}$, becomes

$$\hat{\boldsymbol{C}}_\mathrm{M} = (\boldsymbol{F}^\mathrm{T}\boldsymbol{C}_\mathrm{D}^{-1}\boldsymbol{F} + \boldsymbol{C}_\mathrm{M}^{-1})^{-1}. \tag{A.42}$$

B

Additional forward modelling results

B.1 GIA over North America

Supplementary to Section 6.3, predictions of the rate of geoid-height change over North America due to the glacial history NAWI are shown for various viscosity distributions. The upper cut-off degree is $j_{\mathrm{max}} = 256$.

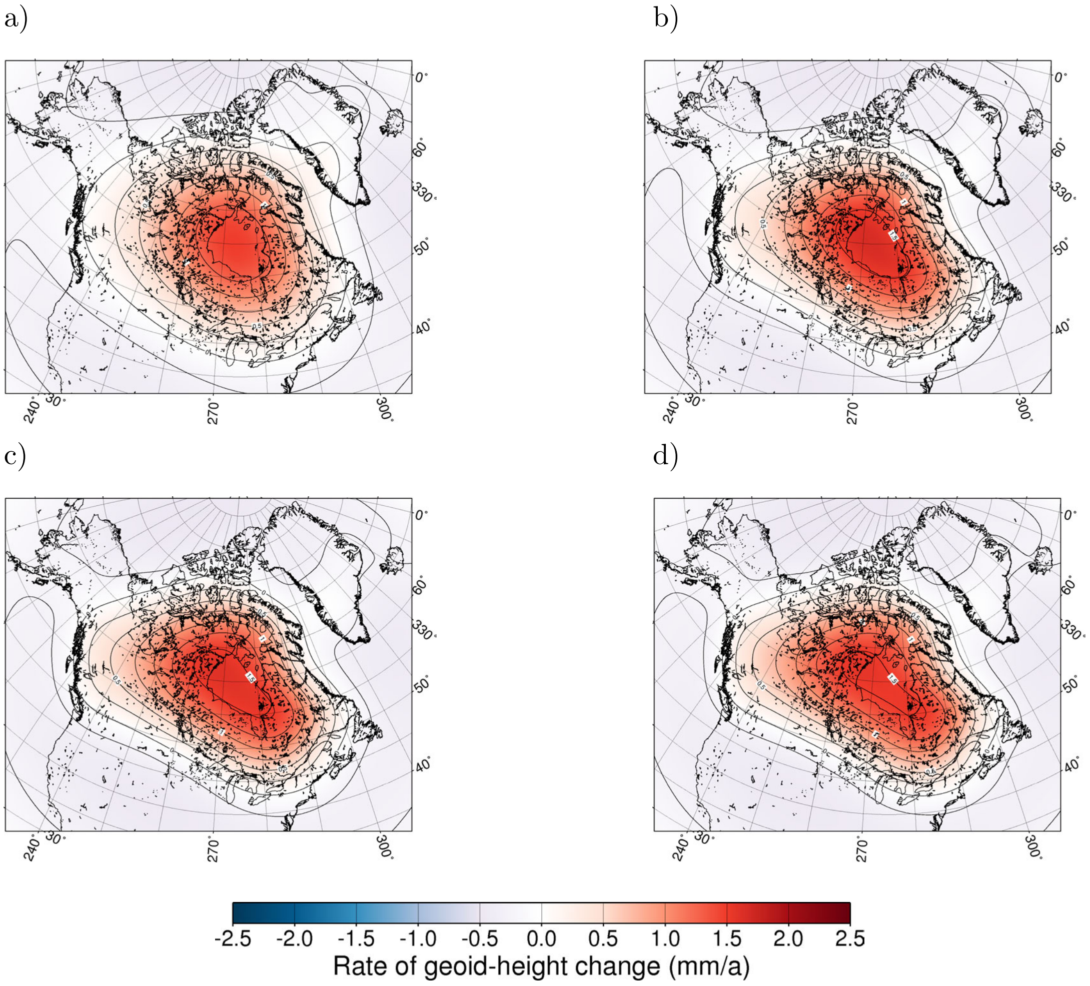

Figure B.1: Predicted rate of geoid-height change over North America due to GIA for load model NAWI and a lower-mantle viscosity η_{LM} of 5×10^{21} Pa s. The upper-mantle viscosities η_{UM} are a) 2×10^{20}, b) 4×10^{20}, c) 6×10^{20} and d) 8×10^{20} Pa s.

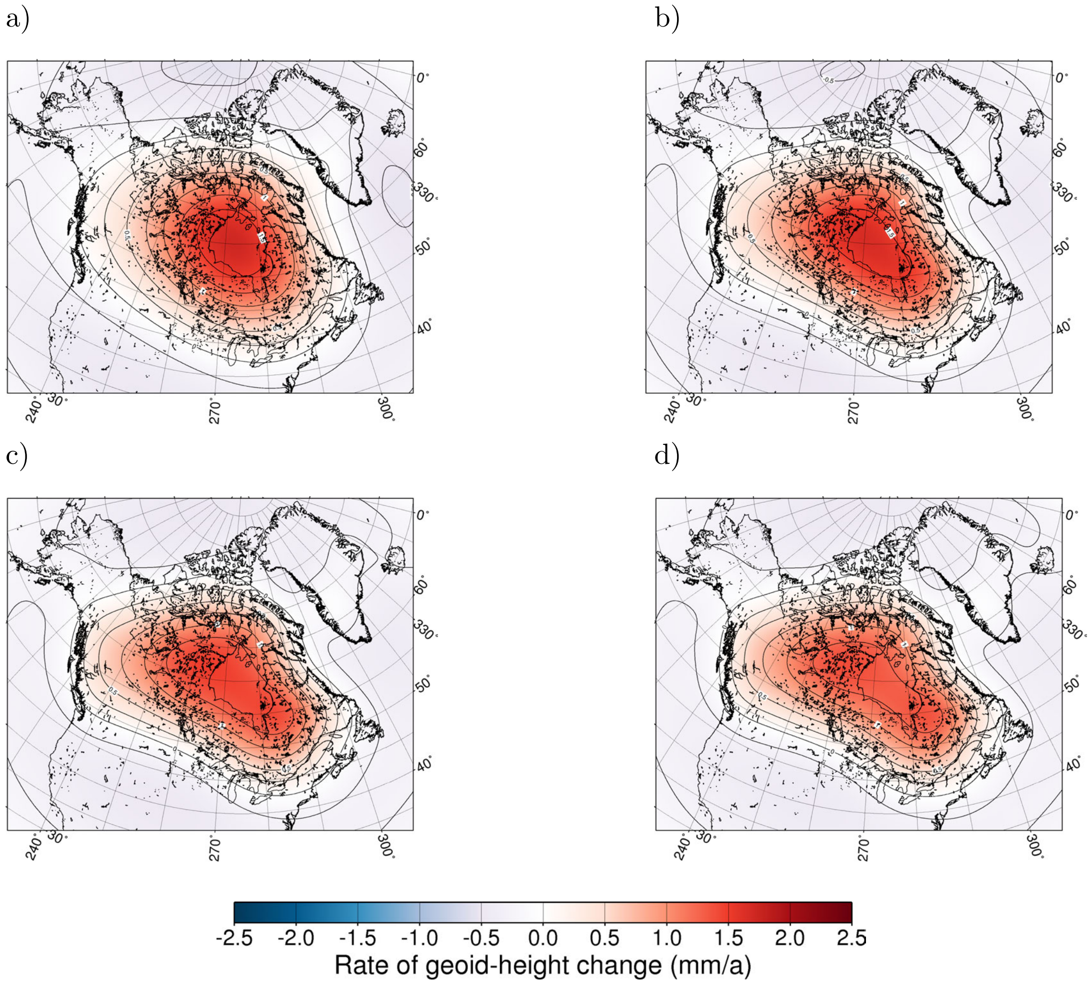

Figure B.2: The same as Figure B.1, but for a lower-mantle viscosity η_{LM} of 1×10^{22} Pa s.

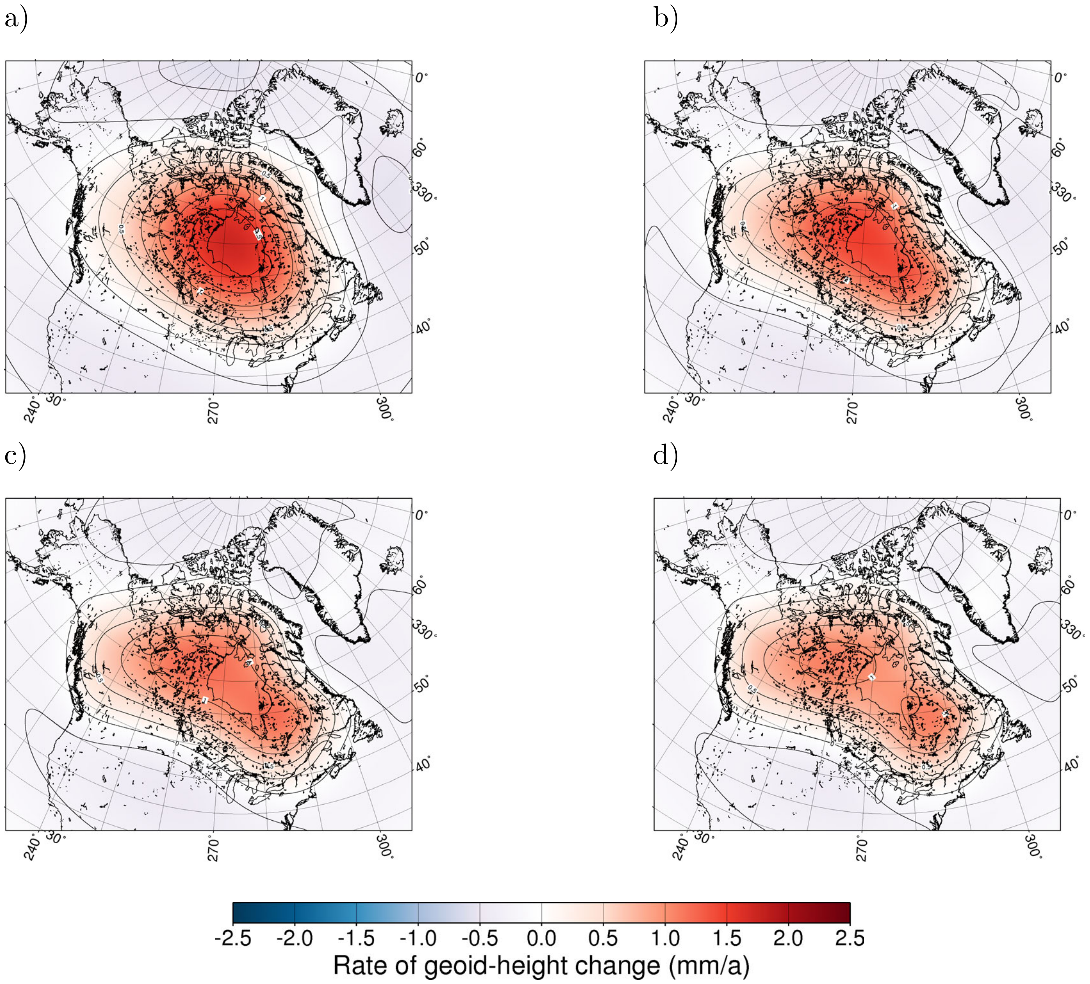

Figure B.3: The same as Figure B.1, but for a lower-mantle viscosity η_{LM} of 2×10^{22} Pa s.

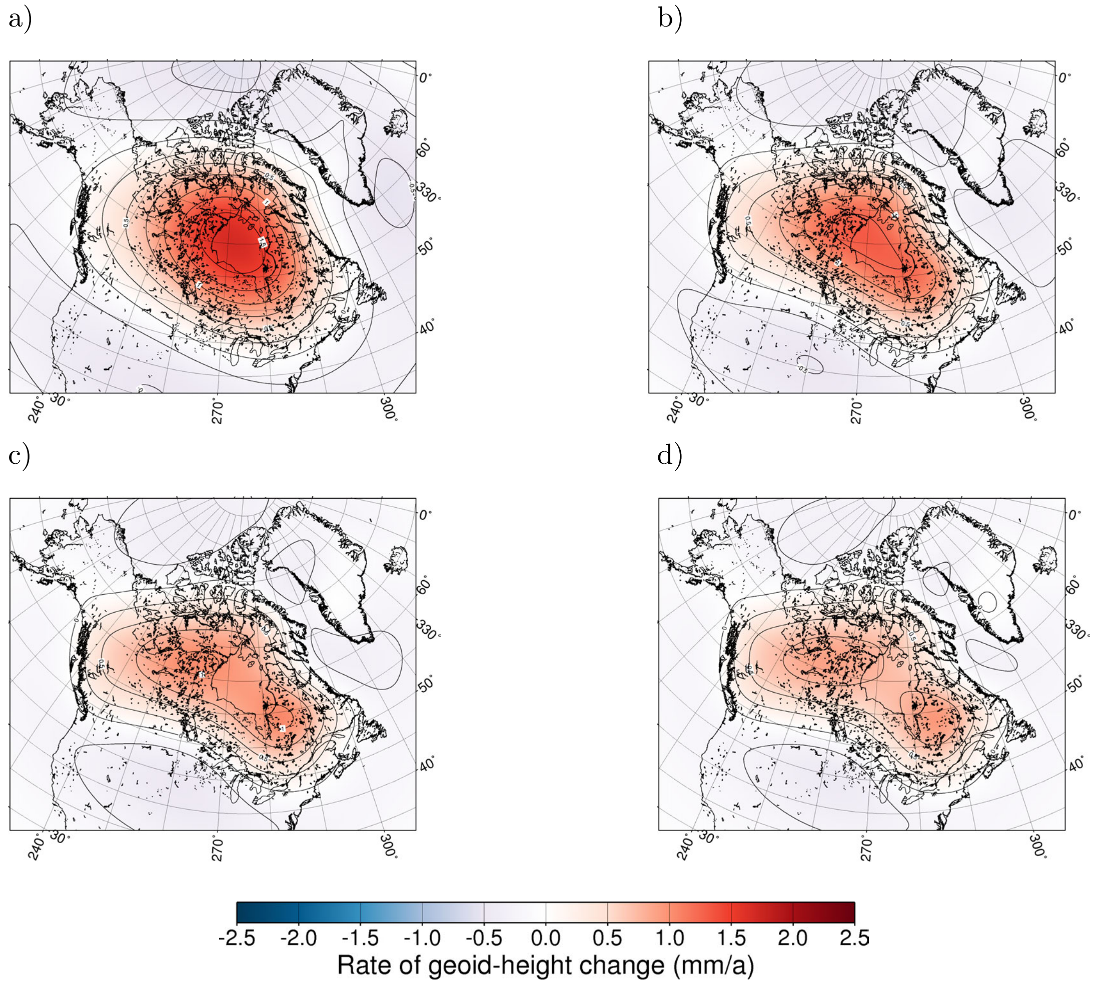

Figure B.4: The same as Figure B.1, but for a lower-mantle viscosity η_{LM} of 4×10^{22} Pa s.

Bibliography

ADD Consortium, 2000. *Antarctica Digital Database, Version 3.0, Database, Manual and Bibliography*, Scientific Commitee on Antarctic Research (SCAR), Cambridge. 89

Anderson, J. B., Shipp, S. S., Lowe, A. L., Wellner, J. S. & Mosola, A. B., 2002. The Antarctic Ice Sheet during the Last Glacial Maximum and its subsequent retreat history: a review. *Quat. Sci. Rev.*, 21(1-3): 49–70. 93

Arendt, A. A., Echelmeyer, K. A., Harrison, W. D., Lingle, C. S. & Valentine, V. B., 2002. Rapid Wastage of Alaska Glaciers and Their Contribution to Rising Sea Level. *Science*, 297(5580): 382–386. 14, 104, 105

Bamber, J. L., R. L., L. & S. P., G., 2001. A new ice thickness and bed data set for the Greenland Ice Sheet, 1. Measurement, data reduction, and errors. *J. Geophys. Res.*, 106(D24): 33773–33780. 7

Bentley, M. J., 1999. Volume of Antarctic ice at the Last Glacial Maximum, and its impact on global sea level change. *Quat. Sci. Rev.*, 18(14): 1569–1595. 71, 93, 97, 98

Bettadpur, S., 2004a. *CSR Level-2 Processing Standards Document for Level-2 Product Release 01, Gravity Recovery and Climate Experiment (GRACE)*. Univ. Texas, Austin, Rev. 1.1, GRACE 327-742 (CSR-GR-03-03). 72

Bettadpur, S., 2004b. GRACE Mission Status and Gravity Field Product Improvement Plan. *Eos Trans. AGU*, 85(47), Fall Meet. Suppl. G23A-01. 67

Bettadpur, S., 2007a. *CSR Level-2 Processing Standards Document for Level-2 Product Release 04*. Univ. Texas, Austin, Rev. 3.1, GRACE 327-742 (CSR-GR-03-03). 28, 90

Bettadpur, S., 2007b. *Gravity Recovery and Climate Experiment Product Specification Document*. Univ. Texas, Austin, Rev. 4.5, GRACE 327-720 (CSR-GR-03-02). 90

Bettadpur, S., Flechtner, F. & Schmidt, R., 2006. *Technical Note 04, Usage Guidelines for GFZ RL03 and JPL RL02 GRACE Gravity Fields & Atmosphere/Ocean Background Models*. GeoForschungsZentrum Potsdam, Ver. 1.1. 72

Biancale, R., Lemoine, J.-M., Loyer, S., Bruinsma, S., Perosanz, F., Marty, J.-C., Sarrailh, M., Vales, N. & Balmino, G., 2006. Monitoring variations of the geoid every 10 days from GRACE and LAGEOS satellite missions. *Geophys. Res. Abstr.*, 8(05546). 28, 72, 90

Braithwaite, R. J., 1995. Positive degree-day factors for ablation on the Greenland icesheet studied by energy-balance modelling. *J. Glaciol.*, 41: 153–160. 104

Case, K., Kruizinga, G. & Wu, S.-C., 2004. *GRACE Level 1B Data Product User*

Handbook. Jet Propulsion Laboratory, Pasadena, Rev. 1.2, JPL D-2207. 27, 28, 29

Cathles, L. M., 1975. *The Viscosity of the Earth's Mantle*. Princeton University Press, Princeton. 11, 20

Chen, J. L., Wilson, C. R. & Tapley, B. D., 2006a. Satellite gravity measurements confirm accelerated melting of Greenland Ice Sheet. *Science*, 313: 1958–1960. 88

Chen, J. L., Wilson, C. R., Blankenship, D. D. & Tapley, B. D., 2006b. Antarctic mass rates from GRACE. *Geoph. Res. Lett.*, 33, L11502. 88, 97, 98

Chen, J. L., Tapley, B. D. & Wilson, C. R., 2006c. Alaskan mountain glacial melting observed by satellite gravimetry. *Earth Planet. Sci. Lett.*, 248: 368–378. 110

Cuffey, K., 2001. Interannual variability of elevation on the Greenland ice sheet: effects of firn densification, and establishment of a multi-century benchmark. *J. Glaciol.*, 47(158): 369–377. 10

Davis, C., Li, Y., McConnell, J., Frey, M. & Hanna, E., 2005. Snowfall-driven growth in East Antarctic Ice Sheet mitigates recent sea-level rise. *Science*, 308(5730): 1898–1901. 123

Davis, J. L., Tamisiea, M. E., Elósegui, P., Mitrovica, J. X. & Hill, E. M., 2008. A statistical filtering approach for Gravity Recovery and Climate Experiment (GRACE) gravity data. *J. Geophys. Res.*, 113: B04410. 45, 125

Deutsches GeoForschungsZentrum, 2008 *[online]*. *The GRACE Mission*. Deutsches GeoForschungsZentrum, http://www.gfz-potsdam.de/grace. 27

di Leonardo, S. M. & Dickmann, S. R., 2004. Isolation of atmospheric effects on rapid polar motion through Wiener filtering. *Geoph. J. Int.*, 159: 863–879. 68

Dobslaw, H. & Thomas, M., 2007. Simulation and observation of global ocean mass anomalies. *J. Geophys. Res.*, 112. 35

Döll, P., Kaspar, F. & Lehner, B., 2003. A global hydrological model for deriving water availability indicators: model tuning and validation. *J. Hydrol.*, 270(1-2): 105–134. 14, 108

Dziewonski, A. M. & Anderson, D. L., 1981. Preliminary Reference Earth Model. *Phys. Earth Planet. Inter.*, 25: 297–356. 20

Efron, B. & Tibshirani, R., 1993. *An Introduction to the Bootstrap*. Chapman & Hall, New York. 95

ESRI, 2003. *Digital Chart of the World (DCW)*. Pennsilvania State University Libraries., Pennsilvania. 89

Fackler, U., 2005. *GRACE - Analyse von Beschleunigungsmessungen*. Diplomarbeit, Institut für Astronom. und Physik. Geodäsie der Techn. Univ. München, München. 30

Fang, M. & Hager, B. F., 1995. The singularity mystery associated with a radially continuous Maxwell viscoelastic structure. *Geophys. J. Int*, 123: 849–865. 12

Farrell, W. & Clark, J., 1976. On postglacial sea level. *Geophys. J. Astr. Soc.*, 46: 647–667. 12, 82

Farrell, W. E., 1972. Deformation of the earth by surface loads. *Rev. Geophys.*, 10:

761–797. 20, 25, 127

Fjeldskaar, W., 1994. Viscosity and thickness of the asthenosphere detected from the Fennoscandian uplift. *Earth Planet. Sci. Lett.*, 126: 399–410. 12

Flechtner, F., 2001 *[online]*. *GRACE Payload*. Deutsches GeoForschungsZentrum, Potsdam, http://www-app2.gfz-potsdam.de/pb1/op/grace/. 29, 30

Flechtner, F., 2005. *GFZ Level-2 Processing Standards Document for Level-2 Product Release 0003, Gravity Recovery and Climate Experiment (GRACE)*. GeoForschungsZentrum Potsdam, Rev. 1.1, GRACE 327-743 (GR-GFZ-STD-001). 72, 124, 125

Flechtner, F., 2006. *AOD1B Product Description Document, Gravity Recovery and Climate Experiment (GRACE)*. GeoForschungsZentrum Potsdam, Rev. 2.2, GRACE 327-750. 35, 72

Flechtner, F., 2007. *GFZ Level-2 Processing Standards Document for Level-2 Product Release 04*. GeoForschungsZentrum Potsdam, Rev. 1.0, GRACE 327-743 (GR-GFZ-STD-001). 28, 34, 90

Flechtner, F., Bettadpur, S. & Watkins, M. Kruizinga, G., 2006 *[online]*. *GRACE Science Data System Monthly Report April 2006*. Deutsches GeoForschungsZentrum. 68

Fleming, K. & Lambeck, K., 2004. Constraints on the Greenland Ice Sheet since the Last Glacial Maximum from sea-level observations and glacial-rebound models. *Quat. Sci. Rev.*, 23: 1053–1077. 112

Fleming, K., Martinec, Z. & Hagedoorn, J., 2004. Geoid displacement about Greenland resulting from past and present-day mass changes of the Greenland ice sheet. *Geophys. Res. Lett.*, 31, L06617. 112

Fleming, K., Sasgen, I. & Martinec, Z., 2006 *[online]*. *Statistical analyzes and comparisons of inferred temporal trends in the GRACE gravity field solutions*. GRACE Science Team Meeting, Dec. 8-9, San Francisco, http://www.csr.utexas.edu/grace/GSTM. 37, 46

Förste, C., Flechtner, F., Schmidt, R., Meyer, U., Stubenvoll, R., F., B., Knig, R., Neumayer, K., Rothacher, M., Reigber, C., Biancale, R., Bruinsma, S., Lemoine, J. & Raimondo, J., 2005. A new high resolution global gravity field model derived from combination of GRACE and CHAMP mission and altimetry/gravimetry surface gravity data. *Geophys. Res. Abstr.*, 7(04561). 34, 40, 61

Gasperini, P. & Sabadini, R., 1989. Lateral heterogeneities on mantle viscosity and post-glacial rebound. *Geophys. J. Int.*, 98: 413–428. 12

Gasperini, P. & Sabadini, R., 1990. Finite-element modeling of lateral viscosity heterogeneities and postglacial rebound. *Tectonophysics*, 179: 141–149. 12

Giunchi, C. & Spada, G., 2000. Postglacial rebound in a non-newtonian spherical earth. *Geophys. Res. Lett.*, 27: 2065–2068. 12

Gubbins, D., 2004. *Time Series Analysis and Inverse Theory for Geophysicists*. Cambridge University Press, Cambride, United Kingdom. 127, 128, 145, 146, 147

Hagedoorn, J., Wolf, D. & Martinec, Z., 2007. An estimate of global sea level rise inferred from tide-gauge measurements using glacial-isostatic adjustment models consistent with the relative sea level record. *Pure Appl. Geophys.*, 164(4): 791–818. 12

Hagedoorn, J. M., 2005. *Glaziale Isostasie und rezente Meeresspiegeländerung*, Scientific Technical Report STR05/13, GeoForschungsZentrum Potsdam. 82, 113

Han, D. & Wahr, J., 1995. The viscoelastic relaxation of a realistically stratified earth, and a further analysis of postglacial rebound. *Geophys. J. Int.*, 120: 287–311. 12, 20, 25

Han, S.-C., 2004. Efficient determination of global gravity field from satellite-to-satellite tracking mission. *Celest. Mech. Dyn. Astr.*, 88: 69–102. 32

Han, S.-C., Shum, K., Jekeli, C., Kuo, C.-Y., Wilson, C. & Seo, K.-W., 2005. Non-isotropic filtering of grace temporal gravity for geophysical signal enhancement. *Geophys. J. Int.*, 163: 18–25. 44, 58, 60, 65

Han, S.-C., Shum, C. K. & Matsumoto, K., 2005b. GRACE observations of m_2 and s_2 ocean tides underneath the Filchner-Ronne and Larsen Ice Shelves, Antarctica. *Geoph. Res. Lett.*, 32: L20311. 97

Heiskanen, W. A. & Moritz, H., 1967. *Physical Geodesy*. W. H. Freeman and C., London. 18, 19, 142

Helmert, F. R., 1884. *Die mathematischen und physikalischen Theorien der höheren Geodäsie*. vol. 2. Teubner (reprinted in 1962 by Minerva GmbH, Frankfurt/Main), Leipzig. 19

Howat, I. M., Joughin, I. & Scambos, T. A., 2007. Rapid changes in ice discharge from Greenland outlet glaciers. *Science*, 315(5818): 1559–1561. 104

Huybrechts, P., 2002. Sea-level changes at the LGM from ice-dynamic reconstructions of the Greenland and Antarctic ice sheets during the glacial cycles. *Quat. Sci. Rev.*, 21: 203–231. 12, 14, 71, 93, 96, 97, 98, 126

Huybrechts, P., Letreguilly, A. & Reeh, N., 1991. The Greenland Ice Sheet and greenhouse warming. *Global Planet. Change*, 3(4): 399–412. 8

Ilk, K.-H., Flury, J., Rummel, R., Schwintzer, P., Haas, B. W., Schröter, J., Stammer, D., Zahel, W., Miller, H., Dietrich, R., Huybrechts, P., Schmeling, H., Wolf, D., Götze, H. J., Riegger, J., Bardossy, A., Güntner, A. & Gruber, T., 2005. *Mass Transport and Mass Distribution in the Earth System*. GOCE-Projektbüro Deutschland, Technische Universität München, GeoForschungsZentrum Potsdam. 6

Ivins, E. R. & James, T. S., 2005. Antarctic glacial isostatic adjustment: A new assessment. *Antarctic Sci.*, 17(4): 541–553. 71, 93, 97

Ivins, E. R., James, T. S., Wu, X., Raymond, C. A. & Yoder, C. F., 2001. Temporal geoid of a rebounding Antarctica and potential measurement by the GRACE and GOCE satellites. In: Sideris, M. (ed.), *Gravity, Geoid and Geodynamics 2000*. Springer, Heidelberg. 97

Jekeli, C., 1981. *Alternative methods to smooth the Earth's gravity field*. Dep. of Geod.

Sci. and Surv., Ohio State Univ., Columbus. 37, 42, 124

Kaufmann, G., 2002. Predictions of secular geoid changes from late Pleistocene and Holocene Antarctic ice-ocean mass imbalance. *Geophys. J. Int.*, 148: 340–347. 97

Kaufmann, G. & Wolf, D., 1996. Deglacial land emergence and lateral upper-mantle heterogeneity in the Svalbard Archipelago – II. Extended results for high-resolution models. *Geophys. J. Int.*, 127: 125–140. 12

Kaufmann, G. & Wolf, D., 1999. Efects of lateral viscosity variations on postglacial rebound: an analytical approach. *Geophys. J. Int.*, 137: 489–500. 12

Kaula, W., 1966. *Theory of satellite geodesy: Applications of satellites to geodesy*. Blaisdell Publishing, Waltham, Massachusetts. 34, 61

King, M. A. & Padman, L., 2005. Accuracy assessment of ocean tide models around Antarctica. *Geoph. Res. Lett.*, 32: L23608. 97

King, M. A., Penna, N. T., Clarke, L. & King, E. C., 2005. Validation of ocean tide models around Antarctica using onshore GPS and gravity data. *J. Geoph. Res.*, 110(B8): B08401. 97

Klemann, V., 2003. *Ebene kompressible viskoelastische Erdmodelle: Anwendung auf glazial-isostatische Deformation der Lithosäre*, Scientific Technical Report STR03/11, GeoForschungsZentrum Potsdam. 20, 22

Klemann, V., Wu, P. & Wolf, D., 2003. Compressible viscoelasticity: stability of solutions for homogeneous plane-earth models. *Geophys. J. Int.*, 153: 569–585. 17

Koch, K. R., 1999. *Parameter Estimation and Hypothsis Testing in Linear Models*. Springer, New York. 95

Kotsakis, C. & Sideris, M. G., 2004. A modified Wiener-type filter for geodetic estimation problems with non-stationary noise. *J. Geodesy*, 75: 647–660. 68

Krabill, W., Abdalati, W., Frederick, E., Manizade, S., Martin, C., Sonntag, J., Swift, R., Thomas, R., Wright, W. & Yungel, J., 2000. Greenland Ice Sheet: High-elevation balance and peripheral thinning. *Science*, 289(5478): 428–430. 14, 104, 105, 111, 112

Krabill, W., Hanna, E., Huybrechts, P., Abdalati, W., Cappelen, J., Csatho, B., Frederick, E., Manizade, S., Martin, C., Sonntag, J., Swift, R., Thomas, R. & Yungel, J., 2004. Greenland Ice Sheet: Increased coastal thinning. *Geophys. Res. Lett.*, 31(24). 111

Křížek, M. & Neittaanmäki, P., 1990. Finite element approximation of variational problems and applications. J. Wiley, New York. 25

Lambeck, K. & Chappell, J., 2001. Sea-level change throughout the last-glacial cycle. *Science*, 292(5517): 679–686. 93, 97, 98, 126

Lambeck, K., Johnston, P. & Nakada, M., 1990. Holocene glacial rebound and sea level change in NW Europe. *Geophys. J. Int.*, 103: 451–468. 12

Larsen, C. F., Eichelmeyer, J. T., Freymueller, J. T. & Motyka, R. J., 2003. Tide gauge records of uplift along the northern Pacific-North American plate boundary. *J. Geophys. Res.*, 108: 2216. 110

Lemke, P., Ren, J., Alley, R. B., Allison, I., Carrasco, J., Flato, G., Fujii, Y., Kaser, G., Mote, P., Thomas, R. & Zhang, T., 2007. Observations: Changes in snow, ice and frozen ground. In: Solomon, S., Qin, D., Manning, M., Chen, Z., Marquis, M., Averyt, K., Tignor, M. & Miller, H. (eds.), *Climate Change 2007: The Physical Science Basis. Contribution of Working Group I to the Fourth Assessment Report of the Intergovernmental Panel on Climate Change (IPCC)*, pp. 337–383. Cambridge University Press, Cambridge, United Kingdom and New York, USA. 7, 112, 123

Lemoine, J.-M., Bruinsma, S., Loyer, S., Biancale, R., Marty, J.-C., Perosanz, F. & Balmino, G., 2007. Temporal gravity field models inferred from GRACE data. *Adv. Space Res.*, pp. 1620–1629. 91

Luthke, S. B. amd Zwally, H. J., Abdalati, W., Rowlands, D. D., Ray, R. D., Nerem, R. S., Lemoine, F. G., McCarthy, J. J. & Chinn, D. S., 2006. Recent Greenland ice mass loss by drainge system from satellite gravity observation. *Sci. Express*, pp. 1286—1289. 32, 88, 112

Lythe, M. B., Vaughan, D. G. & the BEDMAP Consortium, 2001. BEDMAP: A new ice thickness and subglacial topographic model of Antarctica. *J. Geophys. Res.*, 106(B6): 11 335–11 351. 7, 123

Martinec, Z., 1989. Program to calculate the spectral harmonic expansion coefficients of the two scalar fields product. *Comput. Phys. Commun.*, 54: 177–182. 73, 80

Martinec, Z., 1994. The density contrast at the Mohorovičiȟ discontinuity. *Geophy. J. Int.*, 117: 539–544. 73, 145

Martinec, Z., 1998. *Boundary-Value Problems for Gravimetric Determination of a Precise Geoid*. Lecture Notes in Earth Sciences, Springer, Heidelbeg. 19, 79

Martinec, Z., 2000. Spectral-finite element approach to three-dimensional viscoelastic relaxation in a spherical earth. *Geophys. J. Int.*, 142(1): 117–141. 12, 17, 25, 71, 126

Martinec, Z. & Hagedoorn, J., 2005. Time-domain approach to linearized rotational response of a three-dimensional viscoelastic earth model induced by glacial-isostatic adjustment: I. Inertia-tensor perturbations. *Geohys. J. Int.*, 163: 443–462. 12

Martinec, Z. & Wolf, D., 1998. *Explicit Form of the Propagator Matrix of a Multi-Layered, Incompressible Viscoelastic Sphere*. Scientific Technical Report STR98/08, GeoForschungsZentrum Potsdam. 25

Martinec, Z. & Wolf, D., 2005. Inverting the Fennoscandian relaxation-time spectrum in terms of an axisymmetric viscosity distribution with a lithosperic root. *J. Geodyn.*, 39(2): 143–163. 71, 93

Mayer-Gürr, T., 2007. Ein GRACE-Gravitationsfeld berechnet aus der Analyse kurzer Bahnbögen - Die Bonner Lösung ITG-GRACE02S. *Zeitschrift für Vermessungswesen*, 132: 285–291. 32

Mc Carthy, D. D. & Petit, G., 2004. *IERS Conventions (2003)*. IERS Technical Note, 23, Bundesamt fr̈ Kartographie und Geodäsie, Frankfurt am Main. 34

Mitrovica, J., Wahr, J., Matsuyama, I. & Paulson, A., 2005. The rotational stability of an ice-age earth. *Geohys. J. Int.*, 161. 12

Mitrovica, J. X. & Peltier, W. R., 1992. Constraints on mantle viscosity from relative sea level variations in Hudson Bay. *Geophys. Res. Lett.*, 19: 1185–1188. 12

Moore, P. & King, M. A., 2008. Antarctic ice mass balance estimates from GRACE: Tidal aliasing effects. *J. Geophys. Res.*, 113: F02005. 13, 101

Nakada, M., 1999. Implications of a non-adiabatic density gradient for the earth's viscoelastic response to surface loading. *Geohys. J. Int.*, 137. 12

NRC Committee on Earth Gravity from Space, 1997. *Satellite gravity and the geosphere. Contributions to the study of the solid earth and its fluid envelope*. National Academy Press, Washington, D.C. 13, 38

Oppenheimer, M., 1998. Global warming and the stability of the West Antarctic Ice Sheet. *Nature*, 393(6683): 325–332. 7

Paulson, A., Zhong, S. & Wahr, J., 2007a. Limitations on the inversion for mantle viscosity from postglacial rebound. *Geophys. J. Int.*, 168(3): 1195–1209. 13

Paulson, A., Zhong, S. & Wahr, J., 2007b. Inference of mantle viscosity from GRACE and relative sea level data. *Geophys. J. Int.*, 171(2): 497–508. 13, 113, 114, 124

Pearlman, M., Degnan, J. & Bosworth, J., 2002. The International Laser Ranging Service. *Adv. Space Res.*, 30(2): 135–143. 27

Peltier, W. R., 1974. The impulse response of a Maxwell earth. *Rev. Geophys. Space Phys.*, 12: 649–669. 11

Peltier, W. R., 1985. The LAGEOS constraint on deep mantle viscosity: results from a new normal mode method for the inversion of viscoelastic relaxation spectra. *J. Geophys. Res.*, 90: 9411–9421. 25

Peltier, W. R., 2004. Global glacial isostasy and the surface of the ice-age earth: the ICE5G (VM2) model and GRACE. *Annu. Rev. Earth Pl. Sci.*, 32: 111–149. 93, 106, 112, 113, 114

Press, W. H., Teukolsky, S. A., Vetterling, W. T. & Flannery, B. P., 1992. *The Art of Scientific Computing*. Cambridge University Press, Cambrige. 58

Ramillien, G., Lombard, A., Cazenave, A., Ivins, E. R., Llubes, M., Remy, F. & Biancale, R., 2006. Interannual variations of the mass balance of the Antarctica and Greenland ice sheets from GRACE. *Global Planet. Change*, 53(3): 198–208. 88, 97, 124

Rangelova, E. & Sideris, M. G., 2008. Contributions of terrestrial and GRACE data to the study of the secular geoid changes in North America. *J. Geodyn.*, 46: 131–143. 13

Rangelova, E., van der Wal, W., Braun, A., Sideris, M. G. & Wu, P., 2007. Analysis of Gravity Recovery and Climate Experiment time-variable mass redistribution signals over North America by means of principal component analysis. *J. Geophys. Res.*, 112: F03002. 13

Reigber, C., Schmidt, R., Flechtner, F., König, R., Meyer, U., Neumayer, K.-H., Schwintzer, P. & Zhu, S., 2005. An Earth gravity field model complete to gegrees and order 150 from GRACE: EIGEN-GRACE02S. *J. Geodyn.*, 39: 1–10. 57

Remy, F. & Frezzotti, M., 2006. Antarctica ice sheet mass balance. *C. R. Geosci.*, 338: 1084–1097. 93

Rignot, E. & Kanagaratnam, P., 2006. Changes in the velocity structure of the Greenland Ice Sheet. *Science*, 311(5763): 986–990. 14, 112

Rignot, E. & Thomas, R. H., 2002. Mass balance of polar ice sheets. *Science*, 297(5586): 1502–1506. 14, 70, 93, 97, 125

Rignot, E., Casassa, G., Gogineni, P., Krabill, W., Rivera, A. & Thomas, R., 2004. Accelerated ice discharge from the Antarctic Peninsula following the collapse of Larsen B Ice Dhelf. *Geophys. Res. Lett.*, 31(18): L18401. 70, 93, 96, 98

Rignot, E., Bamber, J. L., Van Den Broeke, M. R., Davis, C., Li, Y., Van De Berg, W. J. & Van Meijgaard, E., 2008. Recent Antarctic ice mass loss from radar interferometry and regional climate modelling. *Nature Geosci.*, 1(2): 106–110. 8, 9, 124, 125, 126, 127, 133

Rowlands, D. D., Luthcke, S. B., Klosko, S. M., Lemoine, F. G. R., Chinn, D. S., McCarthy, J. J., Cox, C. M. & Anderson, O. B., 2005. Resolving mass flux at high spatial and temporal resolution using GRACE intersatellite measurements. *Geophys. Res. Lett.*, 32: L04310. 31, 138

Sabadini, R. & Vermeersen, L. L. A., 2002. Long-term rotation instabilities of the earth: A reanalysis. In: Mitrovica, J. X. & Vermeersen, L. L. A. (eds.), *Ice Sheets, Sea Level and the Dynamic Earth*, vol. 29. American Geophys. Union, Washington, D.C. 12

Sasgen, I., Martinec, Z. & Fleming, K., 2006. Wiener optimal filtering of GRACE data. *Stud. Geophys. Geod.*, 50(4): 499–508. 5, 37, 42, 43, 44, 69, 71, 73, 90, 91, 94, 124

Sasgen, I., Martinec, Z. & Fleming, K., 2007b. Regional ice-mass changes and glacial-isostatic adjustment in Antarctica from GRACE. *Earth Planet. Sci. Lett.*, 264: 391–401. 5, 85, 101, 104, 108, 113, 124, 125, 126, 129

Sasgen, I., Martinec, Z. & Bamber, J., 2008. Combined InSAR and GRACE estimate of West Antarctic glacial changes. *Geophys. Res. Lett.*, *in prep.* 5, 85, 104

Sasgen, I., Wolf, D., Martinec, Z., Klemann, V. & Hagedoorn, J., 2005. Geodetic signatures of glacial changes in Antarctica: rates of geoid-height change and radial displacement due to present and past ice-mass variations. *GeoForschungsZentrum Scientific Technical Report*, STR05/01. 17

Sasgen, I., Martinec, Z. & Fleming, K., 2007a. Wiener optimal combination and evaluation of the Gravity Recovery and Climate Experiment (GRACE) gravity fields over Antarctica. *J. Geophys. Res.*, 112(B4). 5, 13, 91

Savitzky, A. & Golay, M., 1964. Smoothing and differentiation of data by simplified least squares procedures. *Anal. Chem.*, 36: 1627–1639. 44, 45

Scambos, T. A., Bohlander, J. A., Shuman, C. A. & Skvarca, P., 2004. Glacier acceleration and thinning after ice shelf collapse in the Larsen B embayment, Antarctica.

Geophys. Res. Lett., 31(18): L18402. 8, 93

Schmidt, R., 2007. *Zur Bestimmung des cm-Geoids und dessen zeitlicher Variationen mit GRACE*, Scientific technical report, Deutsches GeoForschungsZentrum. 13, 30, 31, 34, 38

Schmidt, R., Flechtner, F., Meyer, U., Neumayer, K.-H., Dahle, C., König, R. & Kusche, J., 2008. Hydrological signals observed by the GRACE satellites. *Surv. Geophys.*, 10.1007/s10712-008-9033-3. 40, 124, 125

Schoof, C., 2007. Marine ice-sheet dynamics. part 1. the case of rapid sliding. *J. Fluid Mech.*, 573: 27–55. 7

Schrama, E. J. O. & Visser, P. N. A. M., 2007. Accuracy assessment of the monthly GRACE geoids based upon a simulation. *J. Geodesy*, 81: 67–80. 78, 124

Schwintzer, P., Reigber, C., Massmann, F., Barth, W., Raimondo, J., Gerstl, M., Li, H., Biancale, R., Balmino, G., Moynot, B., Lemoine, J., Marty, J., Boudon, Y. & Barlier, F., 1991. *A New Earth Gravity Field Model in Support of ERS-1 and SPOT-2*, Final report to the german space agency (DARA) and the french space agency (CNES), DGFI München, GRGS Toulouse. 33

Seo, K.-W. & Wilson, C. R., 2005. Simulated estimation of hydrological loads from GRACE. *J. Geodesy*, 78: 442–456. 60, 91

Shepherd, A. & Wingham, D., 2007. Recent sea-level contributions of the Antarctic and Greenland ice sheets. *Science*, 315(5818): 1529–1532. 7, 123, 124, 134

Siegert, M. J., 2001. *Ice Sheets and Late Quaternary Environmental Change*. John Wiley & Sons, Chichester, United Kingdom. 7

Steffen, H., Denker, H. & Müller, J., 2008. Glacial-isostatic adjustment in fennoscandia from grace data and comparison with geodynamical models. *J. Geodyn.*, in press. 13

Swenson, S. & Wahr, J., 2002. Methods for inferring regional surface-mass anomalies from Gravity Recovery and Climate Experiment (GRACE) measurements of time-variable gravity. *J. Geophys. Res.*, 107. 58, 79, 80, 81, 88, 124

Swenson, S. & Wahr, J., 2006. Post-processing removal of correlated errors in GRACE data. *Geophys. Res. Lett.*, 33(8): L08402. 37, 40, 44, 45, 46, 73, 90, 125

Tamisiea, M., Leuliette, E., Davis, J. & Mitrovica, J., 2005. Constraining hydrological and cryospheric mass flux in southeastern Alaska using space-based gravity measurements. *Geophys. Res. Lett.*, 32: L20501. 110

Tamisiea, M. E., Mitrovica, J. X. & Davis, J. L., 2007. GRACE gravity data constrain ancient ice geometries and continental dynamics over Laurentia. *Science*, 316: 881–883. 13, 113, 124

Tapley, B. & Reigber, C., 2001. The GRACE Mission: Status and future plans. *Eos Trans. AGU*, 82(47), Fall Meet. Suppl. G41C-02. 27, 67, 124

Tapley, B., Bettadpur, S., Watkins, M. & Reigber, C., 2004a. The Gravity Recovery and Climate Experiment: Mission overview and early results. *Geophys. Res. Lett.*, 31. 13, 27, 67, 87, 124

Tapley, B. D., Bettadpur, S., Ries, J. C., Thompson, P. F. & Watkins, M. M., 2004. GRACE Measurements of Mass Variability in the Earth System. *Science*. 5, 27, 57, 124

Tarantola, A., 2005. *Inverse Problem Theory and Methods for Model Parameter Estimation*. Society for Industrial and Applied Mathematics, Philadelphia. 128, 145

Thomas, R., Rignot, E., Casassa, G., Kanagaratnam, P., Acuña, C., Akins, T., Brecher, H., Frederick, E., Gogineni, P., Krabill, W., Manizade, S., Ramamoorthy, H., Rivera, A., Russel, R., Sonntag, J., Swift, R., Yungel, J. & Zwally, J., 2004. Accelerated sea-level rise from West Antarctica. *Science*, 306(5694): 255–258. 8, 14, 70, 93, 97, 98, 123

Tromp, J. & Mitrovica, J. X., 1999a. Surface loading of a viscoelastic earth - i. General theory. *Geohys. J. Int.*, 137: 847–855. 12

Tromp, J. & Mitrovica, J. X., 1999b. Surface loading of a viscoelastic earth - ii. Spherical models. *Geohys. J. Int.*, 137: 856–872. 12

Tushingham, A. M. & Peltier, W. R., 1991. ICE-3G: a new approach of the late pleistocene deglaciation based upon geophysical predictions of post-glacial relative sea level change. *J. Geophys. Res.*, 96: 4497–4523. 112, 114

van de Berg, W., van den Broeke, M., Reijmer, C. & van Meijgaard, E., 2005. Characteristics of the Antarctic surface mass balance (1958-2002) using a Regional Atmospheric Climate Model. *Ann. Glaciol.*, 41: 97–104. 8

van de Berg, W., van den Broeke, M., Reijmer, C. & van Meijgaard, E., 2006. Reassessment of the Antarctic surface mass balance using calibrated output of a regional atmospheric climate model. *J. Geophys. Res.*, 111: D11104. 125

van den Broeke, M., van de Berg, W. & van Meijgaard, E., 2006. Snowfall in coastal-West Antarctica much greater than previously assumed. *Geophys. Res. Lett.*, 33: L02505. 125

van den Broeke, M., van de Berg, W. J., van Meijgaard, E. & Reijmer, C., 2006. Identification of Antarctic ablation areas using a regional atmospheric climate model. *J. Geophys. Res.*, 111: D18110. 125

Varshalovich, D. A., Moskalev, A. N. & Khersonskii, V. K., 1989. *Quantum Theory of Angular Momentum*. World Scientific, Singapore. 59, 142, 143

Vaughan, D. G., Bamber, J. K., Giovinetto, M., Russell, J. & Cooper, P. R., 1999. Reassessment of net surface mass balance in Antarctica. *J. Climate*, 12: 933–946. 7

Velicogna, I. & Wahr, J., 2005. Greenland mass balance from GRACE. *Geophys. Res. Lett.*, 32(18): L18505. 88, 112

Velicogna, I. & Wahr, J., 2006. Measurements of time-variable gravity show mass loss in Antarctica. *Science*, 311(5768): 1754–1756. 73, 88, 112, 124

Vermeersen, L. L. A. & Sabadini, R., 1997. A new class of stratified viscoelastic models by analytical techniques. *Geophys. J. Int.*, 129: 531–570. 12

Vermeersen, L. L. A., Sabadini, R. & Spada, G., 1996. Analytical visco-elastic relaxation models. *Geophys. Res. Lett.*, 23: 697–700. 12

Wagner, C., McAdoo, D., Klokočník, J. & Kostelecký, J., 2006. Degradation of geopotential recovery from short repeat-cycle orbits: Application to GRACE monthly fields. *J. Geodesy*, 80: 94–103. 39

Wahr, J., Molenaar, M. & Bryan, F., 1998. Time variability of the Earth's gravity field: Hydrological and oceanic effects and their possible detection using GRACE. *Journal of Geophysical Research*, 103(B12): 30205–30230. 20, 42, 58

Wahr, J., Swenson, S., Zlotnicki, V. & Velicogna, I., 2004. Time-variable gravity from GRACE: First results. *Geophys. Res. Lett.*, 31(B9). 40, 42, 48, 61, 62

Watkins, M., 2003. *JPL Level-2 Processing Standards Document for Product Release 02, Gravity Recovery and Climate Experiment (GRACE)*. Jet Propulsion Laboratory, Pasadena, Rev. 1.0, GRACE 327-744. 72

Watkins, M. & Dah Ning, Y., 2007. *JPL Level-2 Processing Standards Document for Level-2 Product Release 04*. Jet Propulsion Laboratory, Pasadena, Rev. 4.1, GRACE 327-744. 28, 90

Weertman, J., 1974. Stability of the junction of an ice sheet and an ice shelf. *J. Glaciol.*, 13(67): 3–13. 7

Weisstein, E. W., 2008. *A Wolfram Web Resource*. 80

Wickert, J., Beyerle, G., König, R., Heise, S., Grunwaldt, L., Michalak, G., Reigber, C. & Schmidt, T., 2005. GPS radio occultation with CHAMP and GRACE: A first look at a new and promising satellite configuration for global atmospheric sounding. *Ann. Geophys.*, 23: 653–658. 27, 31

Wieczorek, M. A. & Simons, F. J., 2005. Localized spectral analysis on the sphere. *Geophys. J. Int.*, 162(3): 655–675. 44

Wiener, N., 1949. *Extrapolation, Interpolation, and Smoothing of Stationary Time Series*. Wiley, New York. 58

Wolf, D., 1985c. The normal modes of a layered, incompressible Maxwell half-space. *J. Geophys.*, 57: 106–117. 25

Wolf, D., 1987. An upper bound on lithosphere thickness from glacio-isostatic adjustment in Fennoscandia. *J. Geophys.*, 61: 141–149. 12

Wolf, D., 1997. *Gravitational Viscoelastodynamics for a Hydrostatic Planet*. Series C, No. 452, Verlag der Bayerischen Akademie der Wissenschaften, München. 17

Wolf, D., 2003. *Continuum Mechanics in Geophysics and Geodesy: Fundamental Principles*. Schriftenreihe der Institute des Studiengangs Geodäsie und Geoinformatik, Universität Stuttgart, Stuttgart. 17, 22, 24

Wolf, D., Klemann, V., Wünsch, J. & Zhang, F.-P., 2006. A reanalysis and reinterpretation of geodetic and geological evidence of glacial-isostatic adjustment in the Churchill region, Hudson Bay. *Surv. Geophys.*, 27: 19–61. 106, 114

Wolf, M., 1969. Direct measurement of the Earth's gravitational potential using a satellite pair. *J. Geophys. Res.*, 74: 5295–5300. 27

Wu, P. & Ni, Z., 1996. Some analytical solutions for the viscoelastic gravitational relaxation of a two-layer non-self-gravitating incompressible spherical earth. *Geophys.*

J. Int., 126: 413–436. 12

Wu, P. & Peltier, W. R., 1982. Viscous gravitational relaxation. *Geophys. J. Roy. Astr. S.*, 70: 435–486. 12, 25, 81, 92

Wu, P., Ni, Z. & Kaufmann, G., 1998. Postglacial rebound with lateral heterogeneities: from 2D to 3D modeling. In: Wu, P. (ed.), *Dynamics of the Ice Age Earth: A Modern Perspective*, pp. 557–582. Trans Tech Publications, Hetikon. 12

Yuen, D. A. & Peltier, W. R., 1982. Normal modes of the viscoelastic earth. *Geophys. J. Roy. Astr. S.*, 69: 495–526. 12

Zhong, S. J., Paulson, A. & Wahr, J., 2005. Three-dimensional finite-element modelling of earth's viscoelastic deformation: effects of lateral variations in lithospheric thickness. *Geohys. J. Int.*, 155: 679–695. 12

Zwally, H., Giovinetto, M., Li, J., Cornejo, H., Beckley, M., Brenner, A. & Saba, J.L.and Yi, D., 2005. Mass changes of the Greenland and Antarctic ice sheets and shelves and contributions to sea-level rise: 1992-2002. *J. Glaciol.*, 51: 509–527. 124

Zwartz, D., Bird, M., Stone, J. & Lambeck, K., 1998. Holocene sea-level change and ice-sheet history in the Vestfold Hills, East Antarctica. *Earth Planet. Sci. Lett.*, 155: 131–145. 71

Zweck, C. & Huybrechts, P., 2005. Modelling the Northern Hemisphere ice sheet during the last glacial cycle and glaciological sensitivity. *J. Geophys. Res.*, 110: D07103. 11, 14, 105, 114

Abbreviations

1. Acronyms of space-geodetic projects, instrumentation, data bases and organizations

Abbreviation	*Page*	*Description*
ACC	27	Accelerometer (GRACE instrumentation)
CNES	85	Centre National d'Ètudes Spatiales
CSR	27	Center for Space Research
DLR	27	Deutsche Zentrum für Luft- und Raumfahrt
ECMWF	34	European Centre for Medium-Range Weather Forecasts
ERS-1|ERS-2	9	European Remote Sensing Satellites
GFZ	5	Deutsches GeoForschungsZentrum
GPS	13	Global Positioning System
GRACE	5	Gravity Recovery and Climate Experiment (mission launched 17th March 2002)
GRIP	105	Greenland Ice Core Project
ICESat	9	Ice, Cloud, and Land Elevation Satellite (mission launched 12th January 2003)
IERS	34	International Earth Rotation and Reference Systems Service
ILRS	27	International Laser Ranging Service
InSAR	9	Interferometric Synthetic Aperture Radar
ISDC	27	Information Systems and Data Center
JPL	27	Jet Propulsion Laboratory
KBR	27	K-band microwave ranging system (GRACE instrumentation)
LAGEOS	13	Laser Geodynamics Satellite
NASA	27	National Aeronautic and Space Agency
PO.DAAC	27	Physical Oceanography Distributed Active Archive Center
PREM	20	Preliminary Reference Earth Model
SCA	27	Star camera assembly (GRACE instrumentation)
SDS	85	Science Data System centres (CSR, GFZ and JPL)
SST	9	Satellite-to-satellite tracking

2. Text tokens

Abbreviation	*Page*	*Description*
AIS	67	Antarctic Ice Sheet
BP	5	before present
ESL	7	equivalent sea level
GIA	5	glacial-isostatic adjustment
LGM	5	Last Glacial Maximum ($\sim$21 ka BP)

3. Load models

Abbreviation	*Page*	*Description*
ANU	123	Pleistocene deglaciation model for Antarctica based on geomorphological data
GREEN1	111	Pleistocene deglaciation model for Greenland based on geomorphological data
HUY	123	Pleistocene deglaciation model for Antarctica based on numerical modelling
ICE-3G|ICE-5G	105	Global pleistocene deglaciation models based on geomorphological data
NAWI	105	Pleistocene deglaciation model for the Northern Hemisphere based on numerical modelling
OMCT	34	Ocean Model for Circulation and Tides
WGHM	14	WaterGAP Global Hydrology Model

List of Figures

List of Tables

Acknowledgements

I sincerely thank my supervisor Prof. Dr. Zdeněk Martinec; I have profited very much from his expertise as a theoretician, geodesist and solid-Earth geophysicist, and most of all, from his excellent teaching. While being member of the Earth System Modelling group at GFZ for several years, I found the generosity with which Prof. Martinec displays to other peoples' scientific interests, how he contributes his ideas, invests time for thorough explanations and shares his enthusiasm, to be outstanding. I would like to thank Prof. Dr. Maik Thomas for his offer to supervise my work close to its final stage and for writing a review. I would also like to thank Dr. Henryk Dobslaw for providing the ECMWF data, Susanna Werth and Dr. Andreas Güntner for providing me with WHGM model output and Prof. Dr. Jonathan Bamber for the InSAR data for Antarctica. Many thanks also to Dr. Volker Klemann for sharing his numerical codes with me and for his thorough scientific advices, as well as Dr. Kevin Fleming, Dr. Jan Hagedoorn and Dr. Erik Ivins. I thank Dr. Roland Schmidt and Dr. Frank Flechtner for providing background information on GRACE processing and their support during the last years, and Veronika Söllner for her organizational assistance. Finally, I would like to thank Prof. Dr. Detlef Wolf and Prof. Dr. Markus Rothacher for their support in letting me pursue my scientific interest, and Dr. Wolfgang Dierking, Prof. Dr. Lemke of AWI, and Prof. Dr. Christoph Reigber for their interest in my current and future work.

This work was funded within the Helmholtz Earth Observing System (EOS) Ph. D. program *[online]*, Topic 1, Ocean and Cryosphere, headed by Prof. Dr. Lemke (AWI).